Summer 1999

Large Amplitude Pitching of Supermaneuver Delta Wings Including Flow Control

Yahia A. Abdelhamid
Old Dominion University

LARGE AMPLITUDE PITCHING OF SUPERMANEUVER DELTA WINGS INCLUDING FLOW CONTROL

by

Yahia A. Abdelhamid
B.Sc. May 1990, Cairo University, Egypt
M.Sc. October 1993, Cairo University, Egypt

A Dissertation Submitted to the Faculty of Old Dominion University in Partial Fulfillment of the Requirements for the Degree of

DOCTOR OF PHILOSOPHY

AEROSPACE ENGINEERING

OLD DOMINION UNIVERSITY
August 1999

Approved by:

Osama A. Kandil (Director)

Colin P. Britcher

Brett A. Newman

Tin-Chee Wong

ABSTRACT

LARGE AMPLITUDE PITCHING OF SUPERMANEUVER DELTA WINGS INCLUDING FLOW CONTROL

Yahia A. Abdelhamid
Old Dominion University, 1999
Director: Dr. Osama A. Kandil

The unsteady, three-dimensional Navier-Stokes equations are solved to simulate and study the aerodynamic response of a delta wing undergoing large amplitude pitching motion up to 90° angle of attack. The primary model under consideration consists of a 76° swept, sharp-edged delta wing of zero thickness, initially at zero angle of attack. The freestream Mach number and Reynolds number are 0.3 and 0.45×10^6, respectively. The governing equations are solved time-accurately using the implicit, upwind, Roe flux-difference splitting, finite-volume scheme. Both laminar and turbulent flow solutions are investigated. In the laminar flow solutions, validation of the computational results is carried out using existing experimental data, and shows good agreement.

The effect of reduced frequency of the wing motion is then presented and a grid refinement study is introduced. In the turbulent flow simulations, both Baldwin-Lomax and Spalart-Allmaras turbulence models are used and the results are compared with those of the laminar solution and experimental data as well. A sinusoidal pitching motion of the wing is also investigated in the present work. The computational results provide complete information and details about the flowfield response, which are difficult to

obtain from experiment. A feasibility study of using one of the flow control techniques, blowing, to enhance maneuverability is introduced.

The investigation of the unsteady flow over a wide range of angles of attack provides crucial understanding of the variations of the leading edge vortex cores, their breakdown behavior, aerodynamic hysteresis, and wing aerodynamic characteristics at very high angle of attack. The current study shows that numerical simulations in the very high angle of attack range are obtainable. Such calculations were thought to be unattainable as recently as the 1980's.

ACKNOWLEDGMENTS

Praise and thanks are due to GOD to whom I owe everything

I would like to express my sincere thanks and gratitude to my advisor, Professor Osama A. Kandil, Eminent Scholar of Aerospace Engineering, for his advice and encouragement during the course of this research work. Without his support I wouldn't have been able to finish this work.

Special thanks are extended to the members of my dissertation committee, Prof. Colin P. Britcher and Prof. Brett A. Newman of the Aerospace Engineering Department at Old Dominion University and Dr. Tin-Chee Wong, for their review of this dissertation.

I would like also to express my love, gratitude and appreciation to my parents, my wife, Abir, and my children, Omar and Asmaa, for their continuous support, encouragement and patience.

This research work has been supported partially by the Unsteady Aerodynamics Branch of NASA Langley Research Center under NASA Grant No. NAG-1-648.

TABLE OF CONTENTS

LIST OF TABLES

LIST OF FIGURES

LIST OF SYMBOLS

a	Local speed of sound
a_w	Wing body acceleration
A	Inviscid Jacobian matrix, Aspect ratio
C	Sutherland's constant, Root chord
C^-, C^-	Wave velocities
C_D	Drag coefficient
C_L	Lift coefficient
Cp	Specific heat at constant pressure, Pressure coefficient
CFL	Courant-Fridrichs-Lewy number
e	Total energy per unit mass
E, F, G, H	Inviscid fluxes
E_v, F_v, G_v, H_v	Viscous fluxes
f	Frequency, cycles/second
i , j , k	Grid indices
I	Identity matrix
J, J^{-1}	Jacobian and inverse Jacobian of coordinate transformations
k	Thermal conductivity coefficient, Reduced frequency (Ω C / 2 a_∞)
L	Characteristic length
M	Mach number
n	Normal to the surface
$\hat{n}$	Unit normal to the surface

p	Static pressure
Pr	Prandtl number
$\bar{q}$	Flow field vector
Q	Heat-flux component
$\bar{r}$	Position vector
Re	Reynolds number
R^+, R^-	Non-negative and non-positive Riemann invariants
t	Nondimensional time
T	Static temperature
u_1, u_2, u_3	Cartesian components of velocity
U_1, U_2, U_3	Contravariant Velocities
x_1, x_2, x_3	Cartesian coordinates (normalized with respect to chord length)
X, Y, Z	Cartesian coordinates (normalized with respect to chord length)
y+	Law-of-the-wall variable

Greek Symbols

α	Angle of attack
γ	Specific heat ratio
δ_{ij}	Kronecker delta function
λ_i	Eigenvalues
Λ	Diagonal eigenvalue matrix
μ	Molecular viscosity
$\xi, \eta, \zeta ; \xi^i$	Body-conformed coordinates (computational coordinates)

ρ	Density
τ	Shear stress tensor
∂	Partial derivative
∇	Backward differencing operator or gradient
Δ	Forward differencing operator, time increment
$\vec{\Omega}$	Angular velocity vector

Subscripts

L	Values obtained from the left side of a cell face
N	Normal
R	Values obtained from the right side of a cell face
∞	Free-stream value

Superscripts

n, n+1	Time levels
–	Non-positive eigenvalues
+	Non-negative eigenvalues

CHAPTER 1

INTRODUCTION

1.1 Motivation

The ability of modern fighter aircraft to fly and maneuver at high angles of attack is of prime importance for aircraft design. At high angles of attack, unsteady aerodynamic effects may have a major impact on the maneuverability and controllability of an airplane. Currently, some modern fighter airplanes are capable of performing transient maneuvers involving high pitch rates to extreme angles of attack. The advent of innovative high angle of attack control effectors such as thrust vectoring and forebody controls will enable ever greater capability to effectively exploit a substantially enlarged envelope for air combat. With the emphasis on aggressive maneuvering capability near or beyond the stall angle of attack for future airplanes, research is needed to understand the effects of large-amplitude unsteady motions at high angles of attack on stability, control and performance.

The complicated physics associated with high angle of attack vortical flows involves massive separation, leading edge vortices, vortex burst, flow interactions, asymmetric flows, buffet, and vortex breakdown, which result in a penalty of undesirable unsteadiness in the flowfield. In order to exploit these flight regimes and extend current

---

This dissertation is based on the format of the Journal of Fluid Mechanics.

performance envelopes, a better understanding of these unsteady, vortical flows associated with maneuvering swept wings is required.

Present prediction methods of the coefficients of aerodynamic derivatives depend on simplified theoretical models, which cannot be applied in all flowfield regimes. In this research work, the aim is focused on analyzing and understanding the flowfield behavior at very high angles of attack and explaining the vortex breakdown phenomena in more detail, which could be useful for further advanced design configurations. Computational Fluid Dynamics (CFD) plays an important role in the design process by providing detailed flowfield information at a relatively low cost that is unavailable with experiment alone. CFD reduces design cycle time and provides information that is complementary to wind tunnel and flight-test data, see Fig. 1.1. The main advantage of CFD over the experimental methods is that results can be obtained for many configurations using the same computational scheme with low cost. Also of prime importance are the flowfield details, which can be obtained extensively using CFD.

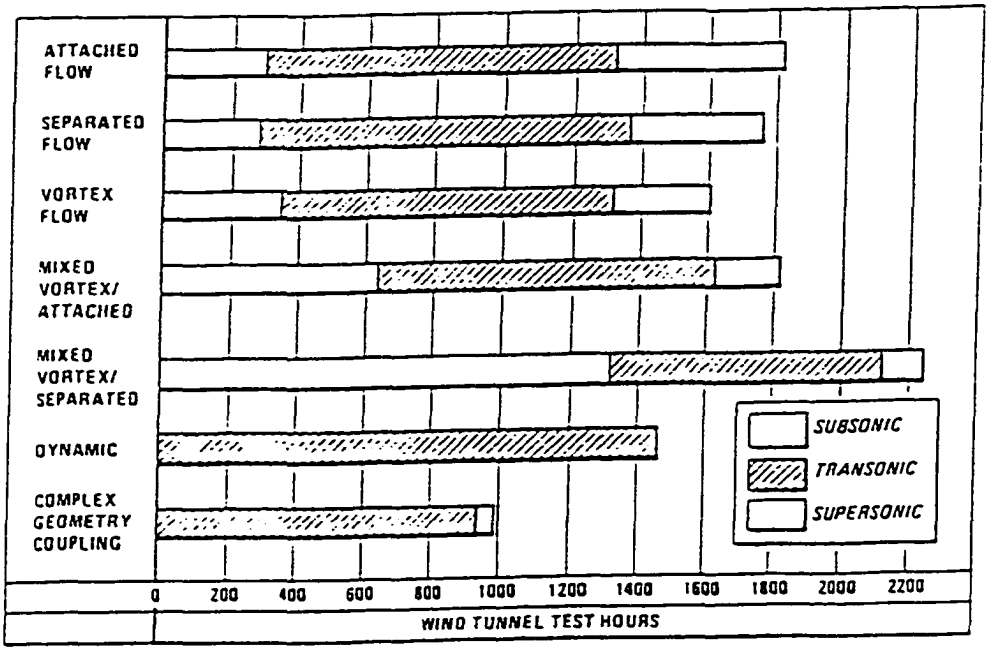

Figure 1.1 Breakout of F-16 wind tunnel testing by flowfield complexity. Young (1983)

Although extensive computational and experimental work has been done in the area of steady vortex-dominated flows, very limited research work exists in the area of unsteady vortex-dominated flows. This is one of the motivations for the present study. Using the limited available experimental data to serve as benchmarks for validating the computational results, the main objective for this study is to accurately and efficiently resolve the unsteady flowfield at very large angle of attack computationally.

1.2 Present Work

In the present study, both the unsteady, laminar, full Navier-Stokes equations and unsteady, Reynolds Averaged Navier Stokes (RANS) equations are used to investigate the aerodynamics of supermaneuver aircraft approximated by a delta wing planform including flow control. All the computational runs are three-dimensional flowfield cases. In Chapter 2 a literature survey of research work concerning high angle of attack aerodynamics is introduced. Reviews of analytical, experimental, and computational research work are covered. Emphasis is focused on work related to low-aspect-ratio delta wings.

The formulation of the problem is presented in Chapter 3. The unsteady, compressible, three-dimensional Navier-Stokes equations are presented. The Navier-Stokes equations are written in the flux-vectored, conservative, dimensionless form in terms of time dependent body conformed coordinates. In Chapter 4, the computational scheme used in the present study is discussed in detail. The computational scheme is an implicit, upwind, flux-difference splitting, finite volume scheme. It employs the flux-difference splitting scheme of Roe, which is based on the solution of the approximate

one-dimensional Riemann problem in each of the three directions. Two turbulence models are used in the current study (Baldwin-Lomax and Spalart-Allmaras) are presented. This Chapter concludes with a discussion of the boundary and initial conditions.

Chapter 5 covers the present computational results for the laminar flow cases. A validation case is presented first to compare the current results with the available experimental data. Three cases with ramp pitching motion and with different reduced frequencies are studied to investigate the effect of reduced frequency. The effects of grid refinement are also investigated. Turbulent-flow cases are presented in Chapter 6. The turbulence models of Baldwin-Lomax (zero order) and Spalart-Allmaras (one equation) are used for turbulent-flow simulations. A comparative study is presented to show the effect of different turbulence models on the computed results. A sinusoidal case is also introduced in this Chapter to study the hysteresis effects of unsteady motion.

In Chapter 7 flow control using a new blowing technique is introduced. Blowing at the trailing edge with an angle equal to 20° downward is used to highlight its applicability for active control of the unsteady vortex breakdown phenomenon and investigate its use to increase the maneuverability of fighter aircraft. Finally, concluding remarks and recommendations for future work are presented in Chapter 8.

CHAPTER 2

LITERATURE SURVEY

2.1 Introduction

Extensive analytical, experimental and numerical research work on the aerodynamic characteristics of wings and bodies at high angles of attack has been reported in literature from the 1930's until the present time. One of the most important developments in airplane design was the swept wing. The swept wing, or a wing that angles back away from the nose, allowed planes to fly faster than straight-winged planes. These swept wings evolved into delta wings, which are shaped like triangles. These wings provide better control and mobility for today's high technology jets. One of the examples of planes that use this type of design is the McDonnell Douglas F-15 Eagle. The structural advantages of delta wings, supersonic cruise characteristics and high subsonic maneuver capability, made them the subject of extensive experimental and theoretical investigation.

Polhamus (1971) reported:

"Throughout the history of aeronautics, one of the major wing design considerations has been the avoidance of flow separation. However, as wing sweep angles were increased and the thickness decreased, to avoid undesirable effects, the maintenance of attached flow became increasingly difficult and the origin and spread of the separated flow was generally unpredictable causing many performance, stability, and control problems. Although many techniques have been developed to alleviate these problems, it has quite often [been] necessary to apply them by means of rather complicated variable geometry devices in order to satisfy the wide range of conflicting flow conditions encountered in the various regions of the flight envelope of modern high speed aircraft. A rather historic departure from the time honored "attached flow" wing design concept occurred in the late 1950's when, based on studies made primarily at the Royal Aircraft Establishment, the British embarked on the design of a supersonic transport aircraft which was based on a slender, sharp-edge wing concept to minimize cruise wave drag but in

which the flow (except for the cruise condition) was allowed to separate along the entire leading edge and produce the well-known leading edge spiral vortex. The primary advantages of this approach are that one type of stable flow can be maintained over a wide range of attitudes and Mach numbers without the need for flow control devices, and that the additional lift resulting from the leading edge vortex flow tends to eliminate the need for high-lift devices. Competing with these advantages, of course, is the disadvantage of increased drag resulting from the loss of leading edge thrust. The resulting British-French "Concorde" project, the similar Russian TU-144 design, and the interest in slender hypersonic vehicles have added impetus to the study of leading edge vortex flows."

Flow around slender wings was initially investigated for supersonic applications. As a result of experimental work in the late 1940's and early 1950's, it was discovered that by replacing the round leading edge by a sharp leading edge, the lift was greatly enhanced. The use of the sharp leading edge created the well-known separation-induced, highly stable, leading edge vortices. For high angles of attack at subsonic speeds, this type of vortex flow forms and results in a large lift increment. The vortex-induced reattachment also avoids the undesirable trailing edge separation and attendant stall characteristics that often plague conventional swept wings. Therefore, at low speeds and moderate angles of attack, the delta wing provides high lift by virtue of the strong leading edge vortices. A good illustration of the type of flows that can be expected on aircraft and missile configurations at moderate and high angles of attack can be obtained from the observation of flows over slender sharp edge delta wings.

According to Polhamus (1971) the total lift generated over delta wings consists of a potential flow term, C_{LP}, and a vortex-lift term, C_{LV}, as seen in Figure 2.1. The expressions for C_{LP} and C_{LV} take the following forms

$$C_{LP} = K_P \sin\alpha \cos^2\alpha \qquad (2.1)$$

$$C_{LV} = K_V \sin^2\alpha \cos\alpha \qquad (2.2)$$

where K_P is the normal force slope given by small disturbance potential flow lifting-surface theory, and K_V is the vortex lift constant and can be obtained from the overall lift

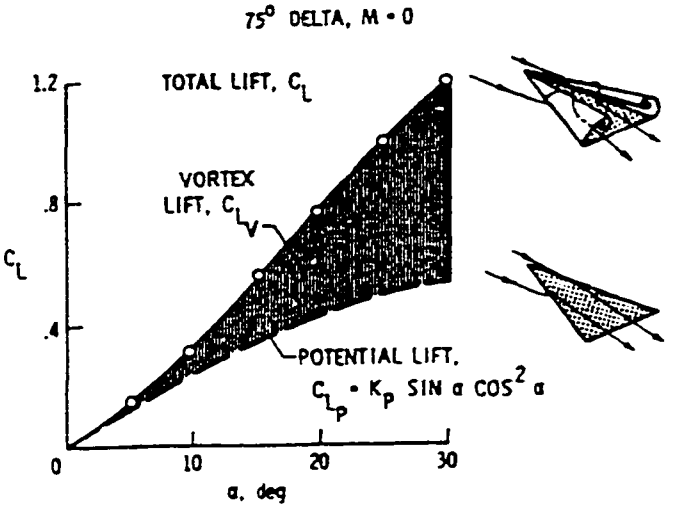

Figure 2.1: Illustration of vortex lift for a 75° delta wing. Polhamus (1971)

and induced drag obtained from an accurate lifting-surface theory, and α is the angle of attack. The above expressions give very good result for angles of attack lower than 20°. Figure 2.2 gives the potential flow lift constant K_P and the vortex lift constant K_V for delta wings in incompressible flow as a function of aspect ratio, where A in Figure 2.2 denotes aspect ratio.

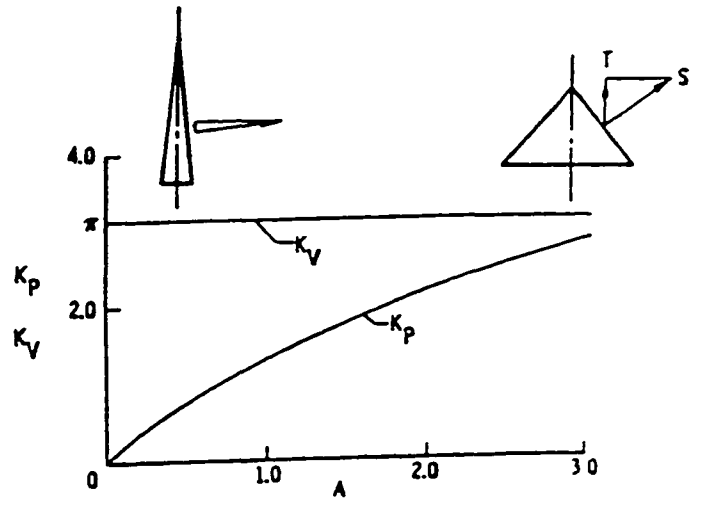

Figure 2.2: Variation of K_P and K_V with A for delta wings; M=0. Polhamus (1971)

While K_P shows rapid increase with aspect ratio, K_V increases only slightly with aspect ratio. Also the magnitude of K_V is larger than K_P for low aspect ratio delta wings.

The flow configurations over a delta wing with leading edge sweep angle Λ, which is positioned at an angle of attack α at Mach number M_∞, can be classified in accordance to the angle of attack measured normal to the leading edge and the normal component of the Mach number $\alpha_N = \tan^{-1}(\tan \alpha/\tan \Lambda)$ and $M_N = [1-\sin^2\Lambda.\cos^2\alpha]^{1/2}$, presented in Figure 2.3. When the Mach number normal to the leading edge M_N is less than 1, the subsonic rolled-up vortex structure is obtained even when the external flow is supersonic. Thus, vortical flow structures which are identical to those obtained at subsonic speeds are also observed over a very slender delta wing in supersonic flow, including the transition to asymmetric vortex structure. However, for supersonic Mach number normal to the leading edge, $M_N > 1$, there is a Prandtl-Meyer expansion at the leading edge on the leeward side of the wing, causing an over-expansion which requires a terminating shock wave. As the angle of attack increases, the terminating shock wave strength increases, causing separation of the boundary layer on the wing surface. At moderate angles of attack, the separated boundary layer reattaches to form a separation bubble. At higher angles of attack, the separating boundary layer detaches from the surface and rolls up to concentrated vortices with the terminating shock waves.

These types of flows are in general the result of three-dimensional separation. The theoretical analyses of such complicated three-dimensional flows with strong-viscous-inviscid interactions are very difficult to obtain. The concentrated vortex lines-tubes, rotating around their viscous cores, are known to "breakdown" under certain flow

conditions. Vortex breakdown affects the induced flowfield and causes loss of aerodynamic lift force, leading to stall of the lifting surface. The breakdown may not be symmetrical and / or steady, causing the appearance of asymmetric loading, lateral forces and moments, and unsteady phenomena such as wing rock.

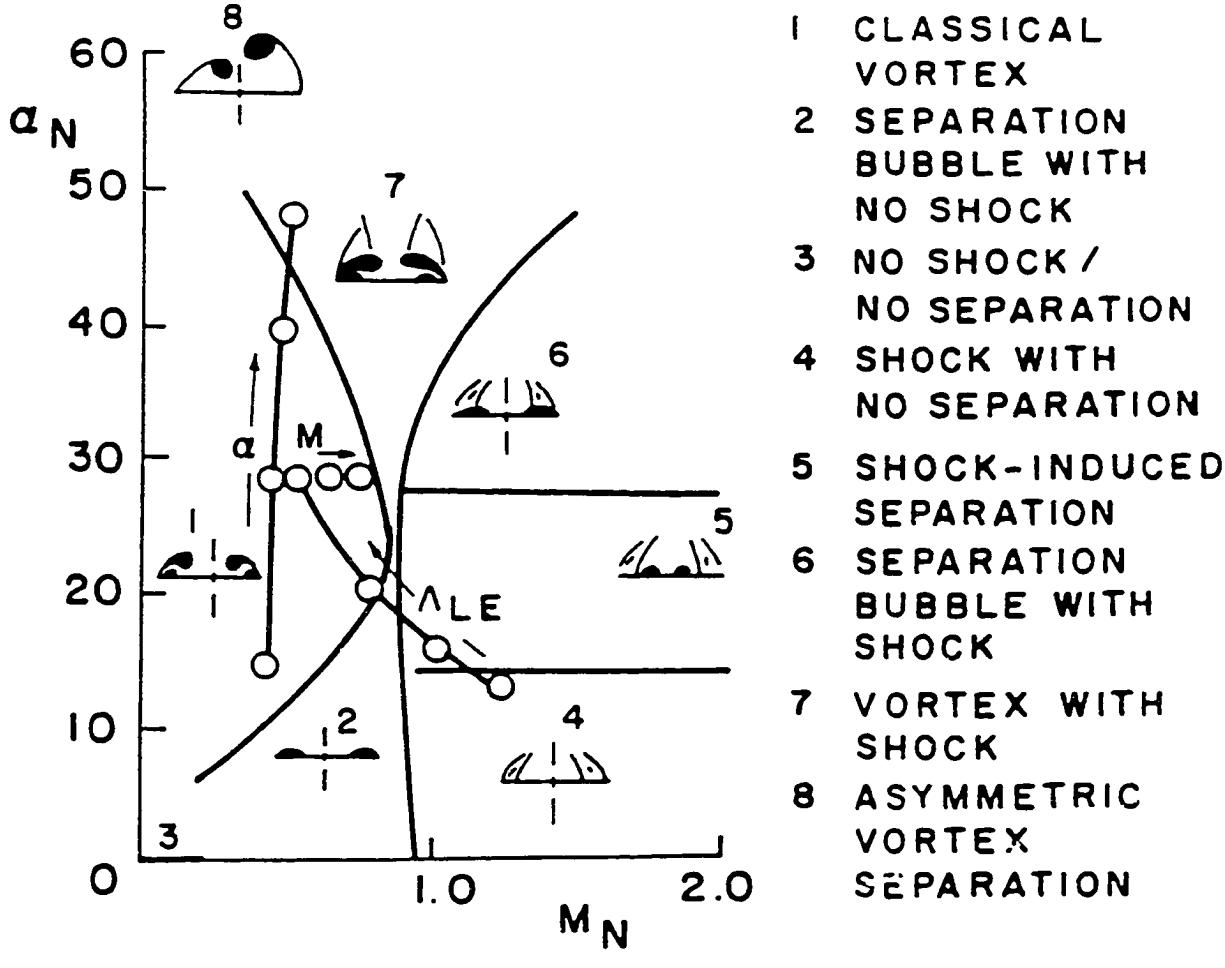

Figure 2.3: Classification of flow structures over slender sharp-edge delta wings. Miller and Wood (1985)

The flow structure induces velocity fields which result from the strong interactions between the generated vortical flows and the outer flow governed by the configuration's geometry, see Figure 2.4.

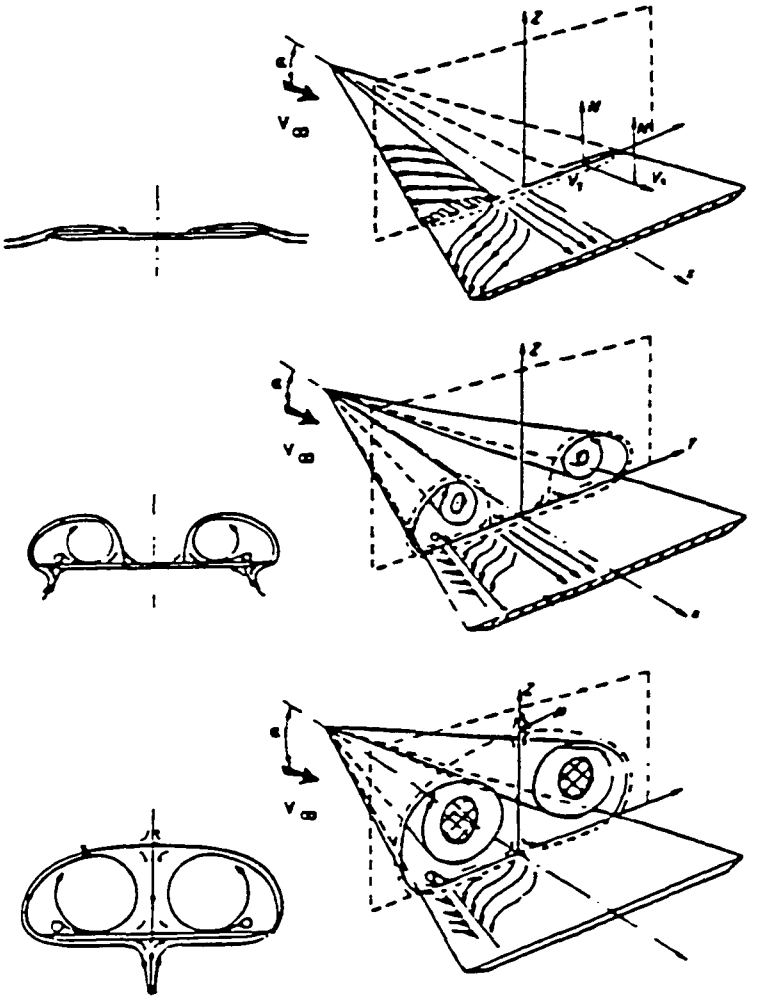

Top - Small α - separation bubble at leading edges

Medium - Medium α - two rolled-up vortices reattaching on surface

Bottom - High α - large rolled-up vortices with one reattachment line on surface and one singularity in free stream

Figure 2.4: Structure of flows over sharp leading edge delta wings. Werle (1958)

Vortex breakdown represents a limiting condition for slender wings. Once vortex breakdown passes through the trailing edge of the wing, the surface pressure field begins to be altered and the lift curve slope is reduced. Delta wing stall occurs when leading edge vortex breakdown moves over the wing. There are a number of theories for vortex breakdown; however, at this time no one theory has been widely accepted. Common vortex breakdown theories are:

1- Instability of swirling shear flow. Ludweig (1961)

2- Finite transition between two states, an upstream supercritical state and a downstream subcritical state, in an analogy to shock wave or hydraulic jump. Benjamin (1962)

3- Standing waves in the vortex core. Leibovich (1978)

4- Stagnation of core flow. Bossel (1969) and Hall (1972)

The vortical flow is generated either by the separated viscous shear layer at the sharp leading and side edges (in addition to the "classical" separation at the trailing edge as expressed by the Kutta condition), or by the three-dimensional boundary layer separation from the surfaces of the wings and bodies. As can be anticipated, many unexpected flow structures may occur in these complicated flowfields. Because the flowfield is complex, the understanding of flow details at high angles of attack is limited and in many cases remains to be established.

Figure 2.5 shows the effect of aspect ratio on the lift coefficient. As the aspect ratio increases the lift coefficient increases. Also the flowfield over delta wing is depicted in Figure 5.6 using leading edge suction analogy of Polhamus (1971).

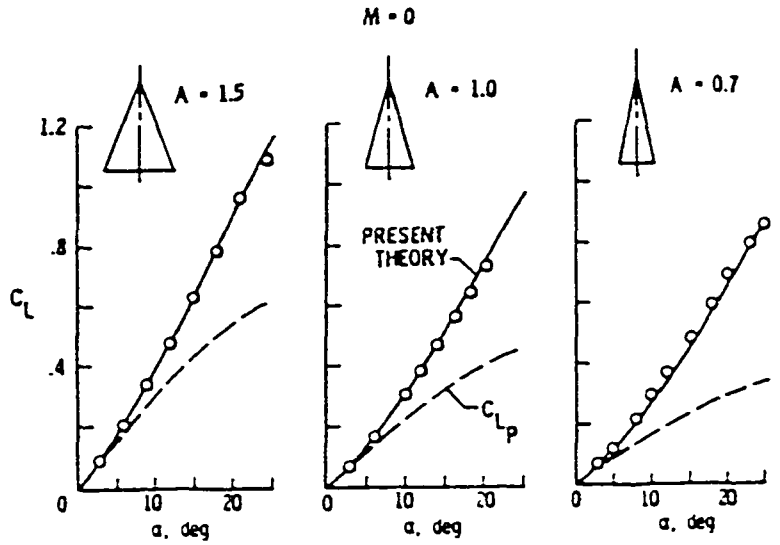

Figure 2.5: Polhamus results for different aspect ratio compared with experimental data. Polhamus (1971)

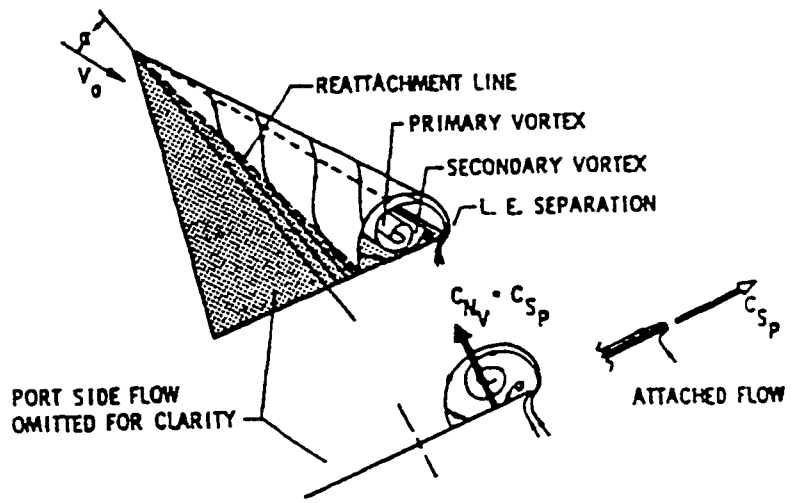

Figure 2.6: Leading-edge suction recovery boundaries for delta wings; M=0. Polhamus (1971)

Much of what is known about vortex breakdown originates from experimental work conducted on an isolated vortex created inside a tube. Many different types of breakdown have been identified in vortex tube experiments. For slender wings at angle of attack only two types of breakdown are generally identified: the bubble and the spiral types. Therefore, it is necessary to study and classify the various aerodynamic configurations at increasing angles of attack. A significant amount of research has been conducted in the area of unsteady aerodynamics at high angles of attack. In the following sections a survey of the analytical, experimental and computational work done in this area is presented.

2.2 Analytical Survey

Analytical research implies the development of mathematical models which are solved in closed form for unsteady 3D flow around delta wings at high angles of incidence. In a very few cases and with some severe approximations one can get an approximate solution, which will be valid in certain ranges of Mach number and Reynolds number and at low angles of attack. Most of the analytical work which has been done focused on modeling the vortex breakdown phenomenon.

Mangler and Smith (1959) were among the pioneers who tried to simulate the vortex sheets over the delta wing. They found a fairly good representation of the vortex sheets and it was a benchmark for other research workers.

Benjamin (1962) claimed that "vortex breakdown is not a manifestation of instability or of any other effect indicated by study of infinitesimal disturbances alone. It is instead, a finite transition between two dynamically conjugate states of axisymmetric

flow, analogous to the hydraulic jump in open channel flow." The transition is from a supercritical flow, which cannot support standing waves, to a subcritical flow, which can support standing waves. A universal characteristic parameter, N, was defined which delineates the critical regions of the flow analogous to the Froude number for open-channel flow and Mach number for compressible flow. This parameter is the ratio of absolute phase velocities of long wavelength waves, which propagate along the vortex in the axial direction. A flow is said to be supercritical if $N > 1$ and subcritical if $N < 1$.

Legendre (1966) has presented a review of the work done of the flow over a delta wing during the 1950's and the early 1960's. Slender body and conical flow theories were discussed and compared. In the same year, Smith (1966) supplemented the previous review by Legendre by covering some of the new theoretical developments bearing on the formation of coherent vortex sheets which were described at the I.U.T.A.M. Symposium on Vortex Motions at Ann Arbor in July 1964.

Hall (1966) presented a review of work on the structure of vortex cores. He began with a discussion of the equations of motion and the appropriate boundary conditions, and continues with a description in general terms of the vigorous but highly responsive character of the flow, of the effects of compressibility and turbulence and the phenomenon of energy separation. In many vortex cores, including those of trailing vortices far downstream behind a body, and those of leading edge vortices above slender wings, the variations of velocity and pressure in the axial direction are small compared with those in the radial direction. Such cores, called quasi-cylindrical, were described in some detail.

Hall (1972) presented a mathematical model for vortex breakdown phenomena. He mentioned "Vortex breakdown has been observed only in highly swirling flows. More precisely, if the angle of swirl φ is defined by $\varphi = \tan^{-1}(v/w)$, where v and w are the swirl (or azimuthal) and axial components of velocity respectively, it is found that the maximum value of φ upstream of breakdown is invariably greater than about 40°. Provided the swirl angle is large enough, the flow along the axis of an initially concentrated vortex core, with an appreciable axial velocity, can decelerate and diverge as if a solid obstacle were met. All the observations that have been capable of showing a free stagnation point have in fact shown one at breakdown, together with a region of reversed axial flow."

Ashenberg (1987) presented a new theoretical model for evaluating the effect of vortex breakdown on the aerodynamics of slender wings. The vortex breakdown phenomenon was represented by a distribution of sources.

Huang, Sun and Hanff (1997a) proposed a parabolic distribution for the chordwise axial circulation distribution over slender delta wings. Leading edge vortex breakdown locations were predicted on the basis of a critical value of the circulation.

2.3 Experimental Survey

Harvey (1962) described an experiment in which a cylindrical vortex, formed in a long tube, was used to study the 'vortex breakdown' that has been previously reported in investigations of the flow over slender delta wings. By varying the amount of swirl that was imparted to the fluid before it entered the tube, it was found that the breakdown was

the immediate stage between the two basic types of rotating flows, that is, those that do and those that do not exhibit axial velocity reversal.

Hummel (1967) reported an investigation with slender delta wings at large angles of attack. His investigation was limited to the angle of attack range before the onset of the vortex breakdown and he reported the reasons for the lift decrease in the angle of attack range beyond the onset of the vortex breakdown.

Hummel (1977) presented an experimental study of the flowfield around an AR=1.0 delta wing at an angle of attack of $\alpha = 20.5^{\circ}$. The effect of Reynolds number on the formation of the secondary vortex is studied in detail. Boundary layer measurements were carried out for laminar and turbulent boundary layers and the bound vortex lines in the lifting surface were determined for both cases.

Leibovich (1978) mentioned "vortex flows are subject to a number of major structural changes involving very large disturbances when a characteristic ratio of azimuthal to axial velocity components is varied. Vortex breakdowns are among the structural forms that may occur."

Werle (1982) presented a progress review of the principal methods of visualizing flows using solid, liquid or gas tracers, in water tunnels and wind tunnels, especially in the experimental facilities at ONERA. Such visualization brought to light the physical flow patterns with all their partial singularities as well as the evolution of these parameters as a function of their principal parameters: incidence, yaw angle, Reynolds number, etc. These visualizations also revealed the separation phenomena which characterized high angles of attack; in addition, they defined with precision all vortical,

transitional and unsteady aspects. Some examples of results were obtained for swept-back and slender bodies.

Wendt (1982) studied the effects of compressibility on the flowfields and overall aerodynamic characteristics of low aspect ratio, sharp-edged planforms at high incidence. Emphasis was placed on the leeside vortex-dominated flow structure, including vortex bursting. Both subsonic and supersonic regimes were considered; unsteady effects were not considered.

Orlik-Ruckemann (1982) presented a progress review of some of the fluid dynamics phenomena that are associated with the oscillatory flight at high angles of attack. The emphasis was on asymmetric shedding of forebody vortices, asymmetric breakdown of leading edge vortices, the oscillatory motion of such vortices, and the time lag between the motion of the vortices and that of the aircraft.

Gad-el-Hak and Blackwelder (1985) conducted flow visualization experiments in a low Reynolds number towing tank to study the time dependent flow around two generic classes of wings. Delta and swept(including zero sweep) wings were sting mounted to a four-bar mechanism, which generated a large-amplitude, harmonic pitching motion around the one-quarter chord location at a reduced frequency that varied in the range of 0.2-3.0. Fluorescent dye layers were placed in the weakly stratified water channel prior to towing the wing. The horizontal dye sheets were excited using a vertical sheet of laser light parallel to or perpendicular to the flow direction. The dye marked the flow in the separation region around the wing, the flow in the wake region, and the potential flow away from the lifting surface.

Payne, et al. (1986) presented an experimental investigation of vortex breakdown on delta wing at high angles of attack. Smoke flow visualization and the laser light sheet technique were used to obtain cross-sectional views of the leading edge vortices as they breakdown for a series of flat-plate delta wings having sweep angles of 70°, 75°, 80°, and 85°. The dynamic characteristics of the breakdown process were recorded using high-speed movies. Velocity measurements were obtained using a laser Doppler anemometer. The measurements showed that, when breakdown occurs, the core flow is transformed from a jet-like to a wake-like flow. In the same year, Lamar (1986) studied nonlinear lift control at high speed and high angle of attack using vortex flow technology.

Atta and Rockwell (1987) investigated the hysteresis of vortex development and breakdown on an oscillating delta wing. The investigation focused on the development and breakdown of the core of the vortex, defined by the vorticity fed into the vortex at and near the tip of the wing.

Jarrah (1987,1988,1989) presented a comprehensive experimental program for unsteady aerodynamics of delta wings performing maneuvers to high angle of attack. These tests were conducted in one of the 7 ft by 10 ft low-speed wind tunnels at NASA Ames Research center on a series of flat delta-wing models with sharp leading edges. He conducted his experimental study on an "agile" fighter aircraft with three different aspect ratios, 1, 1.5 and 2, simulating rapid motions. These motions involved sinusoidal or ramp variation of angle of attack from 0° to 90° and with reduced frequencies between 0.01 and 0.08. The three delta wings used in this investigation are shown in Figure 2.7 and table 2.1. They were constructed from a 6.4 mm (0.25 in) thick flat aluminum plate. The sharp leading edge had a roughly 30° angle cut on the lower surface.

Table 2.1: Geometry of delta wings. Jarrah (1988)

AR	Wing Type	Λ, deg	Edge Angle, deg	Root Chord, (mm / in.)	Span, (mm / in.)	Thickness, (mm / in.)
1.0	smoke	76	29.3	406 / 16	203 / 8	7.6 / 0.30
1.0	force	76	29.3	305 / 12	152 / 6	6.4 / 0.25
1.5	force	69.5	28.4	305 / 12	229 / 9	6.4 / 0.25
2.0	force	63.5	27.3	305 / 12	305 / 12	6.4 / 0.25

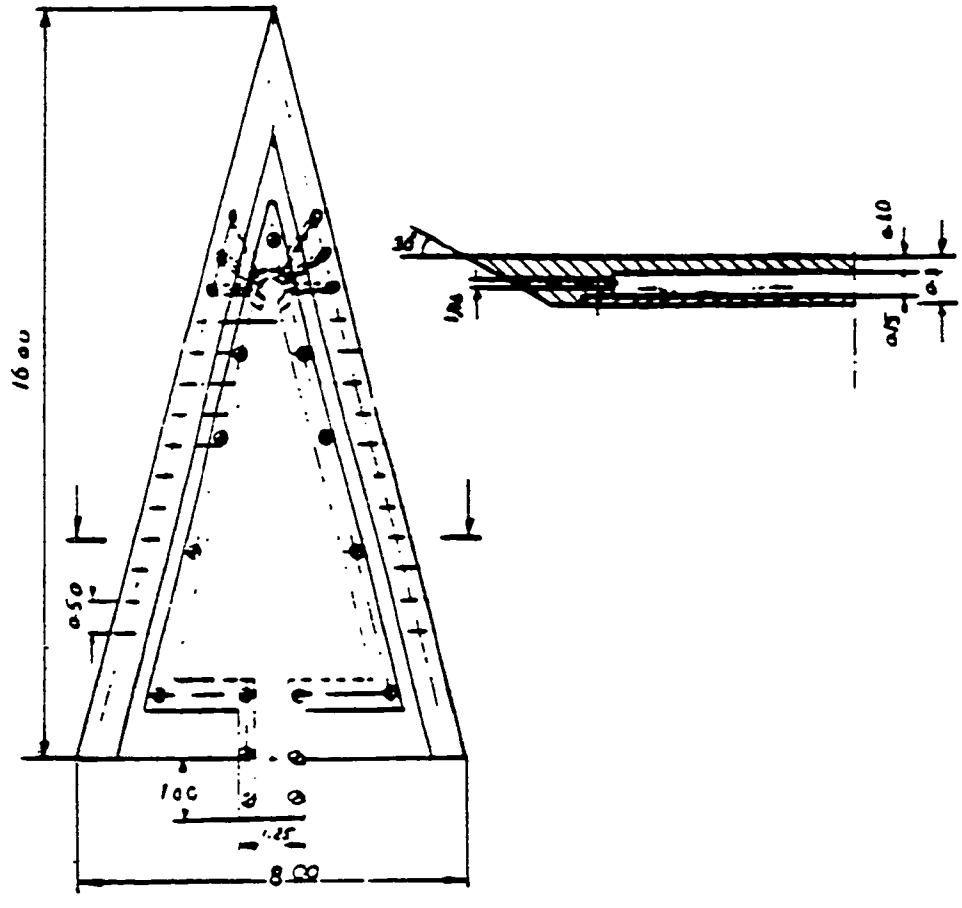

Figure 2.7: Sketches of the delta wing used for flow visualization. Jarrah (1988)

He concluded that pitching motion with large angle of attack produced large hysteresis in the aerodynamic loads and in the vortex breakdown position relative to the wing. The primary α time histories that were examined are shown in Figure 2.8. The author of this study has used this experimental data for validating the present computational results.

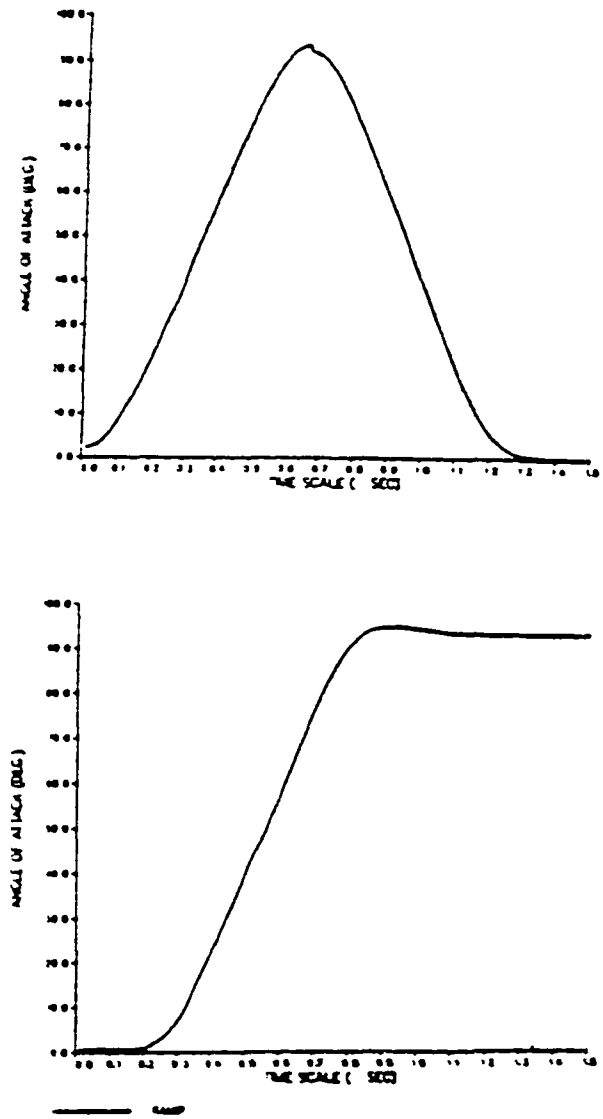

Figure 2.8: Typical angle of attack time variation. Jarrah (1988)

Jarrah (1988) reported "It is expected that a high pitch rate will delay the onset of vortex breakdown to much higher angles of attack than in the steady case during pitch up. The opposite effect is anticipated during pitch down."

In the same year, Soltani, et al. (1988) investigated the aerodynamic loads on a delta wing oscillated up to post-stall angles of attack. Their model was a 70° sweep flat delta wing with its leading and trailing edges beveled symmetrically. A six component strain gauge balance was mounted on the pressure side of the wing producing a significant negative camber. The wing was pitched continuously at the 57% root chord station and could be rotated up to 15° of sideslip. The motion was a simple harmonic one with angle of attack changes between 0 to 55°. The Reynolds number was 1.1×10^6 to 1.97×10^6, and the reduced frequency range reported in the paper ranged from 0.015 to 0.0825. Measurements at a sideslip angle of 0°, 5°, and 15° were reported, and the corresponding lift, normal force, drag, pitching moment, and rolling moment coefficients were plotted for various reduced frequencies and Reynolds number. Moderate effects of Reynolds number were reflected in this study.

Solignac, et al. (1989) made a detailed study of the flow around a 75° sweep angle delta wing. Experiments were carried out in three different facilities to generate data for different Reynolds numbers. The upper surface flow was visualized and the external flow was probed by 3D Laser Doppler Velocimetry (LDV) and a five-hole pressure probe. In the analysis of the results, it appeared that the secondary vortex was larger for a laminar boundary layer than it was for a turbulent one. The primary vortex presented a good conical similitude whereas the pressure distribution on the wing depended on the wing dimensions.

Brandon (1990) presented recent research conducted at NASA Langley Research Center on the effects of large amplitude pitching motion on the aerodynamic characteristics of modern fighter airplane configurations. Wind tunnel tests were conducted on simple flat-plate wings to gain understanding of the complex flow phenomena during unsteady motion at high angles of attack. Using a computer controlled dynamic apparatus, tests were conducted to investigate the effects of pitch rate and motion time history, and to determine the persistence of unsteady effects. Force and moment data were obtained using a 6-component internal strain-gage balance. Flow visualization using a laser light-sheet system was also obtained.

Soltani (1990) has performed wind tunnel experiments to study the flow mechanism on a 70° sharp leading edge delta wing model at both static and dynamic conditions at a Reynolds number of 1.43×10^6. Large amplitude oscillatory motions (up to 60°) were produced by sinusoidal pitching the model over a range of reduced frequencies. Ramp motions were obtained using an initial sinusoidal increase in angle of attack and hold. Aerodynamic forces and moments were obtained from a six-component strain-gauge balance. In addition, smoke flow visualization was conducted to study the development and breakdown of the leading edge vortices under static, dynamic, and ramp conditions. The visualization experiment was performed at a Reynolds number of 0.16×10^6. Dynamic data varied substantially with reduced frequency. Large forces and moments overshoots, a delay in dynamic stall, and a hysteresis loop between the values of aerodynamic loads in upstoke and downstroke motion were observed.

Nelson and Visser (1991) performed an experimental X-wire measurement of the flowfield above a 70° and 75° flat plate delta wing at a Reynolds number of 250,000.

Grids were taken normal to the wing at various chordwise locations for angles of attack of 20° and 30°. The dependence of circulation on distance from the vortex core and on chordwise location was also examined.

Elsenaar and Hoeijmakers (1991) investigated the flow about a sharp edge cropped delta wing experimentally. The experiment comprised detailed surface pressure measurements at low-subsonic, transonic and low-supersonic freestream Mach numbers for angles of attack up to 27°. The major part of the measurements were carried out at a Reynolds number of 9 million, but some data was also obtained at lower and at higher Reynolds numbers. The investigation included continuous schlieren flow-field visualization as well as surface flow visualization at a limited number of freestream conditions.

Nelson (1991) presented a review of unsteady aerodynamics for slender wings undergoing large amplitude motions. Static and unsteady aerodynamic characteristics were discussed and the relationship between the aerodynamic loads and the leeward structure was investigated. Data was presented showing the influence of the wing motion on the aerodynamic loads. Both large amplitude pitching and rolling motion experimental results were discussed.

Rediniotis, et al. (1992) investigated the transient flowfield over a delta wing during pitch-up motions to very large angles of attack. Emphasis was directed at the growth and the eventual breakdown of leading edge vortices. Delta wing models were tested in a wind tunnel at Reynolds number of order 10^5. Instantaneous pressure measurements were obtained, while the flowfield was mapped out via a seven-hole probe designed, constructed and calibrated to generate time-varying information.

Moreira and Johari (1995) investigated the effectiveness of steady and pulsed blowing as a method of controlling delta wing vortices during ramp pitching in flow visualization experiments conducted in a water tunnel. The recessed angled spanwise blowing technique was utilized for vortex manipulation. The technique was implemented on a beveled 60° delta wing using a pair of blowing ports located beneath the vortex core at 40% chord. The flow was injected primarily in the spanwise direction but was also composed of a component normal to the wing surface. The location of vortex burst was measured as a function of blowing intensity and pulsing frequency under static conditions, and the optimum blowing case was applied at three different wing pitching rates. Experimental results have shown that, when the burst location is upstream of the blowing port, pulsed blowing delays vortex breakdown in static and dynamic cases. Dynamic tests verified the existence of a hysteresis effect and demonstrated the improvements offered by pulsed blowing over both steady blowing and no-blowing scenarios.

Huang, Sun, and Hanff (1997b) investigated the effect on leading edge vortex breakdown of geometric modification on slender flat delta wings by means of water-tunnel flow visualization experiments. Effectiveness of the leading edge bevel in delaying breakdown appeared to be related to the ratio between leading edge width and pre-separation boundary layer thickness. The trailing edge bevel mainly delayed breakdown in the aft part of the wing and a centerbody had a small delaying effect everywhere.

Kowal and Vakili (1998) have conducted an investigation of vortex breakdown using quantitative flow visualization in the Royal Military College (RMC) of Canada

water tunnel using a 70° delta wing under varying steady and unsteady conditions and combinations of pitch and roll oscillatory motion. All unsteady analysis was conducted at four distinct values of reduced frequencies. For all unsteady motions, a hysteresis effect and a phase lag existed that increased with reduced frequency.

2.4 Computational Survey

Numerical methods for the prediction of vortical flow can be classified under two categories as:

1- Methods which model the vortex in an approximate manner (Leading edge suction analogy, Vortex-lattice, Panel, ..etc).

2- Methods which capture the vortical region as a part of solution to the governing equations (Navier-Stokes CFD computations).

A substantial volume of research work has been, and still continues to be done by many researchers using different levels of mathematical models.

Kandil, et al. (1976) developed a numerical method to predict the distributed and total aerodynamic loads on nonplanar lifting surfaces for steady, inviscid, incompressible flow. There were no restrictions on aspect ratio, planform, camber, or angle of attack as long as separation occurs along the sharp edges only. The lifting surface was represented by a lattice of discrete vortex lines. The wake generated by leading edge, tip, and trailing-edge separation were represented by families of discrete, nonintersecting vortex lines; each line was composed of a series of straight, finite segments and one straight, semi-infinite segment; the positions of these lines were obtained as part of the solution. Rectangular, arrowhead, and delta wings were considered.

Kandil, et al. (1978) extended the nonlinear-discrete vortex method in a moving frame of reference for asymmetric flows past a wing with leading edge separation. The method was applied to delta wings undergoing steady or unsteady rolling motions at zero angle of attack and for yawed wings at large angles of attack. Asymmetric flows were obtained due to the forced motion.

Hunt, M.A. and F.I.M.A. (1982) presented the role of computational fluid dynamics in high angle of attack aerodynamics. He pointed out the recent advances in computers and in numerical algorithms at that time. He discussed the prospects of high angle of attack aerodynamic predictions via theoretical methods with particular emphasis on panel methods (including rolling and coning motions), discrete vortex dynamics calculations for the incompressible Euler and Navier-Stokes equations, and some other field methods for the compressible Euler equations.

Hoeijmakers and Vaatstra (1983) described a computational method for two-dimensional vortex sheet motion in incompressible flow. The procedure utilizes a second-order panel method, an adaptive panel scheme, and a concept for treating highly rolled-up portions of the vortex sheet. One of the presented results was for a delta wing with leading edge vortex sheets.

Gordon and Rom (1985) have presented a new vortex lattice model for the calculation of the flow over delta-shaped wing planforms at high angles of attack in subsonic flow. The new vortex lattice model is combined with the panel source singularity for the calculation of the aerodynamic characteristics of thick wings having sharp leading edges.

In the same year, Kandil and Yates (1985) solved the problem of transonic flow around sharp-edge delta wings. They wrote the steady full-potential equation in the form of Poisson's equation, with the solution of the velocity field expressed in terms of an integral equation. The solution consists of a surface integral of vorticity distribution on the wing and its free-vortex sheets and a volume integral of source distribution within a volume around the wing and its free vortex sheets. The solution was obtained through successive iteration cycles.

Krause, Menne and Liu (1986) investigated the initiation of the breakdown process for compressible flow with a numerical solution of the conservation equations for mass, momentum, and energy. Their work was based on the following assumptions: 1) the vortex is isolated, with its axis parallel to the direction of the main stream; 2) the flow is axially symmetric, and 3) the core radius R is small compared to the breakdown length L.

Newsome and Kandil (1987) presented the first survey paper on the numerical prediction of vortical flow due to three-dimensional flow separation about flight vehicles (wings, bodies, and complete configurations) at high angles of attack and quasi-steady flight conditions. While full potential equations with discrete vorticity were briefly reviewed, the predominant emphasis of this paper was on solutions to the Euler and Reynolds-averaged Navier-Stokes equations.

In the same year, Beran (1987) has presented solutions of the steady-state Navier-Stokes equations for the axisymmetric bursting of a laminar trailing vortex with Newton's method and the pseudo-arc length continuation method for wide ranges of vortex strength and Reynolds number. The results indicated that a trailing vortex could

undergo a transition from a state in which the core slowly diffuses to a state marked by large amplitude, spatial oscillations of core radius and core axial velocity. At the transition point the core grows rapidly in size. This event is interpreted as vortex bursting.

Kandil and Chuang (1988) solved the unsteady flow around maneuvering wings using the unsteady Euler equations. The unsteady conservative Euler equations were derived for the flow relative motion with respect to a moving frame of reference. The equations are solved using two computational schemes; an explicit multi-stage finite-volume scheme and an implicit approximately factored finite volume scheme.

Thomas, et al. (1990) applied an upwind-biased finite volume algorithm to the low-speed laminar flow over a low-aspect-ratio delta wing from 0° to 40° angle of attack. They used second order accurate differencing spatially and a multigrid algorithm to promote convergence to the steady state. The governing equations are the thin-layer approximations to the three-dimensional time-dependent compressible Navier-Stokes equations.

In the same year, Kandil, Wong, Kandil (1990) used the unsteady, compressible, thin-layer and full Navier-Stokes equations to numerically simulate steady and unsteady asymmetric, supersonic, locally conical flows around a 5°-semiapex angle circular cone. The main computational scheme, which was used in their work, was the implicit, upwind, flux-difference splitting, finite-volume scheme. Passive control of asymmetric flows was demonstrated and studied using sharp and round-edged, thick and thin strakes. Baron, and et al. (1991) used a nonlinear unsteady vortex lattice method to predict the geometry of the wakes and the distribution of the aerodynamic loads on impulsively started wings.

Agrawal, and et al. (1991) presented a numerical investigation of leading edge vortex breakdown on a delta wing at high angles of attack. The analysis has been restricted to low speed flows on a flat plate wing with sharp leading edges. Both Euler and Navier-Stokes (assuming fully laminar and fully turbulent flows) equations were used in this study. Predictions of vortex breakdown progression with angle of attack with both Euler and Navier-Stokes were presented. The Navier-Stokes predictions showed significant improvements in breakdown location at angles of attack where the vortex breakdown approached the wing apex.

Hoeijimakers (1991) presented a review of mathematical models of different level of approximation and application to the numerical simulation of vortical type of flows occurring in subsonic and transonic aircraft aerodynamics. Luckring (1991) presented a review progress in computational vortex-flow aerodynamics at the Langley Research Center. Emphasis was placed on Navier-Stokes methodology, both for compressible and incompressible flows, and results were presented from central and upwind-biased schemes for laminar, transitional, and fully turbulent flows.

Kandil and Salman (1991) considered the interdisciplinary problems of unsteady fluid dynamics and rigid-body dynamics and control of delta wings with and without leading edge flap oscillation. For the fluid dynamics problem, the unsteady, compressible, thin-layer Navier-Stokes (TLNS) equations were solved along with the unsteady, linearized, Navier-Displacement (ND) equations. The NS equations were solved for the flowfield using an implicit finite-volume scheme. The ND equations were solved for the grid deformation, for oscillating leading edge flap, using an Alternating Direction Implicit (ADI) scheme. For the dynamics and control problem, the Euler

equations of rigid-body dynamics for the wing and its flaps were solved interactively with the fluid equations for the wing-rock motion and subsequently for its control. Wong (1991) solved steady and unsteady vortex-dominated flows around slender bodies at high angles of attack using the unsteady, compressible Navier-Stokes equations.

In the same year, Sawada and Inoue (1991) solved the flowfield over a 3D delta wing having a vortex fence at the apex region by solving the unsteady compressible Navier-Stokes equations. A second order explicit finite volume scheme was used to simulate the temporal evolution of the flowfield. The computational efficiency and the spatial resolution were improved by adopting various multi-zone techniques. Simulations were conducted to show the typical features of the flowfield in the subsonic range. Kandil, et al. (1992) used the unsteady, compressible, full Navier-Stokes (NS) equations to study the critical effects of the downstream boundary conditions on the supersonic vortex breakdown.

Hoeijimakers (1992) applied a cell-centered central-difference finite-volume Euler method to the steady subsonic flow about a 65° sharp-edged cropped delta wing at incidences close to the incidence at which leading edge vortex breakdown is observed in wind tunnel experiments. Above a critical value of the incidence the pseudo-time dependent numerical procedure failed to attain a steady-state solution.

Liu and Hsu (1992) developed an implicit finite-difference scheme for solving three-dimensional incompressible Navier-Stokes equations. Computations for complicated vortical flows past several sharp and round-edged delta and double-delta wings at high angles of attack and sideslip were discussed.

Longo (1992) presented a progress review in numerical simulation of vortex-flow aerodynamics at the Institute for Design Aerodynamics of the DLR-Braunschweig. He focused on the prediction of vortex lift including vortex breakdown, vortex-vortex interaction and shock-vortex interaction. Results were obtained both for compressible and incompressible flow using the DLR Euler/Navier-Stokes CEVCATS-RANS solver.

Bannink and Houtman (1992) used a 3D Euler code of a flux difference-splitting type upwind scheme to investigate the high-speed flow over a sharp-edged plane delta wing with 65° sweep. Salman (1992) considered in more details the unsteady flows around rigid or flexible delta wings with and without oscillating leading edge flaps. Both unsteady Euler and Navier-Stokes equations were used in the investigation.

Kandil (1993) presented computational simulation of supersonic vortex breakdown for internal and external flow applications. The problem was formulated using the unsteady, compressible, full Navier-Stokes equations. Kandil, et al. (1994) carried out computation of transonic flow around a 65° sharp-edged, cropped delta wing undergoing a forced pitching oscillating using the unsteady, compressible, full Navier-Stokes equations. The wing mean angle of attack was kept at 20° and the freestream Mach number and Reynolds number were 0.85 and 3.23×10^6, respectively. The wing was forced to oscillate in pitch around an axis at the 0.25 root-chord station with amplitude of 4° and a reduced frequency of π. For the initial conditions, a shock system consisting of a ray shock beneath the primary vortex core and a transverse terminating shock have been captured. Behind the terminating shock, the primary vortex core breaks down. The flow behind the terminating shock was reconstructed accurately. For the pitching wing, it was shown that both the terminating shock and the vortex-breakdown bubble behind it,

experience oscillatory backward and forward motion including the disappearance and appearance of the vortex-brekdown buuble. This is a significant finding for the transonic regime since vortex breakdown occurs at moderate angles of attack, $\alpha = 20°$. Kandil and Menzies (1996) studied the coupled rolling and pitching oscillation in transonic flow. The focus was to analyze the effects of coupled motion on the wing response and vortex breakdown flow by varying oscillation frequency and phase angle while the maximum pitch and roll amplitudes were kept at 4°.

Kandil and Abdelhamid (1997) carried out computation and validation of a 76° sewpt delta wing, aspect ratio of one, pitching up to 90° amplitude. The Reynolds number and Mach number were 0.85×10^6 and 0.3; respectively. The comparisons of the computational results were in good agreement with those of the experimental data of Jarrah (1988). Abdelhamid and Kandil (1998) studied the effect of the reduced frequency at very large angles of attack. The unsteady, full NS equations were solved time accurately using the implicit, upwind, Roe flux-difference splitting, finite-volume scheme. The computed results were compared with each other as well as to the existing experimental data.

2.5 Flow Control

"Alternative flight control by means of Complete [yaw-pitch-roll] Thrust-Vectoring [CTV] propulsion and CTV-based tailless air-vehicles, post-stall-flight and maximized air safety aerothermodynamics and practice are the biggest contributors to military aviation today – and to safer civil aviation tomorrow – since the invention of the jet engine. At the end of the first one hundred years of Aerodynamic-only Flight Control [AFC] based aviation, CTV emerges as the best alternative, most effective and safest flight technology. It introduces a new era in aviation, an era marked by complete flight control that is nearly free of the limiting and dangerous characteristics of the external air flow regime, AFC-tails, AFC-only education, AFC-stability criteria and AFC-air-safety certification processes. Vectored thrust F-15, F-16, F-18, F-22, JSF, X-36 and Su-37 represent a sample of highly active international development programs today. Any conventional air force fleet can now be upgraded to become 'effectively vectored'.

Proceeding side by side is an emerging international effort to civilize this technology to prevent more than 50% of jet airline crashes and bring the saving of many lives." Gal-Or (1996).

As mentioned before, one of the features of delta wing is the generation of an additional lift, the vortex lift. The use of vortex lift is limited by vortex bursting or breakdown, which is characterized by a sudden expansion of the vortex about a rapidly decelerating core, with subsequent vortex disintegration and loss of the orderly vortical flow. As the angle of attack increases, the point of vortex breakdown moves upstream, causing loss of lift and, finally, stall.

The vortex breakdown control over delta wings can be achieved using several ways, such as the addition of strakes, canards, or Leading Edge Extension (LEX) before the wing. One of the methods that can be used to control vortex breakdown is by using blowing. Some of the factors, which affect the effectiveness of the blowing process, are blowing rate, location of the blowing ports, steady or unsteady blowing, and continuous or pulsating blowing. The main problem with this blowing is the high momentum needed to achieve a significant increase in the lift.

In general, there are five types of blowing reported in the literature:

1- Vortex Core Blowing (VCB)

This attempts to delay vortex breakdown by increasing the momentum of the vortex core, see Figure 2.9a. This is accomplished by injecting a stream of fluid directly into the vortex core along the vortex axis. The result is an energized vortex with increased axial velocity.

2- Spanwise Blowing (SWB)

This method attempts to energize the vortex by ejecting high-momentum fluid in a spanwise direction from ports along the leading edge as shown in Figure 2.9b. The

intent of SWB is to increase the vortex strength by increasing the vorticity of the free shear layer. It is reported in the literature that this method enhance the lift coefficient but also resulted in increased drag. Moreover, vortex breakdown was observed at lower angles of attack in comparison with the wing without blowing. Both effects can be attributed to a larger span perceived by the oncoming flow.

3- **Parallel to the Leading Edge Blowing (PLEB)**

This consists of injecting fluid parallel to the leading edge, see Figure 2.9c. Although this technique is often referred to as SWB, it is significantly different from the SWB in that the blowing ports are located at the wing root (usually on the fuselage) above the wing surface. The injected flow in PLEB acts like a line sink creating suction on the upper surface of the wing, pulling the vortex back to the wing and reattaching it to the surface. This flow strengthens the vortex, thereby delaying breakdown. The stability of the wing is also improved by reducing the wing rock common to delta wings in this flight regime. A drawback of PLEB is the significant bleed momentum required to attain the desired effects. This technique has been used by Bradley and Wray (1974), Anglin and Satran (1980), Seginer and Salomon (1986), and Meyer and Seginer (1994).

4- **Tangential to the Leading Edge Blowing (TLEB)**

This method uses slots located on the leading edge to inject fluid tangent to the wing's leading edge bevel or normal to the wing surface (in a rounded geometry), see Figure 2.9d. The phenomenon of Coanda jet attachment to convex surface is the basis for TLEB on rounded leading edge wings. By being able to affect the cross-flow separation point on rounded leading edge delta wings, the location (with respect to the wing surface) and strength of the vortices can be controlled. This technique has a strong effect on the

vortices and lift is increased for even small amounts of blowing. Experimental results reveal that TLEB can improve the lift coefficient. Wood, et al. (1988), Wood, et al. (1990), and Gu, et al. (1993) have used this technique.

5- **Recessed Angled Spanwise Blowing (RASB)**

This method can be achieved using blowing ports, located on the suction side of the wing and beneath the vortex core. The blowing ports are canted upward in the spanwise direction such that the blowing flow is injected in the spanwise direction from the top surface of the wing, parallel to the sharp leading edge bevel, see Figure 2.9e. The intent of the momentum injection in this scheme is on increasing the stability of the vortex, thus delaying vortex breakdown. Johari, et al. (1995), has used this technique.

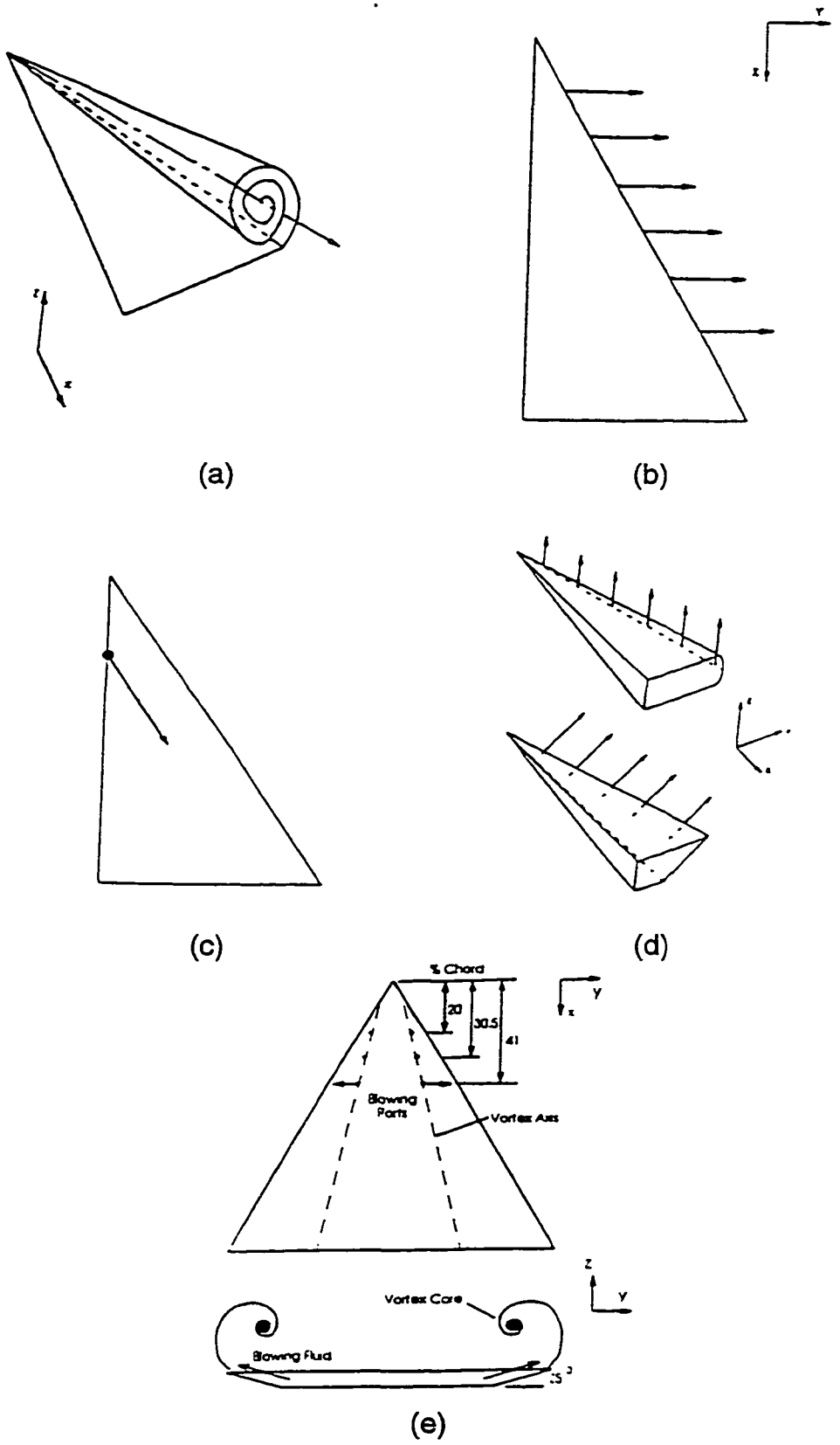

Figure 2.9: Vortex control techniques: (a) VCB, (b) SWB, (c) PLEB, (d) TLEB, and (RASB). Johari, et al. (1995)

2.6 Summary

Design trends for future fighter aircraft indicate continued emphasis on maneuver capability in the stall/post-stall high angle of attack flow regime. Aggressive exploitation of the high angle of attack envelope will likely encounter large unsteady effects. These effects need to be identified and analyzed in order to ensure that adequate predictions of airplane flight dynamics can be obtained.

A complete literature survey has been presented. A more general analytical model is very difficult to obtain. Most of the analytical work was done during the 1960's before the advent of supercomputers and Personal Computers (PC's), which provide significant advantages for the computational techniques relative to the analytical models. The experimental data is very expensive but necessary for the final design.

The viscous effects can be accounted for by solving the unsteady full Navier-Stokes equations. Solving the viscous conservation equations (i.e., the full Navier-Stokes equations) will enable full simulation of the complex viscous-inviscid interactions in the three-dimensional separated flows at high angles of attack, even on complex configurations. This is true provided that the correct algorithm and an appropriate grid generation scheme are given, which can be solved on a large memory and high speed computer. However, there are still fundamental difficulties in modeling the turbulent shear layer and of predicting the transition from laminar to turbulent flows. Therefore, the present "exact numerical" solutions of the full Navier-Stokes equations are limited by the lack of appropriate modeling of flow turbulence and transition. So, there is a need for reliable numerical solutions, which can be used in the preliminary design stages to

obtain quantitative description of complex flow fields that cannot easily be obtained from experimentation.

CHAPTER 3

PROBLEM FORMULATION

3.1 Introduction

The nature and details of the fluid flow that is predicted by a particular flow solver depend on the governing equations that are discretized in the solver. The order of the governing flow equations can vary from the potential equations level to the full Navier-Stokes equations level. Before 1970, most numerical solutions of fluid dynamic problems were obtained using the potential flow formulation. However, due to the isentropic and irrotational flow assumptions, many fluid problems cannot be accurately represented using this formulation. In the last two decades, rapid advancements in computer technology have enabled computational fluid dynamicists to use more complete equations, such as Euler equations and Navier-Stokes (NS) equations, rather than the potential flow equation. While Euler equations can model distributed vorticity and shocks, they do not model the viscous effects.

For complex flow fields with strong viscous-inviscid interactions, reduced forms of the equations of fluid motion do not provide an adequate model of the flow physics. In vortex flows, viscous effects are of great importance especially within and downstream of a vortex breakdown region. In high Reynolds number viscous flows, viscous effects are concentrated near the vortex axis, adjacent to solid walls and in wake regions. The full NS equations are clearly superior for modeling these viscous flows. They can more accurately model flow separations, shock development and motion, and shock-boundary

layer interaction as well as vortex breakdown and vorticity evolution, convection and shedding. In this study, strong viscous-inviscid interactions in the form of large-scale three-dimensional boundary layer separation require that full NS equations be considered rather than the simplified Euler equations or even the thin-layer Navier-Stokes (TLNS) equations. Therefore, for this research work, the laminar, and Reynolds Averaged (RA), unsteady, compressible, full NS equations are used to formulate the current problem.

In this Chapter, the three-dimensional NS equations are presented followed by discussion of the boundary conditions.

3.2 Governing Equations

The conservative form of the nondimensional, unsteady, compressible, full NS equations in terms of Cartesian coordinates (x_1,x_2,x_3) is given by

$$\frac{\partial \vec{q}}{\partial t} + \frac{\partial (\vec{E}_j - \vec{E}_{vj})}{\partial x_j} = 0 \quad ; \mathrm{j} = 1\text{-}3 \tag{3.1}$$

where the flow field vector, $\vec{q}$ is given by

$$\vec{q} = [\rho, \rho u_1, \rho u_2, \rho u_3, \rho e]^t \tag{3.2}$$

and the inviscid flux vectors are given by

$$\vec{E}_j = \left[\rho u_j, \rho u_1 u_j + \delta_{j1} p, \rho u_2 u_j + \delta_{j2} p, \rho u_3 u_j + \delta_{j3} p, \rho u_j (e + \frac{p}{\rho}) \right]^t \quad ; \mathrm{j} = 1\text{-}3 \tag{3.3}$$

where δ_{ij} is the Kronecker delta function, $\delta_{ij} = \begin{cases} 1 & i = j \\ 0 & i \neq j \end{cases}$ (3.4)

and the viscous fluxes are

$$(\vec{E}_v)_j = [0, \tau_{j1}, \tau_{j2}, \tau_{j3}, u_m \tau_{jm} - q_j]^t \quad ; \mathrm{j} = 1\text{-}3, \mathrm{m} = 1\text{-}3 \tag{3.5}$$

In the equations above, the variables are nondimensionalized using the corresponding freestream variables. The reference parameters are L, a_∞, L/a_∞, ρ_∞ and μ_∞ for the length, velocity, time, density and molecular viscosity, respectively. The total energy per unit mass, e, is nondimensionalized by $(a_\infty)^2$ and the pressure, p, is nondimensionalized by $\rho_\infty(a_\infty)^2$. The pressure is related to the total energy per unit mass and density by the perfect gas equation

$$p = (\gamma - 1)\rho\left[e - \frac{1}{2}u_j u_j\right] \quad ; \mathrm{j} = 1\text{-}3 \tag{3.6}$$

where γ is the specific heat ratio which is assumed to be constant and its value is 1.4 in this study.

In Equation (3.5), the τ_{jm} terms represent the Cartesian components of the shear-stress tensor for a Newtonian fluid, where Stokes hypothesis is employed and the fifth term represents the shear-dissipation power, and heat flux components. The Cartesian components of the shear-stress tensor are given by

$$\tau_{ij} = \frac{\mu M_\infty}{\mathrm{Re}}\left(\frac{\partial u_i}{\partial x_j} + \frac{\partial u_j}{\partial x_i} - \frac{2}{3}\delta_{ij}\frac{\partial u_k}{\partial x_k}\right) \; ; \; \mathrm{i, j, k} = 1\text{-}3 \tag{3.7}$$

The shear-dissipation power and the heat flux components are given by

$$u_m \tau_{jm} = \frac{\mu M_\infty}{\mathrm{Re}} u_m \left(\frac{\partial u_j}{\partial x_m} + \frac{\partial u_m}{\partial x_j} - \frac{2}{3}\delta_{jm}\frac{\partial u_k}{\partial x_k}\right) \; ; \; \mathrm{j, k, m} = 1\text{-}3 \tag{3.8}$$

$$q_j = \frac{-\mu M_\infty}{(\gamma - 1)\,\mathrm{Pr}\,\mathrm{Re}}\frac{\partial T}{\partial x_j} \; ; \; \mathrm{j} = 1\text{-}3 \tag{3.9}$$

where the dimensionless viscosity, μ, is calculated from Sutherland's law

$$\mu = T^{\frac{3}{2}}\left(\frac{1+c}{T+c}\right) \tag{3.10}$$

where T is the dimensionless temperature and c is Sutherland's constant, c≈0.4317. The Prandtl number, Pr, is assumed to be constant with a value of 0.72 throughout the calculations. The freestream Reynolds number, Re, is defined by

$$\mathrm{Re} = \frac{\rho_\infty U_\infty L}{\mu_\infty} \tag{3.11}$$

According to the characteristic parameters, the freestream flow variables are given by

$$\rho_\infty = 1.0$$

$$u_{1\infty} = M_\infty$$

$$u_{2\infty} = u_{3\infty} = 0.0$$

$$e_\infty = \frac{1}{\gamma(\gamma-1)} + \frac{M_\infty^2}{2} \tag{3.12}$$

$$p_\infty = \frac{1}{\gamma}$$

$$a_\infty = T_\infty = 1.0$$

$$U_\infty = \sqrt{u_{1\infty}^2 + u_{2\infty}^2 + u_{3\infty}^2} = u_{1\infty}$$

$$M_\infty = \frac{U_\infty}{a_\infty} = u_{1\infty}$$

where M_∞ is the freestream Mach number.

The unsteady Navier-Stokes equations in the Cartesian system are transformed into time-dependent body-conformed coordinates, ξ^1, ξ^2, and ξ^3; where

$$\xi^m = \xi^m(x_1, x_2, x_3; t) \tag{3.13}$$

The conservative form of the equations, in terms of the body-conformed coordinates, is given by

$$\frac{\partial \vec{Q}}{\partial t}+\frac{\partial \vec{E}_m}{\partial \xi^m}-\frac{\partial (\vec{E}_v)_s}{\partial \xi^s}=0 \quad ; \quad m=1\text{-}3; s=1\text{-}3 \tag{3.14}$$

and

$$\vec{Q}=\frac{\vec{q}}{J}=\frac{1}{J}[\rho, \rho u_1, \rho u_2, \rho u_3, \rho e]^t \tag{3.15}$$

where $1/J = J^{-1}$ is the Jacobian of the transformation from the Cartesian coordinates to the body-conformed coordinates, which is given by

$$J^{-1}=\frac{\partial(x_1,x_2,x_3;t)}{\partial(\xi^1,\xi^2,\xi^3;\tau)}=\begin{bmatrix} \frac{\partial x_1}{\partial \xi^1} & \frac{\partial x_1}{\partial \xi^2} & \frac{\partial x_1}{\partial \xi^3} & \frac{\partial x_1}{\partial \tau} \\ \frac{\partial x_2}{\partial \xi^1} & \frac{\partial x_2}{\partial \xi^2} & \frac{\partial x_2}{\partial \xi^3} & \frac{\partial x_2}{\partial \tau} \\ \frac{\partial x_3}{\partial \xi^1} & \frac{\partial x_3}{\partial \xi^2} & \frac{\partial x_3}{\partial \xi^3} & \frac{\partial x_3}{\partial \tau} \\ 0 & 0 & 0 & 1 \end{bmatrix} \tag{3.16}$$

The inviscid fluxes are given by

$$\begin{aligned} \hat{E}_m &= \frac{1}{J}\left[\partial_k \xi^m \hat{E}_k + \frac{\partial \xi^m}{\partial t}\vec{q}\right]^t \\ &= \frac{1}{j}\left[\rho U_m, \rho u_1 U_m + \partial_1 \xi^m p, \rho u_2 U_m + \partial_2 \xi^m p, \rho u_3 U_m + \partial_3 \xi^m p, (\rho e + p)U_m - \frac{\partial \xi^m}{\partial t} p\right]^t \end{aligned} \tag{3.17}$$

where the contravariant velocity component in the ξ^m direction, U_m, is given by

$$U_m = \partial_k \xi^m u_k + \frac{\partial \xi^m}{\partial t} \quad ; \quad k=1,2,3 \tag{3.18}$$

and $\partial_k \equiv \frac{\partial}{\partial x_k}$

The viscous and heat-transfer terms in the ξ^s direction, are given by

$$\left(\hat{E}_v\right)=\frac{1}{J}\left[0,\partial_k\xi^s\tau_{k1},\partial_k\xi^s\tau_{k2},\partial_k\xi^s\tau_{k3},\partial_k\xi^s(u_p\tau_{kp}-q_k)\right]^T ;\ \mathrm{k,p=1\text{-}3} \tag{3.19}$$

The shear stress and heat-transfer terms in the above equation are given by

$$\begin{aligned}\tau_{kl}&=\frac{\mu M_\infty}{\mathrm{Re}}\left(\partial_l\xi^m\frac{\partial u_k}{\partial\xi^m}+\partial_k\xi^m\frac{\partial u_l}{\partial\xi^m}-\frac{2}{3}\delta_{kl}\partial_j\xi^m\frac{\partial u_j}{\partial\xi^m}\right)\\ q_k&=-\frac{\mu M_\infty}{(\gamma-1)\,\mathrm{Pr}\,\mathrm{Re}}\partial_k\xi^m\frac{\partial a^2}{\partial\xi^m}\end{aligned} \tag{3.20}$$

Expanding the first element of the three momentum elements of Equation (3.19) to get

$$\partial_k\xi^s\tau_{k1}=\frac{\mu M_\infty}{\mathrm{Re}}\left[\left(\partial_k\xi^s\partial_1\xi^n-\frac{2}{3}\partial_1\xi^s\partial_k\xi^n\right)\frac{\partial u_k}{\partial\xi^n}+\partial_k\xi^s\partial_k\xi^n\frac{\partial u_1}{\partial\xi^s}\right] \tag{3.21}$$

The second and third elements of the momentum elements are obtained by replacing the subscript "1", everywhere in Equation (3.21), with 2 and 3, respectively. The last element of Equation (3.19) is given by

$$\begin{aligned}\partial_k\xi^s(u_p\tau_{kp}-q_k)=\frac{\mu M_\infty}{\mathrm{Re}}\Bigg[&\left(\partial_k\xi^s\partial_p\xi^n-\frac{2}{3}\partial_p\xi^s\partial_k\xi^n\right)u_p\frac{\partial u_k}{\partial\xi^n}\\ &+\partial_k\xi^s\partial_k\xi^n u_p\frac{\partial u_p}{\partial\xi^n}+\frac{1}{(\gamma-1)\,\mathrm{Pr}}\partial_k\xi^s\partial_k\xi^n\frac{\partial a^2}{\partial\xi^n}\Bigg];\quad \mathrm{k,s,n,p=1\text{-}3}\end{aligned} \tag{3.22}$$

where a is the dimensionless local speed of sound, $a^2=T$.

3.3 Turbulence Modeling

For the case of turbulent flow, the NS equations are transformed to the Reynolds Averaged equations. Using the concepts of eddy viscosity and turbulent conductivity,

the molecular viscosity, μ, is replaced by an effective viscosity, μ_e in the momentum equations

$$\mu_e = \mu + \mu_t \tag{3.23}$$

where μ_t is the turbulent viscosity. Similarly, in the energy equation, the molecular thermal conductivity, k, is replaced by the effective thermal conductivity, k_e

$$k_e = k + k_t = \frac{Cp}{\mathrm{Pr}}(1 + \frac{\mathrm{Pr}}{\mathrm{Pr}_t}\frac{\mu_t}{\mu}) \tag{3.24}$$

where Pr_t is the turbulent Prandtl number, which is chosen as 0.92 in this research work, and Cp is the constant pressure specific heat. For closure, μ_t is commonly handled through a turbulence model, which is discussed in the next Chapter. To compute the mathematical model of flow problems using the Navier-Stokes equations, initial and boundary conditions need to be specified.

Two turbulence models were used in the current investigation. The first one is an algebraic model (Baldwin-Lomax) and the second one is a one-equation model (Spalart-Allmaras).

3.3.1 Baldwin-Lomax Model

This model was first developed by Cebeci for the boundary-layer equations and modified by Baldwin and Lomax for the Navier-Stokes equations. It is a conventional two-layer model. The Prandtl mixing length with Van Driest damping governs the inner layer, and the outer layer follows the closure approximation. Computed vorticity is used in defining the reference mixing length required for the outer layer. The turbulent viscosity is given by

$$\mu_t = \begin{cases} (\mu_t)_i & r \le r_c \\ (\mu_t)_o & r > r_c \end{cases} \tag{3.25}$$

Where r is the normal distance from the body surface and r_c is the smallest value of r at which the inner-layer turbulent viscosity $(\mu_t)_i$ is equal to the outer-layer turbulent viscosity $(\mu_t)_o$. For the inner layer, the turbulent viscosity is calculated by using the Van Driest algebraic formula given by

$$(\mu_t)_i = \rho l^2 |\omega| \tag{3.26}$$

Where $|\omega|$ is the magnitude of vorticity and the mixing length l is given by

$$l = kr[1 - \exp^{-(r^+/A^+)}] \tag{3.27}$$

Where k is the von Karman constant, A^+ is a damping constant and r^+ is given by

$$r^+ = \frac{r\sqrt{\rho_w \tau_w}}{\mu_w} \tag{3.28}$$

The subscript w refers to the body surface. For the outer layer, the turbulent viscosity is given by

$$(\mu_t)_o = K_c Ccp \ \rho F_w F_{KB}(r) \tag{3.29}$$

Where K_c is the Closure constant and Ccp is another constant. The wake function F_w, is given by

$$F_w = \min(r_{\max} F_{\max}, C_w r_{\max} (\nabla \hat{V})^2 / F_{\max}) \tag{3.30}$$

Where F_{max} is found as the maximum of the following function

$$F(r) = |\omega| r[1 - \exp^{-(r^+/A^+)}] \tag{3.31}$$

And r_{max} is the corresponding value of r. The difference in the total velocity profile, ∇V, is obtained from

$$\nabla \hat{V} = \sqrt{(u_1^2 + u_2^2 + u_3^2)_{max}} - \sqrt{(u_1^2 + u_2^2 + u_3^2)_{min}} \tag{3.32}$$

F_{KB} (r) is the Klebanoff intermittency function given by

$$F_{KB}(r) = \left[1 + 5.5(rC_{KB} / r_{max})^6\right]^{-1} \tag{3.33}$$

The remaining constants are given by

$$A^+ = 26, \quad k = 0.4, \quad Kc = 0.0168, \quad Ccp = 1.6, \quad Cw = 0.25, \quad C_{KB} = 0.3 \tag{3.34}$$

In the current study the Degani and Schiff modification is used to obtain F_{max}.

3.3.2 Degani-Schiff Modification

The Degani-Schiff (1983) modification to the Baldwin-Lomax model is an algorithmic change, which attempts to select the first occurrence of F_{max} in a search from the wall outward. This can be important when there is a vortex somewhere above the body surface. If the code is not forced to select the F_{max} in the boundary layer, it may choose a length scale corresponding to the distance to the vortex, since F can be large in the vortex. In the current study, marching outward away from the body, F_{max} is updated index by index. Then, if $F < 0.9\ F_{max}$, the code stops searching.

3.3.3 Spalart-Allmaras Model

The Spalart-Allmaras model solves a single field equation for a variable ν related to the eddy viscosity through

$$\mu_t = \rho \hat{\nu} f_{v1} \tag{3.35}$$

where

$$f_{v1} = \frac{\chi^3}{\chi^3 + C_{v1}^3} \tag{3.36}$$

$$\chi \equiv \frac{\hat{\nu}}{\nu} \tag{3.37}$$

The equation is

$$\frac{\partial \hat{\nu}}{\partial t} + u_j \frac{\partial \hat{\nu}}{\partial x_j} = C_{b1}[1 - f_{t2}]\Omega \hat{\nu} + \frac{M_\infty}{Re}\left\{C_{b1}[(1 - f_{t2})f_{v2} + f_{t2}]\frac{1}{\kappa^2} - C_{w1} f_w\right\}\left(\frac{\hat{\nu}}{d}\right)^2 - \frac{M_\infty}{Re}\frac{C_{b2}}{\sigma}\hat{\nu}\frac{\partial^2 \hat{\nu}}{\partial x_j^2} + \frac{M_\infty}{Re}\frac{1}{\sigma}\frac{\partial}{\partial x_j}\left[(\nu + (1 + C_{b2})\hat{\nu})\frac{\partial \hat{\nu}}{\partial x_j}\right] \tag{3.38}$$

$$f_{t2} = C_{t3}\exp(-C_{t4}\chi^2) \tag{3.39}$$

d ≡ distance to the closest wall ≡ minimum distance function

$$f_w = g\left[\frac{1 + C_{w3}^6}{g^6 + C_{w3}^6}\right]^{\frac{1}{6}} = \left[\frac{g^{-6} + C_{w3}^{-6}}{1 + C_{w3}^{-6}}\right]^{-\frac{1}{6}} \tag{3.40}$$

$$g = r + C_{w2}(r^6 - r) \tag{3.41}$$

$$r = \frac{\hat{\nu}}{\hat{S}\left(\frac{Re}{M_\infty}\right)\kappa^2 d^2} \tag{3.42}$$

where

$$\hat{S} = f_{v3}\Omega + \frac{\hat{\nu} f_{v2}}{\left(\frac{Re}{M_\infty}\right)\kappa^2 d^2} \tag{3.43}$$

$$f_{v3} = \frac{(1 + \chi f_{v1})(1 - f_{v2})}{\chi} \tag{3.44}$$

$$f_{v2} = \frac{1}{\left(1 + \frac{\chi}{C_{v2}}\right)^3} \tag{3.45}$$

The constants are

$C_{b1} = 0.1355 \quad \sigma = 2/3 \quad C_{b2} = 0.622 \quad \kappa = 0.41 \quad C_{w2} = 0.3$

$C_{w3} = 2.0 \quad C_{v1} = 7.1 \quad C_{t3} = 1.2 \quad C_{t4} = 0.5 \quad C_{v2} = 5.0$

(3.46)

$$C_{w1} = \frac{C_{b1}}{\kappa} + \frac{(1+C_{b2})}{\sigma} \tag{3.47}$$

3.4 Initial and Boundary Conditions

3.4.1 Initial Conditions

All initial conditions for the present study (except for the flow control solution) correspond to the flow around a stationary wing at zero angle of attack, for which the wing surface is parallel to the streamwise direction. This is equivalent to impulsively inserting the wing into a uniform freestream. The initial conditions for the flow control solutions correspond to the flow around a stationary wing at an angle of attack of 20° that was impulsively inserted into a freestream with Mach number and Reynolds number of 0.3 and 0.45 x 10^6, respectively. The solution after 17,000 time steps with a time step of $\Delta t = 0.001$ is then used as an initial condition for the flow control case.

3.4.2 Boundary Conditions

All boundary conditions are explicitly implemented. They include inflow-outflow conditions, solid-boundary conditions and plane of geometric symmetry conditions. At the plane of geometric symmetry, periodic conditions are enforced. At the inflow boundaries, the Riemann-invariant boundary conditions are enforced. At the outflow boundaries, first-order extrapolation from the interior point is used.

The theoretical far-field boundary conditions for any external flow problem are that the gradient of disturbances vanishes at infinity. Unfortunately, the extent of the computational domains is always finite, and hence it is inappropriate to implement the physical far-field boundary conditions on a limited domain. Therefore, the numerical far-field boundary conditions are specified such that the reflection of waves at the boundaries should be minimized and the actual implementation is stable and well posed.

The non-reflecting boundary condition is based on characteristic theory. Using a local orthogonal coordinate system, one assumes that one of the coordinates outward unit vector is normal to the far-field boundary, and the others are tangential to the boundary surface. The eigenvalues of the flow-Jacobian matrix are u_n, u_n+a, and u_n-a with u_n being repeated three times for three-dimensional flows, where u_n is the local outward normal component of velocity at the boundary. The corresponding characteristic variables associated with each of the eigenvalues are s, u_{t1}, u_{t2}, $u_n+2a/(\gamma-1)$, and $u_n-2a/(\gamma-1)$, where $s = p/\rho^{\gamma}$ is the entropy and u_{t1} and u_{t2} are the two tangential components of velocity at the boundary. The last two characteristic variables are called the Riemann invariants. The characteristic variables are invariant along the characteristic lines and the sign of the eigenvalues determines the slope of the characteristics, which will indicate the direction of propagation, either into or out of the domain.

Since the wing is undergoing pitching motion, the grid is moved with the same angular motion as that of the body. The grid speed, $\partial\xi_m/\partial t$, and the metric coefficient, $\partial\xi_m/\partial x_n$, are computed at each time step of the computational scheme. Consequently, the kinematic boundary conditions at the inflow-outflow boundaries and at the wing surface are expressed in terms of the relative velocities. The dynamic boundary condition,

$\partial p/\partial n$, on the wing surface is no longer equal to zero. This condition is modified for the oscillating wing as

$$\left.\frac{\partial p}{\partial n}\right|_{wing} = -\rho\ \vec{a}_w \bullet \hat{n} \tag{3.48}$$

where $\vec{a}_w$ is the acceleration of a point on the wing flat surface; $\hat{n}$, the unit normal to the wing surface. The acceleration is given by

$$\vec{a}_w = \dot{\vec{\Omega}} X \vec{r} + \vec{\Omega} X (\vec{\Omega} X \vec{r}) \tag{3.49}$$

where $\vec{\Omega}$ is the angular velocity, noting that for a rigid body, the position vector $\vec{r}$, is not a function of time and hence, $\dot{\vec{r}} = \ddot{\vec{r}} = 0$. Finally, the boundary condition for the temperature is obtained from the adiabatic boundary condition and is given by

$$\left.\frac{\partial T}{\partial n}\right|_{wing} = 0 \tag{3.50}$$

The boundary conditions for the flow control case are the same as before but the wake of the wing is given an angle equal to the angle of attack to simulate the flow in the wake region. The grid, which has been generated for the flow case, has been modified to include the tilting of the wake region.

CHAPTER 4

COMPUTATIONAL SCHEME

4.1 Introduction

An upwind, finite-volume scheme, with Roe flux-difference splitting, is applied to the conservative form of the full Navier-Stokes equations in a generalized body-conformed coordinate system. The unsteady, full Navier-Stokes equations are integrated time accurately. Two types of schemes, explicit and implicit, may be used to integrate the equations in time. Although explicit schemes are simpler and require less computational effort per time step, an implicit scheme is used in this study. The implicit scheme has less restrictive stability boundaries. Ultimately, the implicit scheme, while more costly per time step, allows larger time steps and is more economical overall.

Central-differencing schemes while generally more accurate, produce oscillations in the vicinity of discontinuities which must be numerically damped with second and fourth order dissipation terms. By implementing an upwind scheme, the physical propagation of disturbances in the flow equations is mimicked by the difference equations without adding artificial viscosity. Using the theory of characteristics, the direction of propagation of information is determined and the time-dependent differencing is introduced in a separate and stable manner. While upwind schemes require two or three times more computational operations when compared to an equivalent central-differencing method, the increase in computational effort per iteration is offset by an improved rate of convergence and a wider applicability to general problems. Therefore, the upwind scheme is used for this study.

Upwind schemes can be used with either conservative or non-conservative forms of the governing equations. The advantage of using the conservative form is that shock waves and contact discontinuities evolve as parts of the solution process. The disadvantage is that upwind differencing can be implemented more economically in a non-conservative formulation but must be supplemented with a shock-fitting scheme for accurate results.

In this Chapter, the finite-volume implementations of conservative methods are discussed. Then, the application of the upwind flux-difference scheme to the three-dimensional Navier-Stokes equation is presented. The scheme is capable of solving time-dependent problems by using global time stepping and steady-flow problems by using pseudo time stepping to get asymptotic steady solutions. Because of the unsteady nature of the vortex-breakdown flows, a global time-integration technique was used in all the presented calculations. At the end of this Chapter, the computational resources used in the current study are also discussed.

4.2 Time Advancement

For a nondeforming mesh, the governing equations can be written as

$$\frac{1}{J}\frac{\partial Q}{\partial t} = R(Q) \tag{4.1}$$

where

$$R = -\left[\frac{\partial(\hat{F}-\hat{F}_v)}{\partial\xi} + \frac{\partial(\hat{G}-\hat{G}_v)}{\partial\eta} + \frac{\partial(\hat{H}-\hat{H}_v)}{\partial\varsigma}\right] \tag{4.2}$$

The time term can be discretized with backward differencing

$$\frac{(1+\Phi)(\underline{Q}^{n+1}-\underline{Q}^{n})-\Phi(\underline{Q}^{n}-\underline{Q}^{n-1})}{J\Delta t}=E(\underline{Q}^{n+1}) \tag{4.3}$$

where the superscripts indicate time level. When Φ = 0 the method is first-order temporally accurate; when Φ = ½ the method is second-order accurate. This equation is implicit because the right-hand side is a function of the unknown flow variables at time level n+1.

The implicit derivatives are written as spatially first-order accurate, which results in block-tridiagonal inversions for each sweep. However, for solutions that utilize Flux Difference-Splitting (FDS) scheme, the block-tridiagonal inversions are usually further simplified with a diagonal algorithm.

4.3 Spatial Discretization

4.3.1 Inviscid Fluxes

The spatial derivatives of the convective and pressure terms are written conservatively as a flux balance across a cell as, for example,

$$(\delta_{\xi}\hat{F})_{i}=\hat{F}_{i+\frac{1}{2}}-\hat{F}_{i-\frac{1}{2}} \tag{4.4}$$

where the i index denotes a cell-center location and i $\mp$1/2 corresponds to a cell-interface location. The interface flux is determined from a state-variable interpolation and a locally one-dimensional flux model.

For FDS, the interface flux is written as an exact solution to an approximate Riemann problem as

$$\left(\delta_\xi \hat{F}\right)_i = \frac{1}{2}\left[\hat{F}(q_L)+\hat{F}(q_R)-\left|\tilde{A}_{inv}\right|(q_R-q_L)\right]_{i+\frac{1}{2}} - \frac{1}{2}\left[\hat{F}(q_L)+\hat{F}(q_R)-\left|\tilde{A}_{inv}\right|(q_R-q_L)\right]_{i-\frac{1}{2}} \tag{4.5}$$

Interpolated values q_L and q_R at each interface are required. The state variable interpolation determines the resulting accuracy of the scheme. The values of q_L and q_R are constructed from interpolation of the primitive variables. For first-order fully-upwind differencing

$$\begin{aligned}(q_L)_{i+\frac{1}{2}} &= q_i \\ (q_R)_{i+\frac{1}{2}} &= q_{i+1}\end{aligned} \tag{4.6}$$

Higher order accuracy is given by the family of interpolations

$$\begin{aligned}(q_L)_{i+\frac{1}{2}} &= q_i + \frac{1}{4}\left[(1-K)\Delta_- + (1+K)\Delta_+\right]_i \\ (q_R)_{i+\frac{1}{2}} &= q_{i+1} - \frac{1}{4}\left[(1-K)\Delta_+ + (1+K)\Delta_-\right]_{i+1}\end{aligned} \tag{4.7}$$

where

$$\begin{aligned}\Delta_+ &\equiv q_{i+1} - q_i \\ \Delta_- &\equiv q_i - q_{i-1}\end{aligned} \tag{4.8}$$

The parameter $K \in [-1,1]$ forms a family of difference schemes. $K = -1$ corresponds to second-order fully upwind differencing, $K=1/3$ to third-order upwind-biased differencing, and $K = 1$ to central differencing.

4.3.2 Flux Limiting

For solutions with discontinuities (such as shock waves), high-order schemes generally require a flux limiter to avoid numerical oscillations in the solution. There are

several limiter options available in the computational scheme which has been used in the current study.

The smooth limiter is implemented via

$$(q_L)_{i+\frac{1}{2}} = q_i + \left\{\frac{s}{4}\left[(1-Ks)\Delta_- + (1+Ks)\Delta_+\right]\right\}_i$$
$$(q_R)_{i+\frac{1}{2}} = q_{i+1} - \left\{\frac{s}{4}\left[(1-Ks)\Delta_+ + (1+Ks)\Delta_-\right]\right\}_{i+1} \tag{4.9}$$

where

$$s = \frac{2\Delta_+\Delta_- + \varepsilon}{(\Delta_+)^2 + (\Delta_-)^2 + \varepsilon} \tag{4.10}$$

and ε is a small number ($\varepsilon = 1 \times 10^{-6}$) preventing division by zero in regions of null gradient.

The min-mod limiter is implemented via

$$(q_L)_{i+\frac{1}{2}} = q_i + \frac{1}{4}\left[(1-K)\bar{\Delta}_- + (1+K)\bar{\Delta}_+\right]_i$$
$$(q_R)_{i+\frac{1}{2}} = q_{i+1} - \frac{1}{4}\left[(1-K)\bar{\Delta}_+ + (1+K)\bar{\Delta}_-\right]_{i+1} \tag{4.11}$$

where

$$\bar{\Delta}_- = \min\,\mathrm{mod}(\Delta_-, b\Delta_+)$$
$$\bar{\Delta}_+ = \min\,\mathrm{mod}(\Delta_+, b\Delta_-) \tag{4.12}$$

$$\min\,\mathrm{mod}(x, y) = \max\{0, \min[x\, sign(y), b\, y\, sign(x)]\} sign(x) \tag{4.13}$$

The parameter b is a compression parameter, b = (3-K)/(1-K).

The smooth limiter tuned to K=1/3 is implemented as follows

$$(q_L)_{i+\frac{1}{2}} = q_i + \frac{1}{2}(\delta_L q)_i$$
$$(q_R)_{i+\frac{1}{2}} = q_{i+1} - \frac{1}{2}(\delta_R q)_{i+1} \tag{4.14}$$

where

$$(\delta_L q)_i = I(q_{i+1} - q_i, q_i - q_{i-1})$$
$$(\delta_R q)_i = I(q_i - q_{i-1}, q_{i+1} - q_i) \tag{4.15}$$

$$I(x,y) = \frac{x(y^2 + 2\varepsilon^2) + y(2x^2 + \varepsilon^2)}{2x^2 - xy + 2y^2 + 3\varepsilon^2} \tag{4.16}$$

and I is designed to recover the state variable to third-order accuracy in the one-dimensional case in smooth regions of the flow and interpolate without oscillations near discontinuities. The parameter ε^2 is a small constant of order $\Delta x3$, which is used to improve the accuracy near smooth extremum and reduce the nonlinearity of the interpolation in regions of small gradient.

4.3.3 Flux-Difference Splitting

The approximate Riemann solver of Roe is based on a characteristic decomposition of the fluid differences while ensuring the conservation properties of the scheme.

Consider a one-dimensional equation in the form

$$\frac{\partial \vec{q}}{\partial t} + \frac{\partial \vec{E}}{\partial x_1} = 0 \tag{4.17}$$

where E is a linear function of $\vec{q}$, Equation (4.17) can be written as

$$\frac{\partial \vec{q}}{\partial t} + A\frac{\partial \vec{q}}{\partial x_1} = 0 \tag{4.18}$$

where

$$A = \frac{\partial \vec{E}}{\partial \vec{q}} \tag{4.19}$$

The exact solution of the Riemann problem in terms of the flux difference is given by

$$\vec{E}_R - \vec{E}_L = \sum_{k=1}^{3} \alpha_k \lambda_k e_k \tag{4.20}$$

where λ_k and e_k are the eigenvalues and eigenvectors of the Jacobian matrix A, respectively, and α_k represents the projection of the difference in q between the initial right and left states onto the eigenvectors of A. The flux at the cell interface can be determined by either of the two following equations

$$E_{i+\frac{1}{2}}(\vec{q}_L, \vec{q}_R) = \vec{E}_L + \sum^{-} \alpha_k \lambda_k e_k \tag{4.21}$$

$$E_{i+\frac{1}{2}}(\vec{q}_L, \vec{q}_R) = \vec{E}_R - \sum^{-} \alpha_k \lambda_k e_k \tag{4.22}$$

where the signs on the summation symbols refer to the directions of the wave speeds. Averaging the previous two equations, one can obtain

$$E_{i+\frac{1}{2}}(\vec{q}_L, \vec{q}_R) = \frac{1}{2}\left[(\vec{E}_L + \vec{E}_R) - \sum_{k=1}^{3} \alpha_k |\lambda|_k e_k \right] \tag{4.23}$$

If E is not a linear function of q, e.g. one-dimensional Euler equations, Roe developed the following solution for the approximate linearized problem

$$\frac{\partial \vec{q}}{\partial t} + \tilde{A} \frac{\partial \vec{q}}{\partial x_1} = 0 \tag{4.24}$$

where A is called the Roe-average matrix. However, this matrix must have the following list of properties to ensure uniform validity across flow discontinuities

1- For any pair of q_i, q_{i+1},

$$E_{i+1} - E_i = \tilde{A}(\bar{q}_i, \bar{q}_{i+1}) \cdot (\bar{q}_i - \bar{q}_{i+1}) \tag{4.25}$$

2. If $q_i = q_{i+1} = q$, the matrix

$$\tilde{A}(\bar{q}, \bar{q}) = A(\bar{q}) = \frac{\partial \bar{E}}{\partial \bar{q}} \tag{4.26}$$

3. A must have real eigenvalues with linearly independent eigenvectors.

From this, the flux difference between the left and right states can be written as

$$\vec{E}_R - \vec{E}_L = \tilde{A}(\vec{q}_R - \vec{q}_L) \tag{4.27}$$

The interface flux is thus

$$E_{i+\frac{1}{2}}(\vec{q}_R, \vec{q}_L) = \frac{1}{2}\left[(\vec{E}_L + \vec{E}_R) - \left|\tilde{A}\right|(\vec{q}_R, -\vec{q}_L)\right]_{i+\frac{1}{2}} \tag{4.28}$$

For three-dimensional generalized flows, this can be written as

$$\hat{E}_{m_{i+\frac{1}{2}}}(\vec{Q}_R, \vec{Q}_L) = \frac{1}{2}\left[(\hat{E}_{mR} + \hat{E}_{mL}) - \left|\tilde{A}\right|(\vec{Q}_R, -\vec{Q}_L)\right]_{i+\frac{1}{2}}; \text{m} = 1\text{-}3 \tag{4.29}$$

where j, k and n are kept constant. The last term in the above equation represents the dissipation contribution to the interface flux and is given by

$$\left|\tilde{A}\right|(\vec{Q}_R - \vec{Q}_L) = \left|\tilde{A}\right|\Delta\vec{Q}$$

$$= \begin{bmatrix} \alpha_4 \\ \tilde{u}_1\alpha_4 + \xi^m_{x_1}\alpha_5 + \alpha_6 \\ \tilde{u}_2\alpha_4 + \xi^m_{x_2}\alpha_5 + \alpha_7 \\ \tilde{u}_3\alpha_4 + \xi^m_{x_3}\alpha_5 + \alpha_8 \\ \tilde{H}\alpha_4 + \tilde{U}_m\alpha_5 + \tilde{u}_1\alpha_6 + \tilde{u}_2\alpha_7 + \tilde{u}_3\alpha_8 - \left(\frac{\tilde{a}^2}{\gamma - 1}\right)\alpha_1 \end{bmatrix} \tag{4.30}$$

where

$$\alpha_1 = \left|\frac{grad(\xi^m)}{J}\right|\left|\tilde{U}_m\right|(\Delta\rho - \frac{\Delta p}{\tilde{a}^2}) \tag{4.31}$$

$$\alpha_2 = \frac{1}{2\tilde{a}^2}\left|\frac{grad(\xi^m)}{J}\right|\left|\tilde{U}_m + \tilde{a}\right|(\Delta p + \tilde{\rho}\tilde{a}\Delta\tilde{U}_m) \tag{4.32}$$

$$\alpha_3 = \frac{1}{2\tilde{a}^2}\left|\frac{grad(\xi^m)}{J}\right|\left|\tilde{U}_m - \tilde{a}\right|(\Delta p - \tilde{\rho}\tilde{a}\Delta\tilde{U}_m) \tag{4.33}$$

$$\alpha_4 = \alpha_1 + \alpha_2 + \alpha_3 \tag{4.34}$$

$$\alpha_5 = \tilde{a}(\alpha_2 - \alpha_3) \tag{4.35}$$

$$\alpha_{5+j} = \left|\frac{grad\,(\xi^m)}{J}\right|\left|\tilde{U}_m\right|(\tilde{\rho}\Delta u_j - \xi^m_{x_1}\tilde{\rho}\Delta\tilde{U}_m)\,;\ \mathrm{j} = 1\text{-}3 \tag{4.36}$$

The ~ superscript denotes Roe-averaged values where

$$\tilde{\rho} = \sqrt{\rho_L \rho_R} \tag{4.37}$$

$$\tilde{u}_j = \frac{u_{jL} + u_{jR}\sqrt{\rho_L\rho_R}}{1+\sqrt{\rho_L\rho_R}} \tag{4.38}$$

$$\tilde{H} = \frac{H_L + H_R\sqrt{\rho_L\rho_R}}{1+\sqrt{\rho_L\rho_R}} \tag{4.39}$$

$$\tilde{a}^2 = (\gamma - 1)[\tilde{H} - u_j u_j/2] \quad ;\ \mathrm{j} = 1\text{-}3 \tag{4.40}$$

where $\tilde{H}$ is the Roe-averaged enthalpy.

The contravariant velocity normal to the cell interface is given by

$$\overline{U}_m = \hat{\xi}^m_{x_j} u_j \ ;\ \mathrm{j} = 1\text{-}3 \tag{4.41}$$

4.3.4 Discretization of the Viscous Fluxes

The viscous terms, which represent shear stress and heat transfer effects, are discretized with second-order central differences. The second derivatives are treated as differences across cell interfaces of first-derivative terms. The viscous flux contribution on the left-hand side of the difference equations are given by

$$\delta\xi^1\frac{\partial\hat{E}_{v1}}{\partial\bar{Q}} + \delta\xi^2\frac{\partial\hat{E}_{v2}}{\partial\bar{Q}} + \delta\xi^3\frac{\partial\hat{E}_{v3}}{\partial\bar{Q}} \equiv \delta\xi^m\frac{\partial\hat{E}_{vm}}{\partial\bar{Q}}\,;\ \mathrm{m} = 1\text{-}3 \tag{4.42}$$

Differentiating the terms that are functions of ξ^n (where n≠m) will produce cross-derivative terms. The presence of these terms on the left-hand side of the difference equation would destroy the advantage of solving a tri-diagonal matrix by requiring a central differencing of these terms. Also, the viscous terms containing derivatives parallel to the solid body surface can be neglected relative to those in the normal direction. This approximation is known as the thin-layer approximation where only the viscous terms containing derivatives normal to the body surface (along the coordinate line), are retained. In this study, the thin-layer approximation was used only to simplify the viscous terms on the left-hand side of the difference equation for better efficiency of the computer code; while the cross derivative terms were retained on the right-hand side of the difference equation where they can be evaluated explicitly.

The thin-layer type viscous terms are obtained from the momentum and energy equations by retaining only terms with derivatives in the direction under consideration. Therefore, the momentum equation becomes

$$\partial_k \xi^m \tau_{kn} \equiv \frac{\mu M_\infty}{Re}\left[\frac{1}{3}\partial_k \xi^m \partial_n \xi^m \frac{\partial u_k}{\partial \xi^m} + \partial_k \xi^m \partial_k \xi^m \frac{\partial u_n}{\partial \xi^m}\right]; \; k, m, n = 1\text{-}3 \tag{4.43}$$

and the energy equation becomes

$$\begin{aligned}\partial_k \xi^s (u_p \tau_{kp} - q_k) = \frac{\mu M_\infty}{Re}\Bigg[&\frac{1}{3}\partial_p \xi^s \partial_k \xi^s u_p \frac{\partial u_k}{\partial \xi^s} \\ &+ \partial_k \xi^s \partial_k \xi^s \left(\frac{\partial u_n}{\partial \xi^s} + \frac{1}{(\gamma - 1)\,Pr}\frac{\partial (a^2)}{\partial \xi^s}\right)\Bigg]; \; k, n, p, s = 1\text{-}3\end{aligned} \tag{4.44}$$

On the right-hand side of the difference equation, the viscous term contribution in the residual is given by

$$\hat{R}_v = \delta_{\xi^1}\hat{E}_{v1} + \delta_{\xi^2}\hat{E}_{v2} + \delta_{\xi^3}\hat{E}_{v3} = \delta_{\xi^m}\hat{E}_{vm} \; ; m = 1\text{-}3 \tag{4.45}$$

The viscous fluxes are linearized in time as follows

$$\hat{E}_{vm}^{n+1} = \hat{E}_{vm}^{n} + O(\Delta t) \tag{4.46}$$

The viscous terms at the n+1 time step are evaluated using information from the previous time step, n. The fluxes are centrally differenced and a second-order approximation to the cross derivative terms is used as follows

$$\frac{\partial^2 u_1}{\partial \xi^1 \partial \xi^2} \equiv \delta_{\xi^1\xi^2}(u_1)_{i,j}$$
$$= \alpha^+\left(\delta_{\xi^1\xi^2}(u_1)_{i+\frac{1}{2},j+\frac{1}{2}} + \delta_{\xi^1\xi^2}(u_1)_{i-\frac{1}{2},j-\frac{1}{2}}\right) + \alpha^-\left(\delta_{\xi^1\xi^2}(u_1)_{i-\frac{1}{2},j+\frac{1}{2}} + \delta_{\xi^1\xi^2}(u_1)_{i+\frac{1}{2},j-\frac{1}{2}}\right) \tag{4.47}$$

where

$$\delta_{\xi^1\xi^2}(u_1)_{i+\frac{1}{2},j+\frac{1}{2}} = (u_1)_{i+1,j+1} - (u_1)_{i,j+1} + (u_1)_{i,j} - (u_1)_{i-1,j} \tag{4.48}$$

and

$$\alpha^+ + \alpha^- = \frac{1}{2} \tag{4.49}$$

4.4 Computational Resources

The modified, full NS equations within the CFL3D code (Versions 1, 2, and 3) of NASA Langley Research Center has been used. The original CFL3D code (all versions) is for Thin Layer Navier Stokes equations. In the beginning of the current study, the modified, full NS equations of CFL3D version 1 have been used for the experimental validation, reduced frequency effect, Baldwin-Lomax, and pitch-up pitch-down solutions. The modified, full NS equations of CFL3D version 2 is used for the refined grid and flow control solutions. Because CFL3D versions 1 and 2 don't have the Spalart-Allmaras

model, the modified, full NS equations of CFL3D version 3 has been used for the Spalart-Allmaras solution.

The computational results obtained for the validation solution and for the Baldwin-Lomax turbulence model were performed using a CRAY-YMP computer at NASA Langley Research Center. On this machine, each case took 82 hours to complete a ramp amplitude of 90°. Also, a CRAY C-90 machine was used in the pitch-up pitch-down case. The refined grid, Spalart-Allmaras, and flow control cases were performed on PC's because of unavailability of supercomputers. Each case took around 3-4 weeks on a Pentium II 300 MHz machine. One of the important differences between the Cray and PC's is that while the Cray is a 64 bit machine, the PC's are 32 bit architecture.

CHAPTER 5

LAMINAR FLOW SOLUTIONS

In this Chapter, the laminar, time accurate, three-dimensional Navier Stokes solution along with the aerodynamic response of a 76° delta wing undergoing pitch-up motion up to 90° amplitude are presented.

5.1 Validation with Experimental Data

The delta wing model used in the present computational study consists of a 76° swept back, sharp-edged wing with zero thickness and an aspect ratio of one, similar to that in Jarrah (1988). The three-dimensional O-H grid topology used in the calculations is shown in Figure 5.1 with a cross-section at the trailing edge. The name of O-H grid comes from the shape of the grid in both lateral and longitudinal directions, respectively. A relatively coarse grid is used to minimize the computational cost of very low non-dimensional pitching rate maneuvers in order to facilitate comparison with the available experimental data. The non-dimensional pitching rate is equal to $(\dot{\alpha} C / 2 a_\infty)$, where $\dot{\alpha}$ is the rate of change of angle of attack, C is the root chord length, and a_∞ is the upstream speed of sound. Because of the large gradients near the wing surface the grid clustering technique has been used to capture any flow details near the solid boundary. Even with the current coarse grid, 84 x 65 x 43 in the axial, wrap-around, and outward directions, respectively, this case took 82 hours on a CRAY-YMP computer at NASA Langley Research Center to complete a ramp amplitude of 90°.

The pitch axis is located at two-thirds of the root chord station, as measured from the wing vertex. The wing is forced to undergo a pitching motion through a ramp

function shown in Figure 5.2 and is described by $\alpha = 0.024$ t, which is related to the reduced frequency. The angle of attack, α, varies from 0° to 90° through this function. In the current study, the reduced frequency word will be used interchangeably with the non-dimensional pitching rate because they are equal in the case of ramp motions.

The freestream Mach number and Reynolds number are 0.3 and 0.45×10^6, respectively. The NS Equations are integrated time accurately with $\Delta t = 0.001$. This translates into 65,450 time steps to complete the solution for the flow response of the ramp motion up to $\alpha = 90°$.

Figure 5.3 shows the variations of C_L with α of the present computational results and the corresponding values of the experimental data of Jarrah (1988). The C_L curve shows a very good agreement until α reaches 40°. For angles of attack greater than 40°, the computed C_L values of the present study over-estimate those of the experimental data by about 12%. The predicted peak of the C_L curve slightly under-estimates the experimental value. The uncertainty in measuring the force coefficients in the experimental data is around 7.5%.

Figure 5.4 shows the variations of C_D with α. An excellent agreement between the computed C_D values of the present study and those of the experimental data is observed until α reaches 60°. After $\alpha = 60°$, the computed results over-estimate the experimental data. However, the present study predicted accurately the angle of attack at which the breakdown point passes upstream of the trailing edge, which is in the current case about 39°.

Figures 5.5-5.20 show the time-dependent vortex core development and breakdown over the wing surface from very low to very high values of angle of attack

(10°-80°). Figure 5.5 shows the particle traces of the leading edge vortices over the delta wing and the spanwise pressure coefficient distributions at three different axial chord stations of 0.3, 0.6 and 0.9 at $\alpha = 10°$. The pressure suction peaks are close to the leading edge at the 80% semi-span location. As one can observe, the vortex flow is developing over the wing surface and the pressure variations are starting to build-up. Figure 5.6 shows the cross-flow instantaneous streamlines at $\alpha = 10°$ for two axial stations of $x = 0.4$ and $x = 0.9$ (one near the apex and one near the trailing edge). A very small separated flow region is located over the wing surface. The vortex core is very tight over the wing surface and its center is located near the leading edge. Figures 5.7 and 5.8 show the axial velocity and Mach number contours at $\alpha = 10°$ and $x = 0.4$ and 0.9. The axial velocity contours do not show significant acceleration inside the vortex core.

Figure 5.9 shows the particle traces over the delta wing and the spanwise pressure coefficient distributions at $\alpha = 20°$ for three different axial chord stations. The vortex core over the wing surface starts to expand laterally and the pressure distribution peaks are higher than those at $\alpha = 10°$. These characteristics can be observed in Figure 5.10, which shows the cross-flow instantaneous streamlines at $\alpha = 20°$ at two different axial stations of 0.4 and 0.9. Figures 5.11 and 5.12 show the axial velocity and Mach number contours at $\alpha = 20°$ and $x = 0.4$ and 0.9. The flow is accelerated inside the vortex core region.

Figure 5.13 shows the particle traces over the delta wing and spanwise pressure coefficient distributions and Figure 5.14 shows the cross-flow instantaneous streamlines at $\alpha = 30°$. Figures 5.15 and 5.16 show the axial velocity and Mach number contours at $\alpha = 30°$ and $x = 0.4$ and 0.9. The flow is symmetric and accelerated further inside the

vortex core. While the magnitude of the axial velocity inside the vortex core at x = 0.4 is 0.47, its value is 0.36 at x = 0.9. Also, the Mach number values, inside the vortex core, at x = 0.4 and 0.9 are 0.54 and 0.37; respectively.

The vortex breakdown passes across the trailing edge at around 39° angle of attack as can be seen from Figure 5.17. The streamlines adapt spiral motions near the trailing edge as can be seen from Figure 5.18. Figures 5.19 and 5.20 show the axial velocity and Mach number contours at α = 40° and x = 0.4 and 0.9. At still higher angles of attack, Figure 5.21 shows that the vortex breakdown is translating further upstream and the vortex core is expanding laterally. The pressure coefficient peak is flattening and the pressure suction peak magnitudes are decaying at x = 0.6 and 0.9. Figure 5.22 shows the cross-flow instantaneous streamlines at α = 50°. The post-breakdown spiral motion is moving upstream toward the apex of the wing. Figures 5.23 and 5.24 show the axial velocity and Mach number contours at α = 50° and x = 0.4 and 0.9. Vortex breakdown is observed at x = 0.4 and 0.9 at α = 50°. The flow is decelerated inside the vortex core region and even undergoes flow reversal as indicated by the negative axial velocity values.

Figures 5.25 and 5.26 show that the breakdown is covering a large portion of the wing surface at α = 60° (from the trailing edge until x = 0.3). The pressure coefficient distribution is flattening near the leading edge of the wing at x = 0.6 and x = 0.9. Figures 5.27 and 5.28 show the axial velocity and Mach number contours at α = 60° and x = 0.4 and 0.9. Axial velocity contours show higher negative velocity values in the core region in comparison with those at α = 50°.

The particle trace shapes, spanwise pressure coefficient distributions, and cross-flow instantaneous streamlines at $\alpha = 70°$ and 80° are shown in Figures 5.29, 5.30, 5.33, and 5.34. Figures 5.31, 5.32, 5.35, and 5.36 show the axial velocity and Mach number contours at $\alpha = 70°$ and 80° at x = 0.4 and 0.9. The asymmetry of the flow over the whole wing surface is clearly observed in Figures 5.30 and 5.34. The pressure coefficient distributions are flat over the wing span for the three axial stations with noticeable lateral unbalance.

In summary, at low angles of attack, a tight vortex core develops at the leading edge of the wing. As the angle of attack increases, the vortex core expands laterally until it breaks down at the trailing edge around $\alpha = 39°$, due to the adverse axial pressure gradient associated with large regions of flow separations. Then, the breakdown point moves upstream expanding the size of the vortex core, due to the axial momentum loss, until it covers the entire wing surface showing asymmetric flow field.

Figures 5.37-5.41 show two snapshots of the flow streamlines along with the wing surface stagnation pressure and the vortex core stagnation pressure surfaces at $\alpha = 30°$, 38°, 40°, 50° and 60°. From these figures, the development of the vortex breakdown over the wing surface with increasing angle of attack is clear. At $\alpha = 70°$ the breakdown moves further upstream to cover a larger area of the wing making this area a non-lifting area with the remaining area of the wing generating a lift force. At $\alpha = 90°$, the whole wing is a non-lifting surface. Figure 5.42 gives four different views of the wing at an angle of attack of 70° showing the vortex core shape and the flow streamlines. After the angle of attack, α, reaches 40°, the breakdown moves upstream of the trailing edge and as the angle of attack increases further, the breakdown moves towards the wing apex.

During this transition period, the vortex core pair flows expand and coalesce in the front portion of the wing as shown in Figure 5.42 (see back and top views).

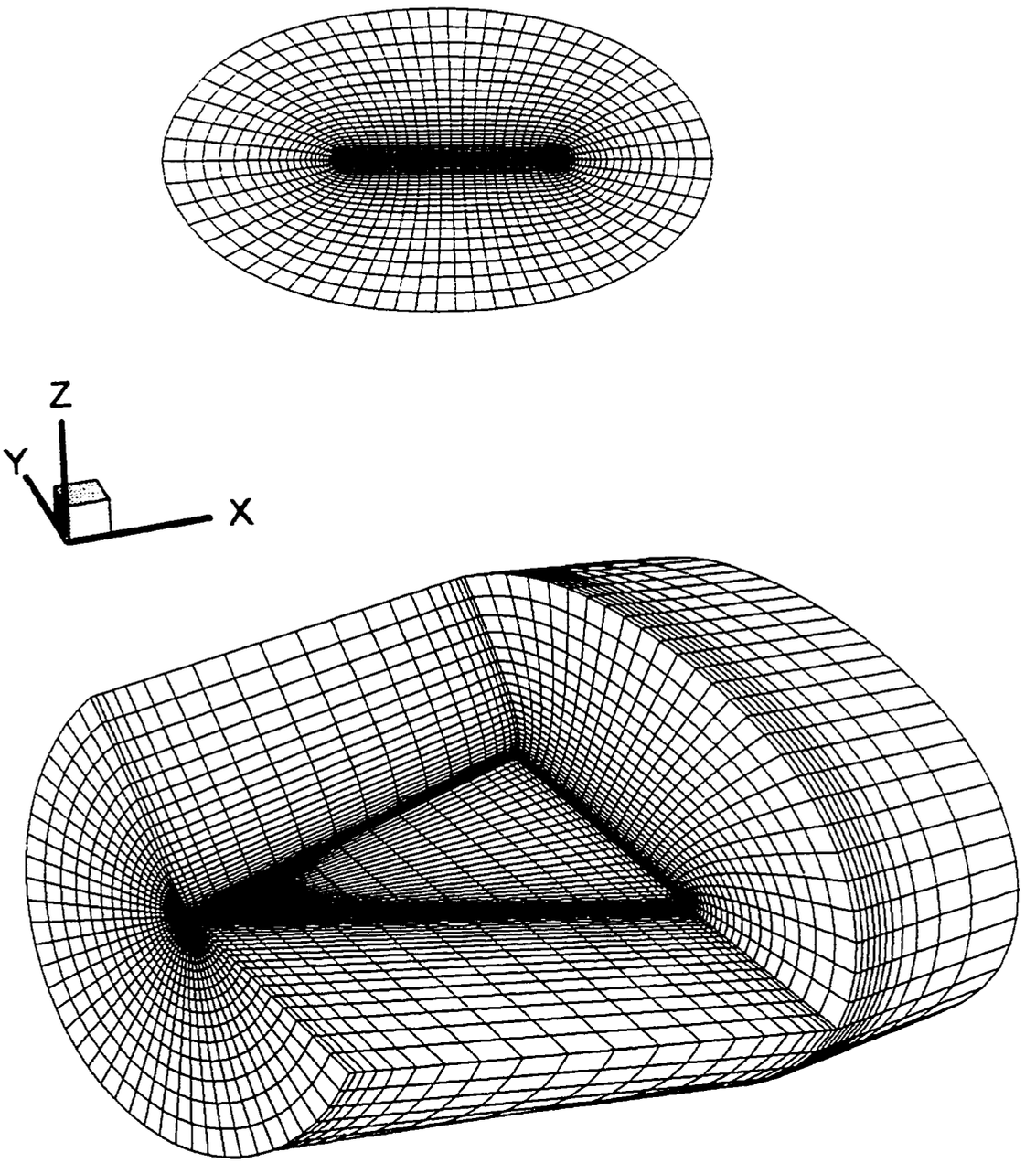

Figure 5.1: Portion of the three dimensional grid and cross section at the trailing edge

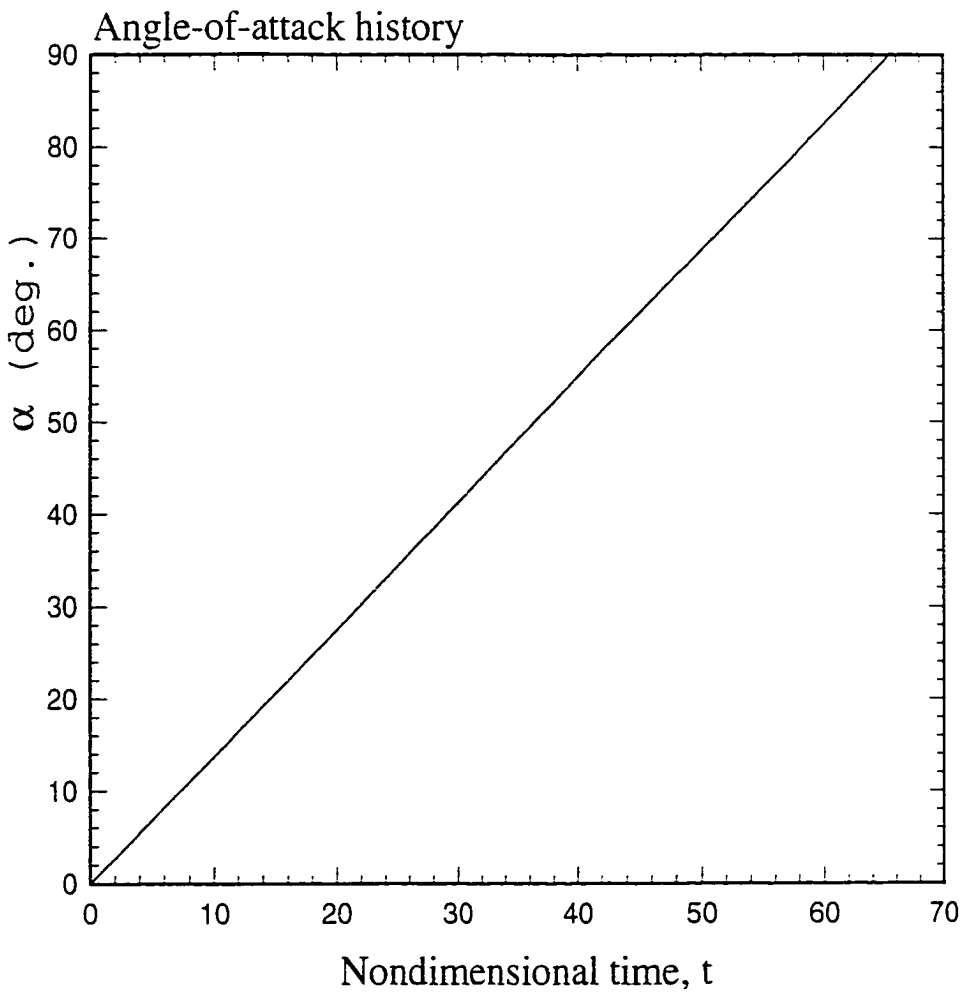

Figure 5.2: Forced ramp function time history

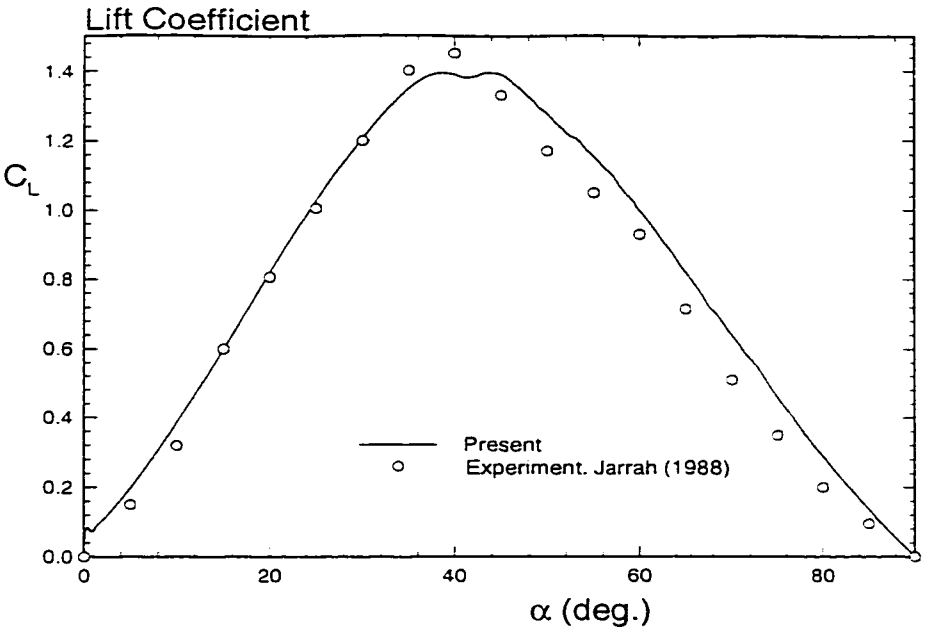

Figure 5.3: Lift coefficient vs. α using laminar NS equations.

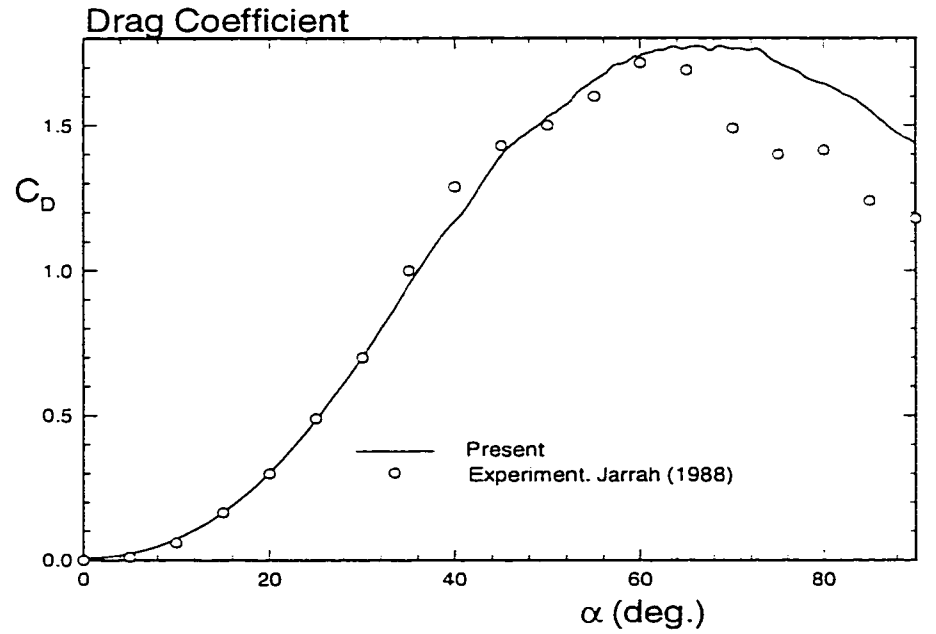

Figure 5.4: Drag coefficient vs. α using laminar NS equations.

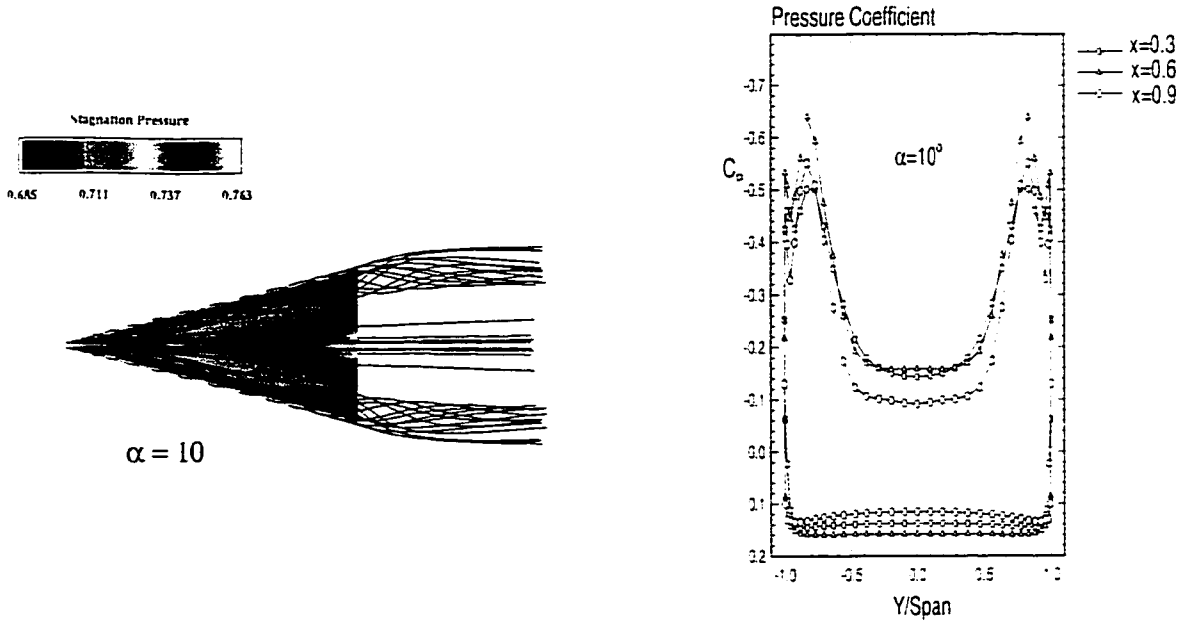

Figure 5.5: Particle traces over the delta wing and spanwise pressure coefficient distributions at $\alpha = 10^o$

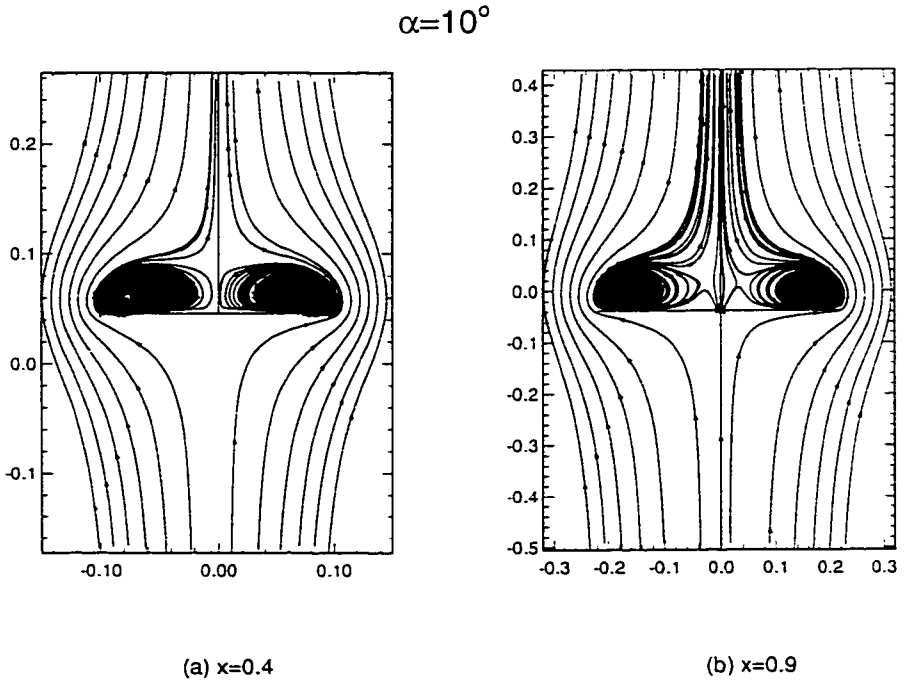

Figure 5.6: Cross-flow instantaneous streamlines at $\alpha = 10^o$ (a) x=0.4 and (b) x=0.9

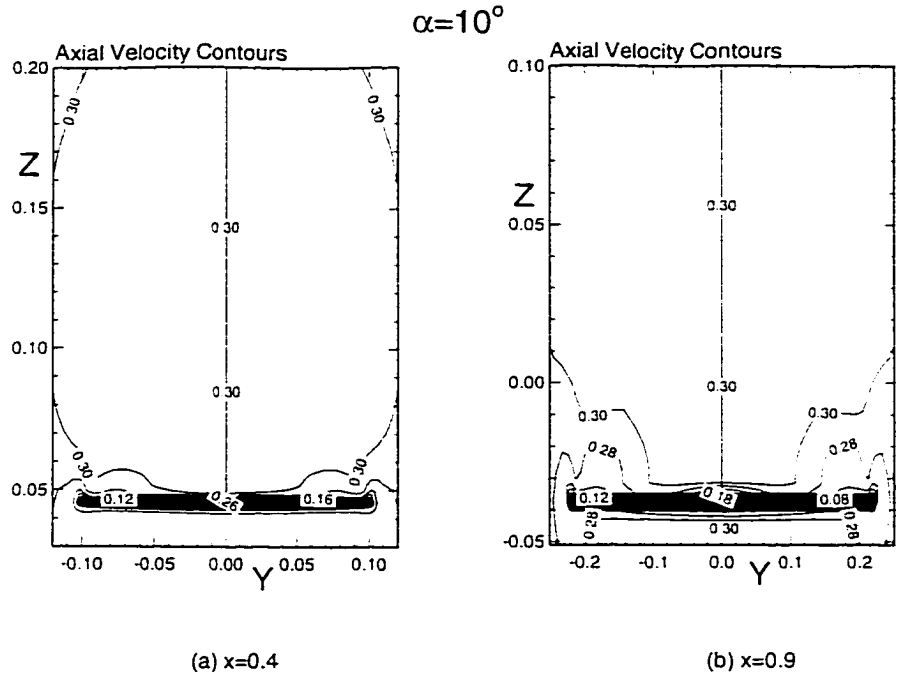

Figure 5.7: Axial velocity contours at $\alpha = 10°$ (a) x=0.4 and (b) x=0.9

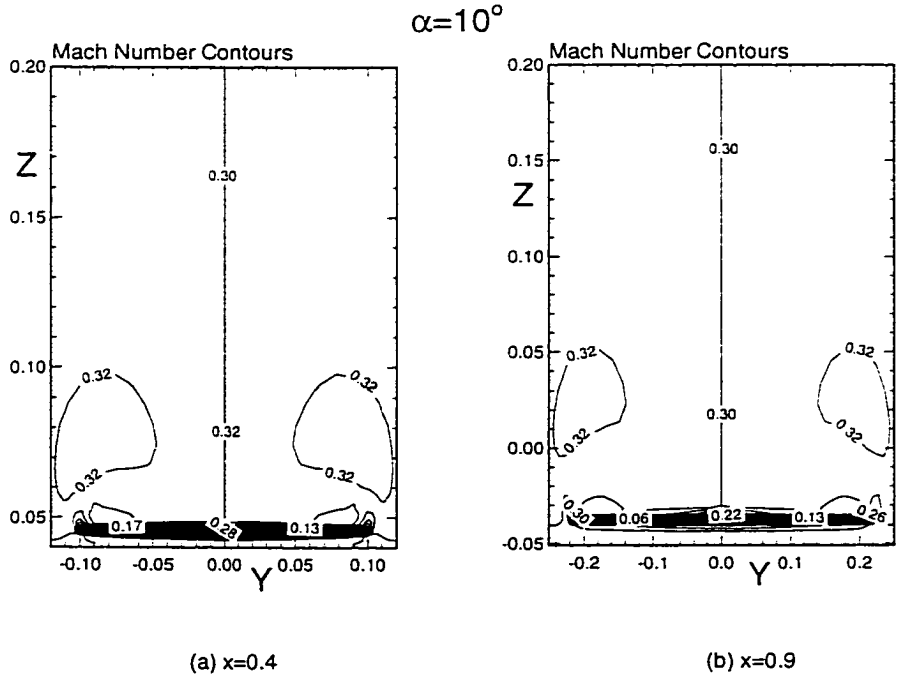

Figure 5.8: Mach number contours at $\alpha = 10°$ (a) x=0.4 and (b) x=0.9

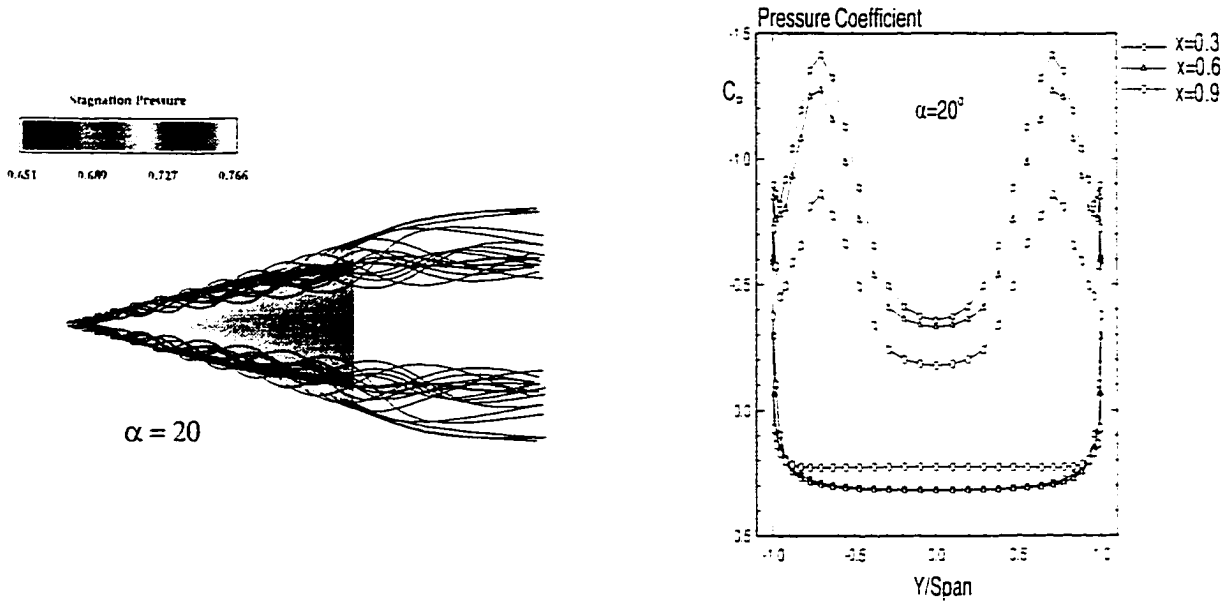

Figure 5.9: Particle traces over the delta wing and spanwise pressure coefficient distributions at $\alpha = 20°$

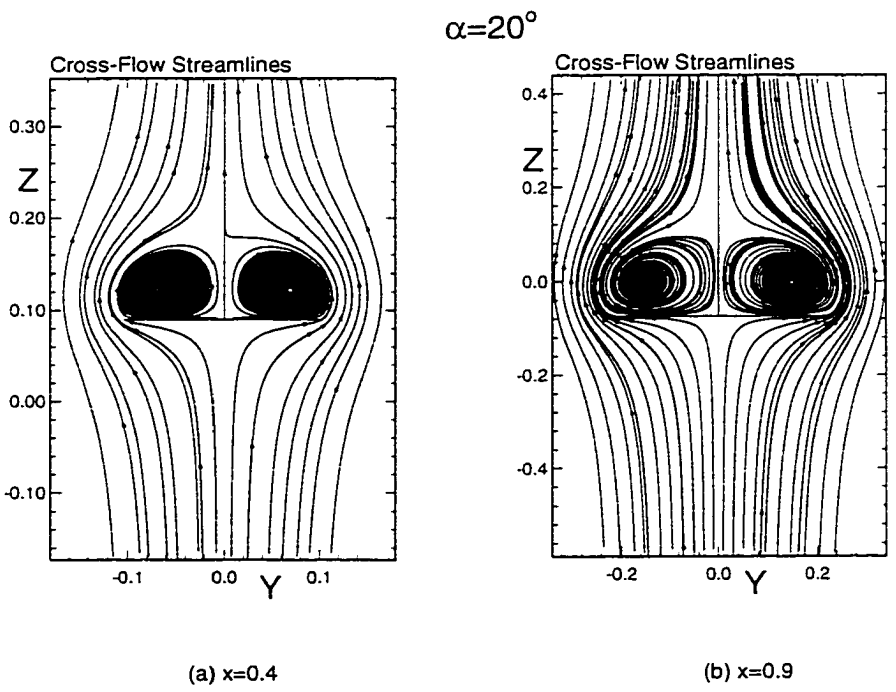

Figure 5.10: Cross-flow instantaneous streamlines at $\alpha = 20°$ (a) x=0.4 and (b) x=0.9

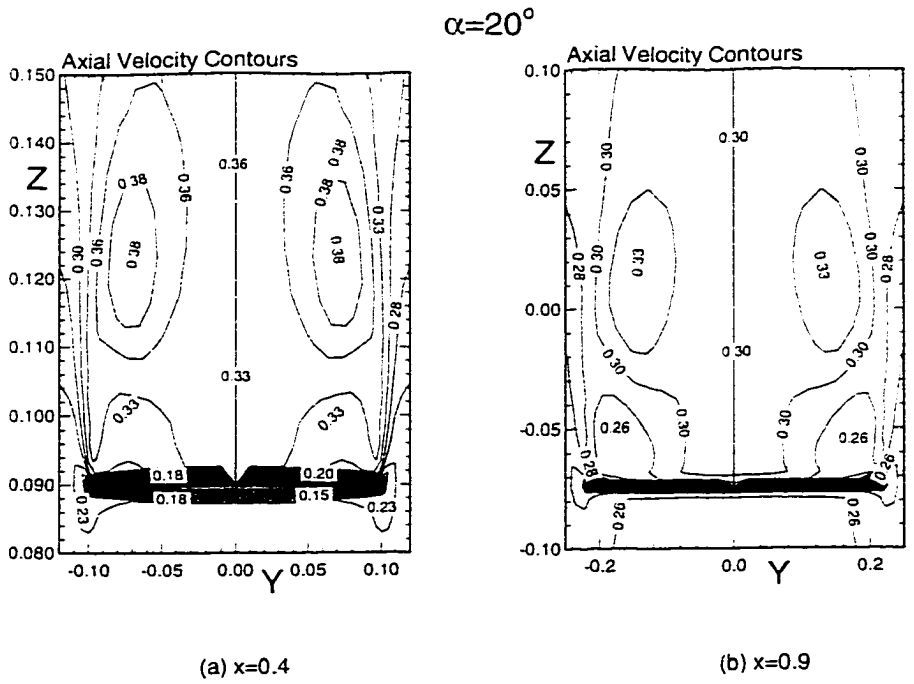

Figure 5.11: Axial velocity contours at $\alpha = 20°$ (a) x=0.4 and (b) x=0.9

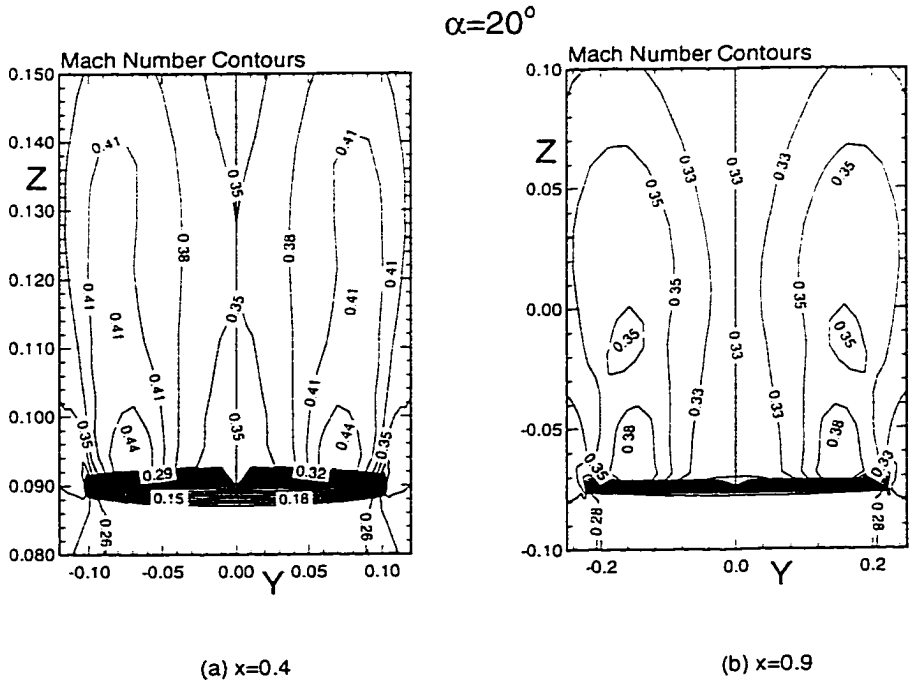

Figure 5.12: Mach number contours at $\alpha = 20°$ (a) x=0.4 and (b) x=0.9

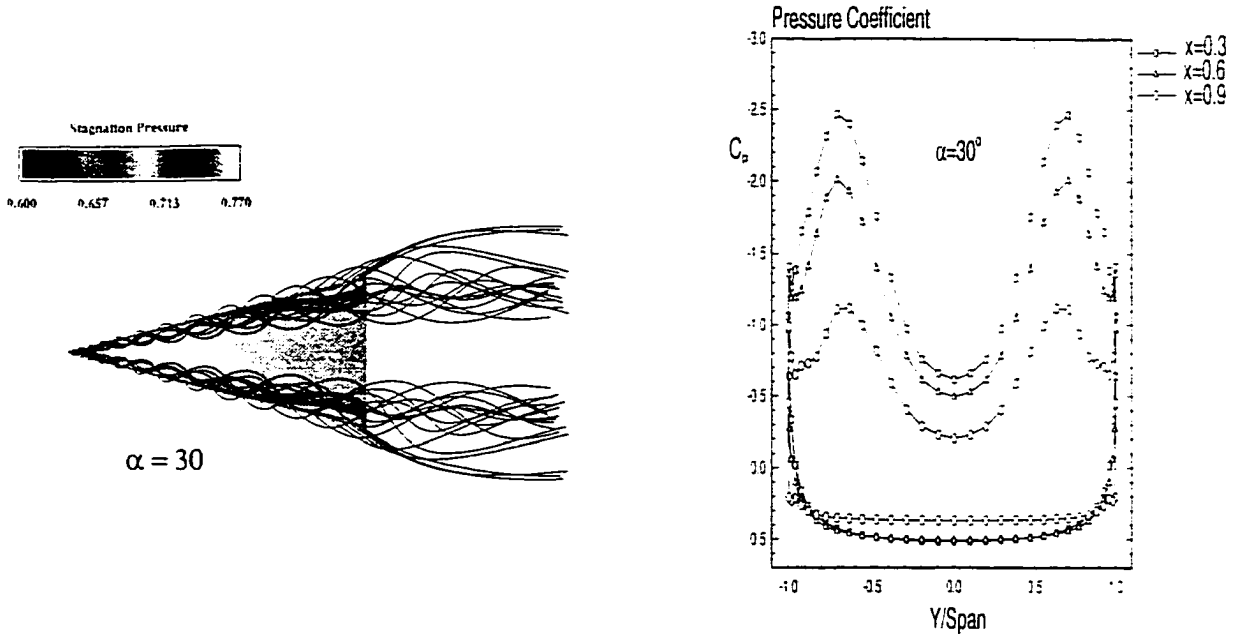

Figure 5.13: Particle traces over the delta wing and spanwise pressure coefficient distributions at $\alpha = 30°$

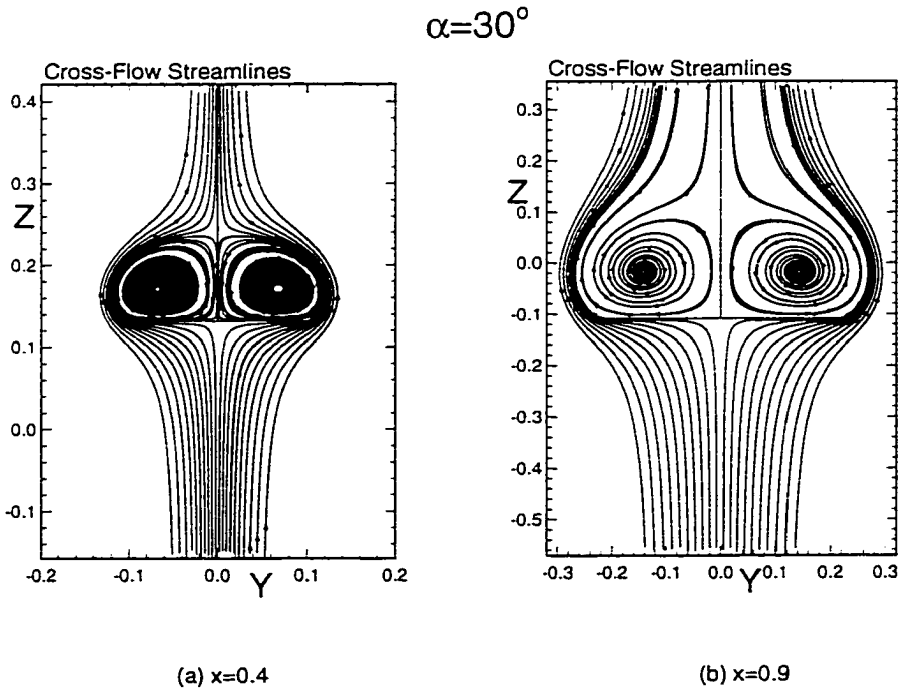

Figure 5.14: Cross-flow instantaneous streamlines at $\alpha = 30°$ (a) x=0.4 and (b) x=0.9

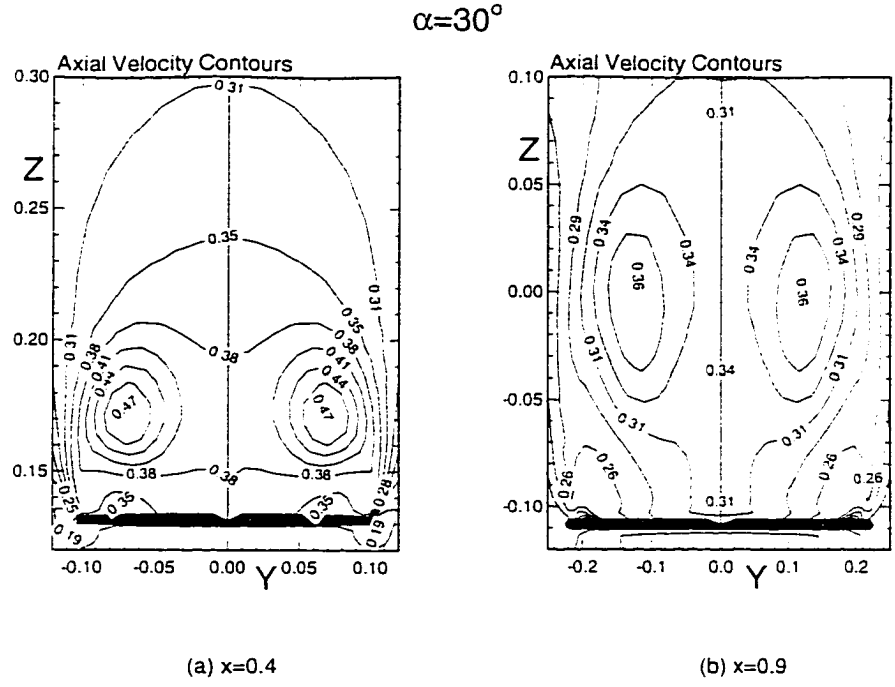

(a) x=0.4 (b) x=0.9

Figure 5.15: Axial velocity contours at $\alpha = 30°$ (a) x=0.4 and (b) x=0.9

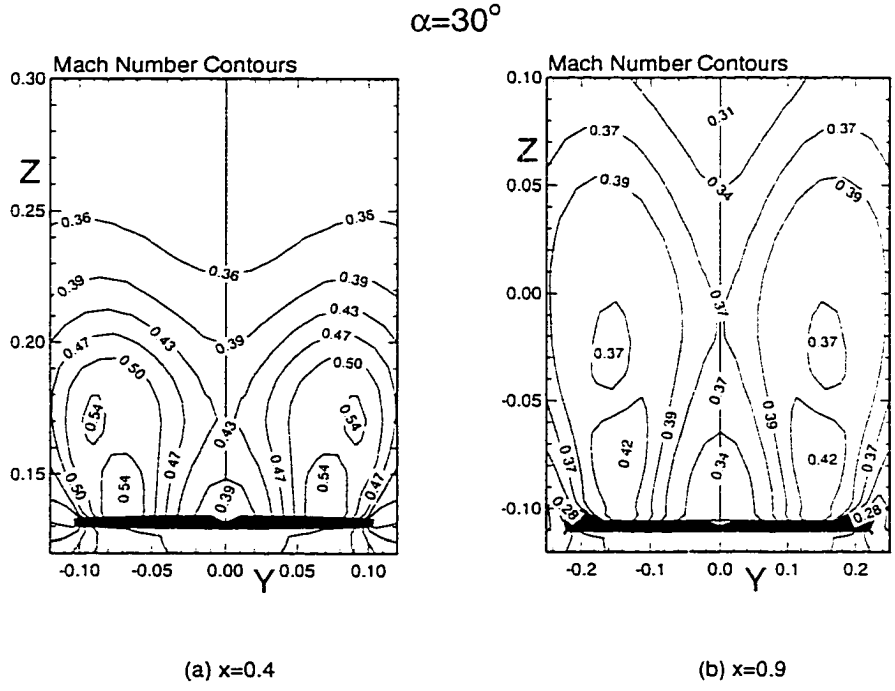

(a) x=0.4 (b) x=0.9

Figure 5.16: Mach number contours at $\alpha = 30°$ (a) x=0.4 and (b) x=0.9

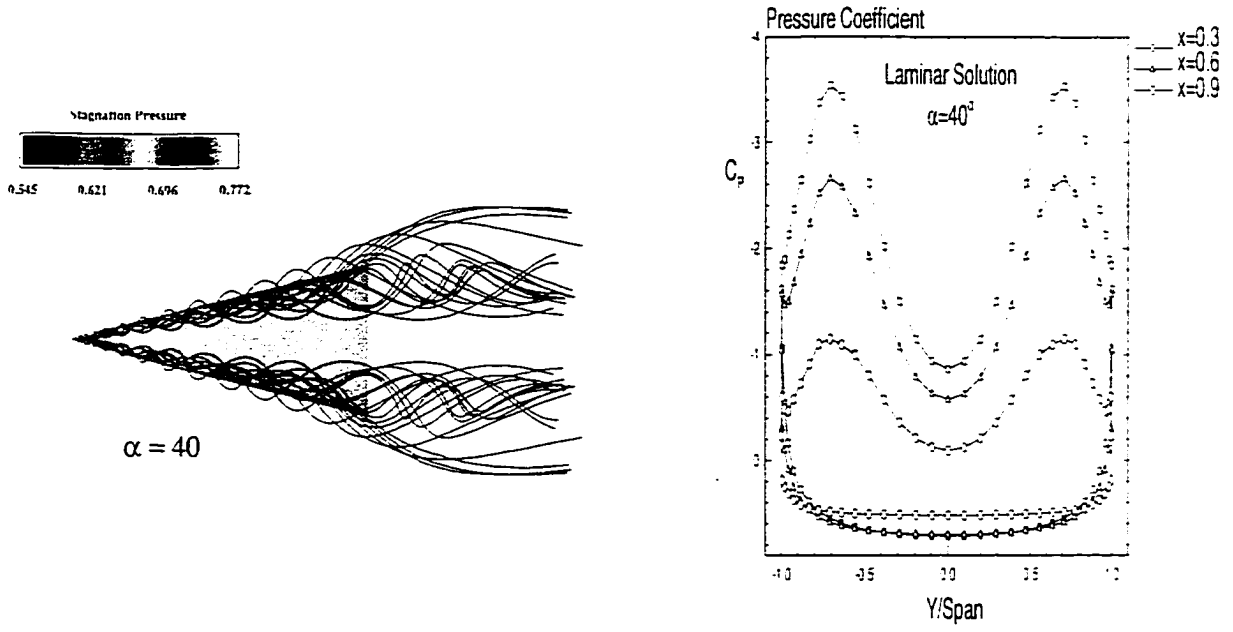

Figure 5.17: Particle traces over the delta wing and spanwise pressure coefficient distributions at $\alpha = 40^{o}$

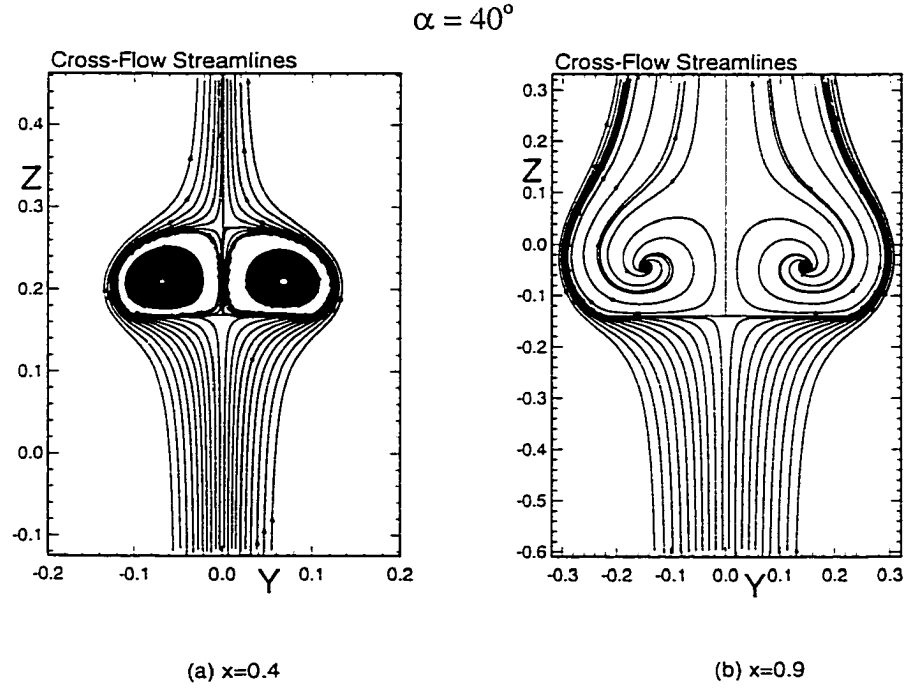

Figure 5.18: Cross-flow instantaneous streamlines at $\alpha = 40^{o}$ (a) x=0.4 and (b) x=0.9

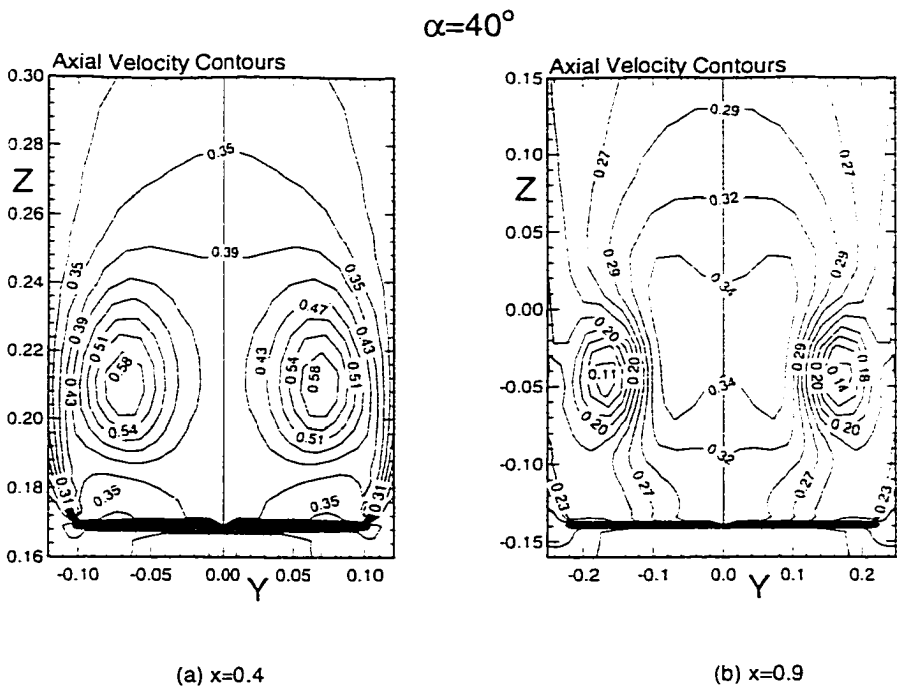

Figure 5.19: Axial velocity contours at $\alpha = 40^{o}$ (a) x=0.4 and (b) x=0.9

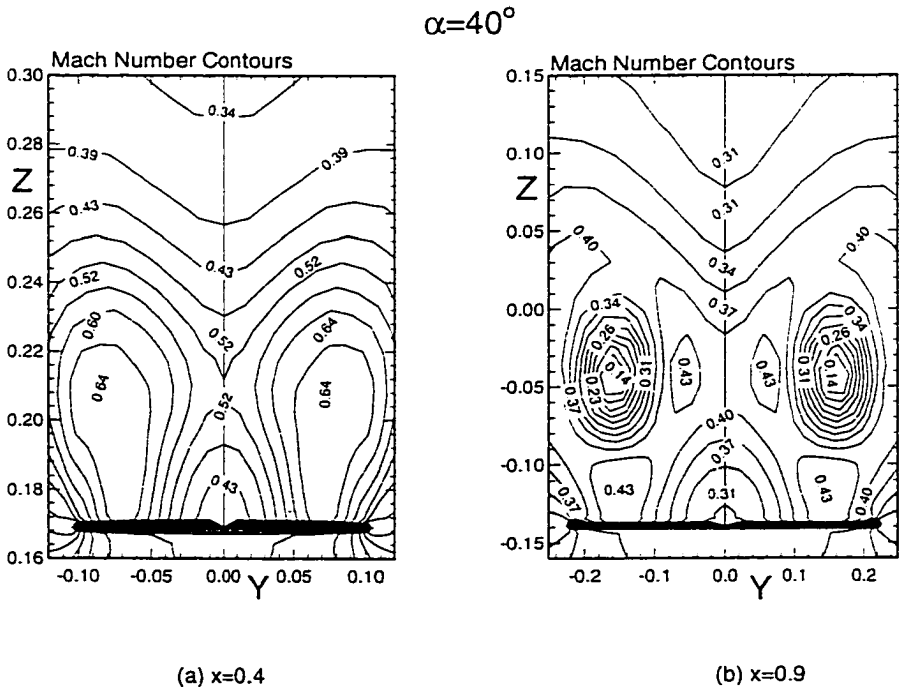

Figure 5.20: Mach number contours at $\alpha = 40^{o}$ (a) x=0.4 and (b) x=0.9

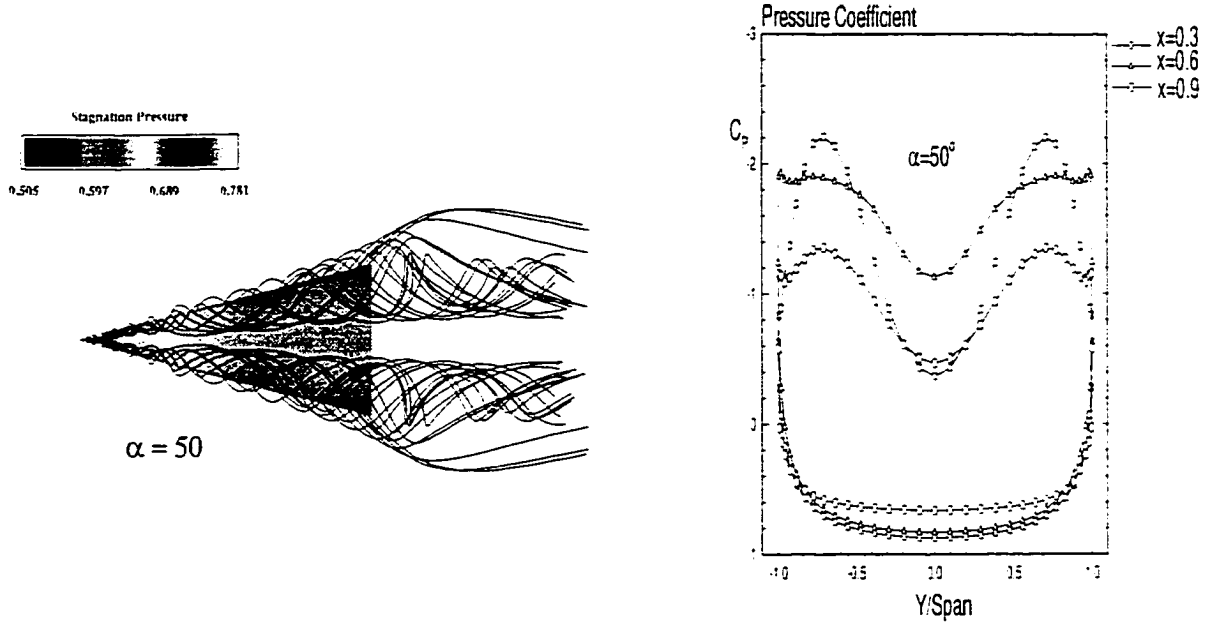

Figure 5.21: Particle traces over the delta wing and spanwise pressure coefficient distributions at $\alpha = 50°$

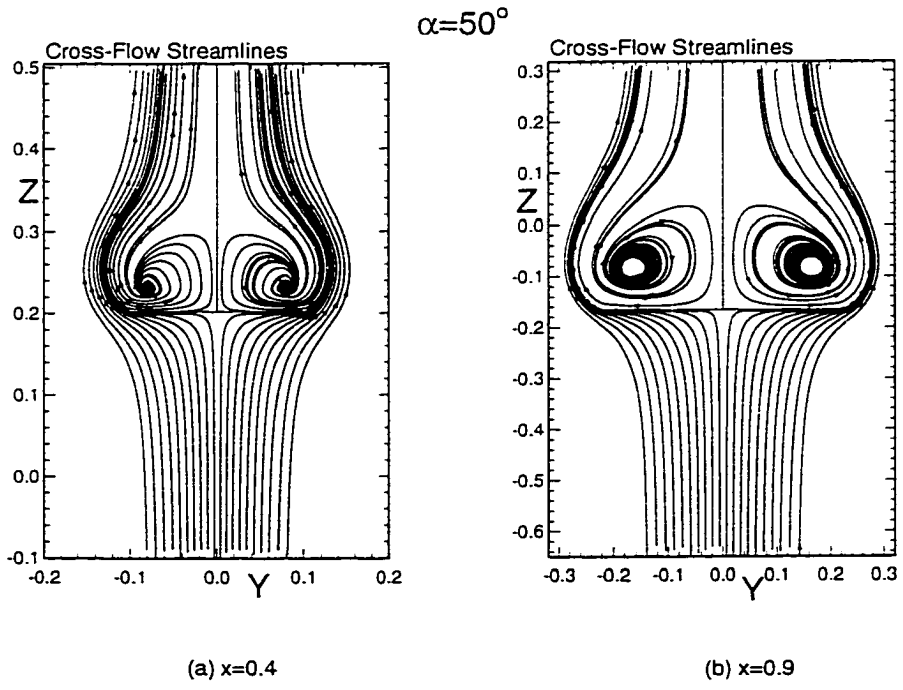

Figure 5.22: Cross-flow instantaneous streamlines at $\alpha = 50°$ (a) x=0.4 and (b) x=0.9

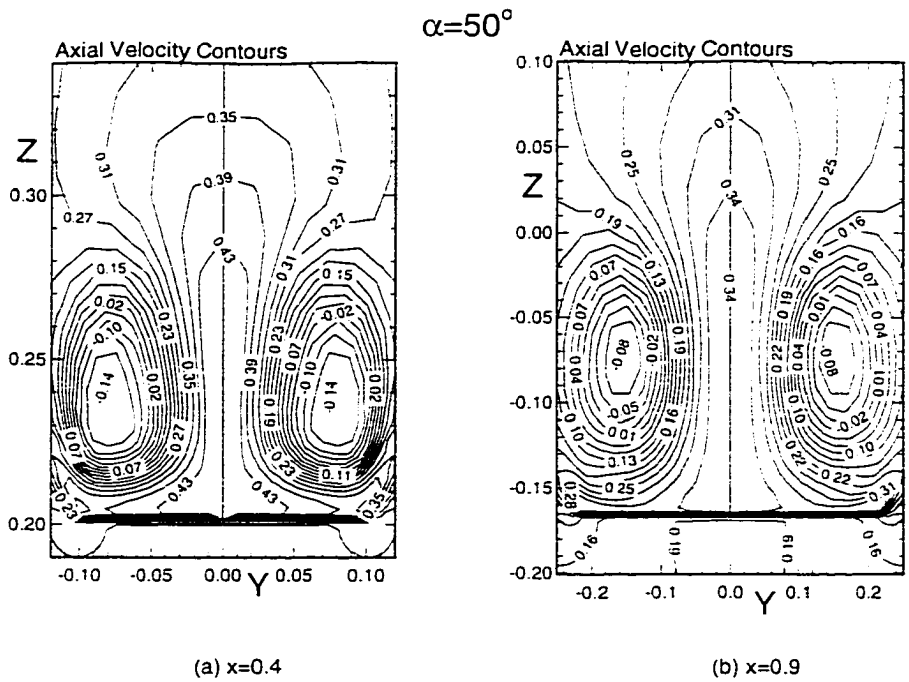

Figure 5.23: Axial velocity contours at $\alpha = 50^{o}$ (a) x=0.4 and (b) x=0.9

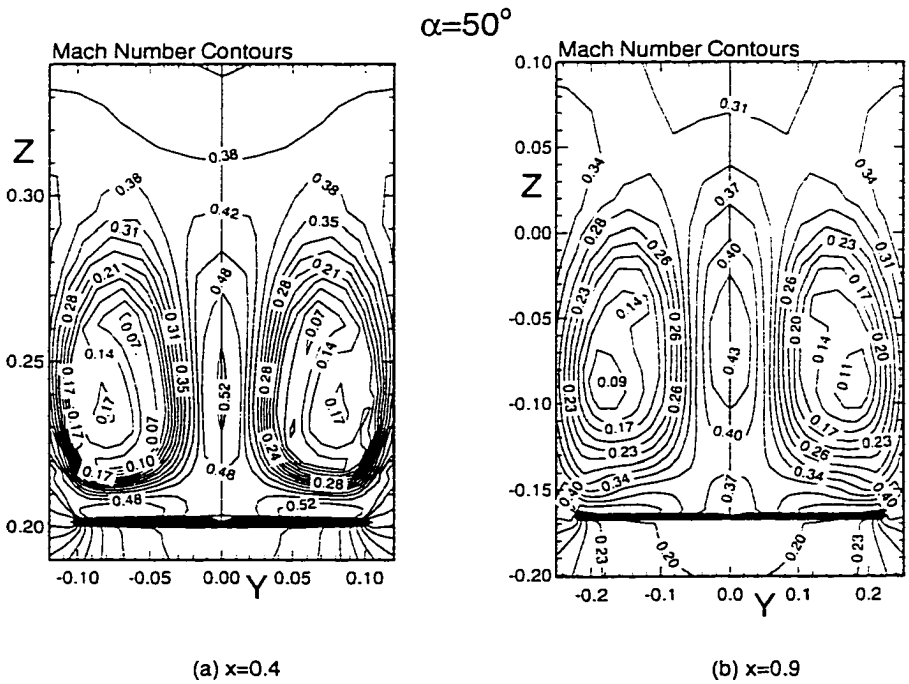

Figure 5.24: Mach number contours at $\alpha = 50^{o}$ (a) x=0.4 and (b) x=0.9

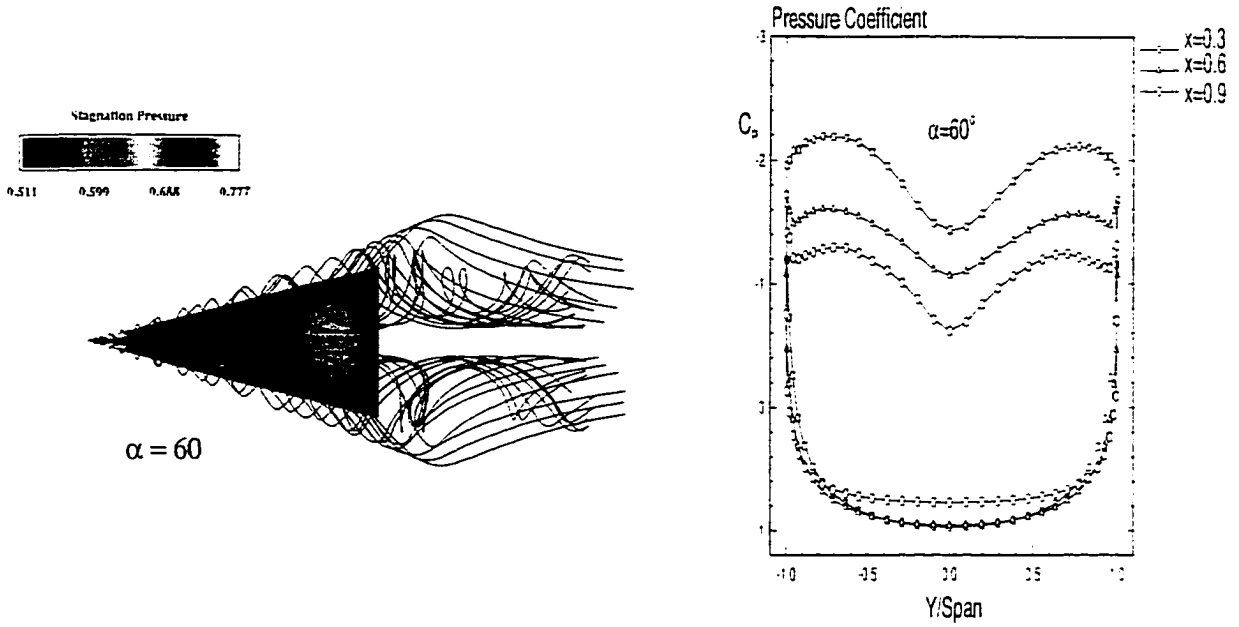

Figure 5.25: Particle traces over the delta wing and spanwise pressure coefficient distributions at $\alpha = 60°$

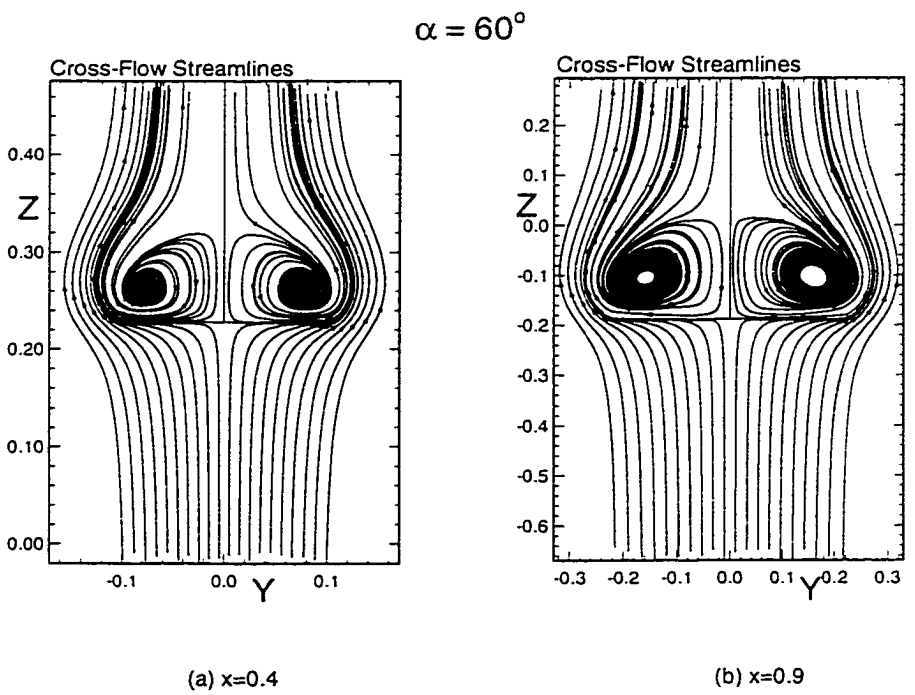

Figure 5.26: Cross-flow instantaneous streamlines at $\alpha = 60°$ (a) x=0.4 and (b) x=0.9

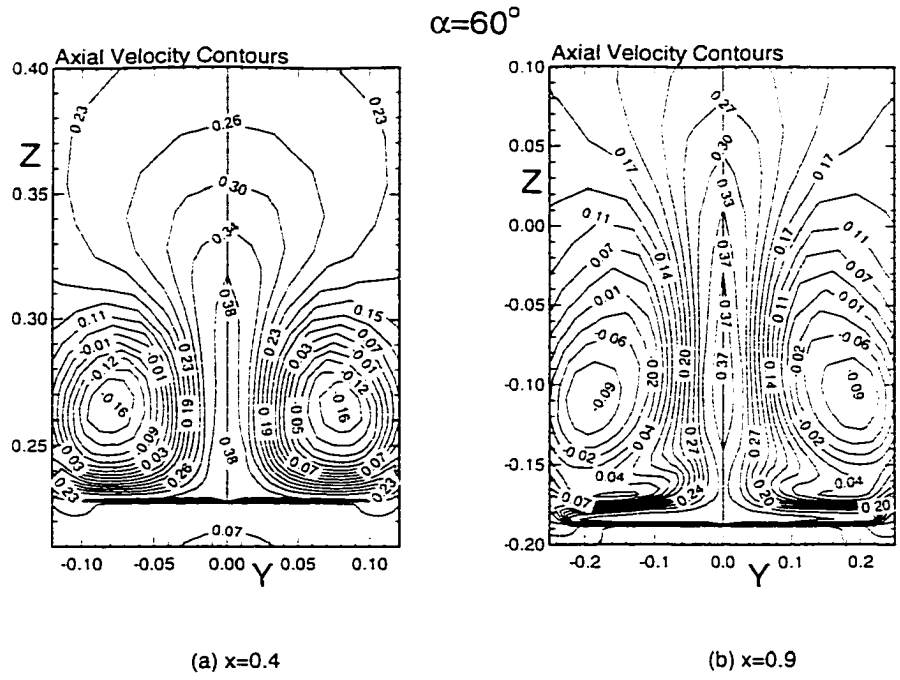

Figure 5.27: Axial velocity contours at $\alpha = 60°$ (a) x=0.4 and (b) x=0.9

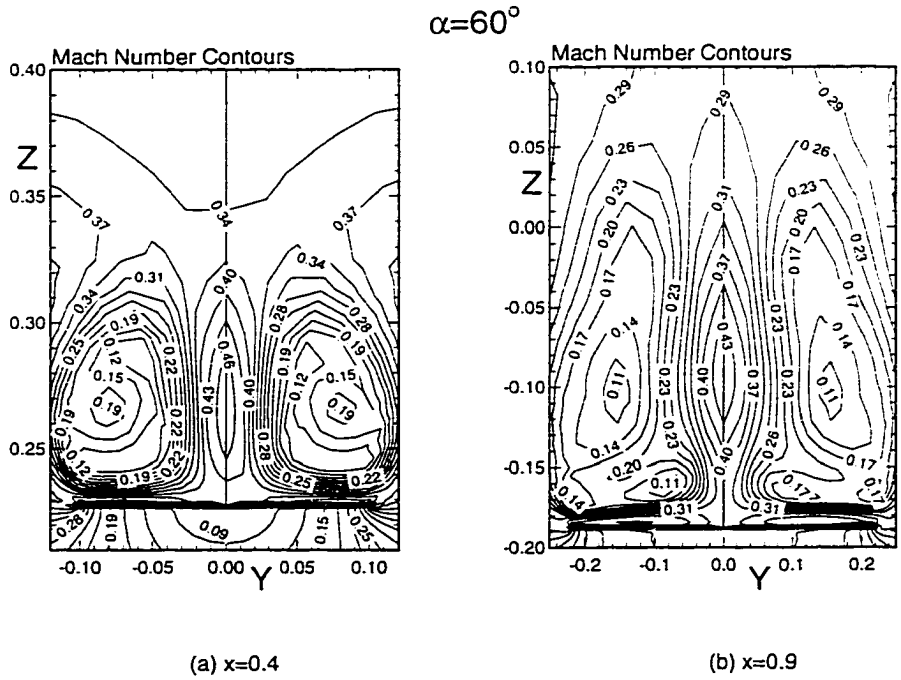

Figure 5.28: Mach number contours at $\alpha = 60°$ (a) x=0.4 and (b) x=0.9

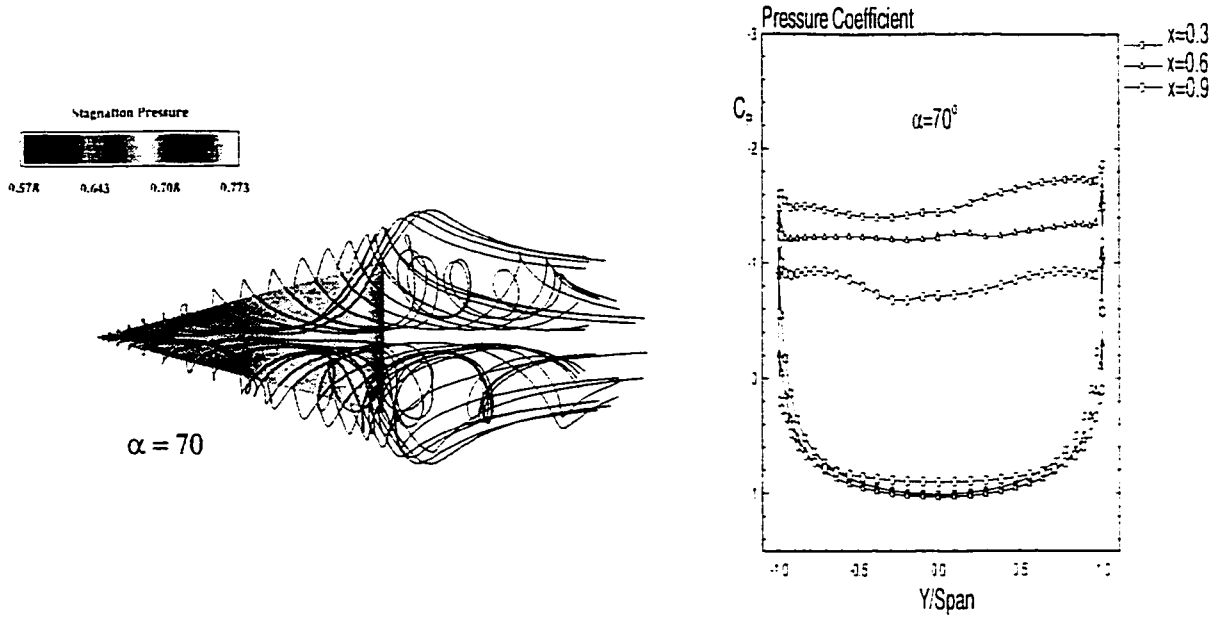

Figure 5.29: Particle traces over the delta wing and spanwise pressure coefficient distributions at $\alpha = 70°$

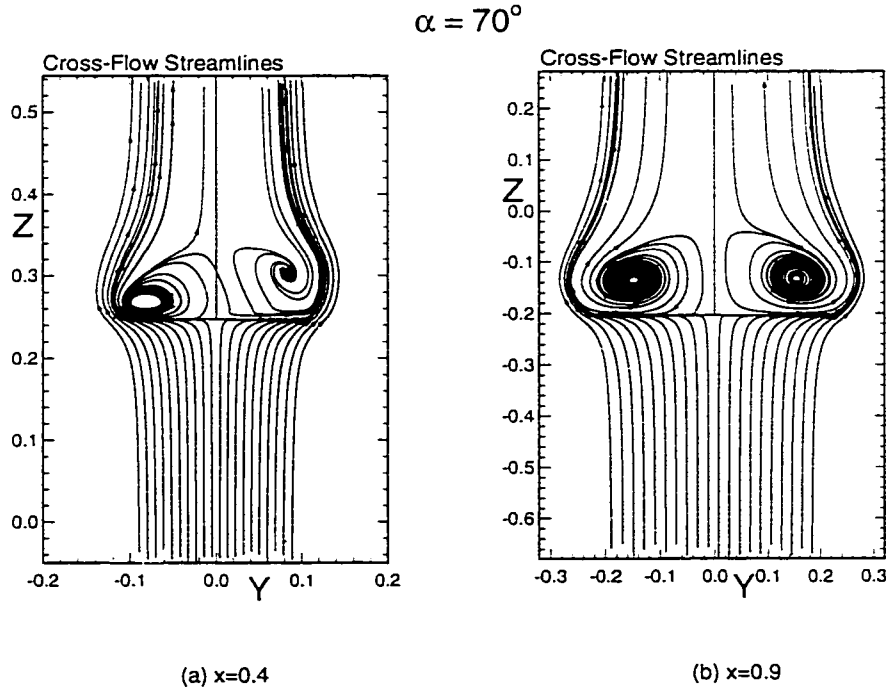

Figure 5.30: Cross-flow instantaneous streamlines at $\alpha = 70°$ (a) x=0.4 and (b) x=0.9

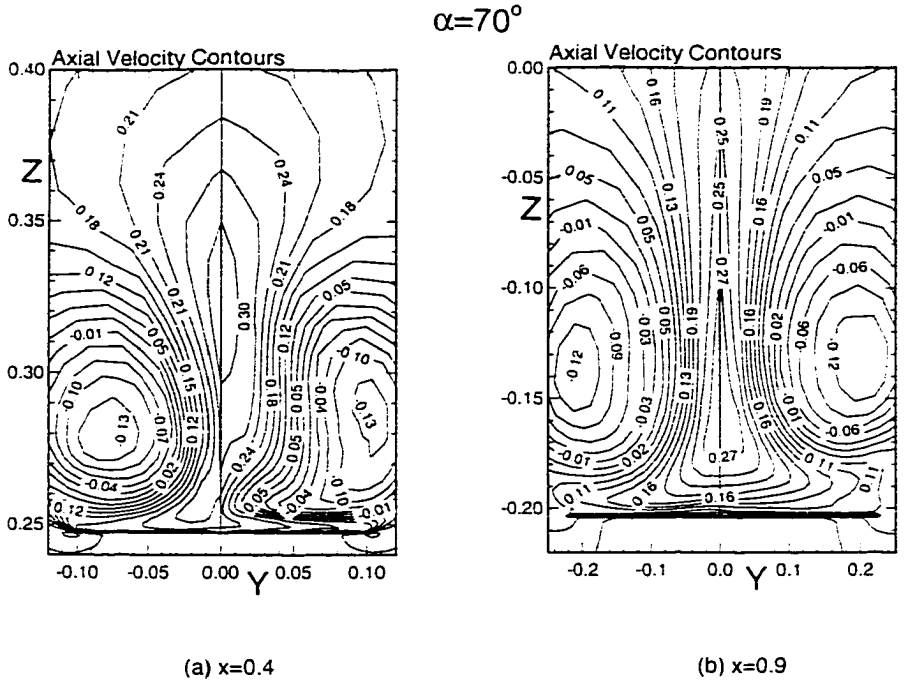

Figure 5.31: Axial velocity contours at $\alpha = 70^{o}$ (a) x=0.4 and (b) x=0.9

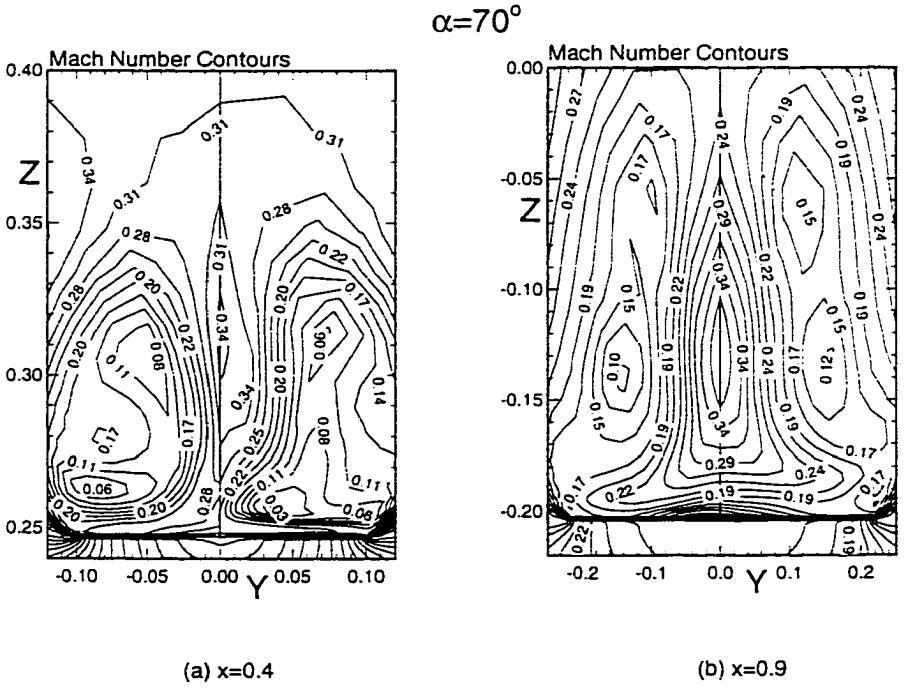

Figure 5.32: Mach number contours at $\alpha = 70^{o}$ (a) x=0.4 and (b) x=0.9

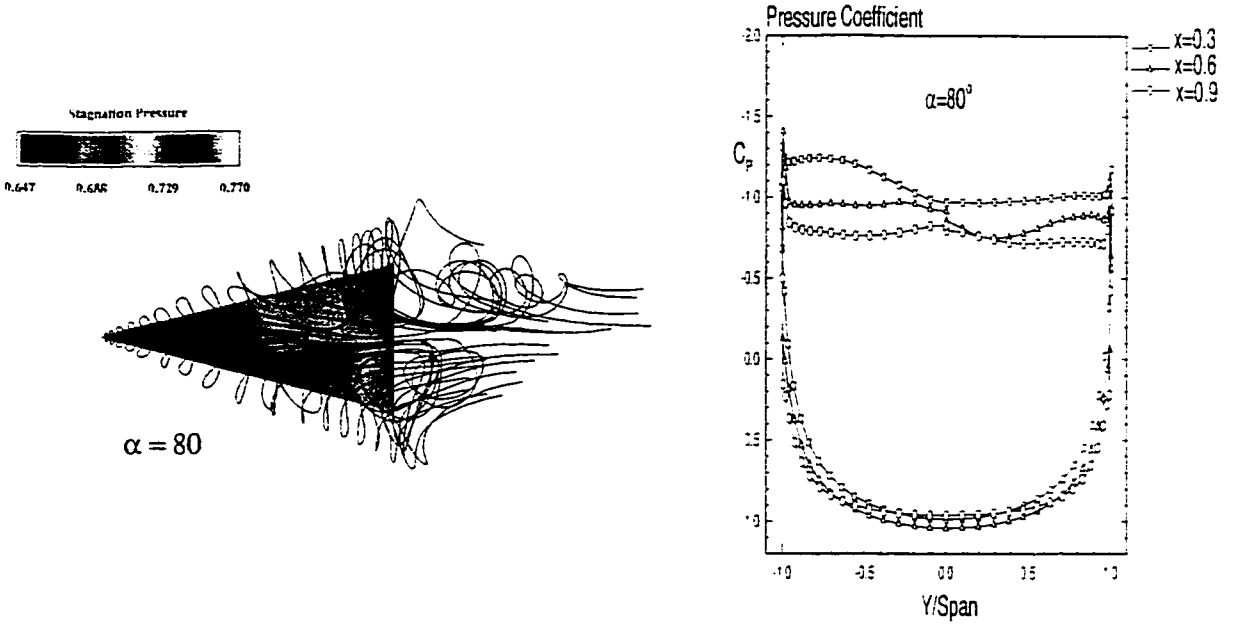

Figure 5.33: Particle traces over the delta wing and spanwise pressure coefficient distributions at $\alpha = 80°$

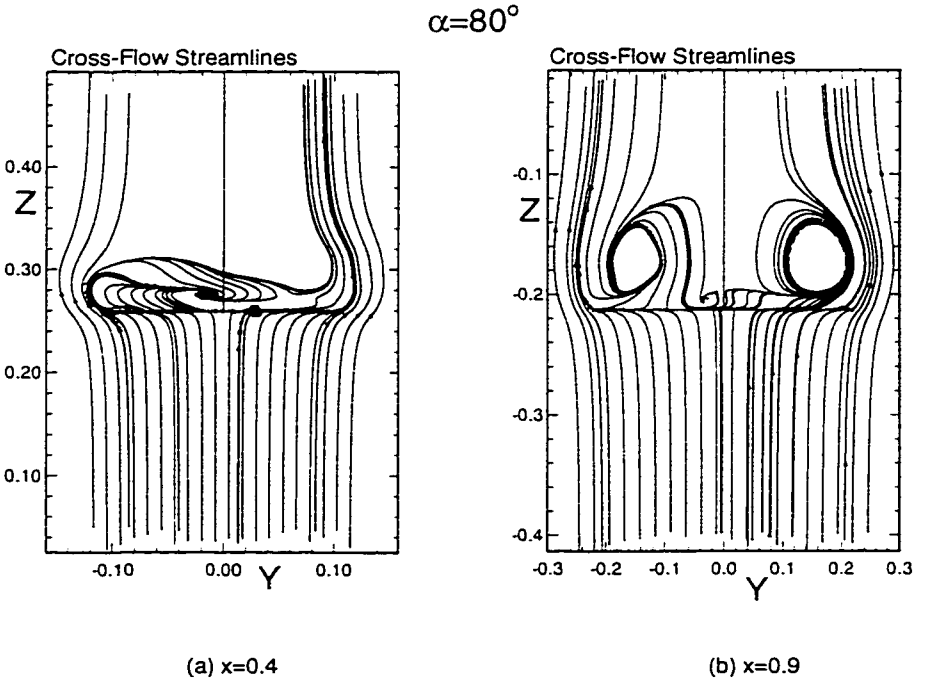

Figure 5.34: Cross-flow instantaneous streamlines at $\alpha = 80°$ (a) x=0.4 and (b) x=0.9

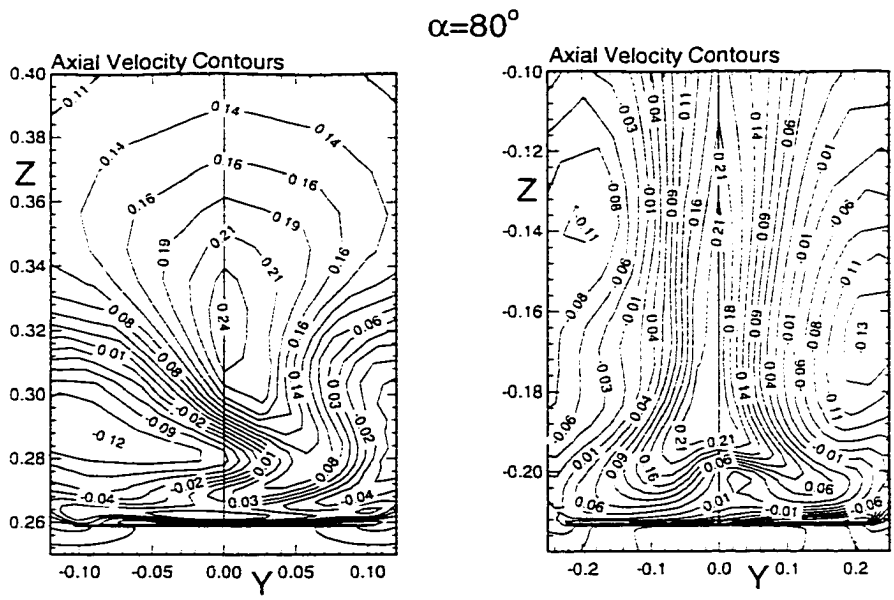

(a) x=0.4 (b) x=0.9

Figure 5.35: Axial velocity contours at $\alpha = 80°$ (a) x=0.4 and (b) x=0.9

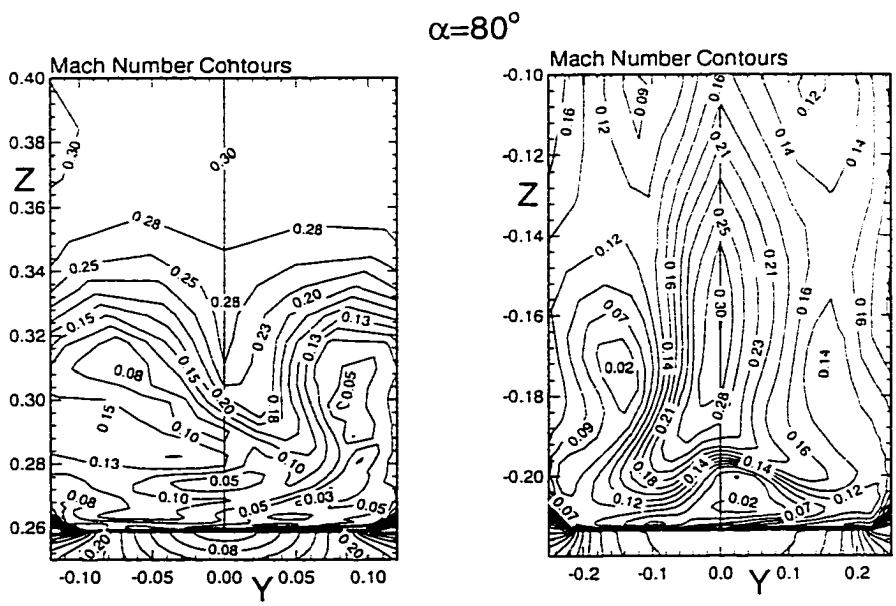

(a) x=0.4 (b) x=0.9

Figure 5.36: Mach number contours at $\alpha = 80°$ (a) x=0.4 and (b) x=0.9

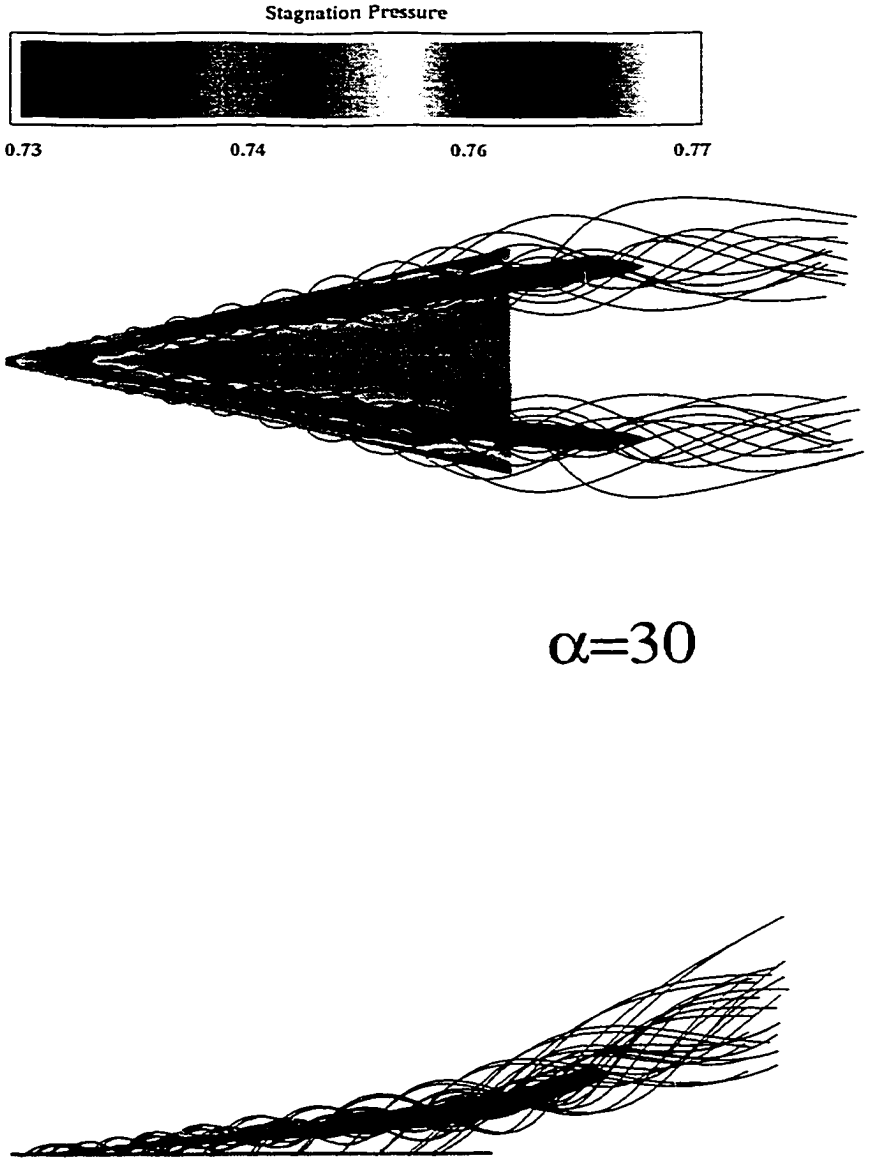

Figure 5.37: Stagnation pressure and particle traces over delta wing at $\alpha = 30^{o}$

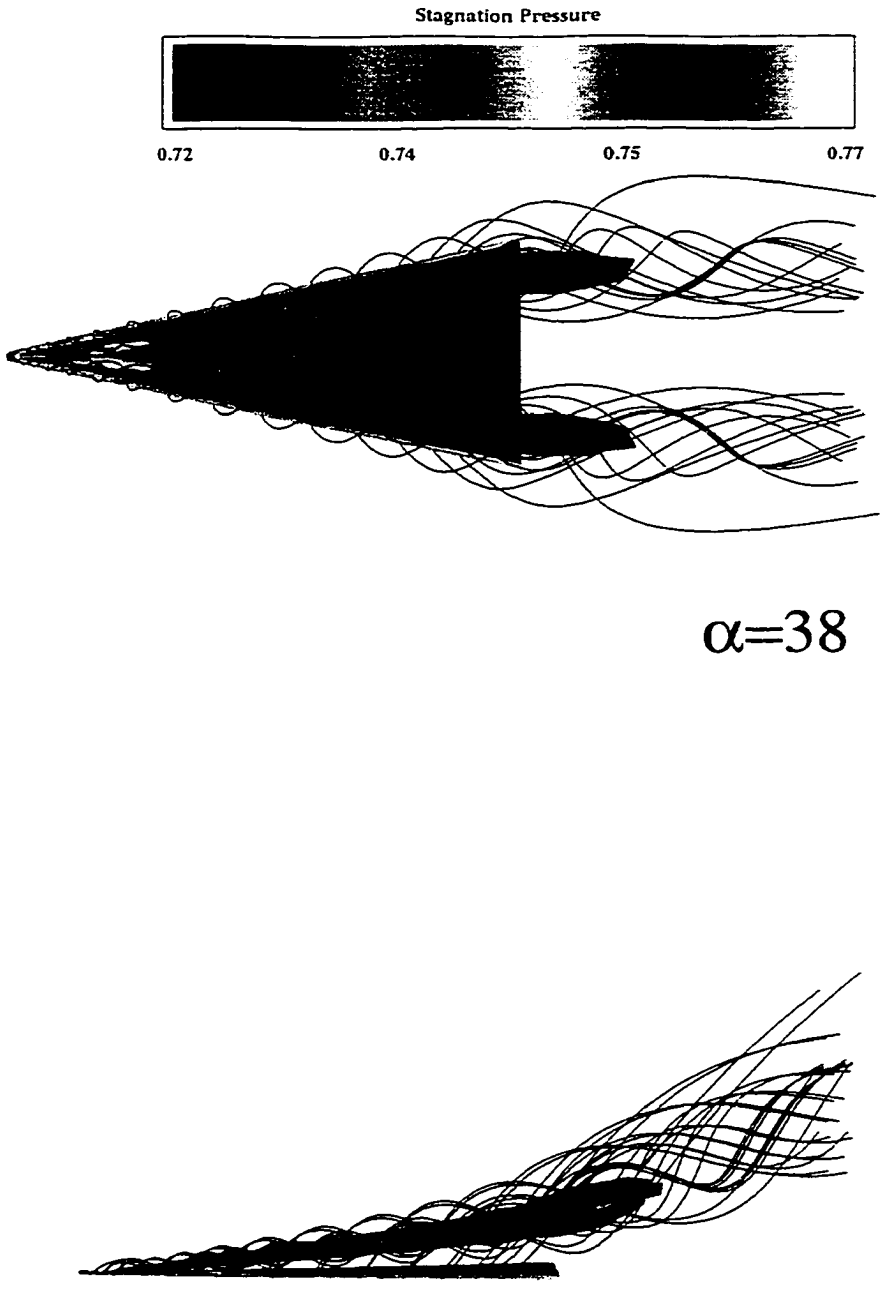

Figure 5.38: Stagnation pressure and particle traces over delta wing at $\alpha = 38^{\circ}$

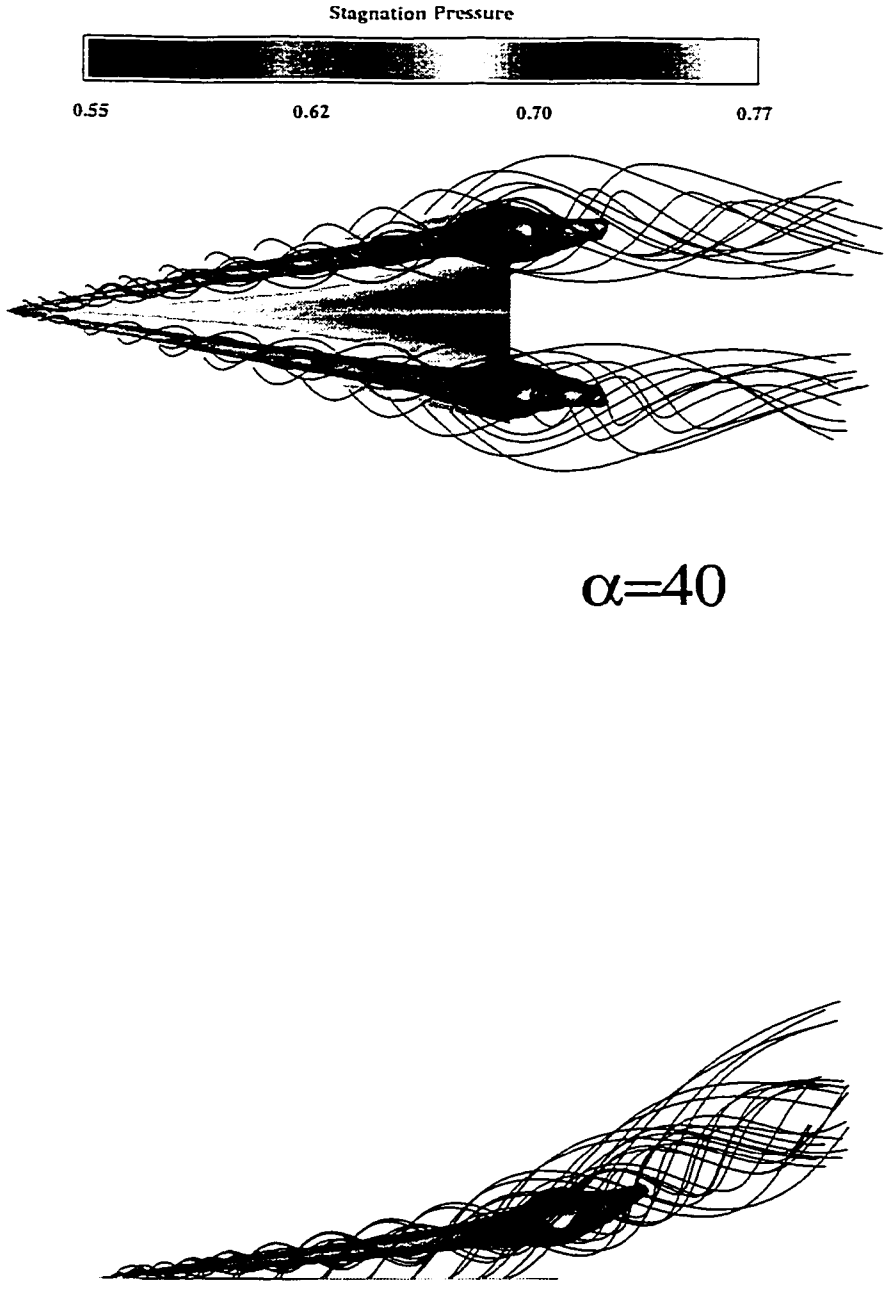

Figure 5.39: Stagnation pressure and particle traces over delta wing at $\alpha = 40^{\circ}$

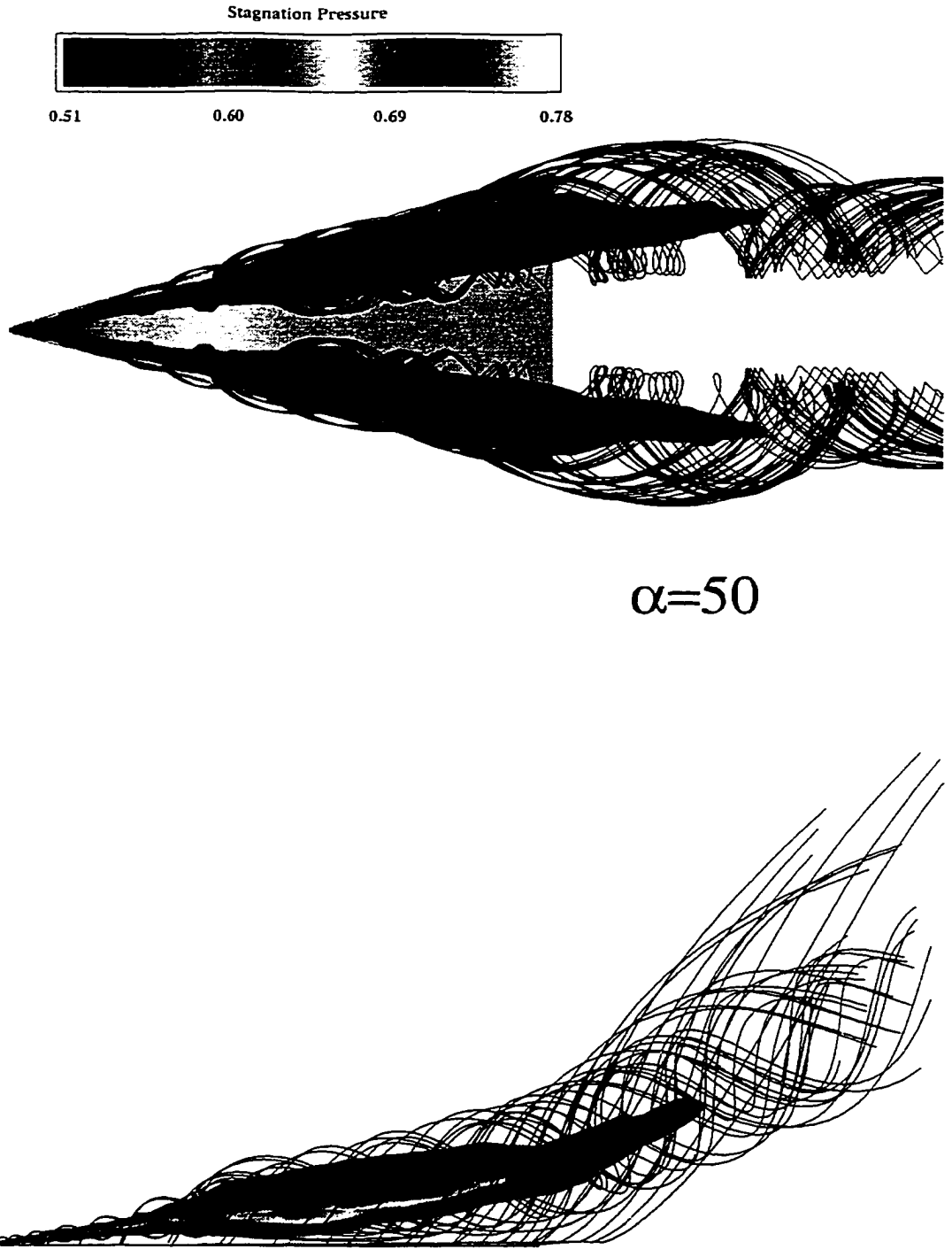

Figure 5.40: Stagnation pressure and particle traces over delta wing at $\alpha = 50°$

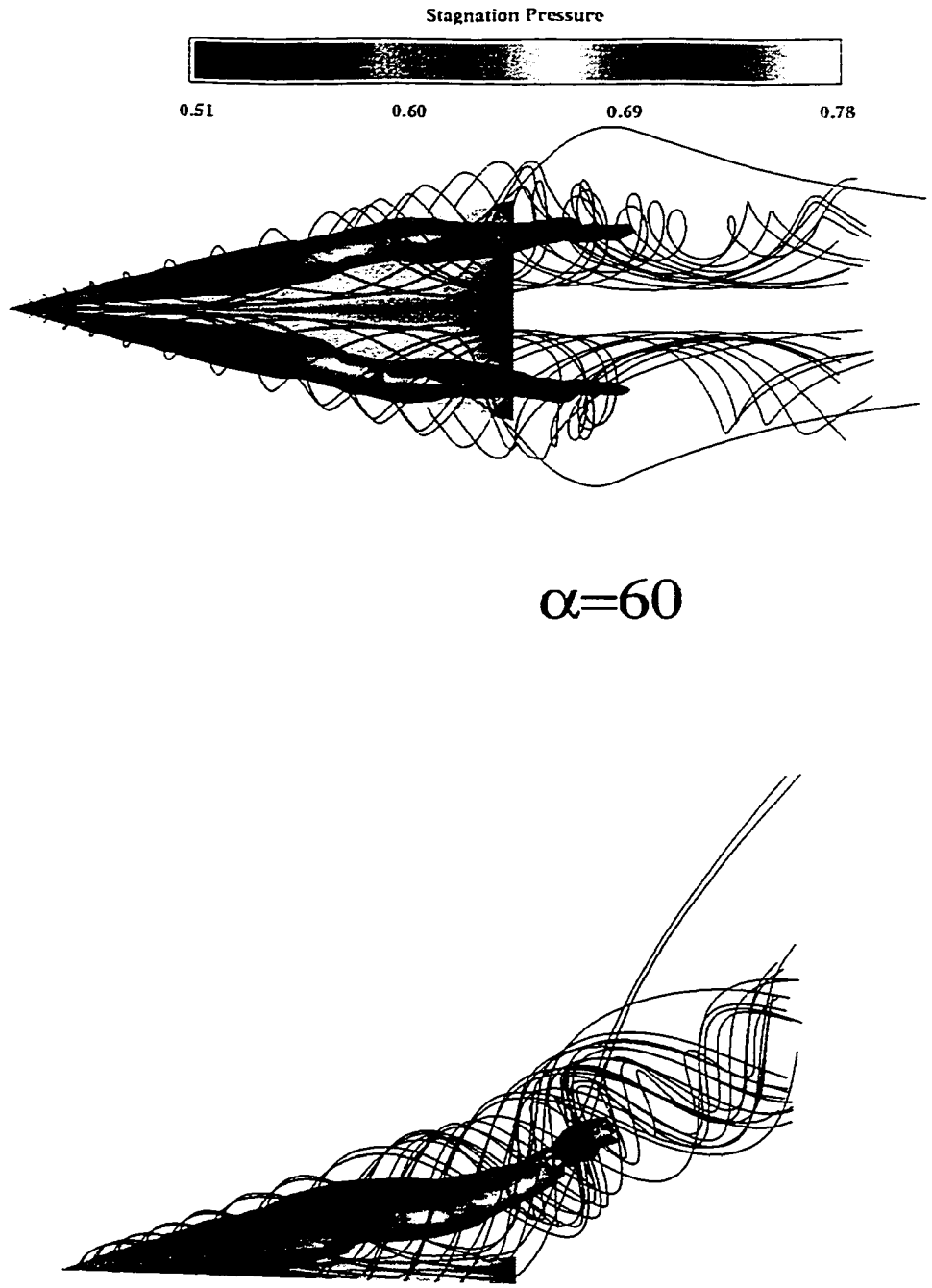

Figure 5.41: Stagnation pressure and particle traces over delta wing at $\alpha = 60^{\circ}$

Front

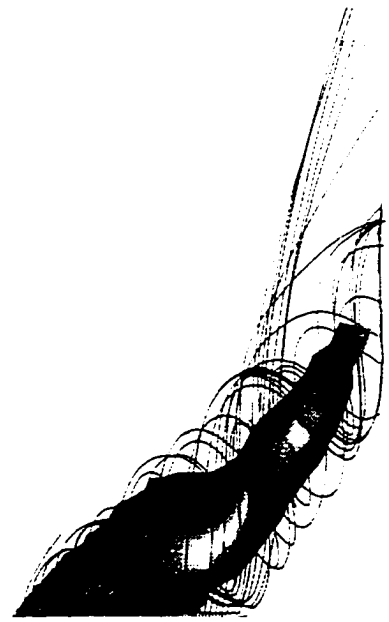

Side

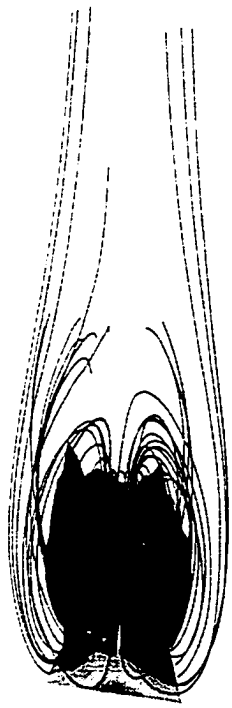

Back

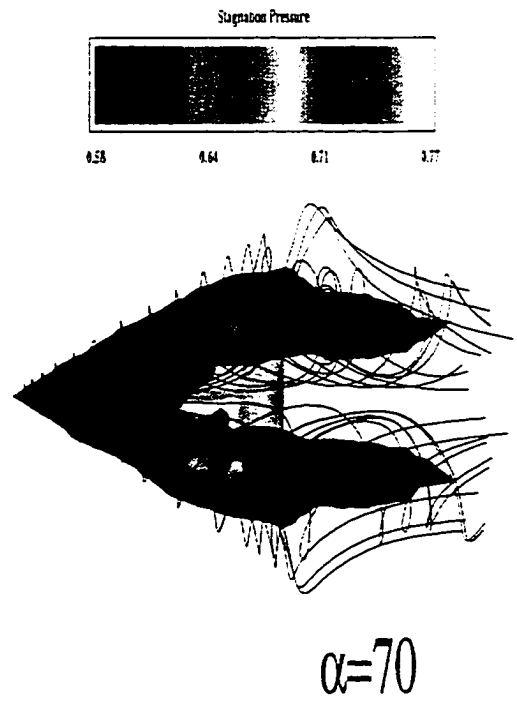

Top

Figure 5.42: Stagnation pressure and particle traces over the delta wing at $\alpha = 70^{\circ}$

5.2 Fine Grid Solution

The delta wing model used in the present computational study consists of a 76° swept back, sharp-edged wing with zero thickness and an aspect ratio of one similar to that used by Jarrah (1988). The three-dimensional O-H grid topology used in the current case is shown in Fig. 5.43 with a cross section at the trailing edge. The dimension of the grid used is 81 x 81 x 50 in the axial, wrap-around, and outward directions; respectively. This grid is relatively finer than the previous grid used in Section 5.1. Since the resolution in the wrap-around and normal directions are very crucial in the boundary layer calculations near the solid boundaries, the number of points in wrap-around and normal directions have been increased by 16 and 7 grid points; respectively, whereas the number of points in the axial direction is decreased by 3 points. This case took about one month of running time on a Pentium II 300 MHz processor to complete a ramp pitching amplitude of 90°.

The pitch axis is located at two-thirds of the root chord length, as measured from the wing vertex. The wing is forced to undergo a pitching motion through a ramp function shown in Fig. 5.2 and is described by $\alpha = 0.024t$, which is related to the reduced frequency. In this case, the reduced frequency is equivalent to $k = 0.04$. The freestream Mach number and Reynolds number are 0.3 and 0.45×10^6, respectively. The NS Equations are integrated time accurately with $\Delta t = 0.001$. This translates into 65,450 time steps to complete the ramp motion up to $\alpha = 90°$. The laminar NS equations have been used in this case.

Figures 5.44 and 5.45 show the variations of C_L and C_D with α of the present computational results and the corresponding values of the experimental data of Jarrah

(1988). The same behavior for both C_L and C_D is noticed again. The C_L curve shows a very good agreement with experimental data until α reaches 40°. For angles of attack greater than 40°, the C_L obtained from the present study over-estimates the experimental data by about 10%. The predicted peak of the C_L curve slightly underestimates the experimental value. This difference may be attributed to the absence of turbulence modeling that is needed for the massive flow separation at very high angles of attack after the onset of the vortex breakdown. Another source might be the grid resolution required to capture the massive flow separation and the vortex breakdown regions. Excellent agreement between C_D obtained from the present study and that obtained experimentally is noticed until α reaches 60°. After α = 60°, the computed results over-estimate the experimental data. Again this could be attributed to the effects of turbulence at high angles of attack and the grid resolution in the vortex breakdown region. Also, the present study predicted accurately the angle of attack at which the breakdown crosses through the trailing edge, which is in the current case about 39°, which is the same critical angle as before.

Figures 5.46-5.60 show the vortex core development over the wing surface from high to very high values of angle of attack (40°-80°). Figure 5.46 shows the spanwise pressure coefficient distributions at four different axial chord stations of 0.3, 0.6, 0.9, and 1.0 and at α = 40°. Two suction peaks are observed in this figure which means that the current grid is able to capture the secondary vortex near the leading edge of the wing. The amplitude of the suction peak is decreasing in the downstream direction. Figure 5.47 shows the axial velocity contours at α = 40° and for two axial stations of 0.3 and 0.9 (one near the apex and one near the trailing edge). The flow is symmetric and decelerating in

the downstream direction. Figure 5.47 also shows that before the onset of the vortex breakdown the most decelerated portions of the flow are inside the vortex core, and that the flow decelerates less in the lateral direction outside the vortex core. Also, the vortex core is observed to expand laterally in the downstream direction.

Figure 5.48 shows the particle traces of the leading edge vortices over the delta wing and the Mach number contours at $\alpha = 40°$. Observe how the vortex breakdown is crossing the trailing edge. The particle traces over the wing are tight until they reach the breakdown position at the trailing-edge and then breakdown and spiral motions start behind the wing trailing-edge. The leading edge vortices show that the flow is symmetric at this angle of attack.

Figures 5.49 shows the spanwise pressure coefficient distributions for three different axial stations, $x = 0.3$, 0.6, and 0.9 and at $\alpha = 52°$. The suction peaks show that the vortex breakdown has passed through the $x = 0.9$ location. Figure 5.50 shows the axial velocity contours at $\alpha = 52°$ for two different axial stations of 0.3 and 0.9. The axial velocity exhibits negative values inside the vortex core at $x = 0.9$ where the vortex breakdown has occurred. Figure 5.51 shows the particle traces over the delta wing and Mach number contours at $\alpha = 52°$. Until the flow reaches the breakdown locations the particle traces show a tight vortex. At and aft of the breakdown regions, the particle traces start to divert and undergo spiral motions over the wing surface. Also, the Mach number decreases behind the breakdown region.

Figure 5.52 shows the spanwise pressure coefficient distributions for $\alpha = 60°$. The suction peaks at all chord stations, $x = 0.3$, 0.6, and 0.9, have disappeared, which implies that the vortex breakdown covers most of the wing surface. Figure 5.53 shows the axial

flow velocity contours at x = 0.3 and 0.9 for α = 60°. The vortex core is expanding laterally, the axial velocity has negative values inside the vortex core for both axial stations, and the flow is asymmetric. Figure 5.54 shows the particle traces over the delta wing along with the Mach number contours for α = 60°. Although the right hand side vortex core shows a bubble type vortex breakdown, the left-hand side shows a spiral type vortex breakdown. The asymmetry of the flow is clearly seen in this figure.

Figure 5.55 shows the spanwise pressure coefficient distribution for α = 72°. Figure 5.56 shows the axial velocity contours at x = 0.3 and 0.9 for α = 72°. The asymmetry of the flow is very clear. Large separated areas within the flow, where the axial velocity is equal or less than zero, are present in the flow. Figure 5.57 shows the particle traces over the delta wing and Mach number contours for α = 72°. The asymmetry of the flow is also seen from the Mach number contours. Moreover, the two vortex cores do not breakdown at the same location when flow asymmetry exists.

Figure 5.58 shows the spanwise pressure coefficient distribution for α = 80°. Figure 5.59 shows the axial velocity contours at x = 0.3 and 0.9 for α = 80°. Again, the asymmetry flow is very clear. Figure 5.60 shows the particle traces over the delta wing and Mach number contours for α = 80°.

At low angles of attack, a tight vortex core develops at the leading edge of the wing. The flow is symmetric and decelerates while traversing downstream. Very little spiral motion is present in the flow. As the angle of attack increases, the vortex core expands until it breaks down at the trailing edge around α = 39°, due to the adverse axial pressure gradient, and the particle traces begin to exhibit strong spiral motions. If the radius of spiral is small, the bubble vortex breakdown type is generated. If the radius of

spiral motion is large, the spiral vortex breakdown type is generated. The vortex breakdown moves upstream expanding the size of the vortex core, due to the axial momentum loss, until it overwhelms the entire wing surface. The symmetry of the vortex flow remains until large separated regions are generated within the vortex core, after which the flow becomes asymmetric. After the flow becomes asymmetric the vortex breakdown on the two sides may not occur at the same axial location.

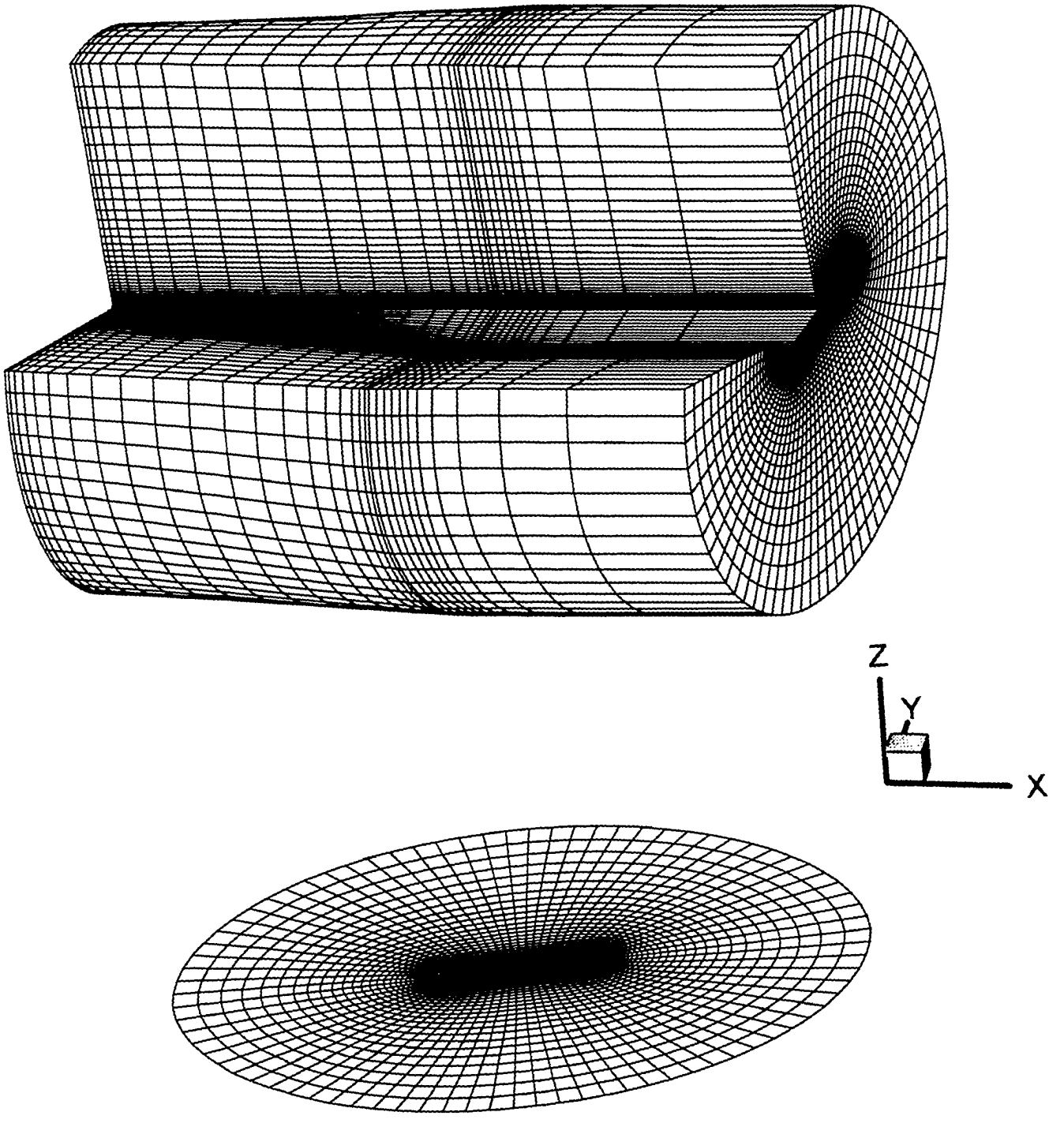

Figure 5.43 Three-dimensional grid topology

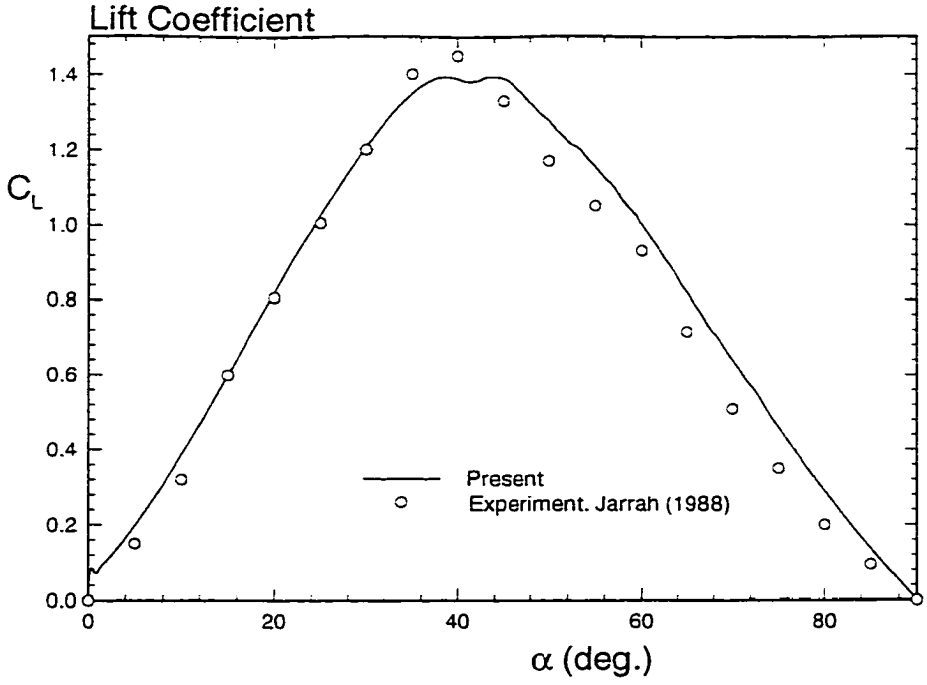

Figure 5.44: Lift coefficient vs. α using finer grid

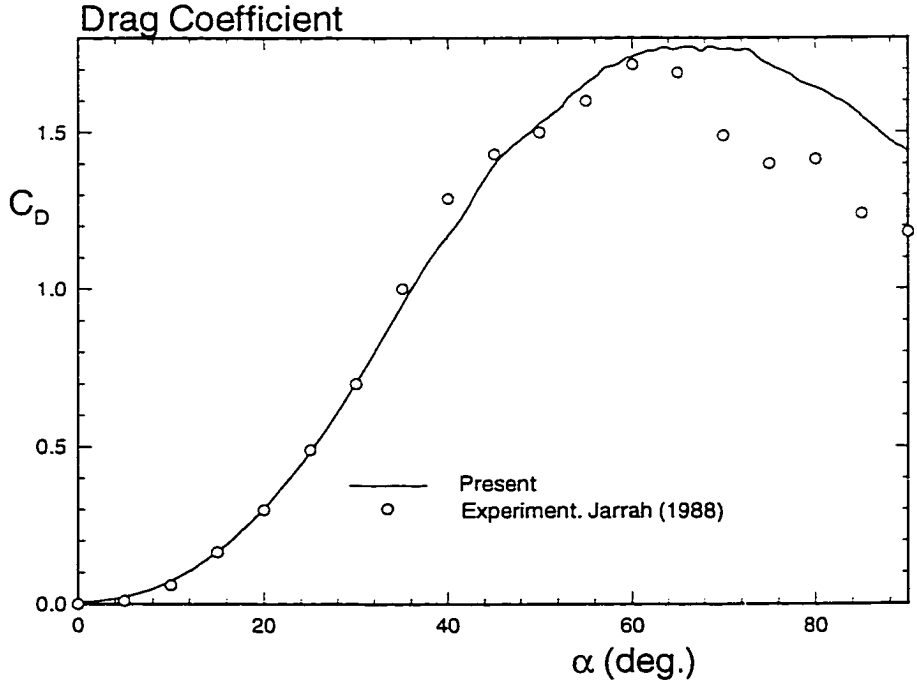

Figure 5.45: Drag coefficient vs. α using finer grid

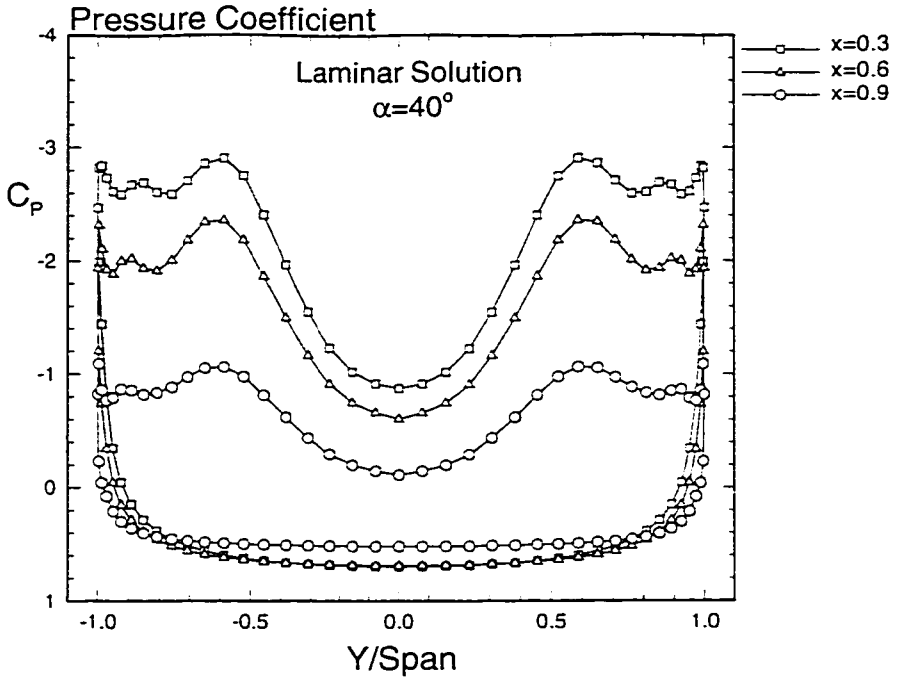

Figure 5.46: Spanwise-pressure-coefficient distribution for $\alpha = 40^{\circ}$

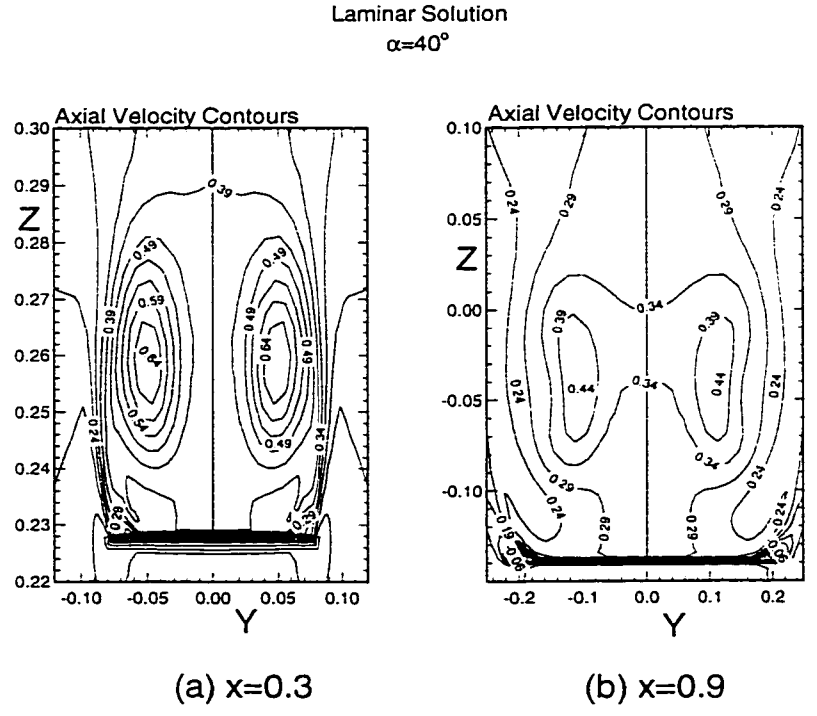

Figure 5.47: Axial flow velocity contours at (a) x=0.3 and (b) x=0.9 for $\alpha = 40^{\circ}$

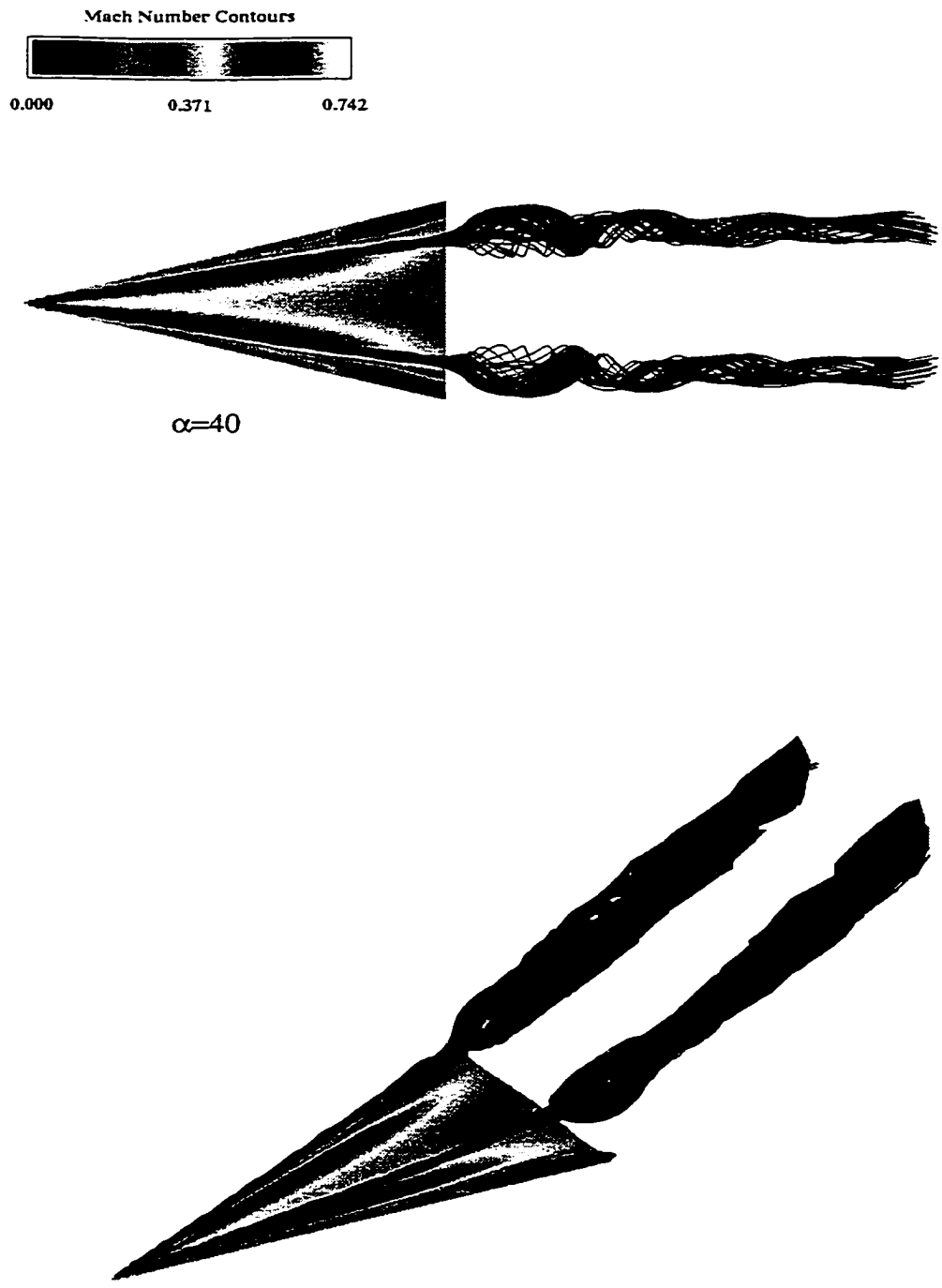

Figure 5.48: Particle traces over the delta wing and Mach number contours for $\alpha = 40^{\circ}$

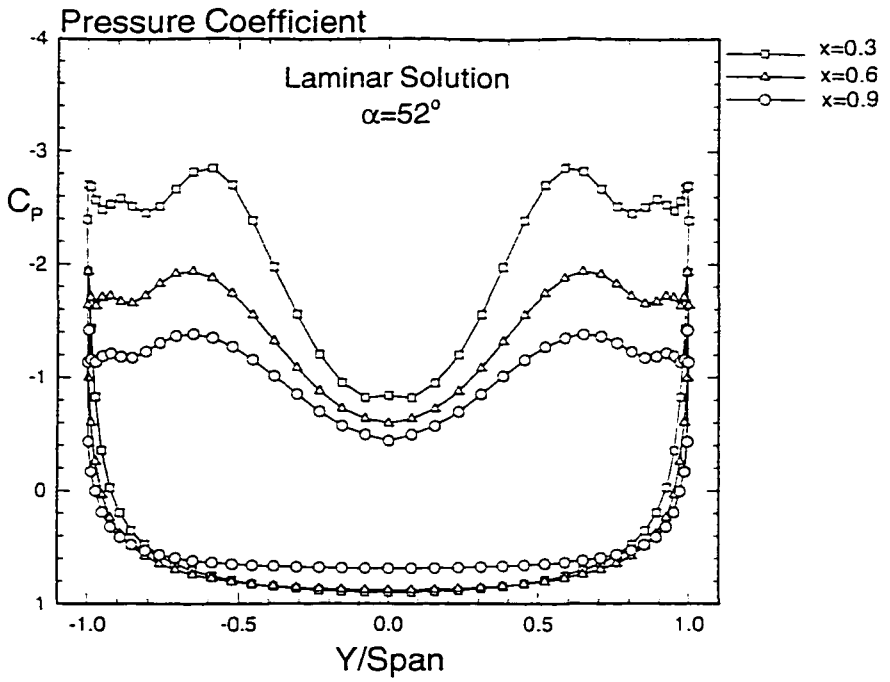

Figure 5.49: Spanwise-pressure-coefficient distribution for $\alpha = 52^{\circ}$

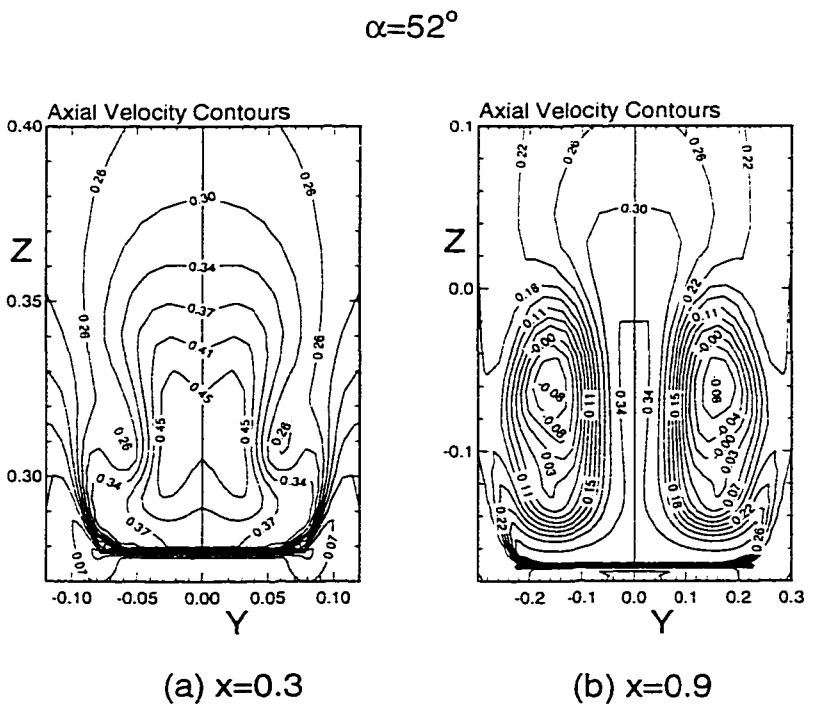

Figure 5.50: Axial flow velocity contours at (a) x=0.3 and (b) x=0.9 for $\alpha = 52^{\circ}$

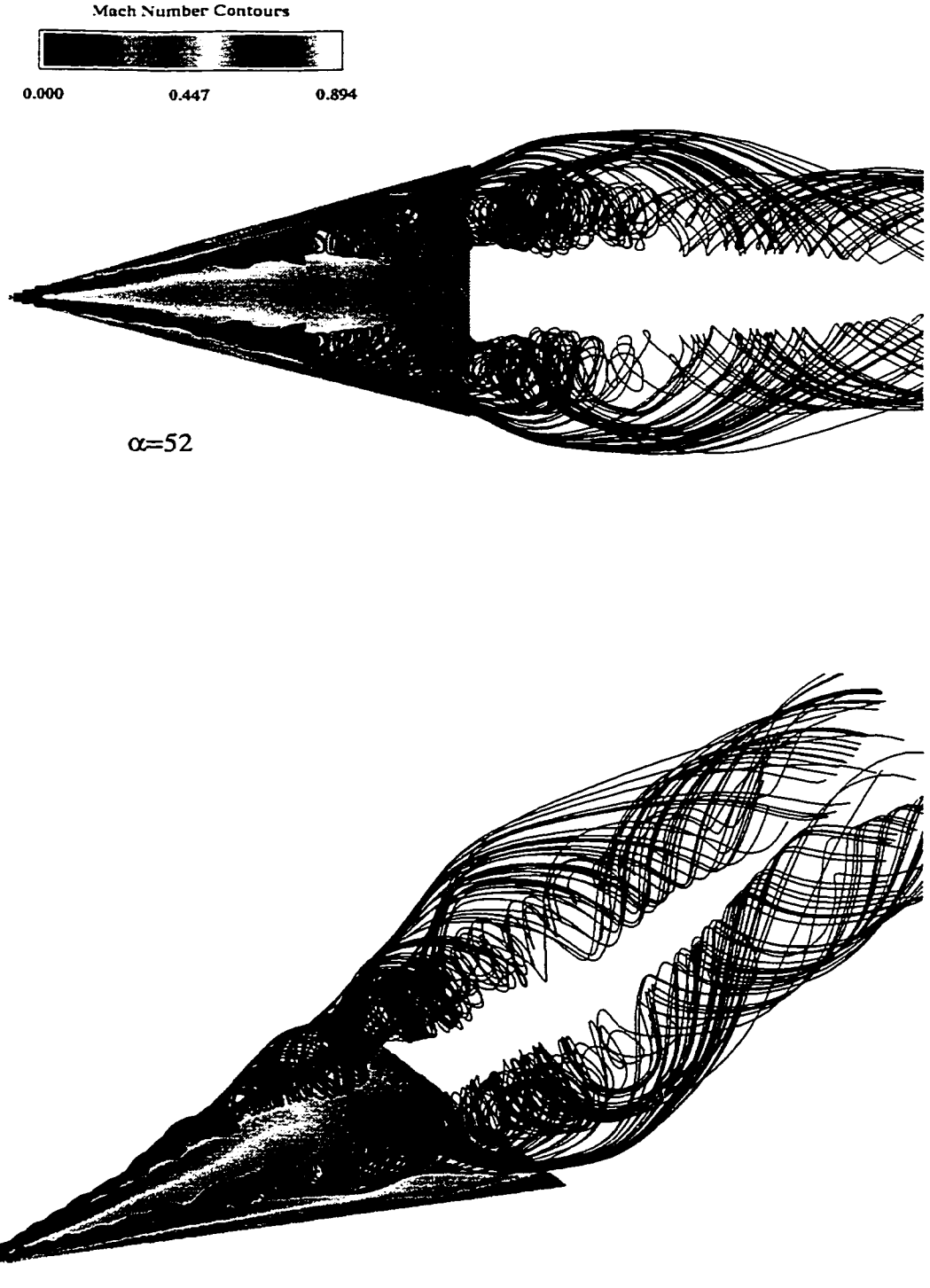

Figure 5.51: Particle traces over the delta wing and Mach number contours for $\alpha = 52^{o}$

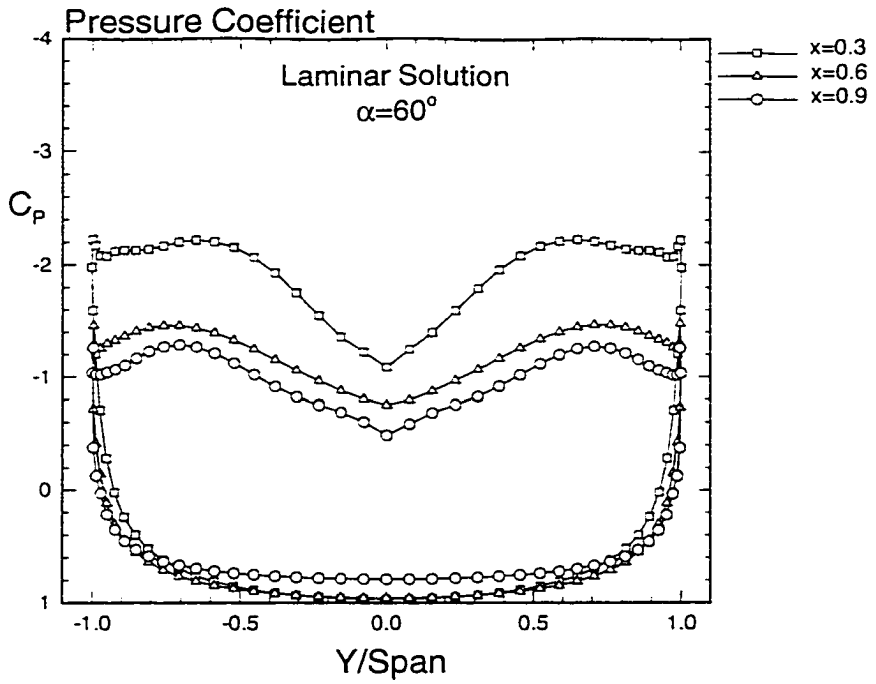

Figure 5.52: Spanwise-pressure-coefficient distribution for $\alpha = 60°$

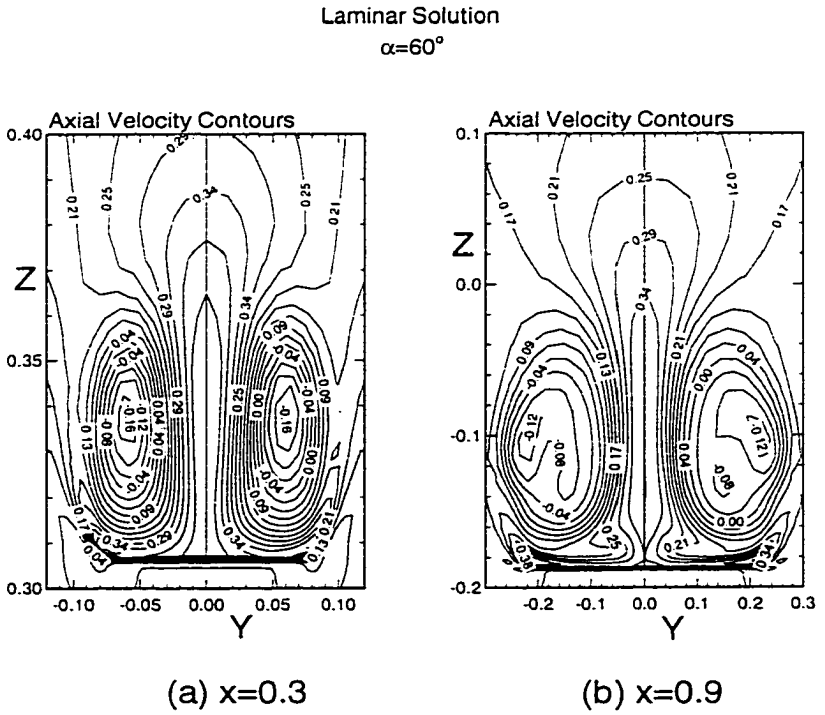

Figure 5.53: Axial flow velocity contours at (a) x=0.3 and (b) x=0.9 for $\alpha = 60°$

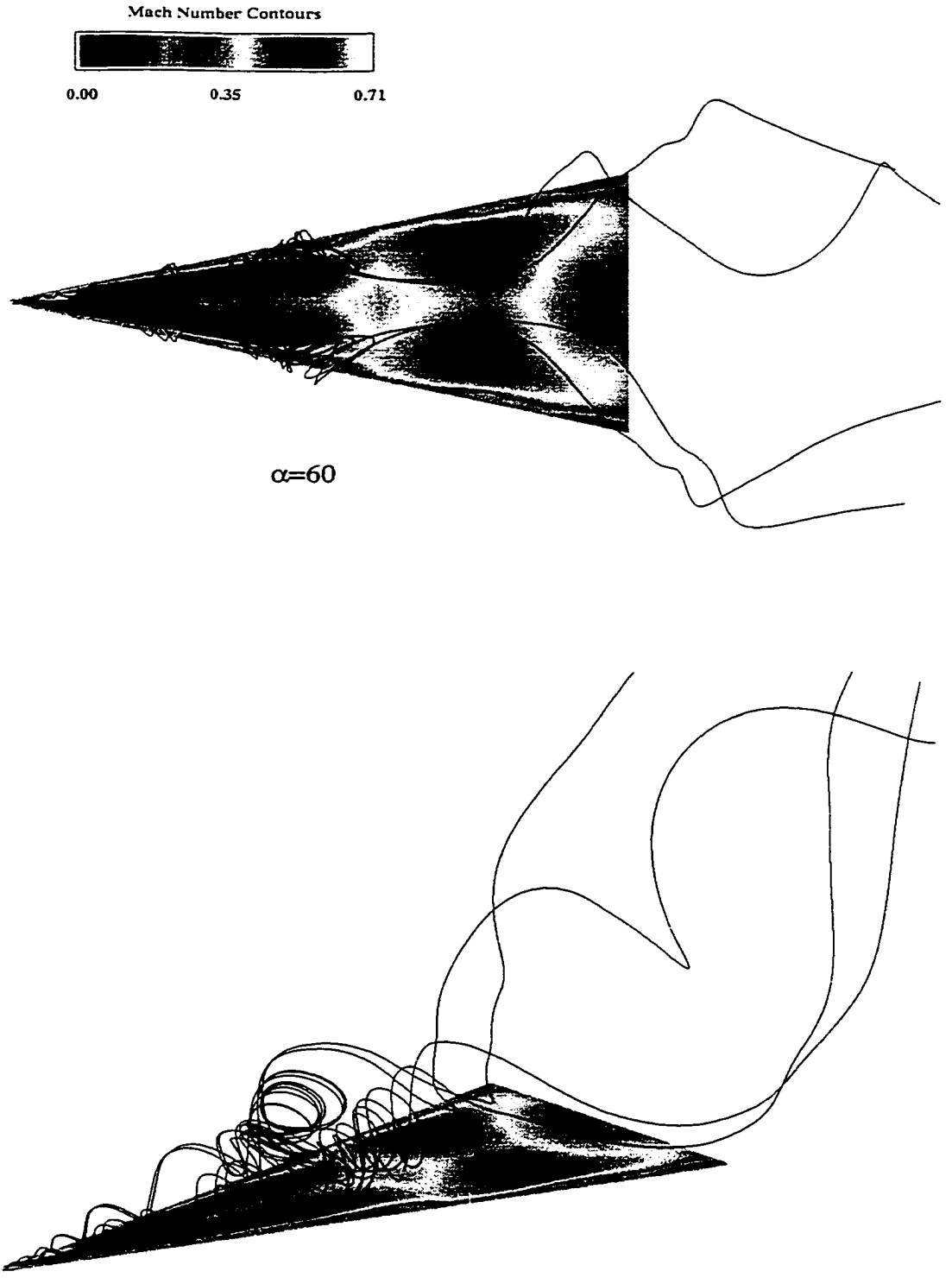

Figure 5.54: Particle traces over the delta wing and Mach number contours $\alpha = 60°$

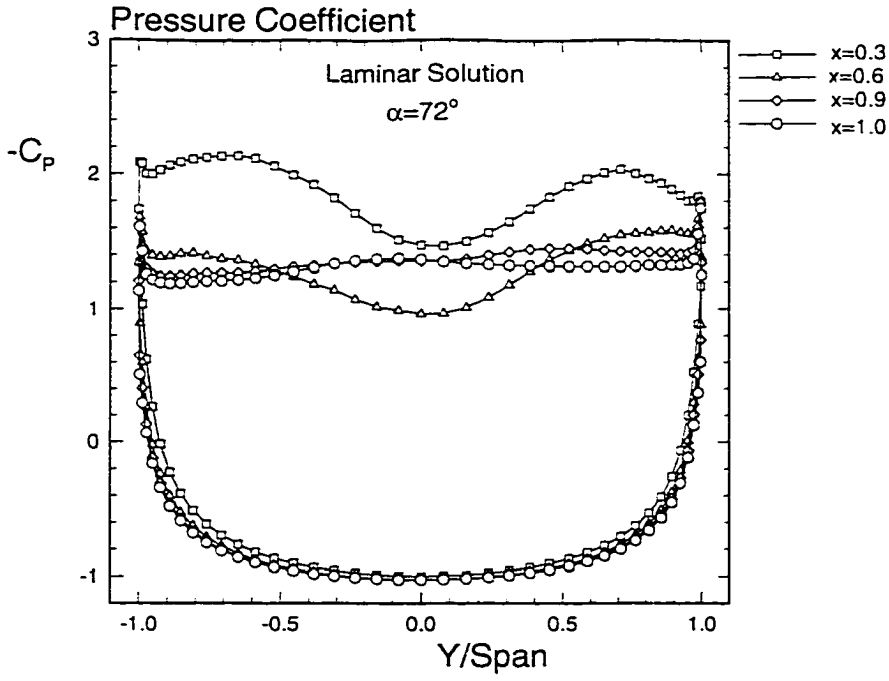

Figure 5.55: Spanwise-pressure-coefficient distribution for $\alpha = 72^{\circ}$

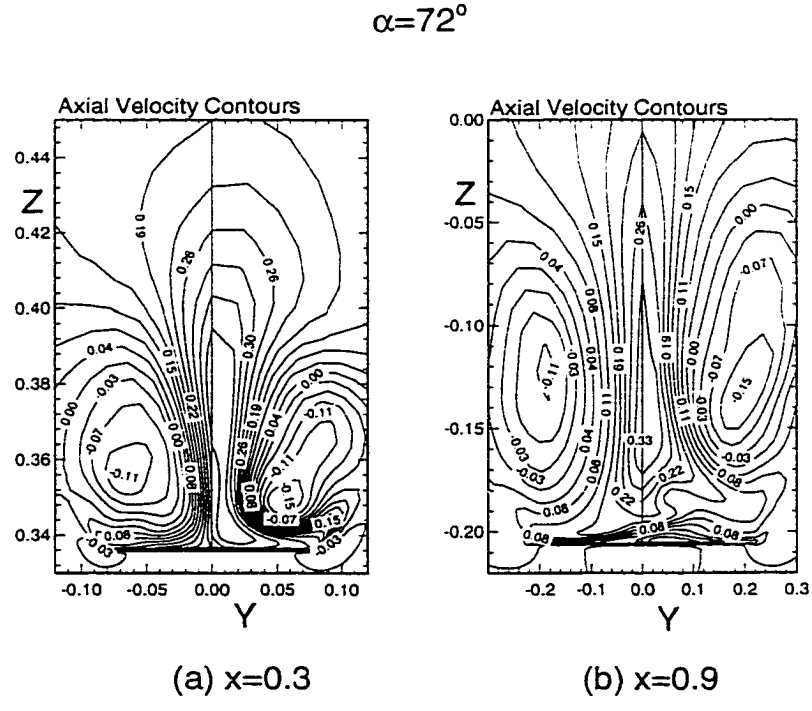

Figure 5.56: Axial flow velocity contours at (a) x=0.3 and (b) x=0.9 for $\alpha = 72^{\circ}$

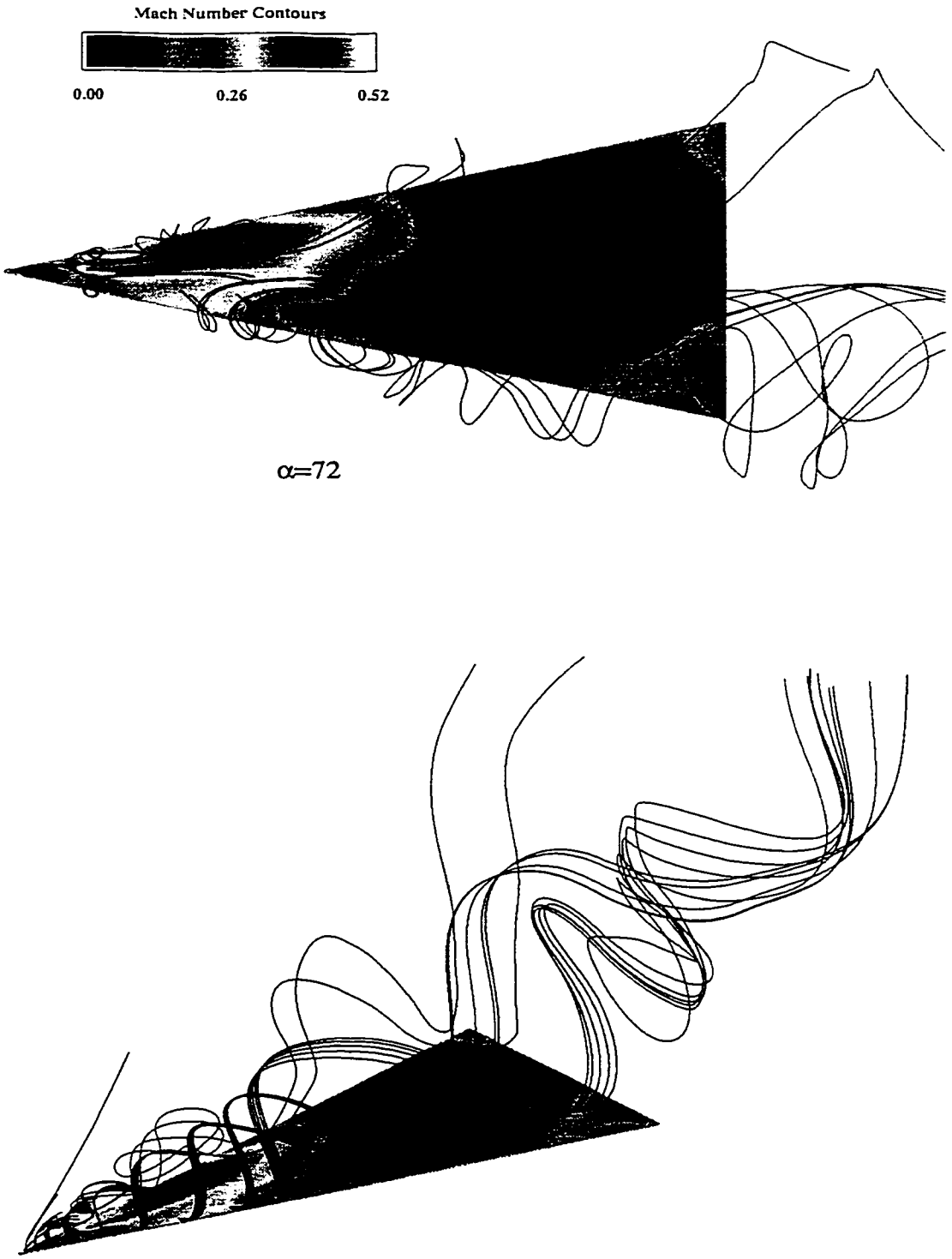

Figure 5.57: Particle traces over the delta wing and Mach number contours for $\alpha = 72^{o}$

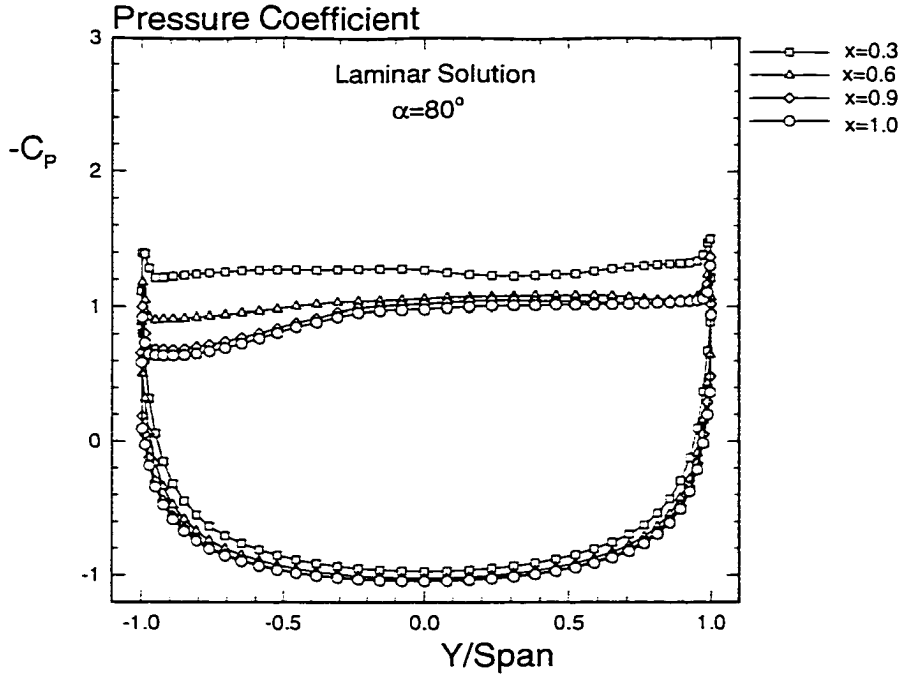

Figure 5.58: Spanwise-pressure-coefficient distribution for $\alpha = 80°$

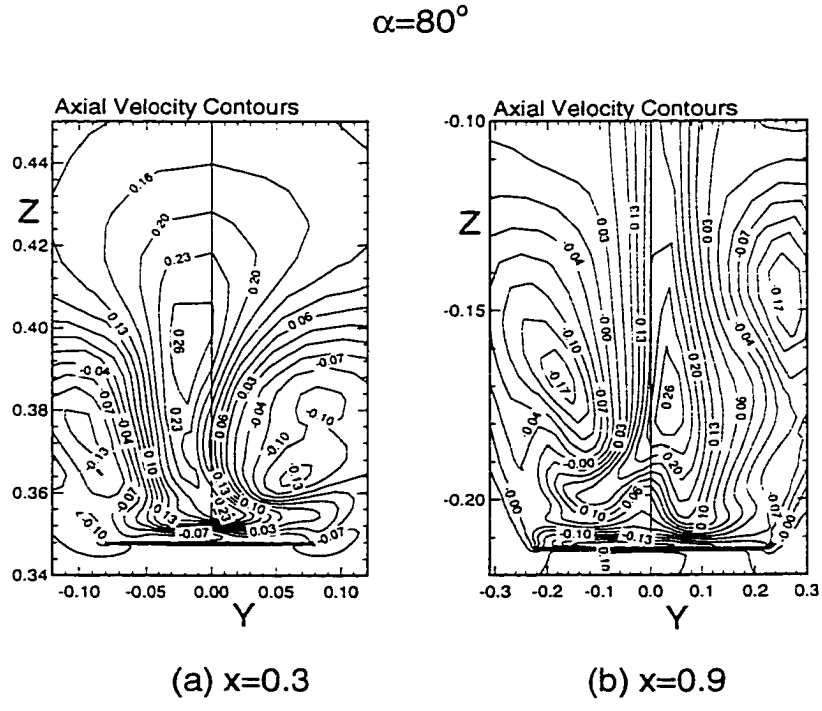

Figure 5.59: Axial flow velocity contours at (a) x=0.3 and (b) x=0.9 for $\alpha = 80°$

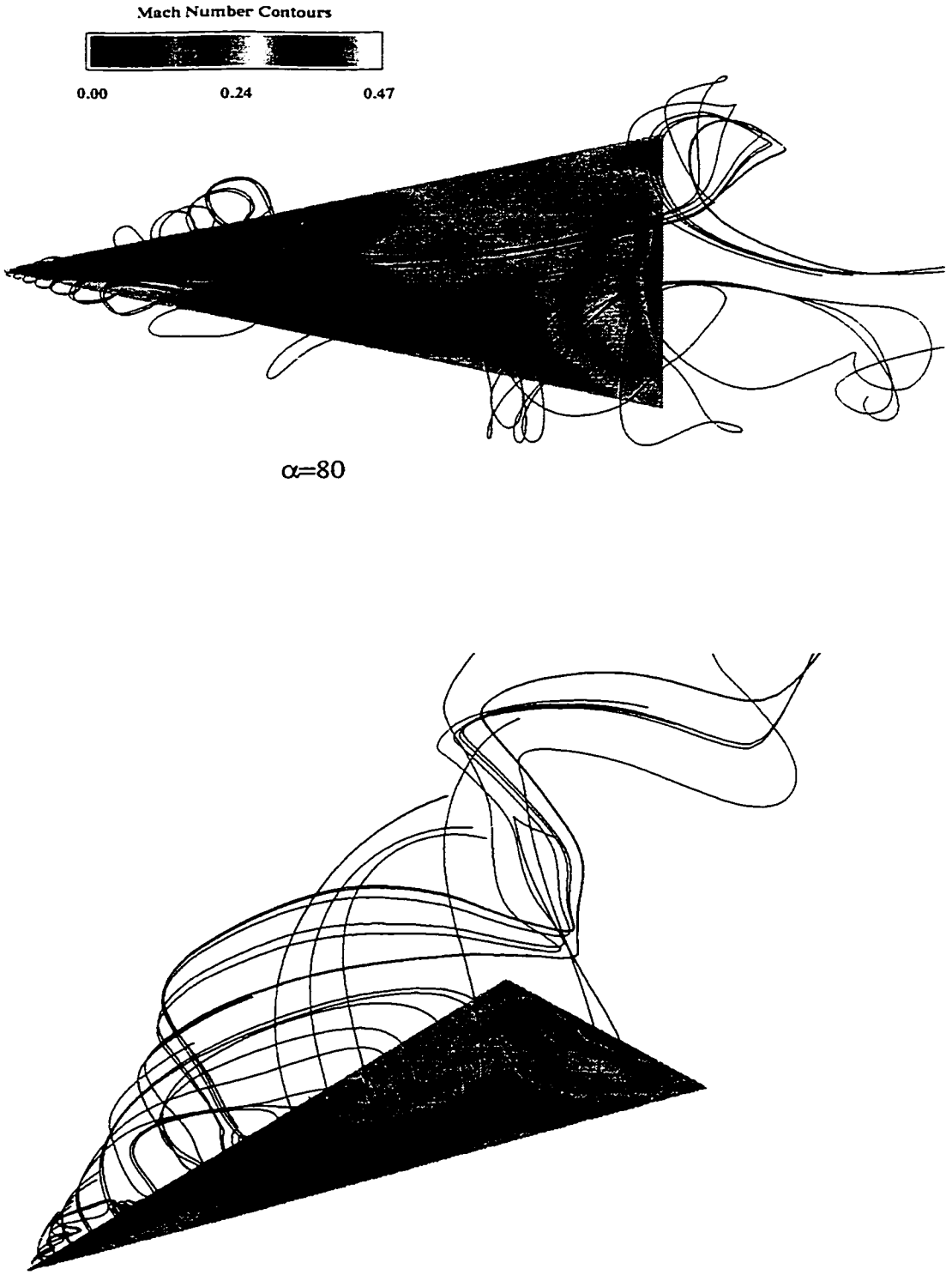

Figure 5.60: Particle traces over the delta wing and Mach number contours for $\alpha = 80^{o}$

5.3 Reduced Frequency Effect

The delta wing model used in the present computational study consists of a 76° swept back, sharp-edged wing with zero thickness and an aspect ratio of one. The three-dimensional grid topology used in these computations is an O-H grid of 84 x 65 x 43 in the axial, wrap-around, and outward directions, respectively, the same as that of Figure 5.1. Again, a relatively coarse grid is used to minimize the computational cost needed to perform very low reduced frequency maneuvers in order to compare with the available experimental data. The pitch axis is located at two-thirds of the root chord length, as measured from the wing vertex.

The wing is forced to undergo a pitch-up motion through ramp functions shown in Figure 5.61, which are related to the reduced frequency. The values of reduced frequency, which are used in the present study, are 0.834, 0.134, and 0.04. Table 5.1 summarizes the three ramp cases used in this study. The running time is based on the CRAY-YMP at NASA Langley Research Center.

Table 5.1 Summary of the test cases

Data	Case 1	Case 2	Case 3
Angle of Attack (rad.)	0.5 t	0.08 t	0.024 t
No. of time steps	3,141	19,635	65,450
Running Time (Hrs)	4.4	27.3	90.9

The freestream Mach number and Reynolds number are 0.3 and 0.45 x 10^6, respectively. The laminar unsteady, full NS equations are integrated time accurately with Δt=0.001.

Figures 5.62 and 5.63 show the variation of C_L and C_D with α for the three values of reduced frequency. In these same figures, experimental validation for three reduced frequency values of 0.01, 0.02, and 0.04 is given to show the same trend for both lift and drag coefficients. As the reduced frequency decreases the C_L and C_D coefficients values decrease. Figure 5.64 shows cross-flow instantaneous streamlines at the chord station x = 0.6 (just ahead of the pitch axis) and α = 30° for the three values of reduced frequencies. The vortex core is largest for the lowest reduced frequency value. Figure 5.65 is similar to Figure 5.64 but for a different chord station of 0.9 (after the pitch axis). The vortex core is largest with the lowest reduced frequency value.

Figure 5.66 shows the spanwise pressure-coefficient distribution for the same angle of attack of 30° for three different chord stations of 0.3, 0.6, and 0.9. The pressure difference between the lowest suction peak and the highest suction peak is larger for the lowest reduced frequency and decreases with increasing reduced frequency. Moreover, the suction peak, corresponding to the primary vortex core location, moves inboard of the wing leading edge as the reduced frequency decreases.

The total-pressure-loss contours, shown in Figure 5.67, show vortex core size increases with a more inboard movement of the leading edge vortex core as the reduced frequency decreases. Figure 5.68 shows snapshots of the particle traces of the leading edge vortices over the wing for the three values of reduced frequency. The roll-up of these vortices become tighter as the reduced frequency decreases.

Figure 5.69 shows the cross-flow instantaneous streamlines at x = 0.6 and α = 60° for the three reduced frequencies. Although vortex breakdown occurs for the reduced frequency values of 0.134 and 0.04, there is no breakdown corresponding to k = 0.834 at this chord station. Figure 5.70 shows the cross-flow instantaneous streamlines at x = 0.9 and α = 60° for the three reduced frequency values. Here, it is clear that for all reduced frequency values the breakdown occurs at this location with various degrees of strength.

The spanwise pressure coefficient distribution for α = 60° for the three chord stations of 0.3, 0.6, and 0.9 for the three reduced frequencies is presented in Figure 5.71. At α = 60° the breakdown reaches all the three chord stations for k = 0.04 whereas the breakdown is at x = 0.6 for k = 0.134 and at x = 0.9 for k = 0.834. Figure 5.72 shows total-pressure-loss contours at x = 0.9. As can be observed from Figure 5.72, the total pressure loss is more pronounced for k = 0.04 and covering larger area over the wing surface. The total pressure loss value inside the vortex core is 0.19, 0.07, and 0.08 for k = 0.04, 0.134, and 0.834; respectively. Figure 5.73 shows snapshots of the flow over the delta wing for α = 60° for the three reduced frequency values. The spiral motion strength increases as the reduced frequency decreases.

Figure 5.74 shows the cross-flow instantaneous streamlines at x = 0.6 and α = 75°. The asymmetry of the flow is very obvious for the lowest reduced frequency value. For k = 0.834, the flow even with the occurrence of the breakdown is slightly asymmetric.

Figure 5.75 shows cross-flow instantaneous streamlines at x = 0.9 and α = 75°. Here, again the flow is more asymmetric for the low reduced frequency value. Figure 5.76 shows the spanwise pressure-coefficient distribution. The pressure coefficient at

each chord station is more uniform without a suction peak for the lowest reduced frequency value. The vortex breakdown covers the upper wing surface up to $x = 0.3$.

Figure 5.77 shows the total-pressure-loss contours at $x = 0.9$ for $\alpha = 75°$. Figure 5.78 shows snapshots of the particle traces of the leading edge vortices over the delta wing for $\alpha = 75°$. The vortex breakdown flow gets larger as the reduced frequency value gets smaller.

The vortex core expands more as the reduced frequency is decreased, and early vortex breakdown occurs, see Figure 5.79. Flow asymmetry is also more pronounced as the reduced frequency decreases. These flow responses are attributed to the fact that as the reduced frequency decreases, the flow will have longer periods of time to adjust to the forced wing motion. Highly swept-back winged aircraft can fly with increased margins from disrupted and undesirable flow conditions (delayed vortex breakdown and consequently delayed stall) during maneuver using high reduced frequency values at high angles of attack.

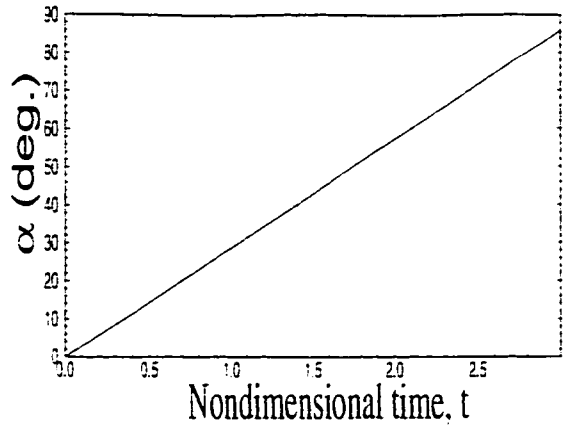

(a) K=0.834

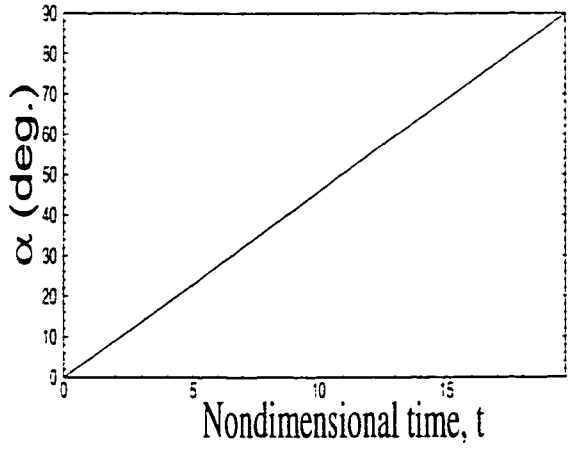

(b) K=0.134

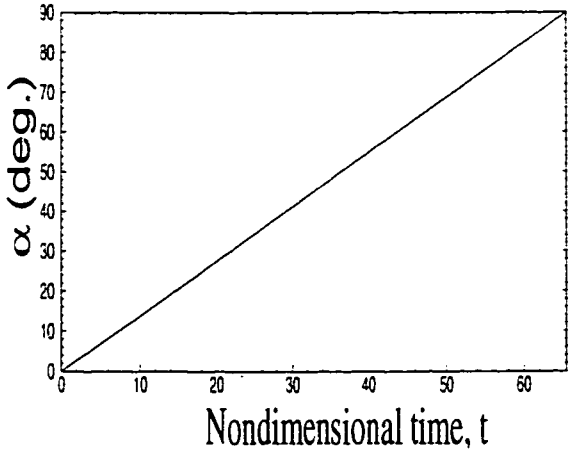

(c) K=0.04

Figure 5.61: Forced ramp function time history for k=0.834, 0.134, and 0.04

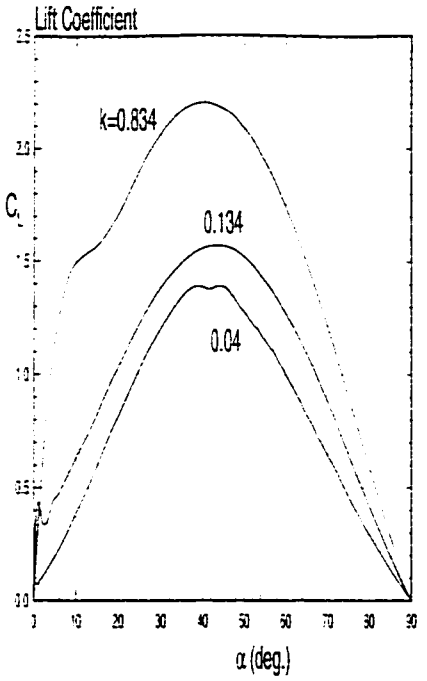

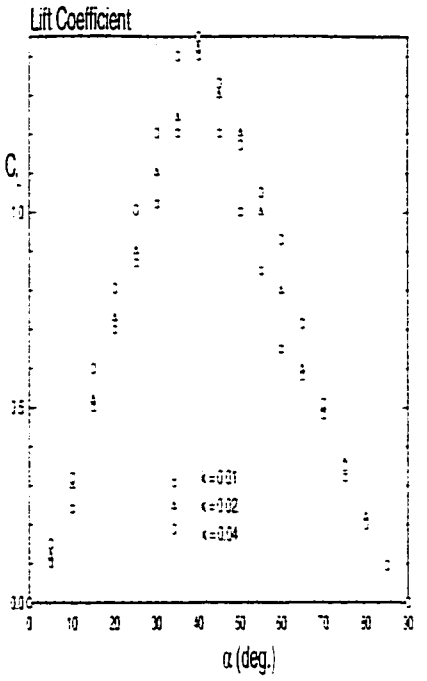

Present Experiment. Jarrah (1988)

Figure 5.62: Lift coefficient vs. α

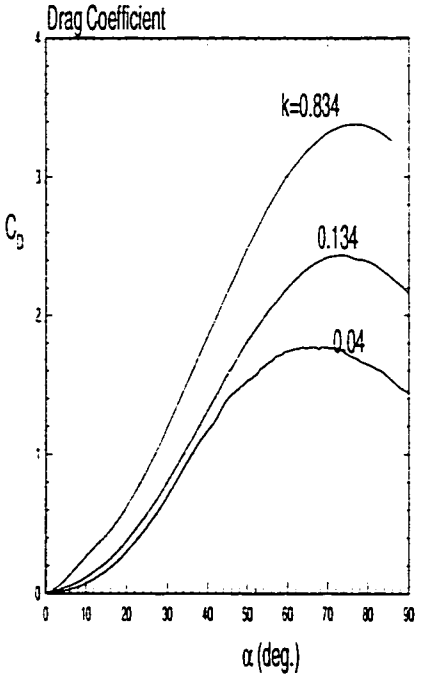

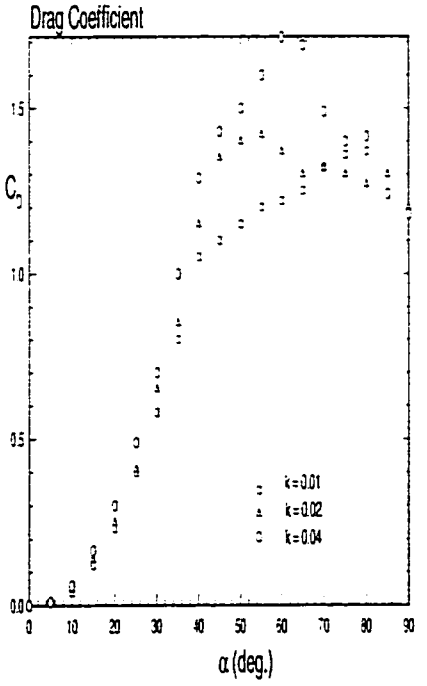

Present Experiment. Jarrah (1988)

Figure 5.63: Drag coefficient vs. α

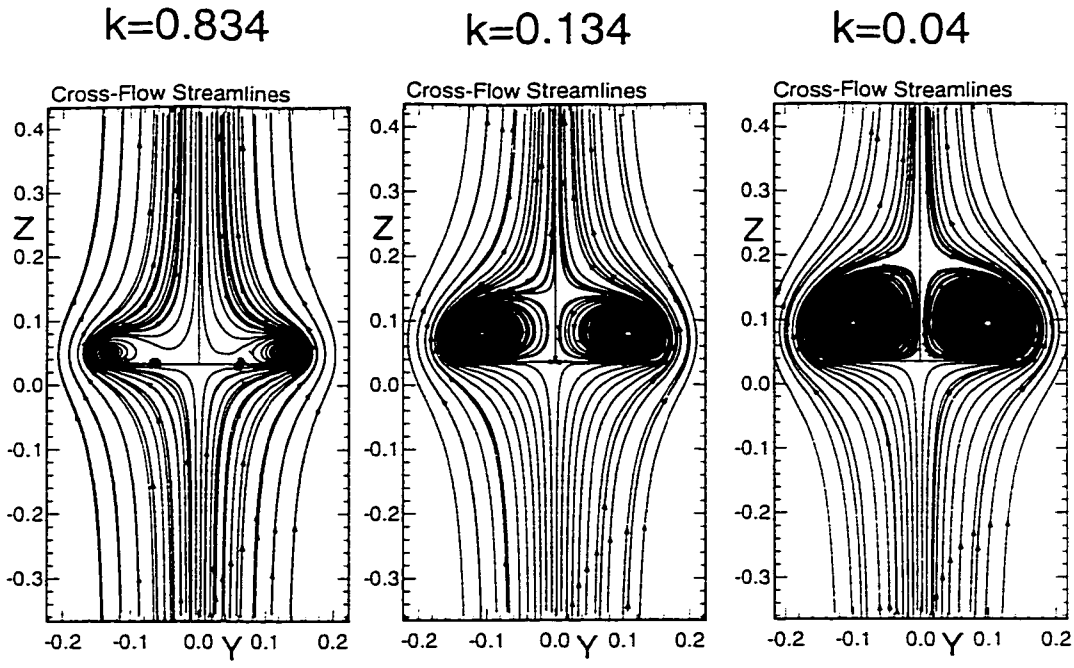

Figure 5.64: Cross-flow instantaneous streamlines at x=0.6 and $\alpha = 30^o$

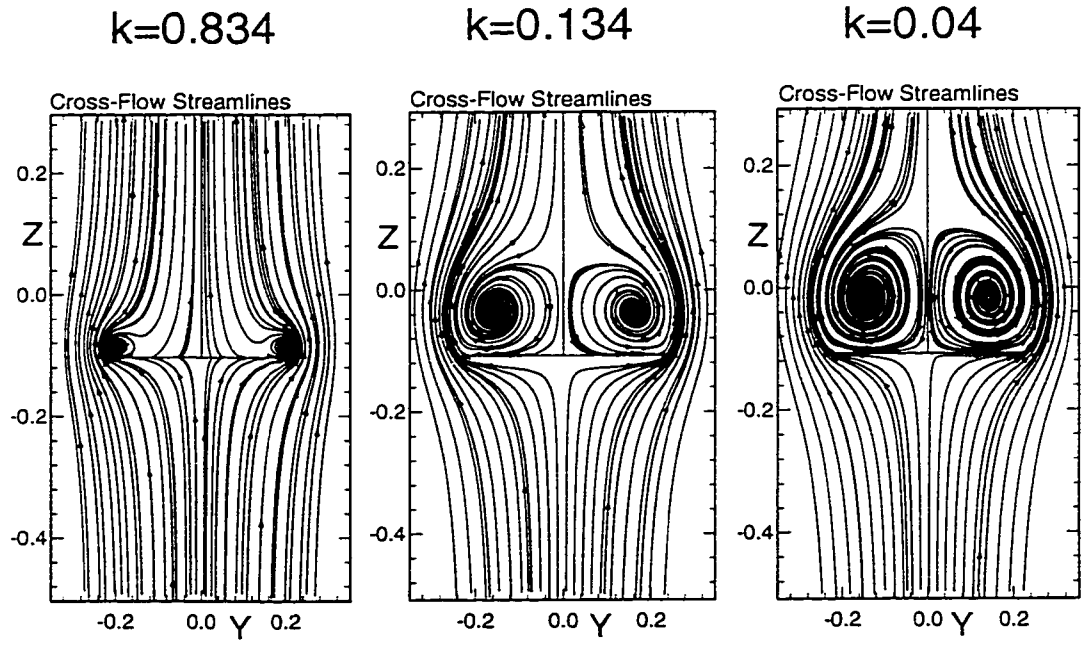

Figure 5.65: Cross-flow instantaneous streamlines at x=0.9 and $\alpha = 30^o$

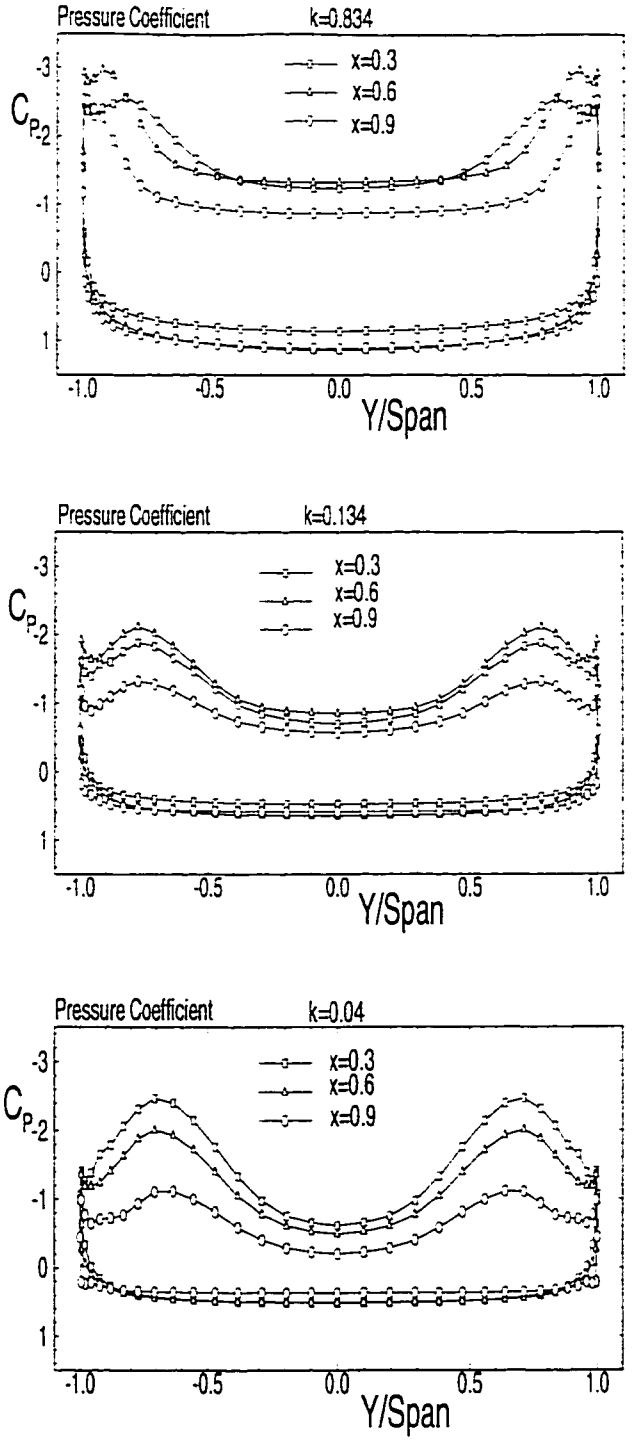

Figure 5.66: Spanwise-pressure-coefficient distribution for $\alpha = 30°$

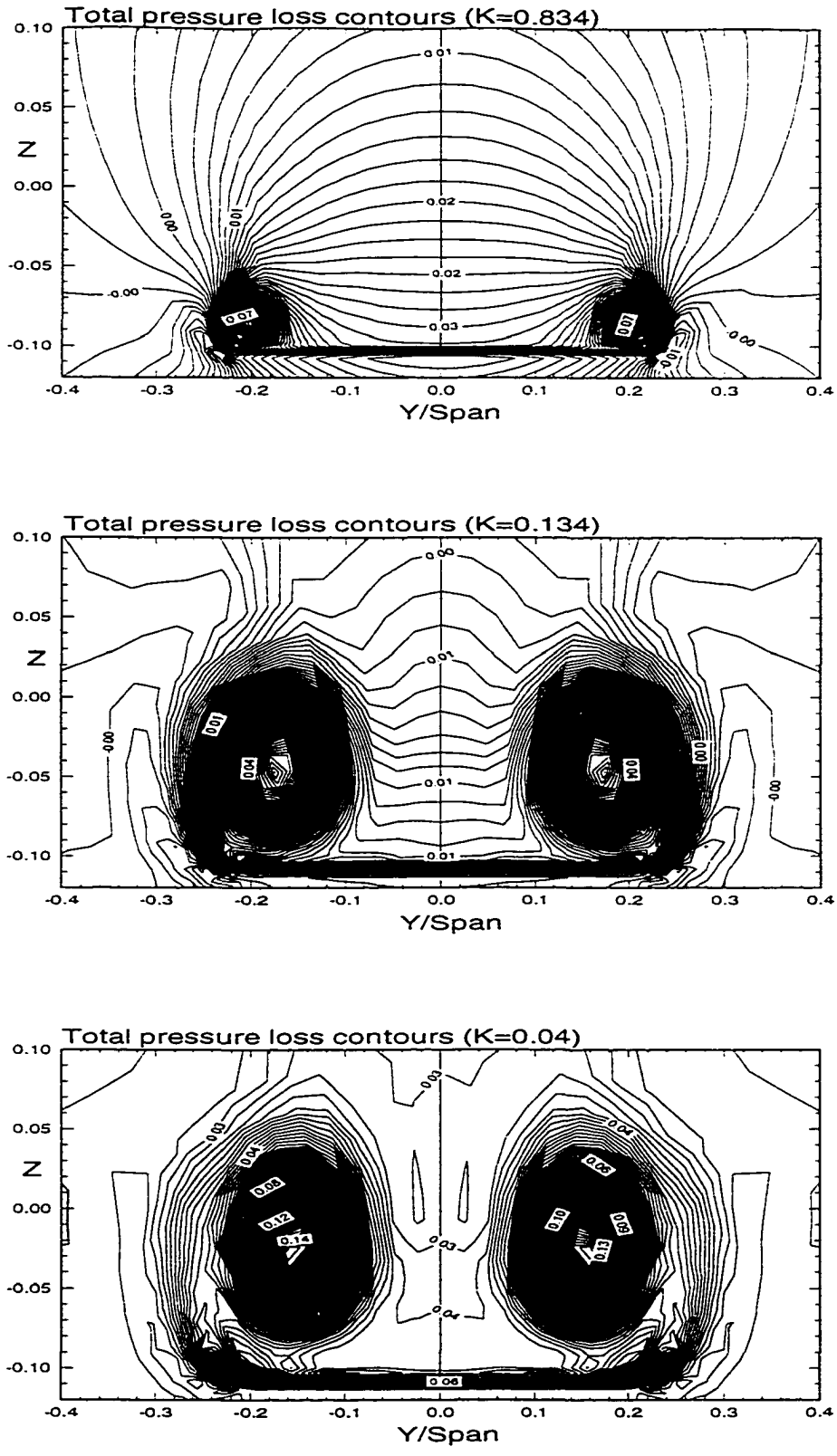

Figure 5.67: Total-pressure-loss contours at x=0.9 and $\alpha = 30^{o}$

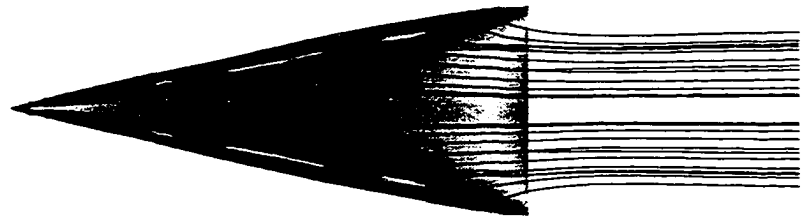

k=0.834

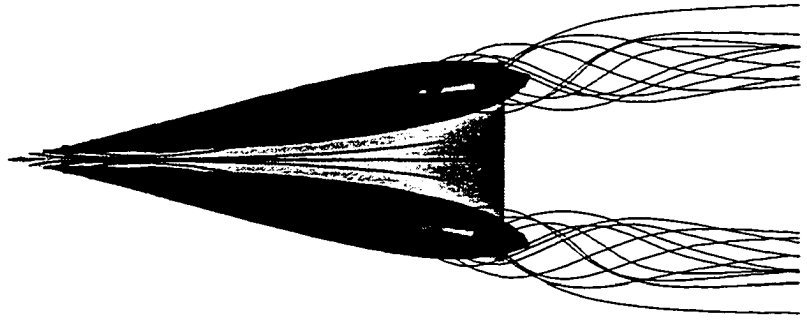

k=0.134

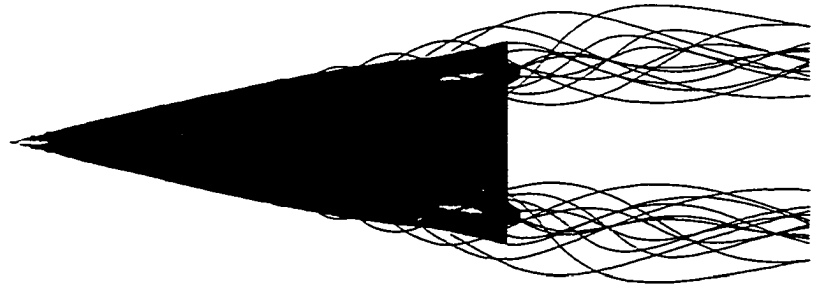

k=0.04

Figure 5.68: Particle traces over the delta wing at $\alpha = 30^o$

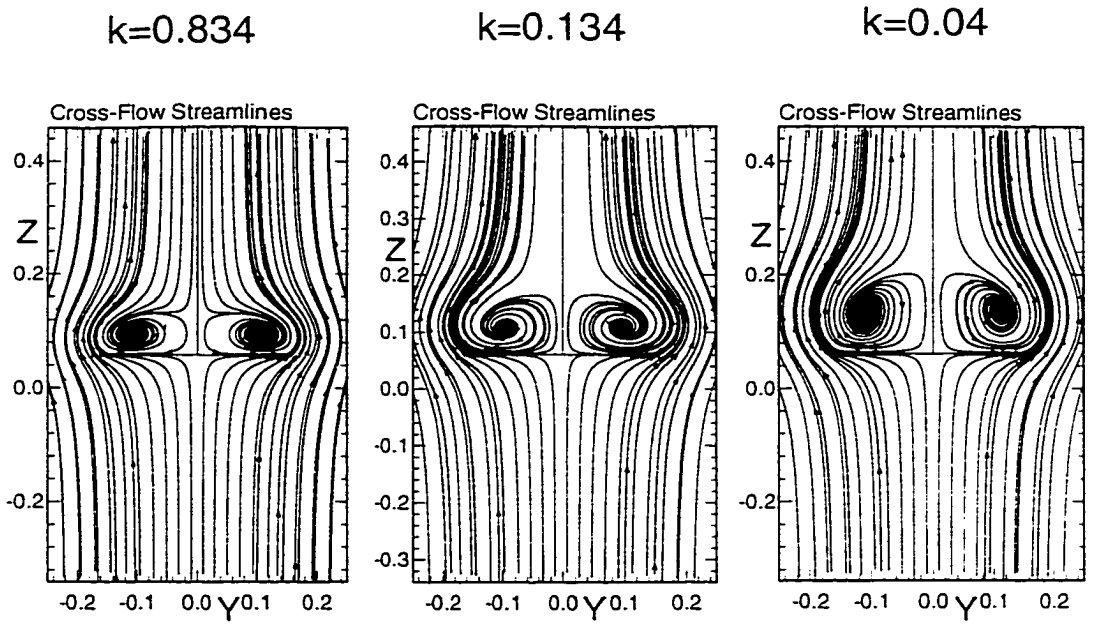

Figure 5.69: Cross-flow instantaneous streamlines at x=0.6 and $\alpha = 60°$

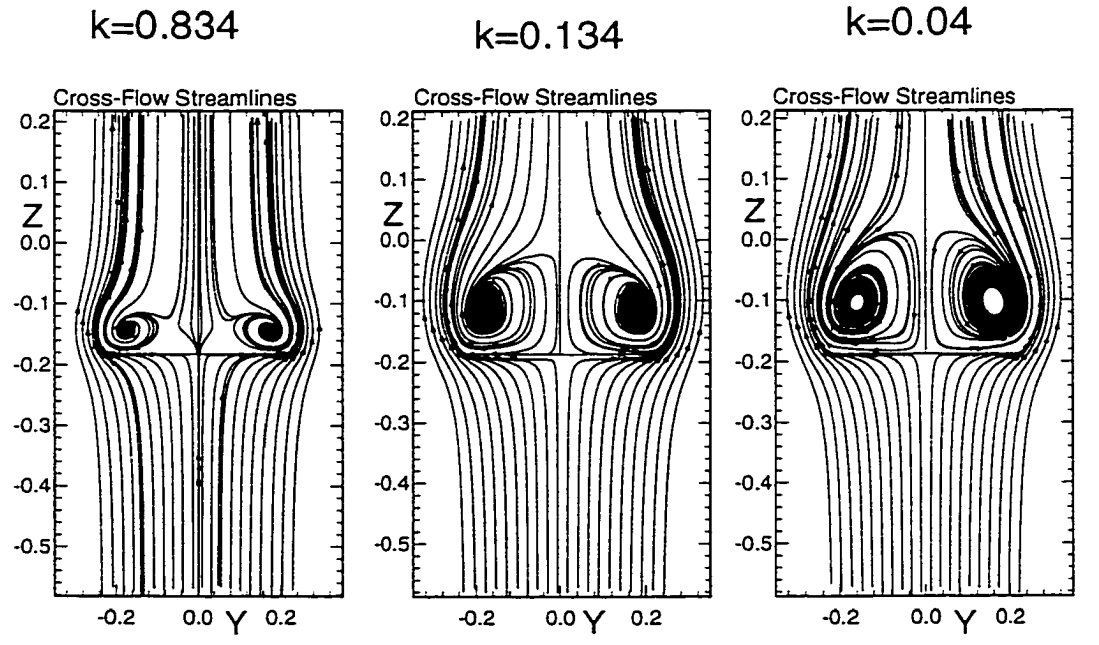

Figure 5.70: Cross-flow instantaneous streamlines at x=0.9 and $\alpha = 60°$

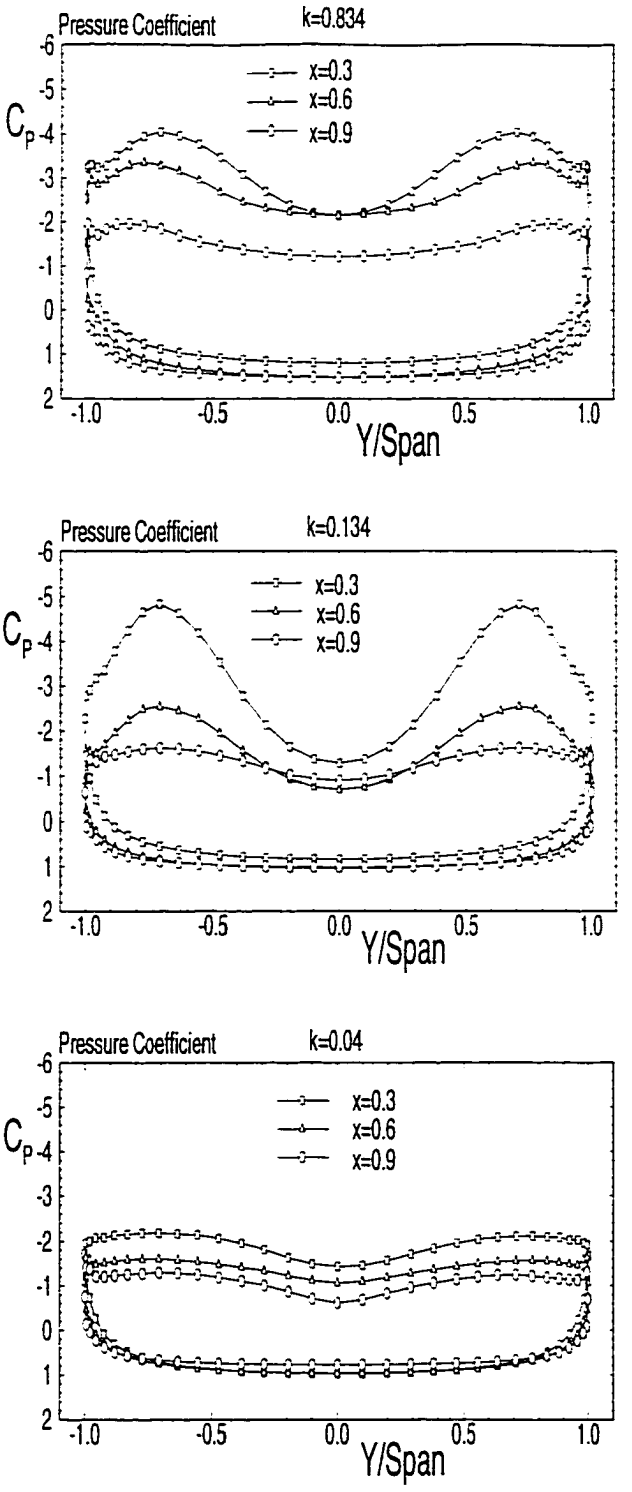

Figure 5.71: Spanwise-pressure-coefficient distribution for $\alpha = 60°$

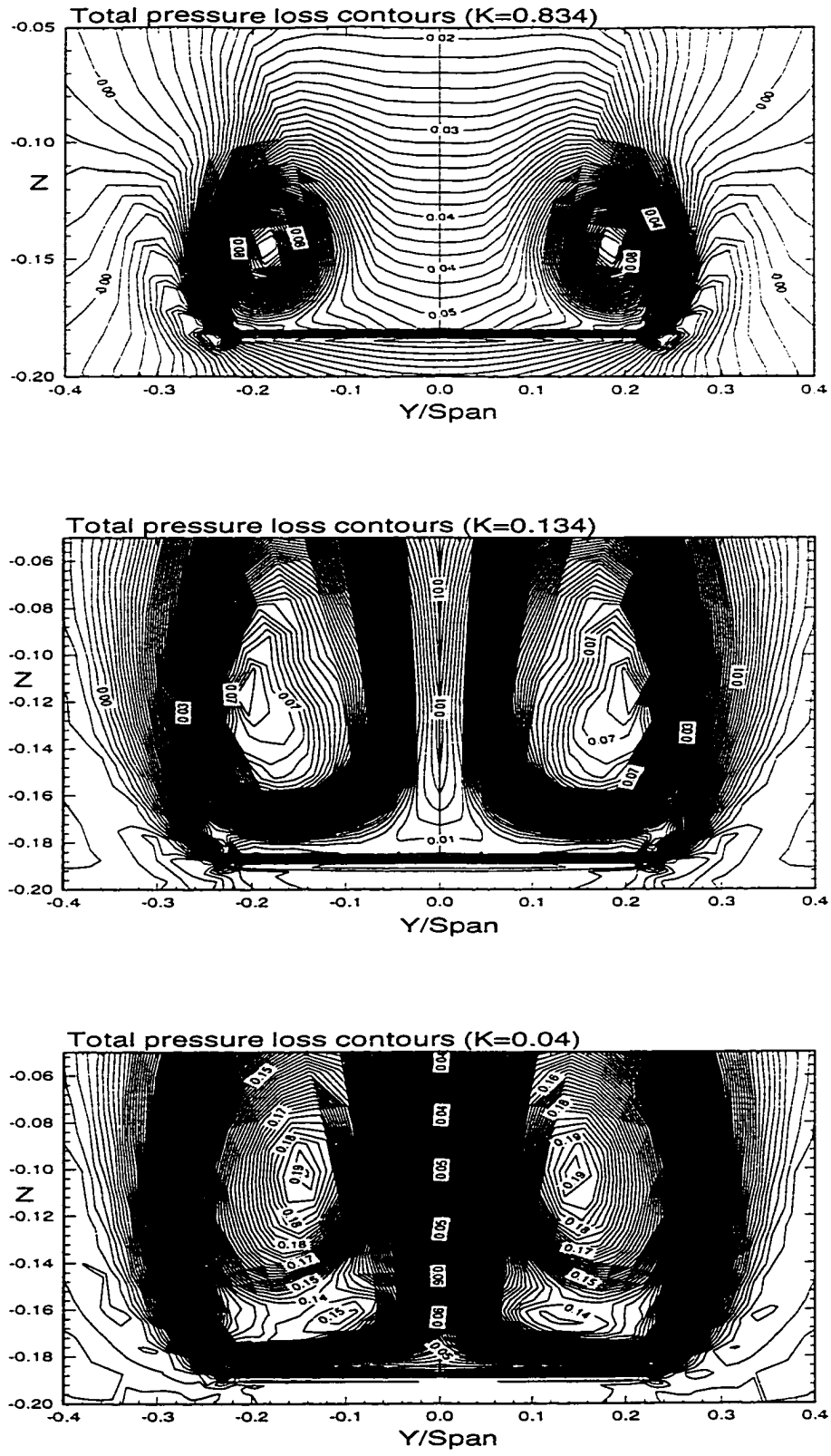

Figure 5.72: Total-pressure-loss contours at x=0.9 and $\alpha = 60°$

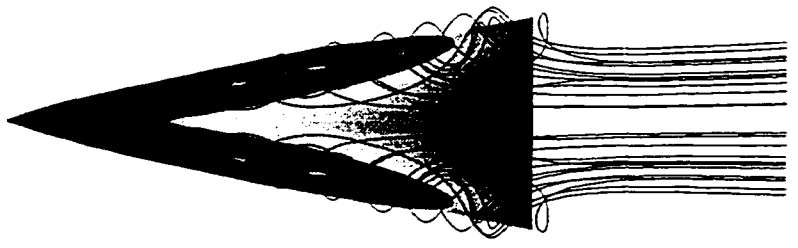

k=0.834

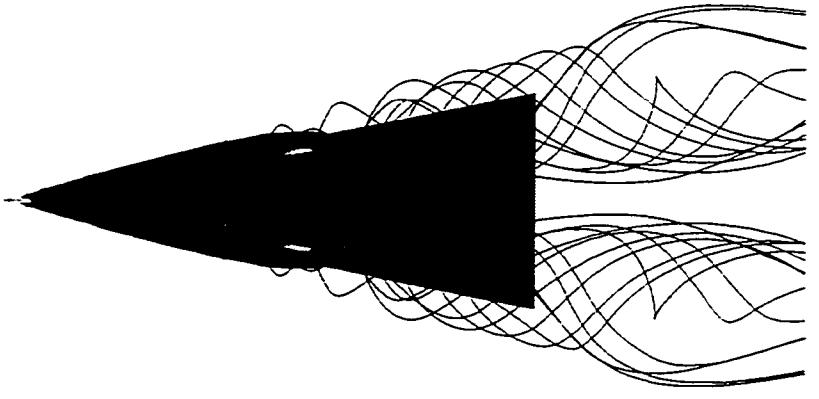

k=0.134

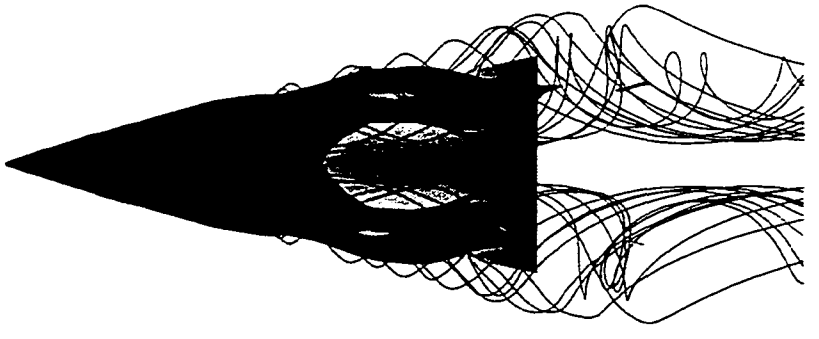

k=0.04

Figure 5.73: Particle traces over the delta wing at $\alpha = 60°$

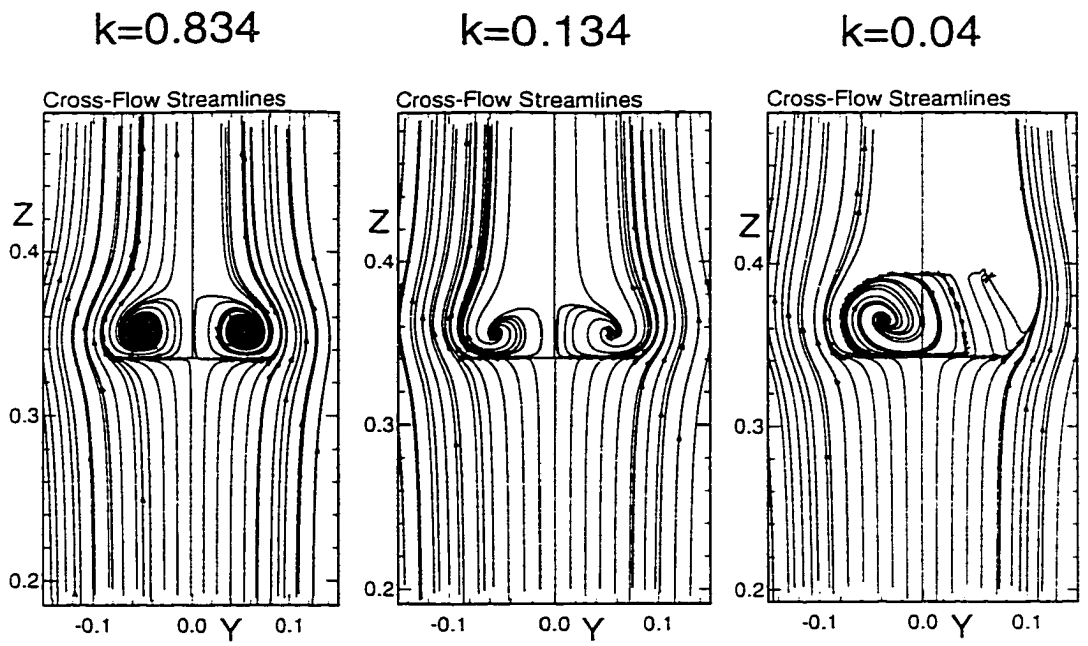

Figure 5.74: Cross-flow instantaneous streamlines at x=0.6 and $\alpha = 75°$

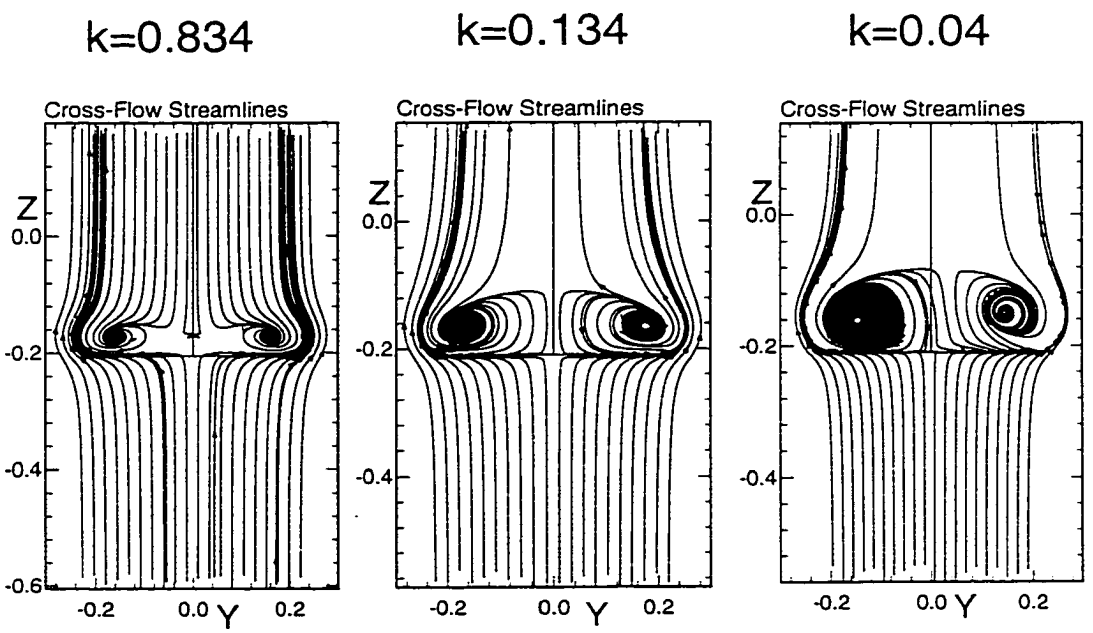

Figure 5.75: Cross-flow instantaneous streamlines at x=0.9 and $\alpha = 75°$

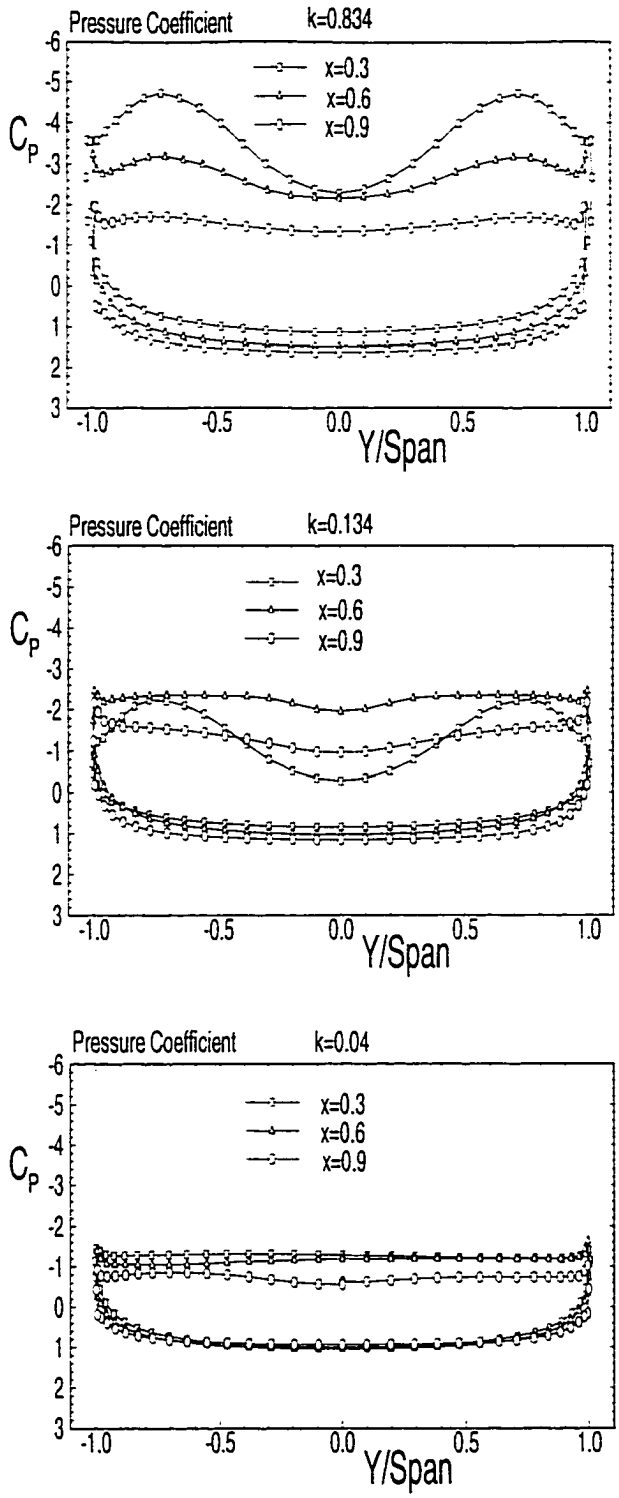

Figure 5.76: Spanwise-pressure-coefficient distribution for $\alpha = 75°$

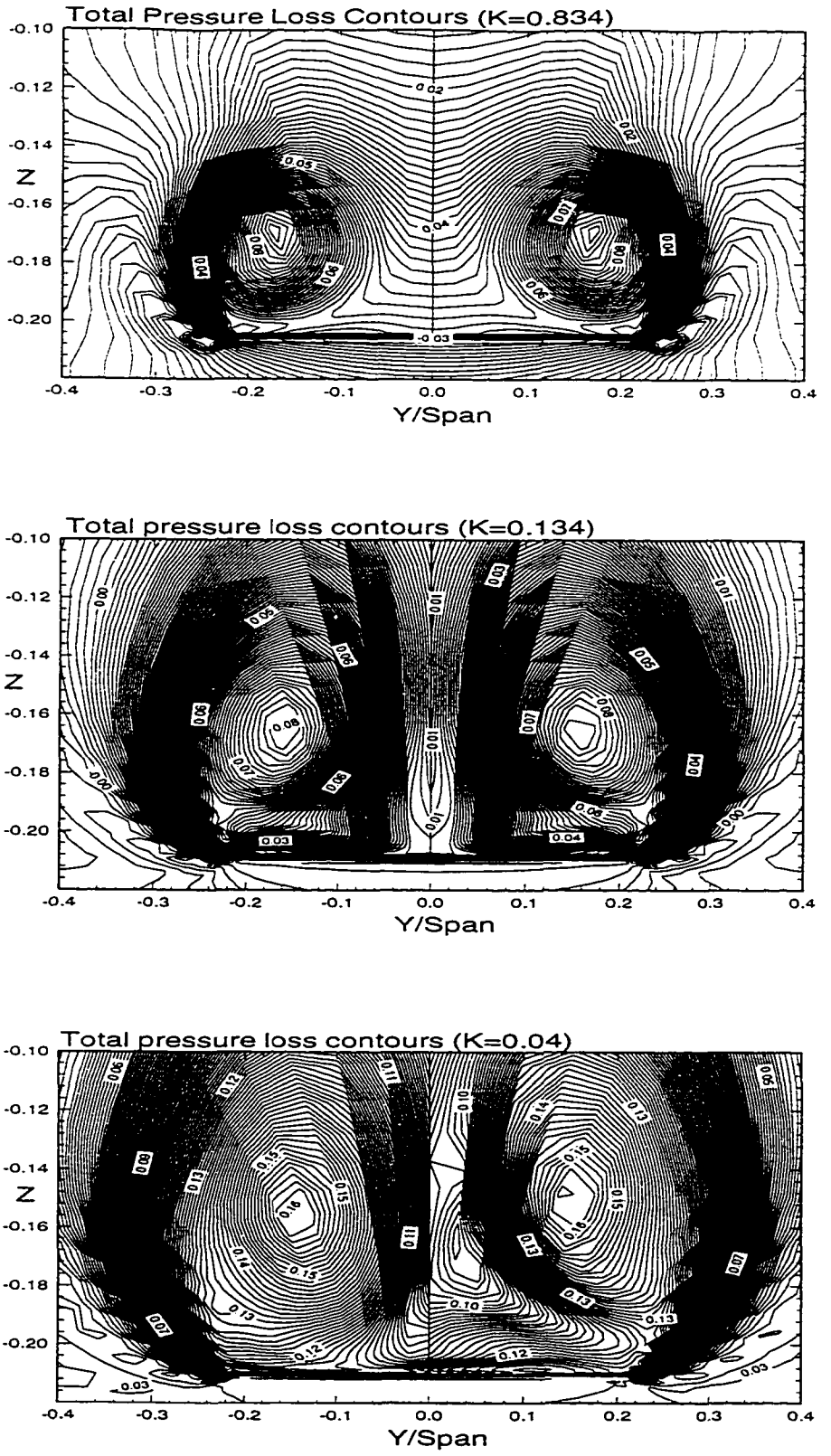

Figure 5.77: Total-pressure-loss contours at x=0.9 and $\alpha = 75^{o}$

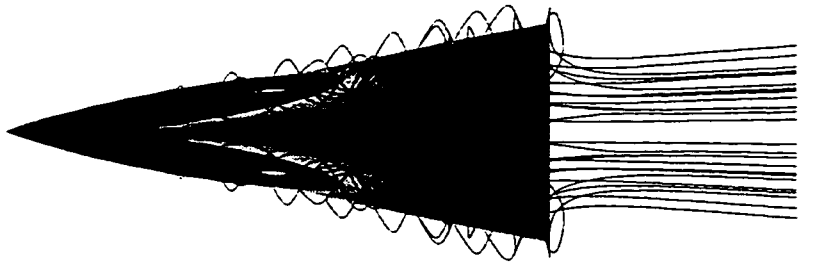

k=0.834

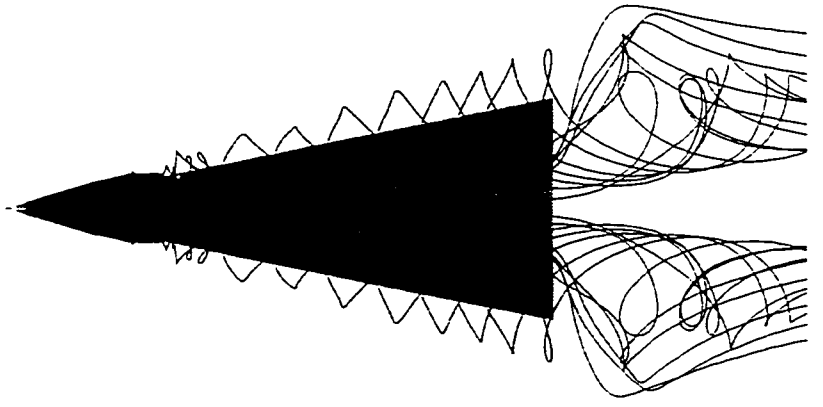

k=0.134

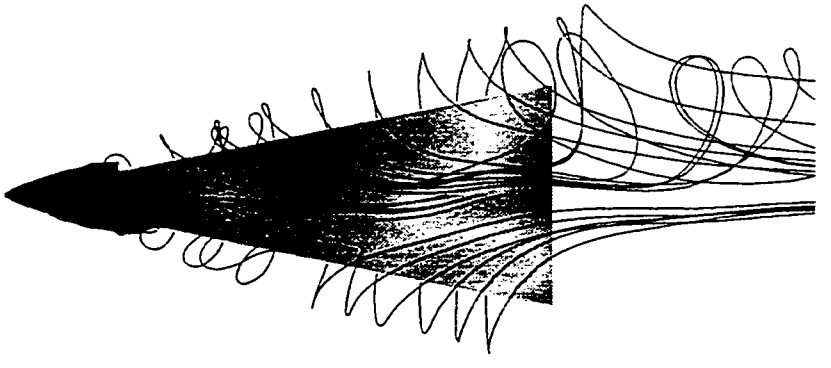

k=0.04

Figure 5.78: Particle traces over the delta wing at $\alpha = 75°$

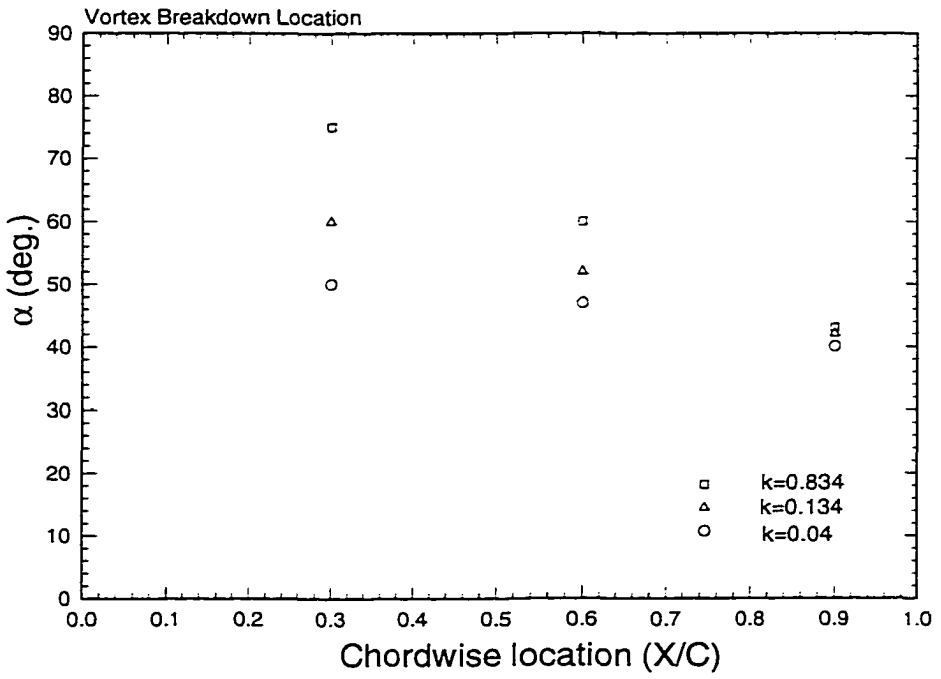

Figure 5.79: Vortex breakdown location for k=0.834, 0.134, and 0.04

5.4 Summary

Validation of the computational results was carried out using existing experimental data of Jarrah (1988). A grid refinement study was introduced and the effect of reduced frequency of the wing motion was then presented. Computational results provide complete information and details about the flowfield response, which were not given in the experimental data. This investigation of the unsteady flow over a wide range of angles of attack provided crucial understanding of the variations of the leading edge vortex cores, their breakdown behavior and wing aerodynamic characteristics at very high angles of attack.

CHAPTER 6

TURBULENT FLOW SOLUTIONS

Two turbulence models are used in conjunction with the Reynolds-Averaged NS equations. The first one is zero order or an algebraic model (Baldwin-Lomax). The second one is a one-equation model (Spalart-Allmaras). The purpose of using these models in our current study is to improve the predicted results at very high angle of attack range (greater than 60°). Three flow cases are shown in this Chapter. The first and third cases are solved using Baldwin-Lomax model whereas the second case is solved using Spalart-Allmaras model.

6.1 Results Using Baldwin-Lomax Model

The delta wing model used in the present computational study consists of a 76° swept back, sharp-edged wing with zero thickness and an aspect ratio of one. The same coarse grid topology is used in the calculations. The pitch axis is located at two thirds of the root chord station. The wing is forced to undergo a pitching motion through a ramp function shown in Figure 5.2 and is described by $\alpha = 0.024t$, which is related to the reduced frequency. In our analysis, the reduced frequency is equivalent to 0.04. The freestream Mach number and Reynolds number are 0.3 and 0.45×10^6, respectively. This flow condition is the same case as that of section 5.1. The Reynolds-Averaged NS equations are integrated time accurately with $\Delta t = 0.001$. This translates Δt into 65,450 time steps to complete the ramp up to $\alpha = 90°$. In this study case, we have used the Reynolds-averaged NS equation with a Baldwin-Lomax turbulence model along with the

Schiff and Degani modification for massively separated flows to study the turbulence model effects on the solution.

Figures 6.1 and 6.2 show variations of the lift and drag coefficients with α. There is an excellent agreement between the computed C_L and C_D values and the corresponding experimental data of Jarrah (1988). For angles of attack less or greater than 40°, C_L shows a very close agreement with the experimental data. For angles of attack around 40°, the difference between the computed C_L and the experimental value is appreciable. This difference may be attributed to the grid resolution at the trailing edge where the vortex breakdown crosses and moves upstream over the wing surface. Using the Baldwin-Lomax turbulence model enhanced the computed C_L values. Further, the computed C_D values are slightly enhanced. The good agreement with the experimental data has been improved up to $\alpha = 65°$.

Figures 6.3-6.18 show the vortex core development over the wing surface from very low to very high values of angle of attack (10°-80°). Figure 6.3 shows the particle traces of the leading edge vortices over the delta wing and the spanwise pressure coefficient distributions at three different axial chord stations of 0.3, 0.6 and 0.9 and at $\alpha = 10°$. The vortex flow is beginning to develop over the wing surface and the pressure distribution has started to build-up. Figure 6.4 shows the cross-flow instantaneous streamlines at $\alpha=10°$ and for two axial stations of 0.4 and 0.9 (one near the apex and one near the trailing edge). The suction peaks of the pressure distributions are weaker than those of the laminar solution. Although the suction peak at $x = 0.9$ for the laminar solution is equal to -0.5 the current turbulent value is -0.4.

Figure 6.5 shows the particle traces of the leading edge vortices over the delta wing and the span-wise pressure coefficient distributions at $\alpha = 20°$ for the same axial chord stations. The vortex core over the wing surface has started to expand laterally and the pressure distribution peaks are higher than the corresponding values at $\alpha = 10°$. The suction peaks show typical turbulent boundary layer flow on the wing surface with one suction peak under the primary vortex and no secondary suction peak. Figure 6.6 shows the cross-flow instantaneous streamlines at $\alpha = 20°$ at two different axial stations of 0.4 and 0.9. Again, the suction peaks of the pressure distributions are weaker than those of the laminar solution. Although the suction peak at $x = 0.9$ for the laminar solution is equal to -0.8 the current turbulent value is -0.7.

Figure 6.7 shows the particle traces over the delta wing and spanwise pressure coefficient distributions and Figure 6.8 shows the cross-flow instantaneous streamlines at $\alpha = 30°$. The vortex breakdown passes through the trailing edge around 40° as one can see from Figure 6.9. The streamlines take expanded spiral paths near the trailing edge as can be seen from Figure 6.10. Figure 6.11 shows that the vortex breakdown is translating further upstream and the C_P curves at $x = 0.6$, and 0.9 show no suction peaks. The front portion of the vortex core is expanding in the lateral direction. Figure 6.12 shows the cross-flow instantaneous streamlines at $\alpha = 50°$. The spiral motion is moving upstream toward the apex of the wing.

Figures 6.13 and 6.14 show that breakdown is covering a significant portion of the wing surface at $\alpha = 60°$. The pressure coefficient curves up to a forward location of $x = 0.3$ do not show any suction pressure peaks. The streamline shapes, spanwise pressure coefficient distributions, and cross-flow instantaneous streamlines at $\alpha = 70°$

and 80° are shown in Figures 6.15-6.18. The asymmetry of the flow over the whole wing surface can be seen from Figure 6.18. In contrast, at low angles of attack, a tight vortex core develops at the leading edge of the wing, the vortex core center is located near the leading edge, and the flow is symmetric (zero side-slip angle).

Figure 6.19 and 6.20 show snapshots of the flow streamlines along with the wing surface stagnation pressure and the vortex core stagnation pressure surfaces at $\alpha = 70°$. At $\alpha = 70°$ the breakdown moves further upstream to encompass a larger area of the wing making this area ineffective in producing lift while the remaining area of the wing continues to generate a lift force. At $\alpha = 90°$, the whole wing is no longer generating any lift. The differences between this case and the laminar solution of Chapter 5 are appreciable. The lift and drag coefficient values obtained using Baldwin-Lomax model underestimate the laminar solution. This discrepancy is attributed to the spanwise coarseness of the grid in the vicinity of the primary and secondary separations.

In general, the Baldwin-Lomax model introduced some improvements of the computational results of C_D-α curve in comparison with the experimental data up to an angle of attack of about 65°. As for the lift coefficient, the Baldwin-Lomax model gives very good agreement with the experimental data except around $\alpha = 40°$. The differences are believed to be due to the grid resolution particularly at the trailing edge where the vortex breakdown crosses this location at $\alpha = 39°$. As the angle of attack increases above the critical angle, the vortex breakdown advances upstream with an upward displacement and lateral expansion. These results call for the development of a dynamic fine grid resolution compatible with the vortex breakdown motion and deformation. Moreover, a higher order turbulence model may improve the predictions at very large angles of attack.

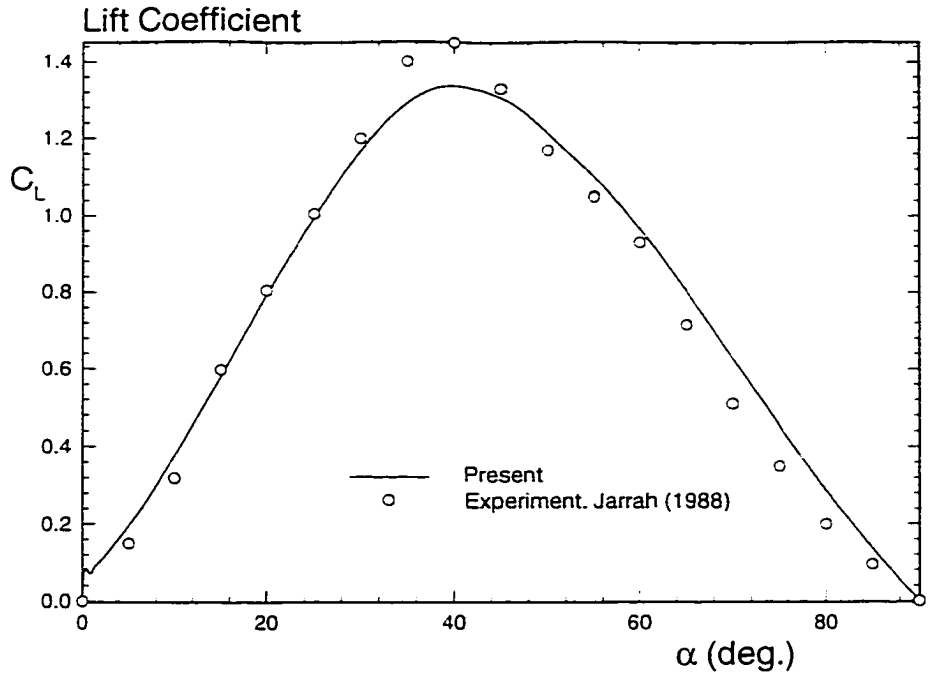

Figure 6.1: Lift coefficient vs. α using Reynolds Averaged NS equations.

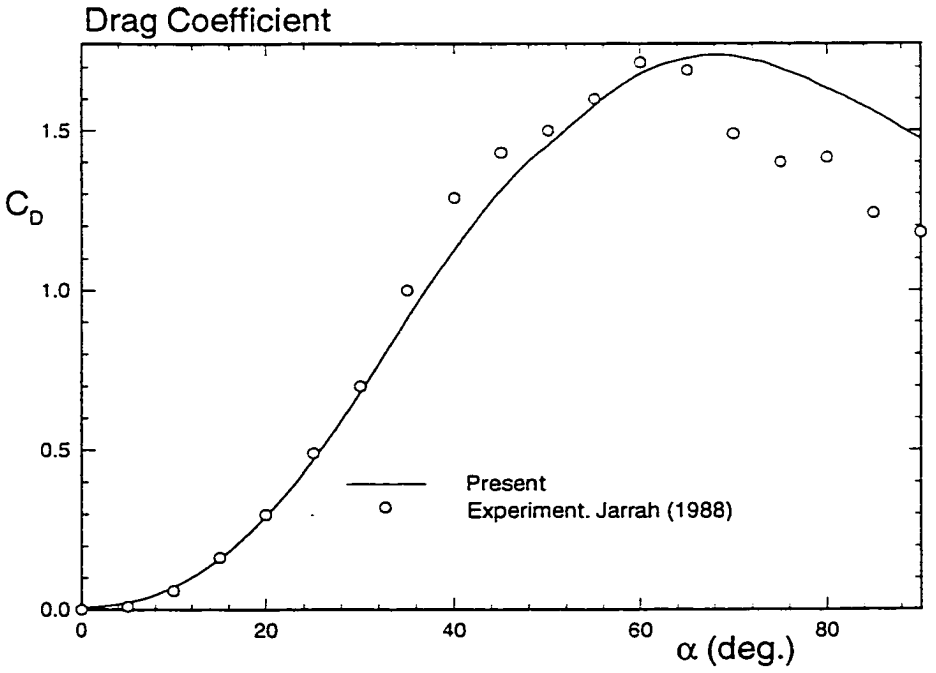

Figure 6.2: Drag coefficient vs. α using Reynolds Averaged NS equations.

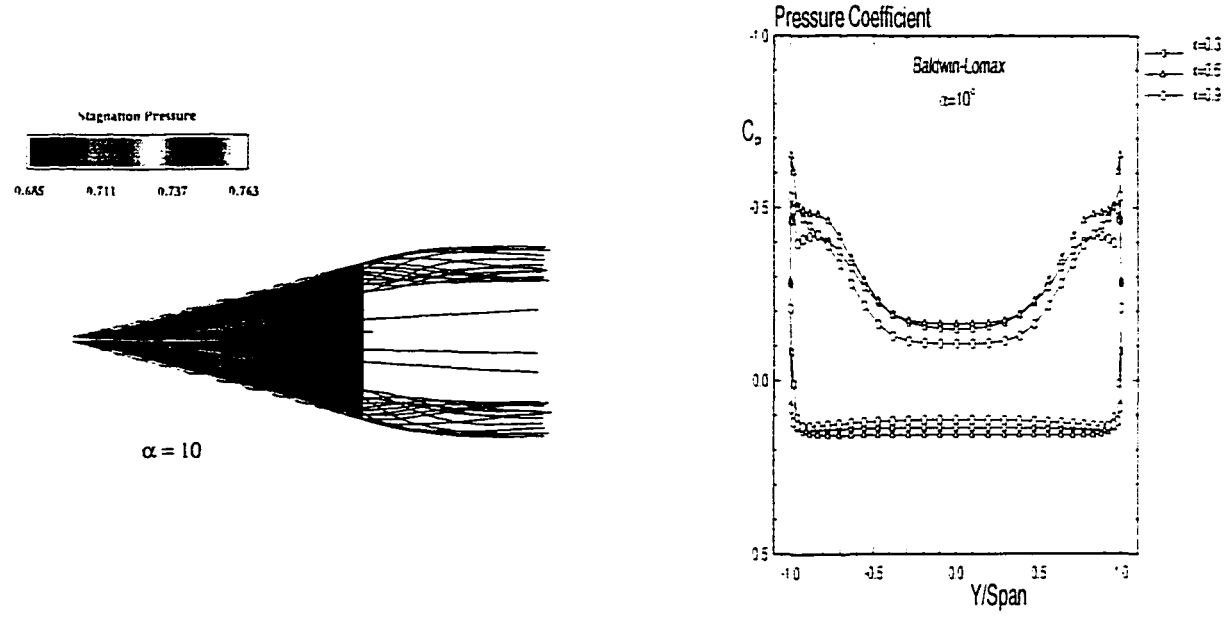

Figure 6.3: Particle traces over the delta wing and spanwise pressure coefficient distributions at $\alpha = 10°$

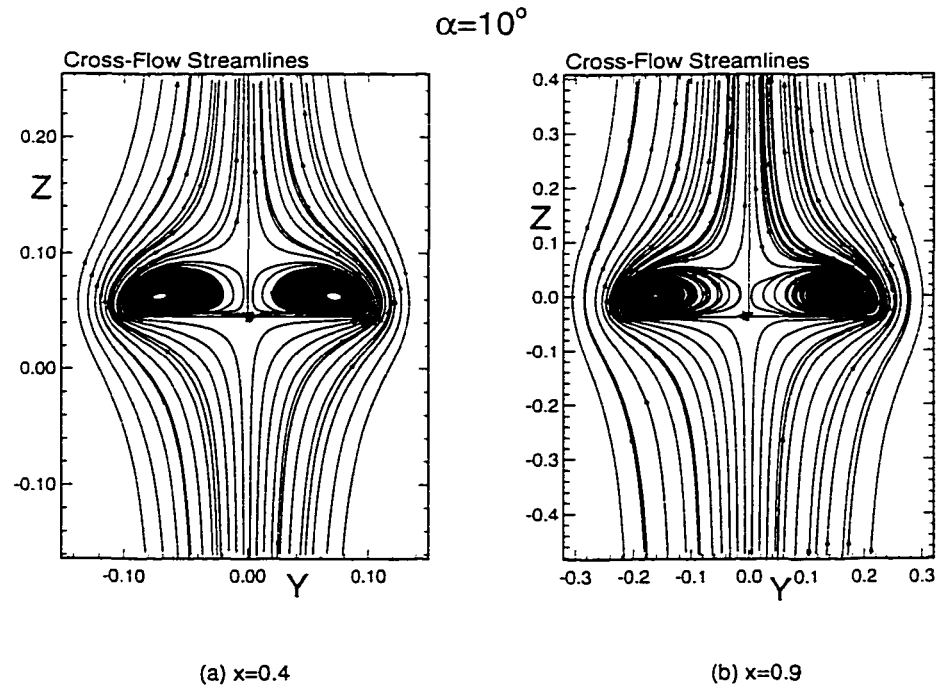

Figure 6.4: Cross-flow instantaneous streamlines at $\alpha = 10°$ (a) x=0.4 and (b) x=0.9

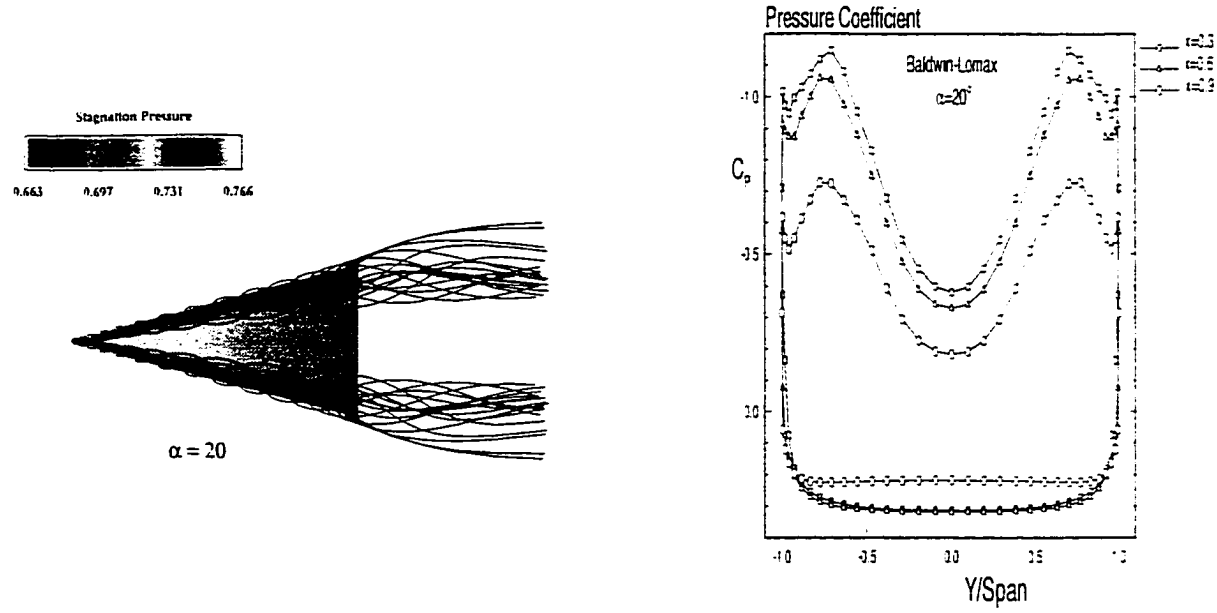

Figure 6.5: Particle traces over the delta wing and spanwise pressure coefficient distributions at $\alpha = 20°$

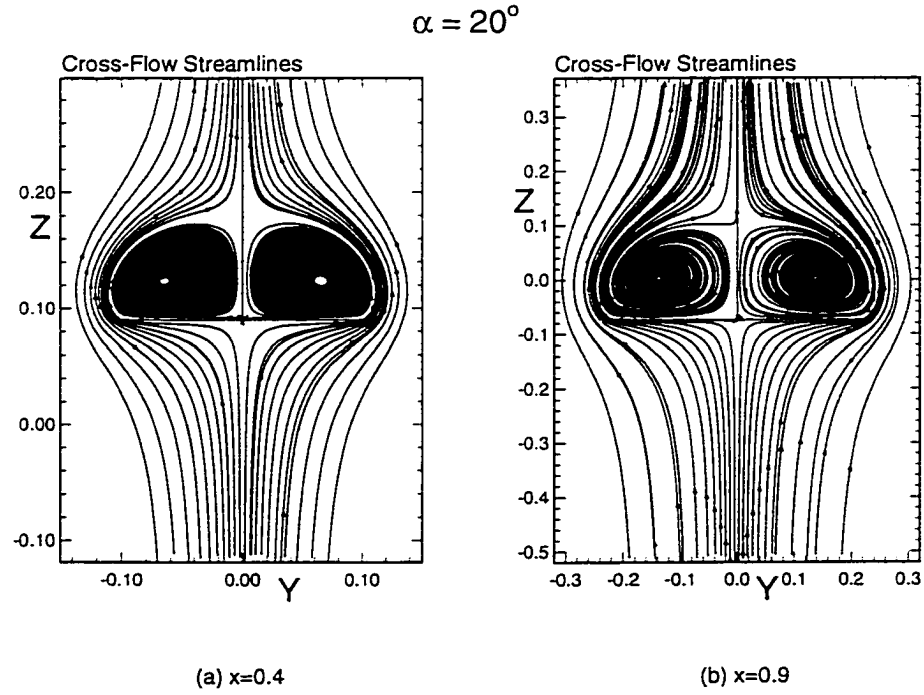

Figure 6.6: Cross-flow instantaneous streamlines at $\alpha = 20°$ (a) x=0.4 and (b) x=0.9

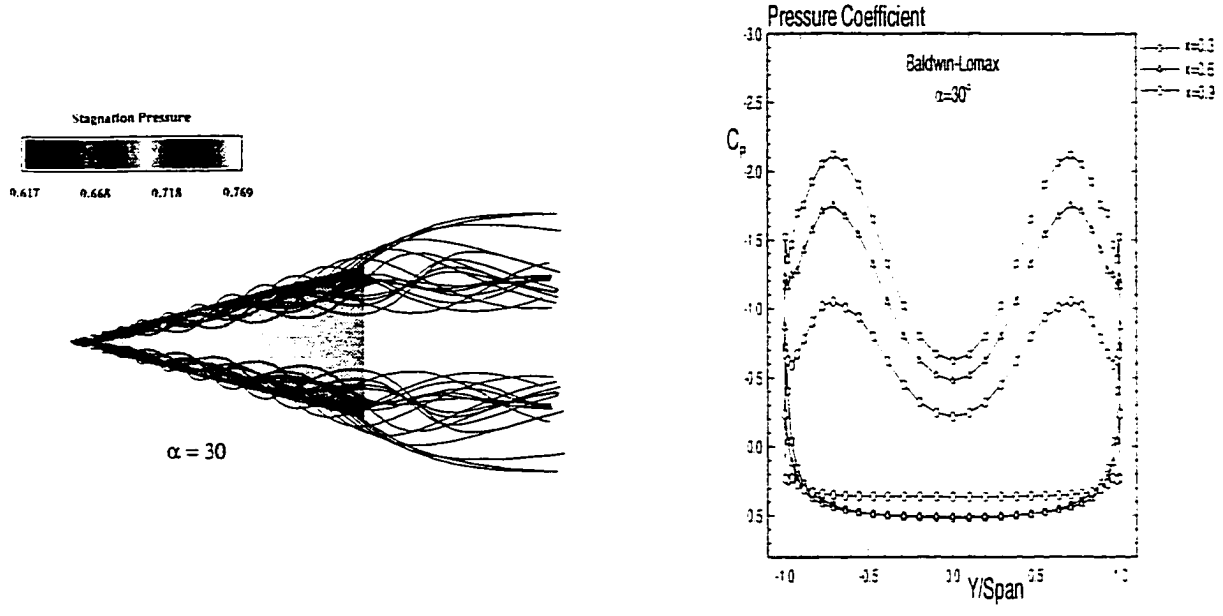

Figure 6.7: Particle traces over the delta wing and spanwise pressure coefficient distributions at $\alpha = 30^o$

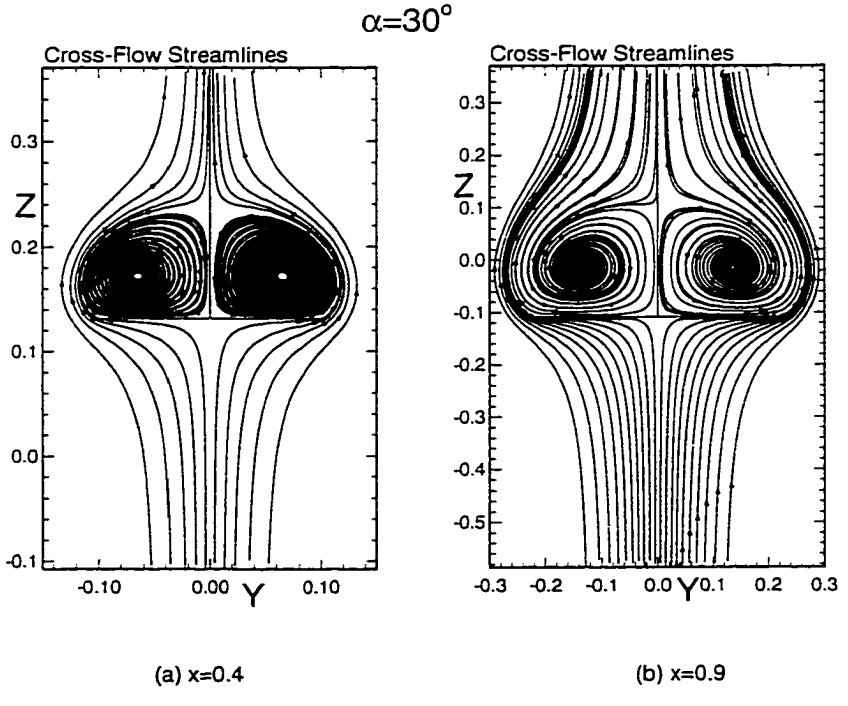

Figure 6.8: Cross-flow instantaneous streamlines at $\alpha = 30^o$ (a) x=0.4 and (b) x=0.9

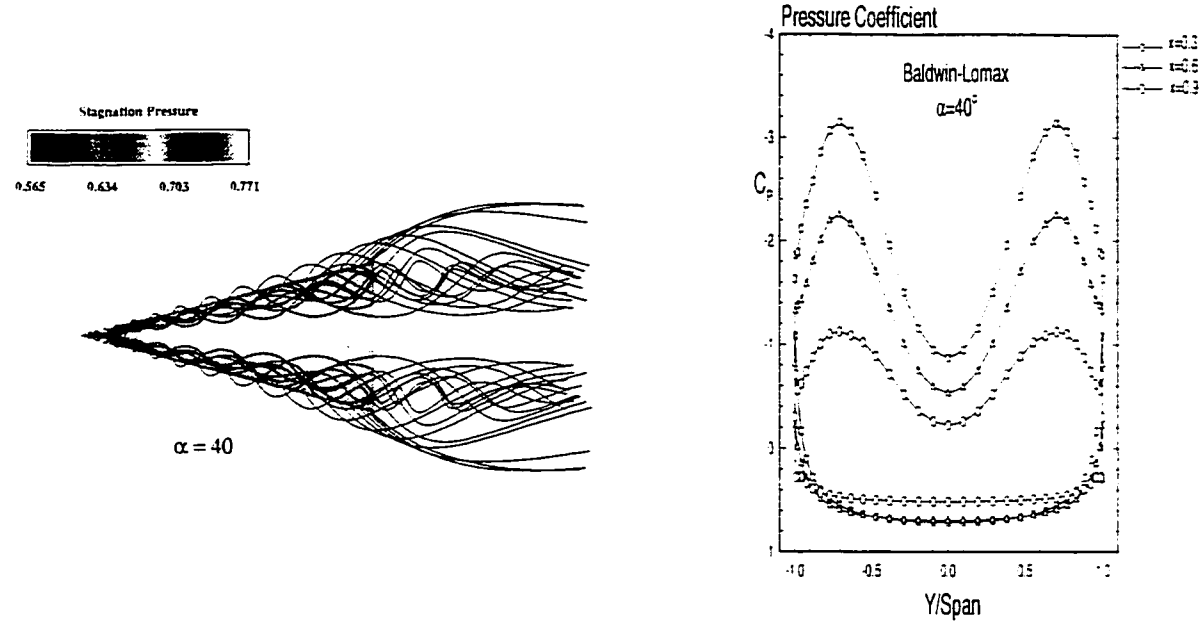

Figure 6.9: Particle traces over the delta wing and spanwise pressure coefficient distributions at $\alpha = 40^{\circ}$

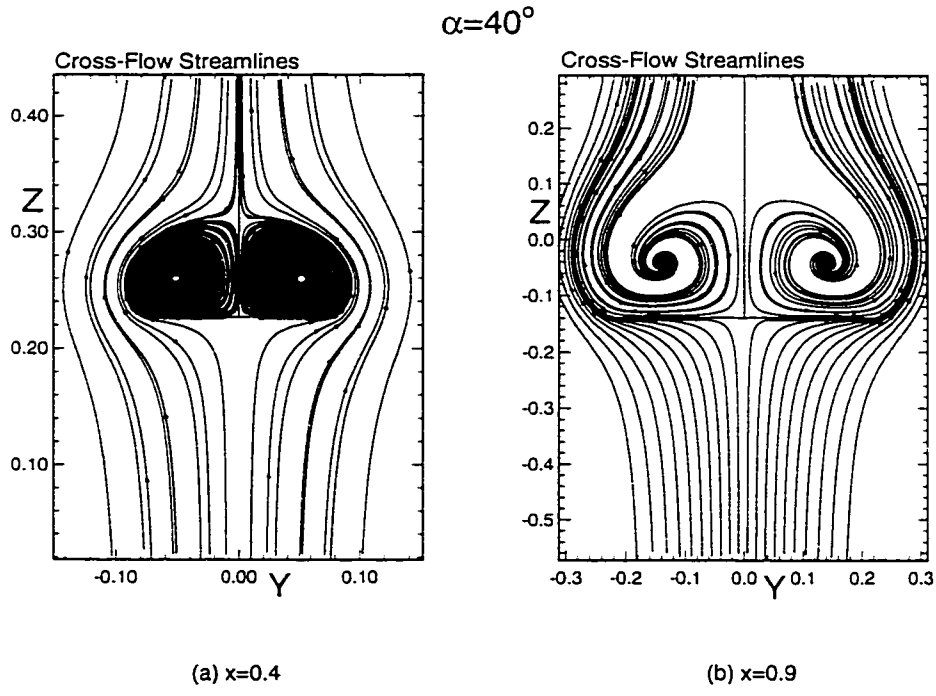

Figure 6.10: Cross-flow instantaneous streamlines at $\alpha = 40^{\circ}$ (a) x=0.4 and (b) x=0.9

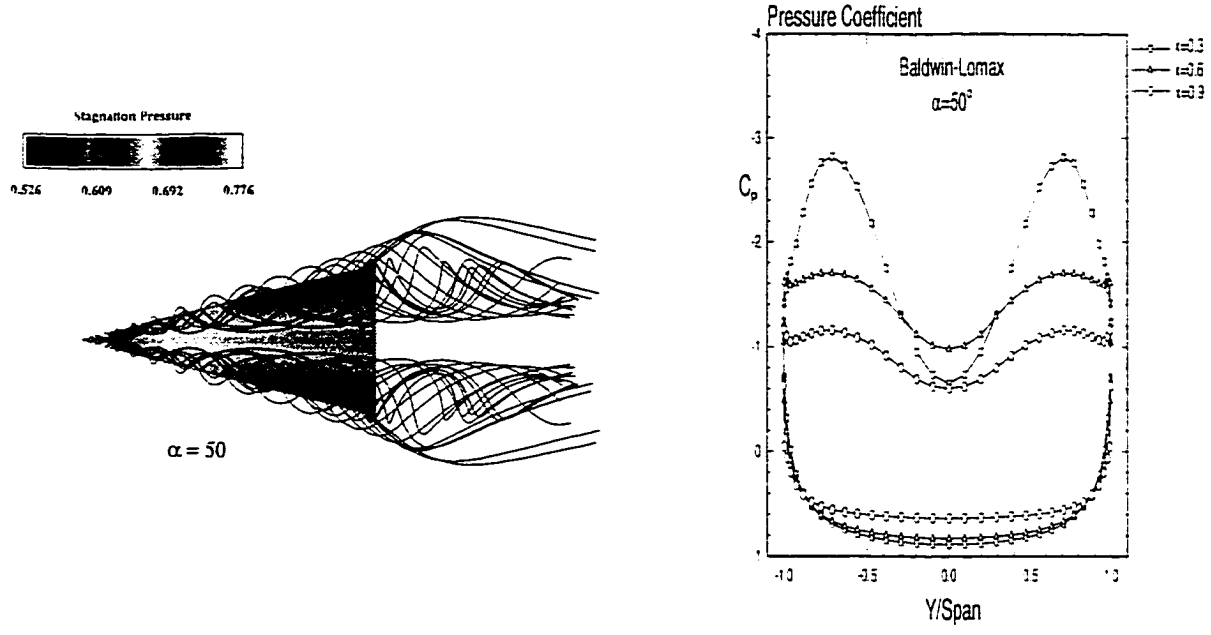

Figure 6.11: Particle traces over the delta wing and spanwise pressure coefficient distributions at $\alpha = 50°$

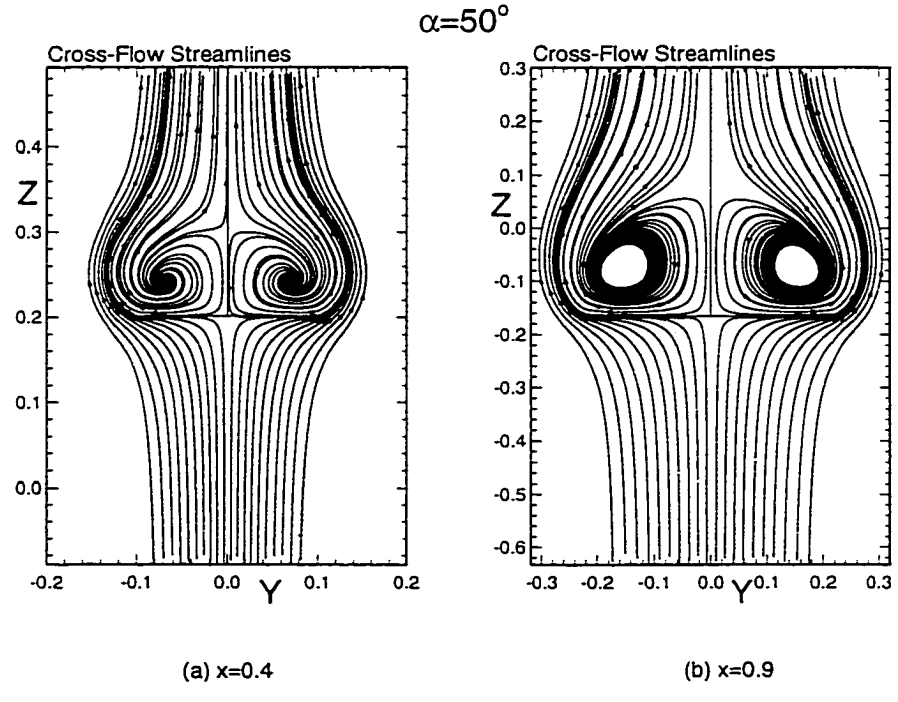

Figure 6.12: Cross-flow instantaneous streamlines at $\alpha = 50°$ (a) x=0.4 and (b) x=0.9

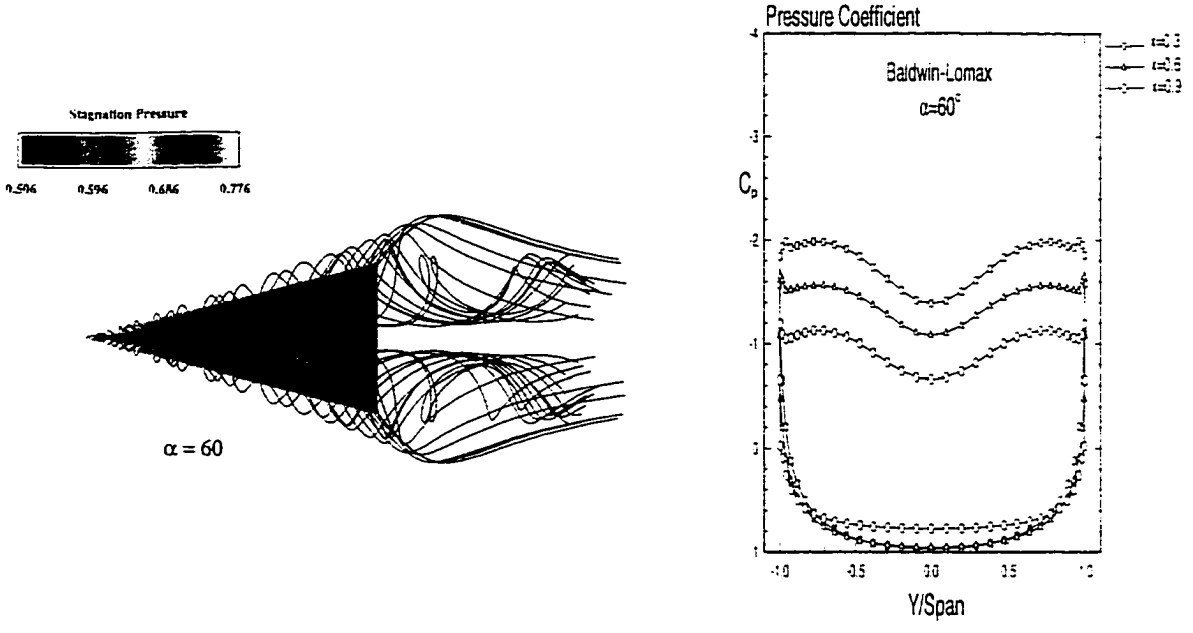

Figure 6.13: Particle traces over the delta wing and spanwise pressure coefficient distr ibutions at $\alpha = 60°$

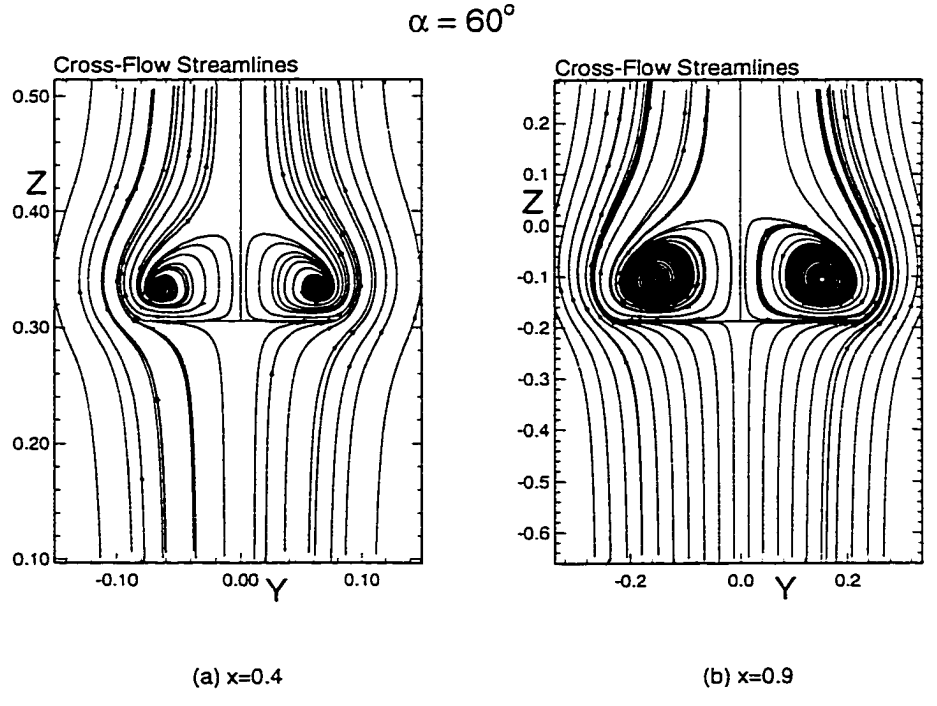

Figure 6.14: Cross-flow instantaneous streamlines at $\alpha = 60°$ (a) x=0.4 and (b) x=0.9

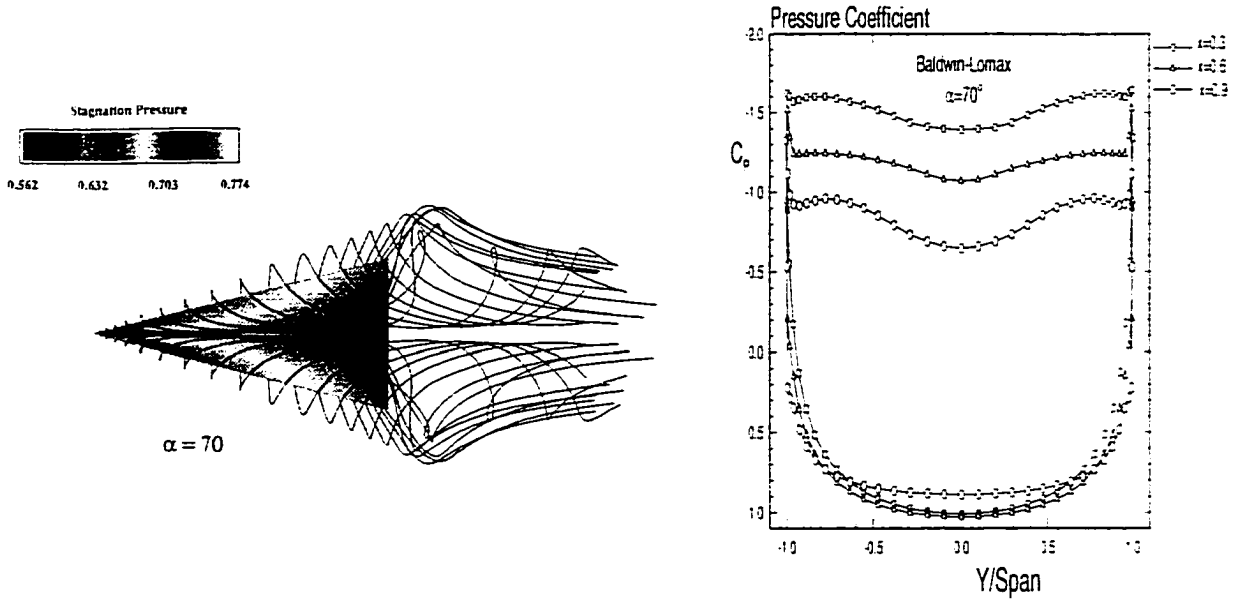

Figure 6.15: Particle traces over the delta wing and spanwise pressure coefficient distributions at $\alpha = 70°$

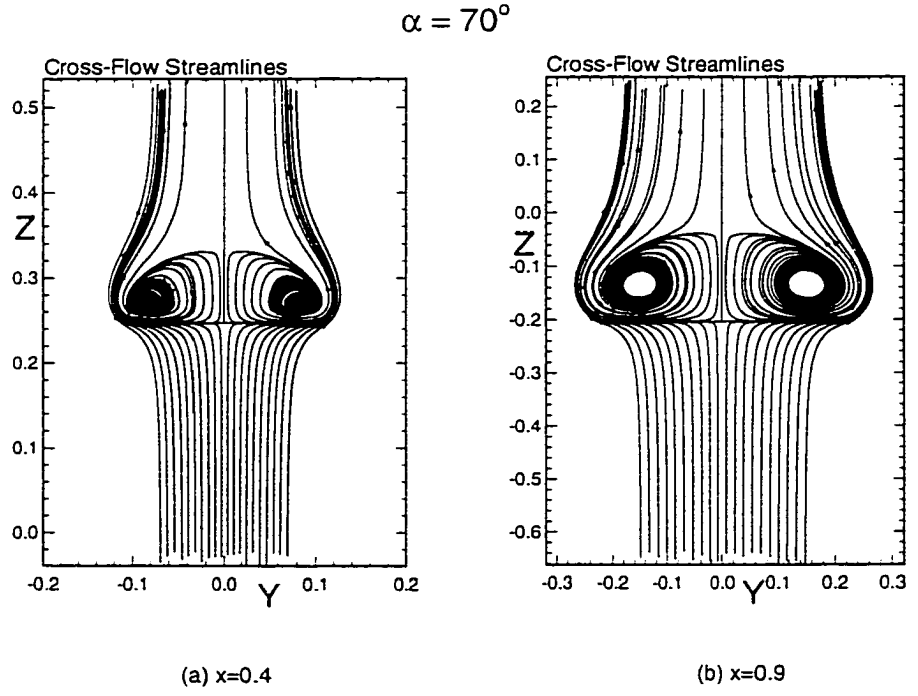

Figure 6.16: Cross-flow instantaneous streamlines at $\alpha = 70°$ (a) x=0.4 and (b) x=0.9

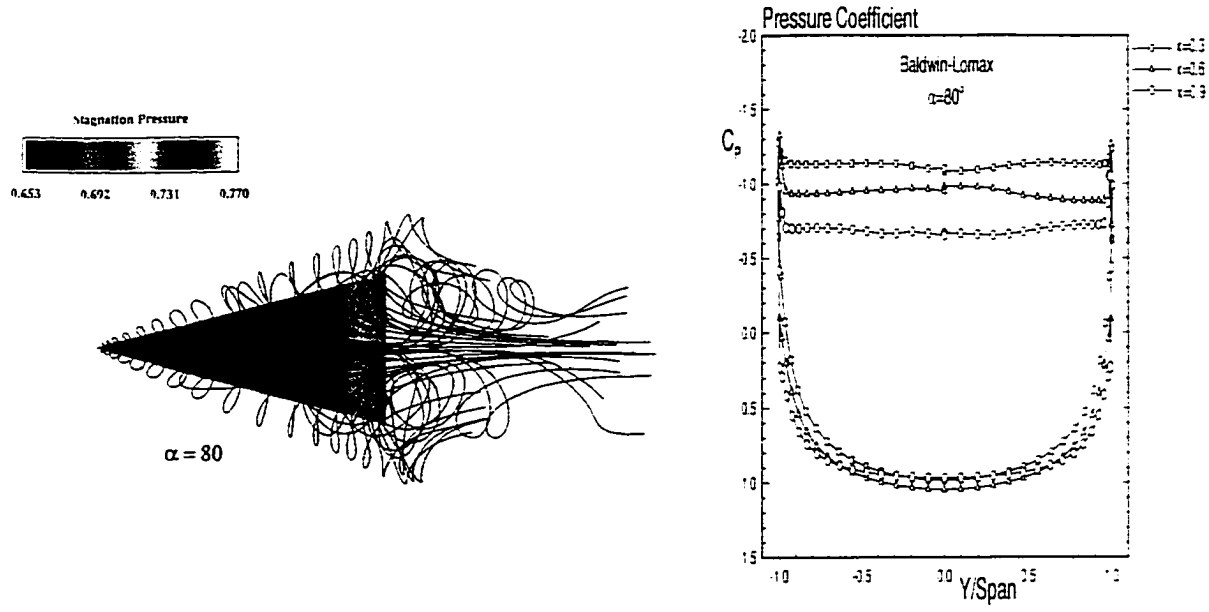

Figure 6.17: Particle traces over the delta wing and spanwise pressure coefficient distributions at $\alpha = 80^{o}$

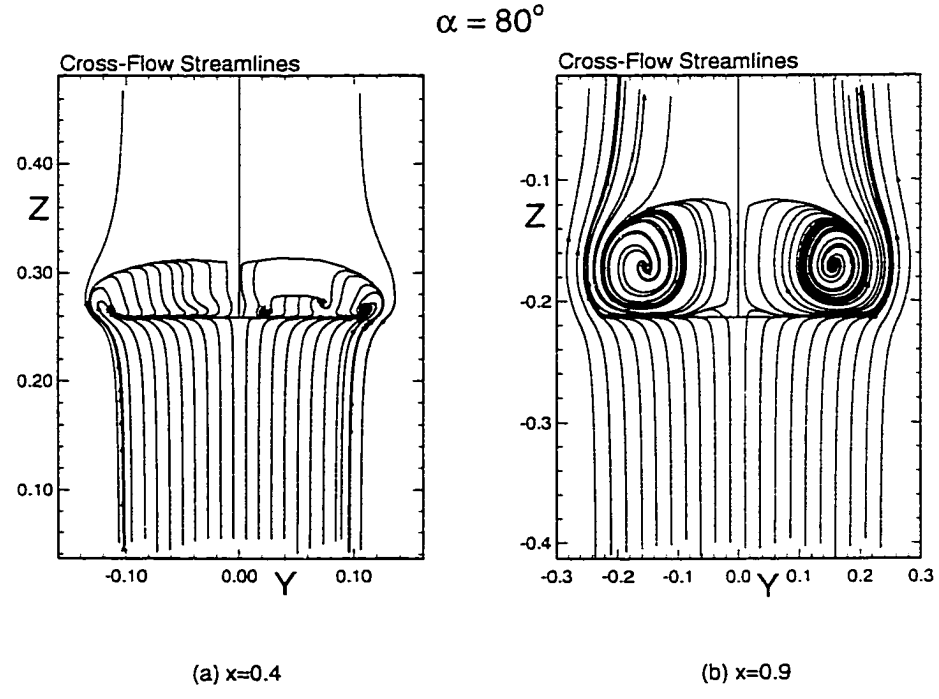

Figure 6.18: Cross-flow instantaneous streamlines at $\alpha = 80^{o}$ (a) x=0.4 and (b) x=0.9

Upper Surface

Lower Surface

Figure 6.19: Particle traces over delta wing at $\alpha = 70^{\circ}$

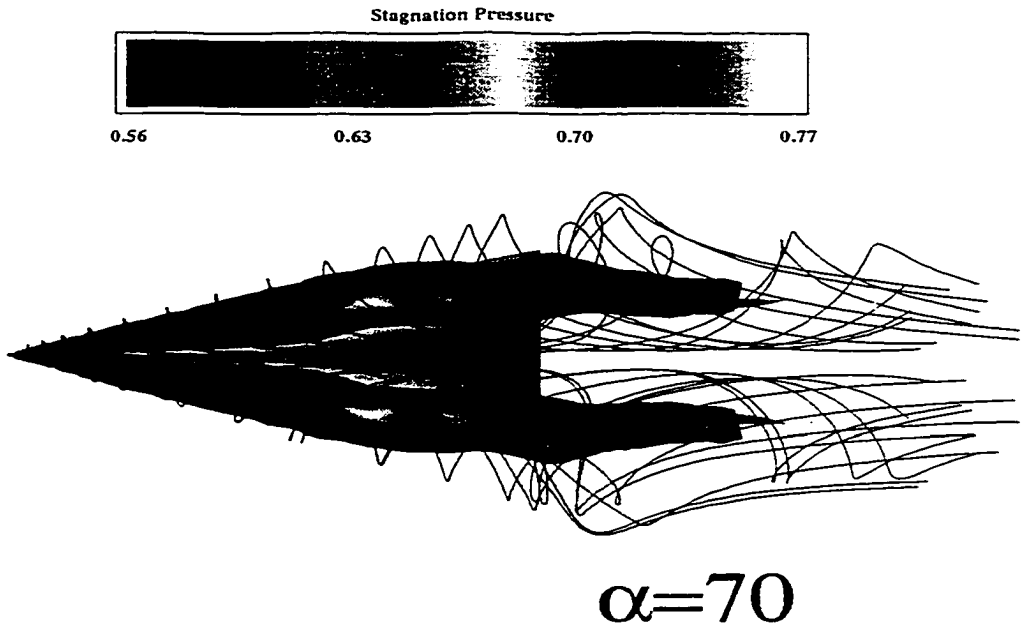

Top View

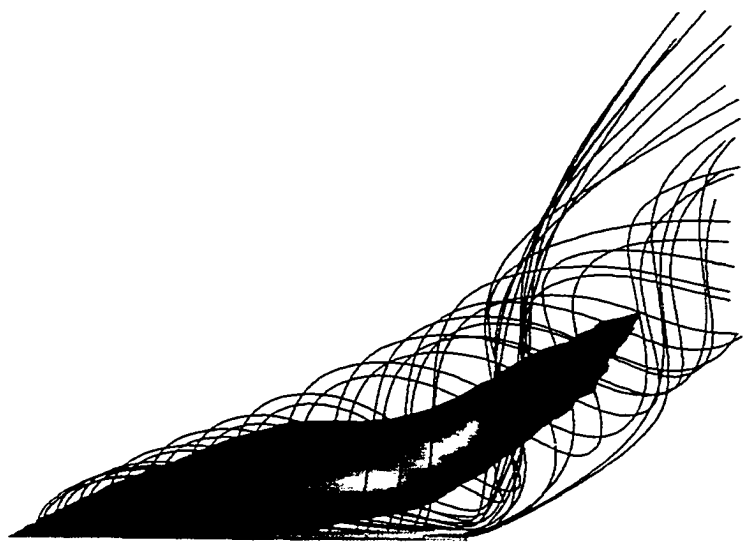

Side View

Figure 6.20: Stagnation pressure and Particle traces over the delta wing at $\alpha = 70°$ from different view angles using Reynolds Averaged NS-equations

6.2 Results Using Spalart-Allmaras Model

The delta wing model used in the current case consists of a 76° swept back, sharp-edged wing with zero thickness and an aspect ratio of one. The three-dimensional grid topology used in the calculations along with a cross section at the trailing edge is shown in Figure 5.1. The grid dimensions are 81 x 65 x 41 in the axial, wrap-around, and normal directions; respectively. The pitch axis is located at two thirds of the root chord station. The wing is forced to undergo a pitching motion through a ramp function shown in Figure 5.2 and is described by $\alpha = 0.024$ t, which is related to the reduced frequency. The reduced frequency is equivalent to 0.04. The freestream Mach number and Reynolds number are 0.3 and 0.45×10^6, respectively. The Reynolds-Averaged NS equations are integrated time accurately with $\Delta t = 0.001$. This case took 65,450 time steps to complete a ramp motion flow response up to $\alpha = 90°$. In this case study, we have used the Reynolds-averaged NS equation with the standard Spalart-Allmaras turbulence model to study the turbulent effects on the solution. The turbulent quantities are applied in only one direction (the normal direction).

Figures 6.21 and 6.22 show variations of the lift and drag coefficients with α. There is an excellent agreement between the computed C_L and C_D and the corresponding experimental data of Jarrah (1988) until $\alpha = 35°$. For angles of attack greater than 35° and less than 60°, C_L and C_D show a significant difference between current results and experimental data. For angles of attack greater than 60°, the difference between the computed C_L and C_D and the experimental value starts to diverge.

Figure 6.23 shows the particle traces of the leading edge vortices over the delta wing and the Mach number contours at $\alpha = 32°$. The vortex core is tight and travels smoothly from the apex to the trailing edge of the wing. The vortex flow is developing over the wing surface and the flow is symmetric. The flow is accelerated around the vortex core region. Small-scale spiral motion is present in the flow.

Figure 6.24 shows the spanwise pressure coefficient distribution for $\alpha = 40°$ for the three cases of laminar, Baldwin-Lomax, and Spalart-Allmaras. The turbulence model is adjusting the flow and removes the secondary suction peaks as expected, since the turbulent boundary layer is thicker than the laminar boundary layer, see Hummel (1973). Although there are two suction peaks on each side of the wing in the laminar solution, there is only one suction peak (corresponding to the primary vortex) in all turbulent cases. The Spalart-Allmaras solution gives slightly higher suction peaks values than the laminar and Baldwin-Lomax solutions. Although the primary vortex suction peak for the laminar solution is equal to –3.0, the suction peaks for Baldwin-Lomax and Spalart-Allmaras models are equal to –3.2 and –3.4; respectively.

Figure 6.25 shows the particle traces over the delta wing and the Mach number contours at $\alpha = 40°$. The vortex core is tight and travels smoothly from the apex until the vortex breakdown region, where the particle traces start to move in a strong spiral motion. The flow is decelerated behind the breakdown region and slightly asymmetric. The high Mach number regions are concentrated in the vortex core up front the breakdown region. Both small-scale and large-scale spiral motions are present in the flow. The small ones are present in front of the breakdown whereas the large ones are present behind the breakdown region.

Figure 6.26 shows the spanwise pressure coefficient distribution comparison among the laminar, Baldwin-Lomax, and Spalart-Allmaras cases for $\alpha = 52°$. The vortex breakdown has reached the x = 0.6 chord station and the pressure peak is attenuated at and behind this location. Again, two suction peaks are noticed in the laminar solution and only one peak in the Baldwin-Lomax and Spalart-Allmaras turbulent solutions at x = 0.3. The Spalart-Allmaras turbulent solution shows breakdown up to x = 0.3 and flow asymmetry. Figure 6.27 shows the streamlines over the delta wing and the Mach number contours at $\alpha = 52°$. The flow is highly asymmetric and large-scale spiral motion exists over large portion of the wing surface. Figure 6.28 shows the spanwise pressure coefficient distribution comparison among the laminar, Baldwin-Lomax, and Spalart-Allmaras cases for $\alpha = 60°$. The vortex breakdown has reached x = 0.3 station and the pressure peaks have disappeared.

Figures 6.29 shows the axial velocity contour comparison among the three cases; laminar, Baldwin-Lomax, and Spalart-Allmaras, for $\alpha = 40°$ at two axial stations of x = 0.3 and 0.9. Although the axial velocity value inside the right vortex core at x = 0.9 in the laminar solution has a value of 0.44 the corresponding value using Baldwin-Lomax model is 0.07 and Spalart-Allmaras model is 0.03; the turbulent quantities decelerate the flow inside the vortex core faster. Also the vortex core is more concentrated for turbulent cases. The flow is symmetric for all cases.

Figure 6.30 shows the axial velocity contours comparison among the three cases; laminar, Baldwin-Lomax, and Spalart-Allmaras, for $\alpha = 60°$ at two axial stations of x = 0.3 and 0.9. Both axial chord stations for all cases have passed through vortex breakdown. The largest axial velocity value inside the vortex core for laminar, Baldwin-Lomax, and Spalart-Allmaras at x = 0.9 is - 0.12, - 0.09, and - 0.13; respectively.

The standard Spalart-Allmaras model failed in modeling this type of flow at very large angles of attack (> 60°) with the current grid resolution. The model should be tailored to suit these kind of large separated flows or the turbulent quantities should be applied in all three directions to take into considerations the boundary layer effects in the wrap-around and axial directions. This big difference at very high angles of attack may also be attributed to the grid resolution at the trailing edge where the vortex breakdown crosses and moves over the wing surface. The Spalart-Allmaras model needs a finer grid than the Baldwin-Lomax model. Utilization of the Baldwin-Lomax turbulence model gives better results than Spalart-Allmaras model for this specific case and flow condition.

The differences between this case and the Baldwin-Lomax solution are appreciable. In general, Baldwin-Lomax model introduced some improvements of the computational results regarding C_D-α curve in comparison with the experimental data up to an angle of attack of about 65°. Moreover, a higher order turbulence model may improve the predictions at very large angles of attack. A requirement for fine grid resolution is suspected for the Spalart-Allmaras model.

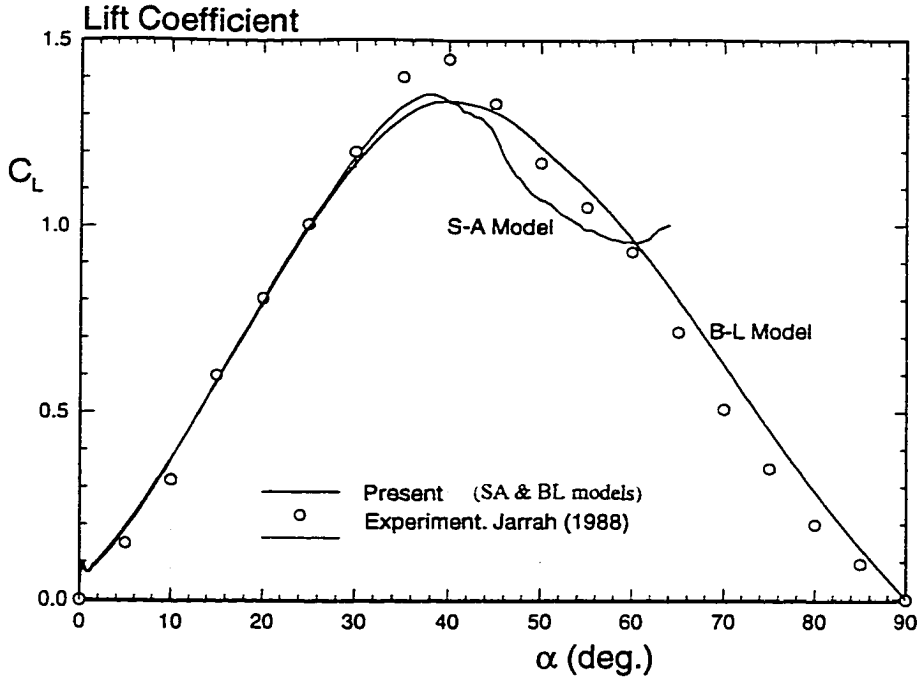

Figure 6.21: Lift coefficient vs. α using Spalart-Allmaras model

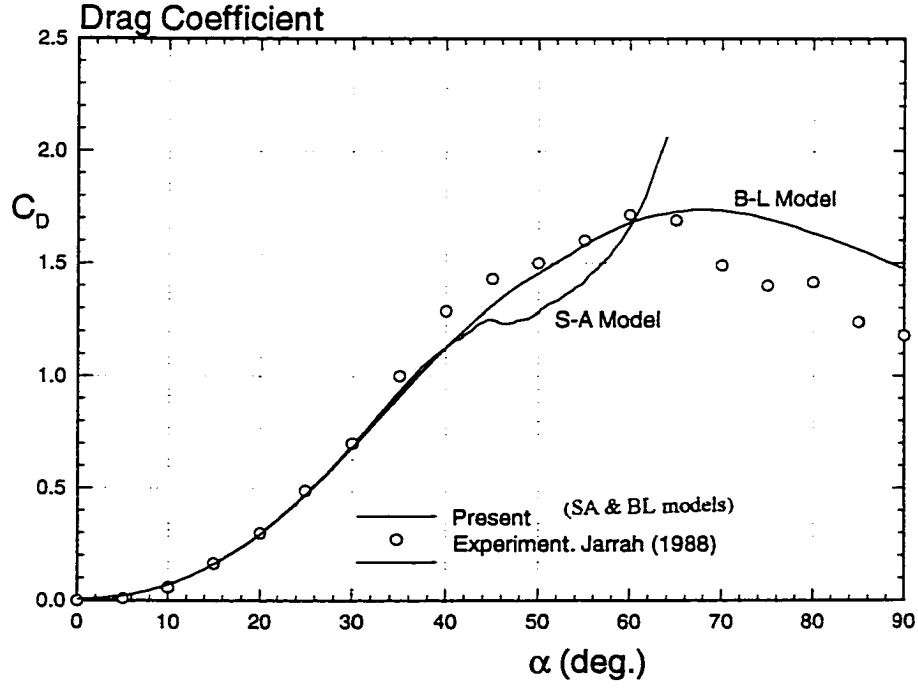

Figure 6.22: Drag coefficient vs. α using Spalart-Allmaras model

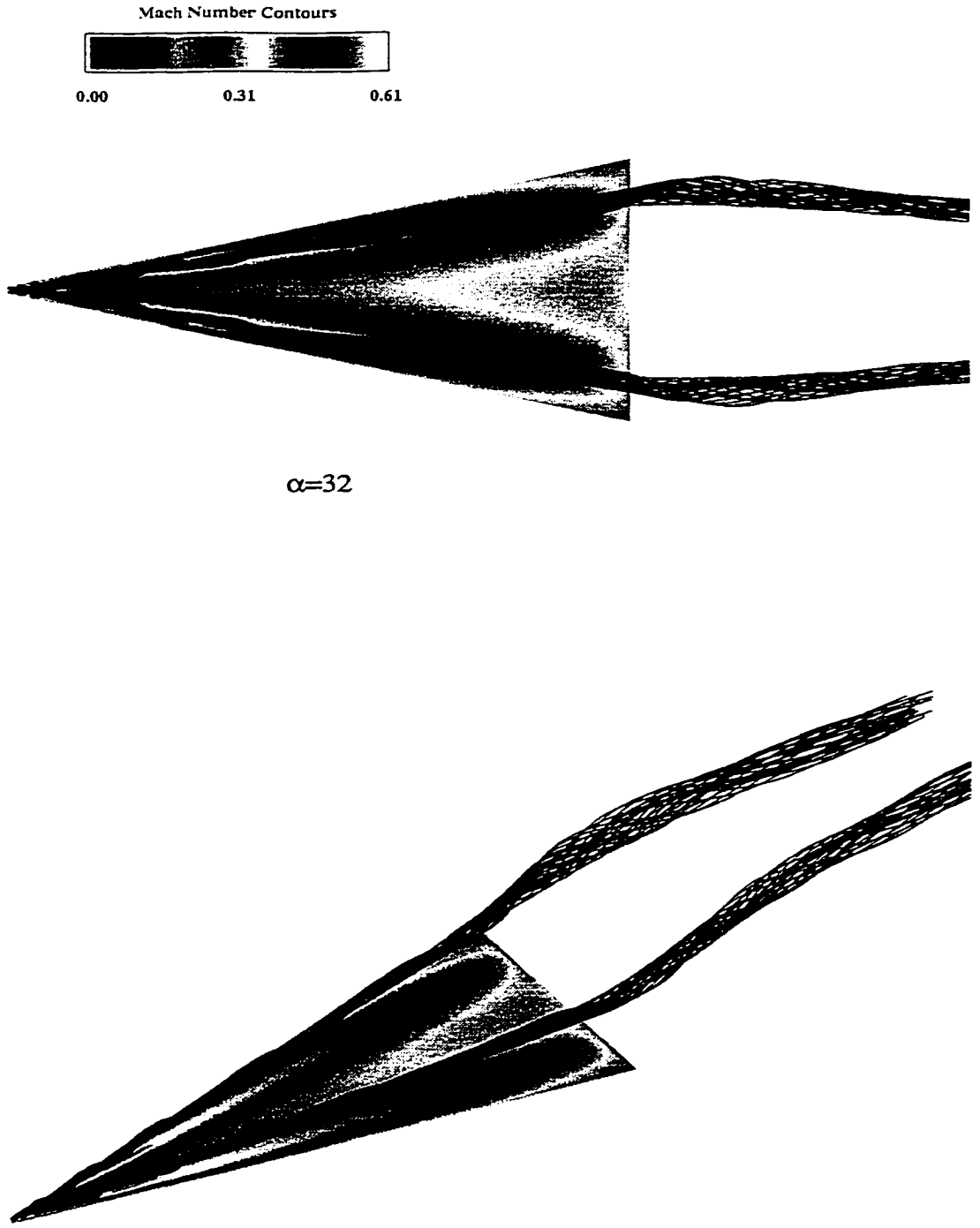

Figure 6.23: Mach number contours and particle traces over the delta wing at $\alpha = 32^{o}$ using Spalart-Allmaras model

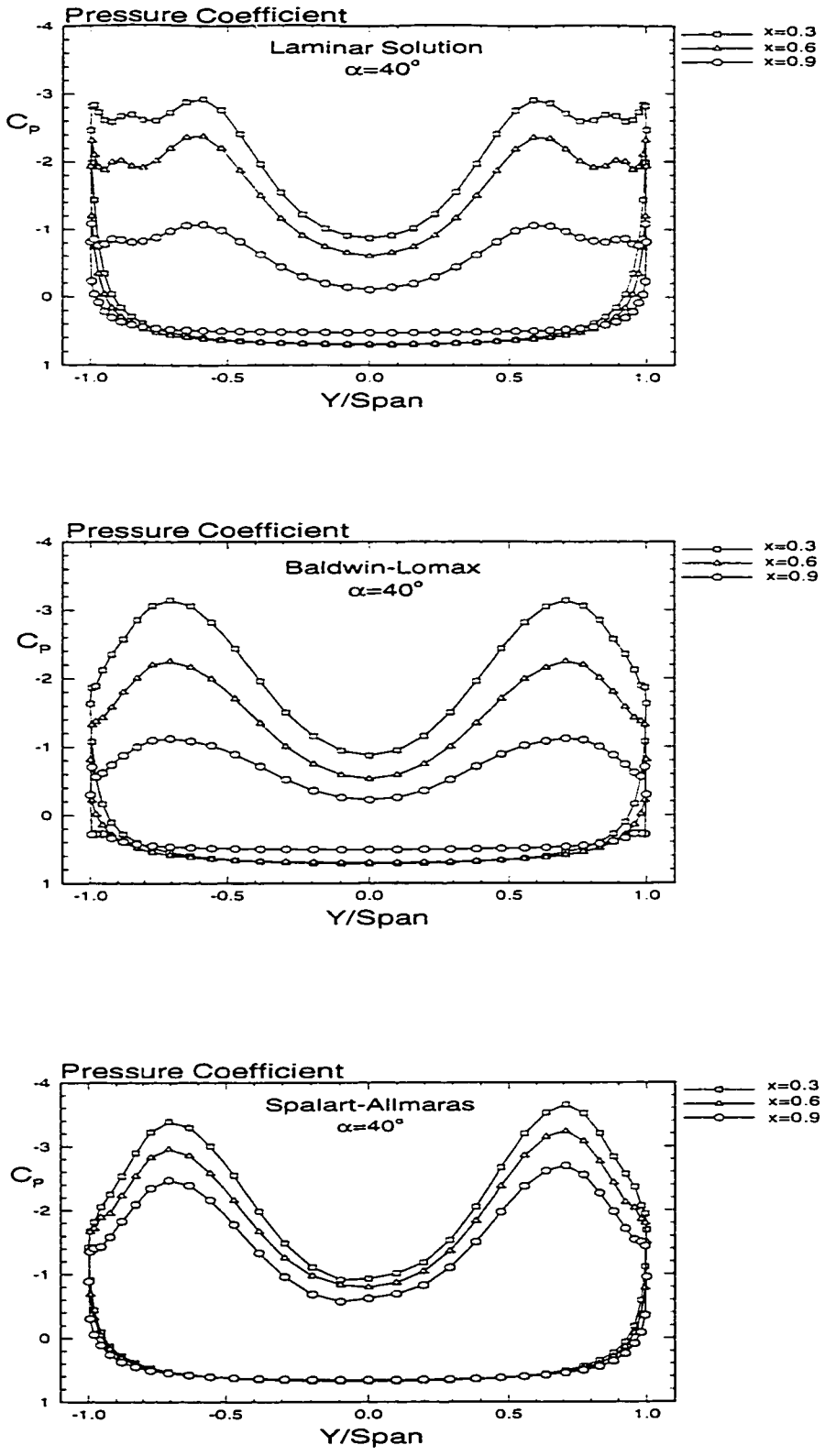

Figure 6.24: Spanwise pressure coefficient distribution for $\alpha = 40^{o}$

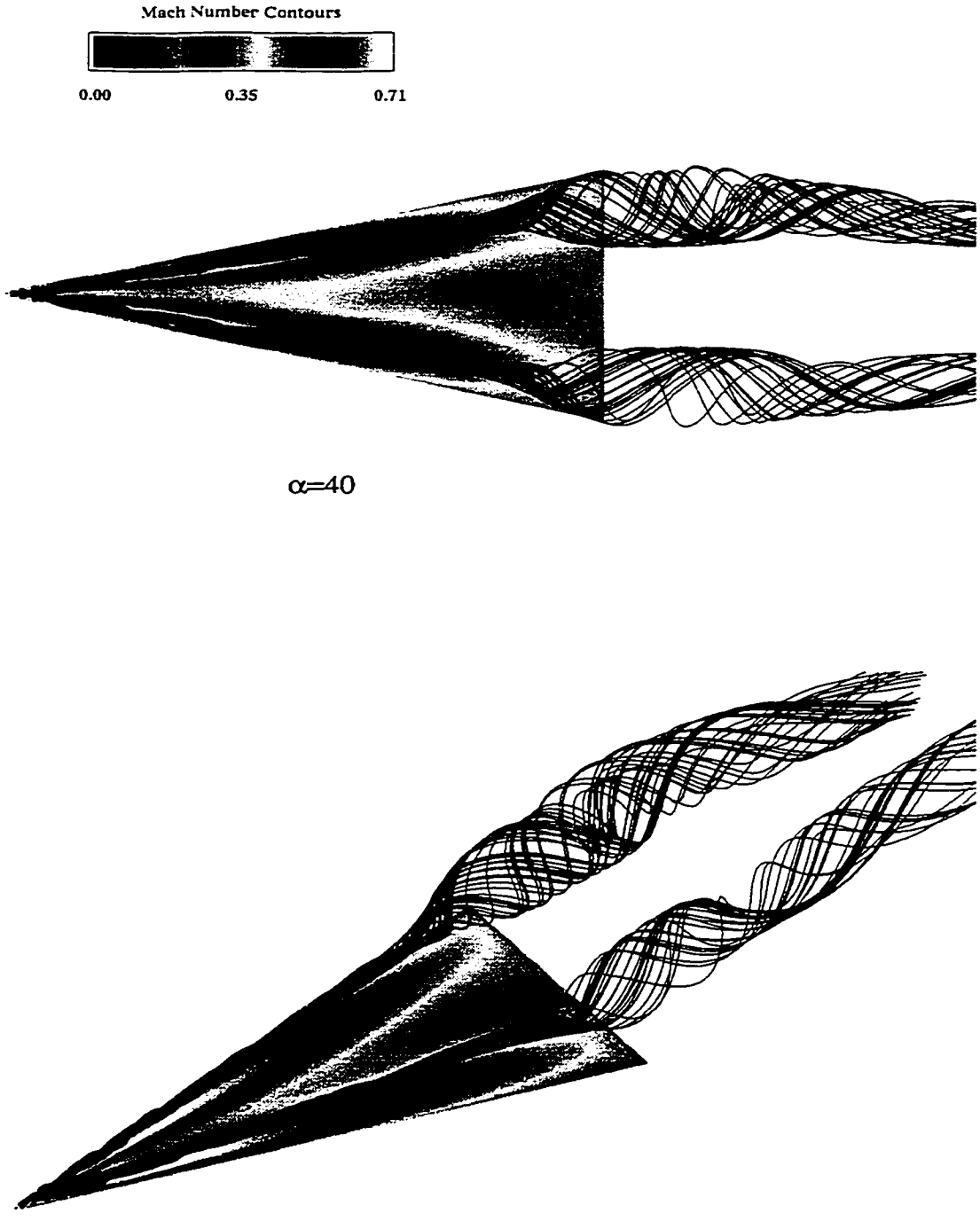

Figure 6.25: Mach number contours and particle traces over the delta wing at $\alpha = 40^o$ using Spalart-Allmaras model

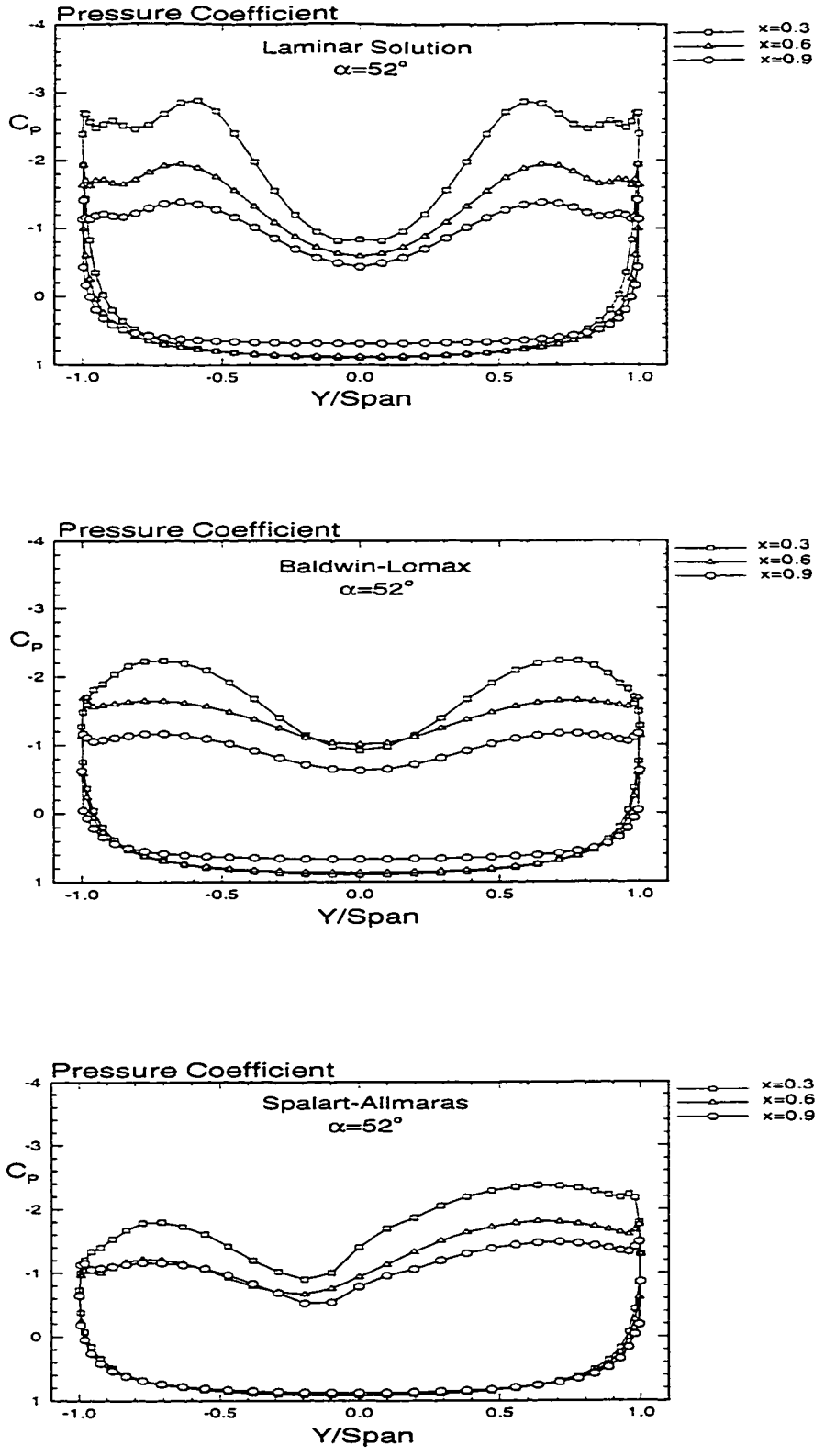

Figure 6.26: Spanwise pressure coefficient distribution for $\alpha = 52^o$

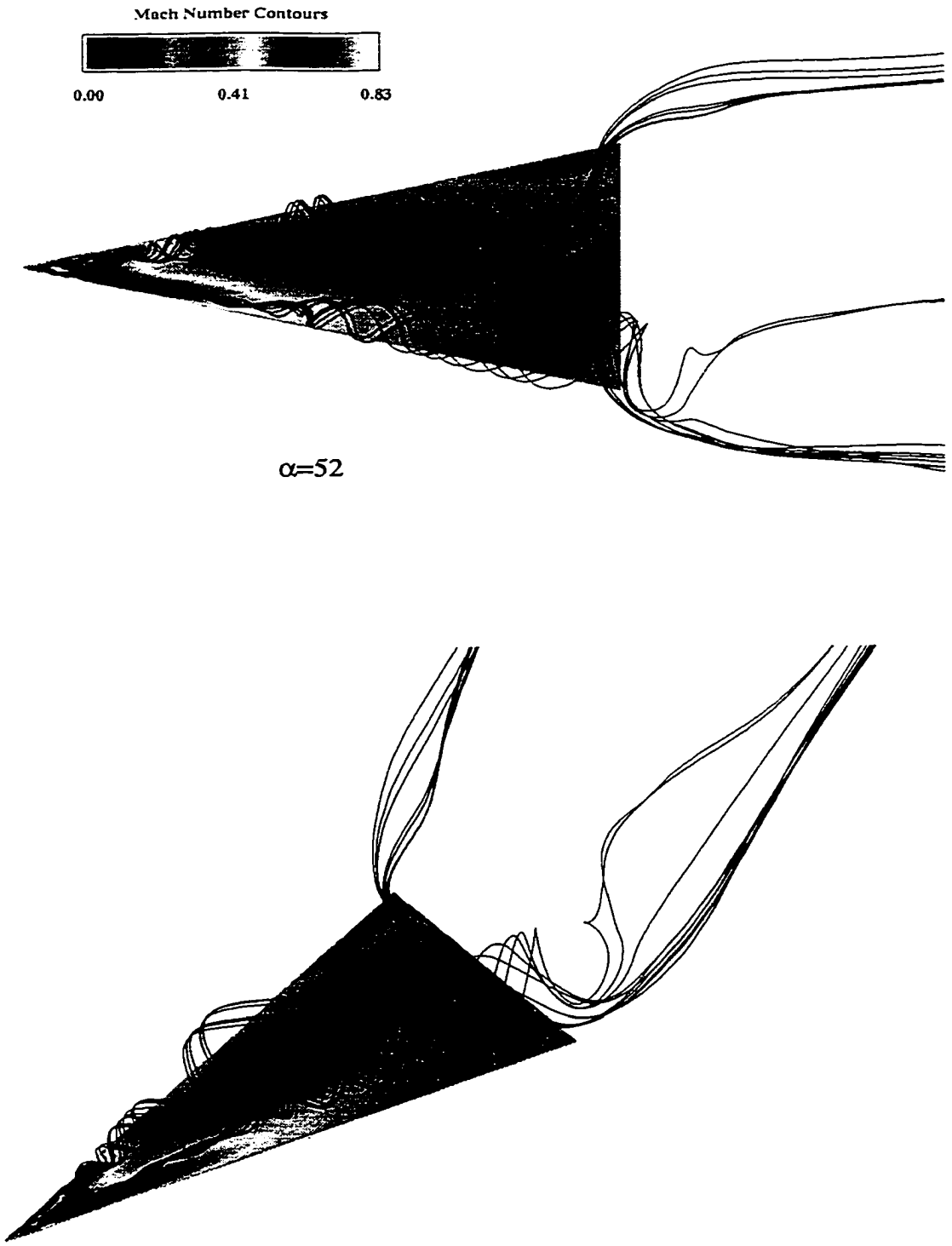

Figure 6.27: Mach number contours and particle traces over the delta wing at $\alpha = 52°$ using Spalart-Allmaras model

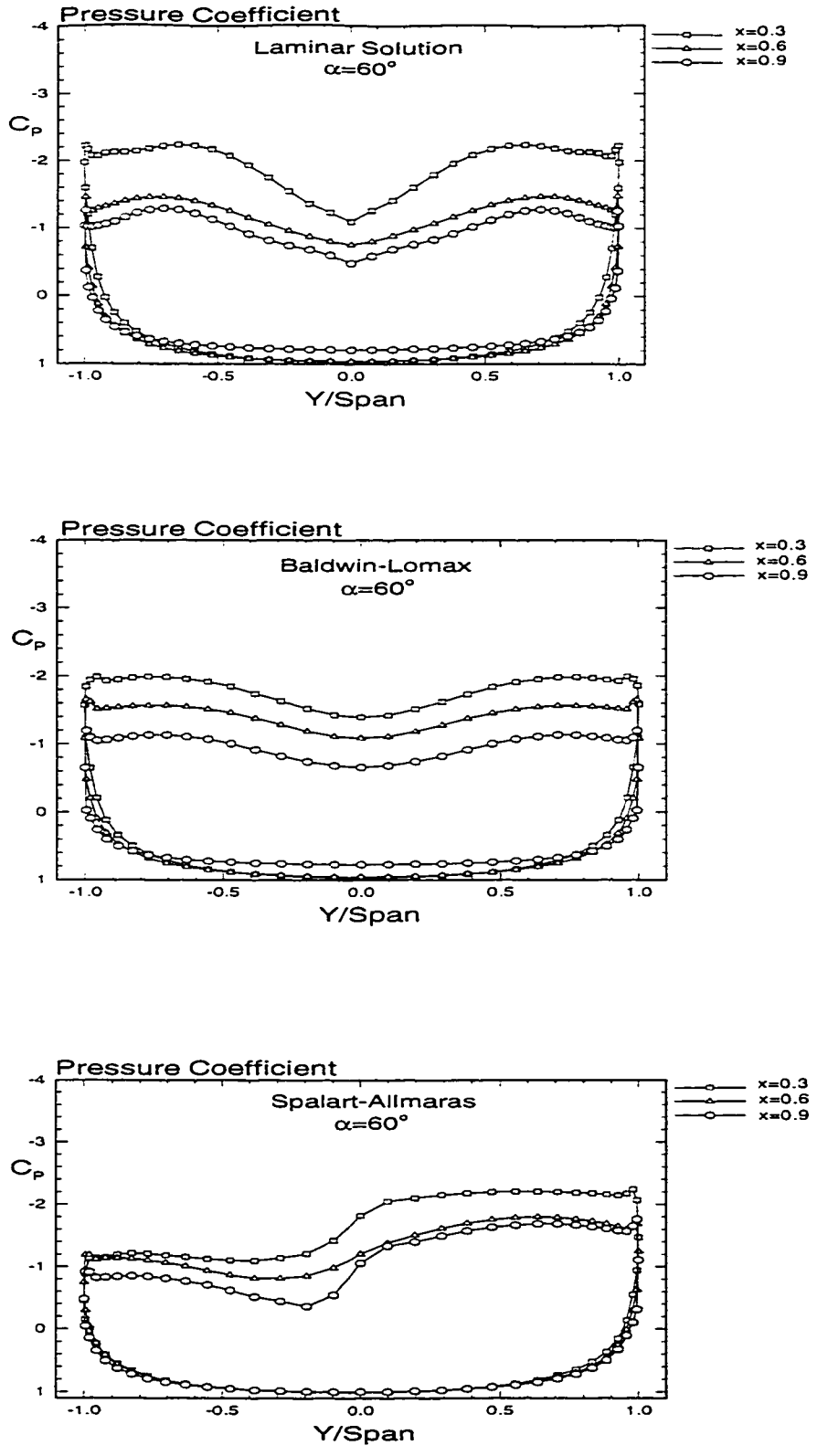

Figure 6.28: Spanwise pressure coefficient distribution for $\alpha = 60°$

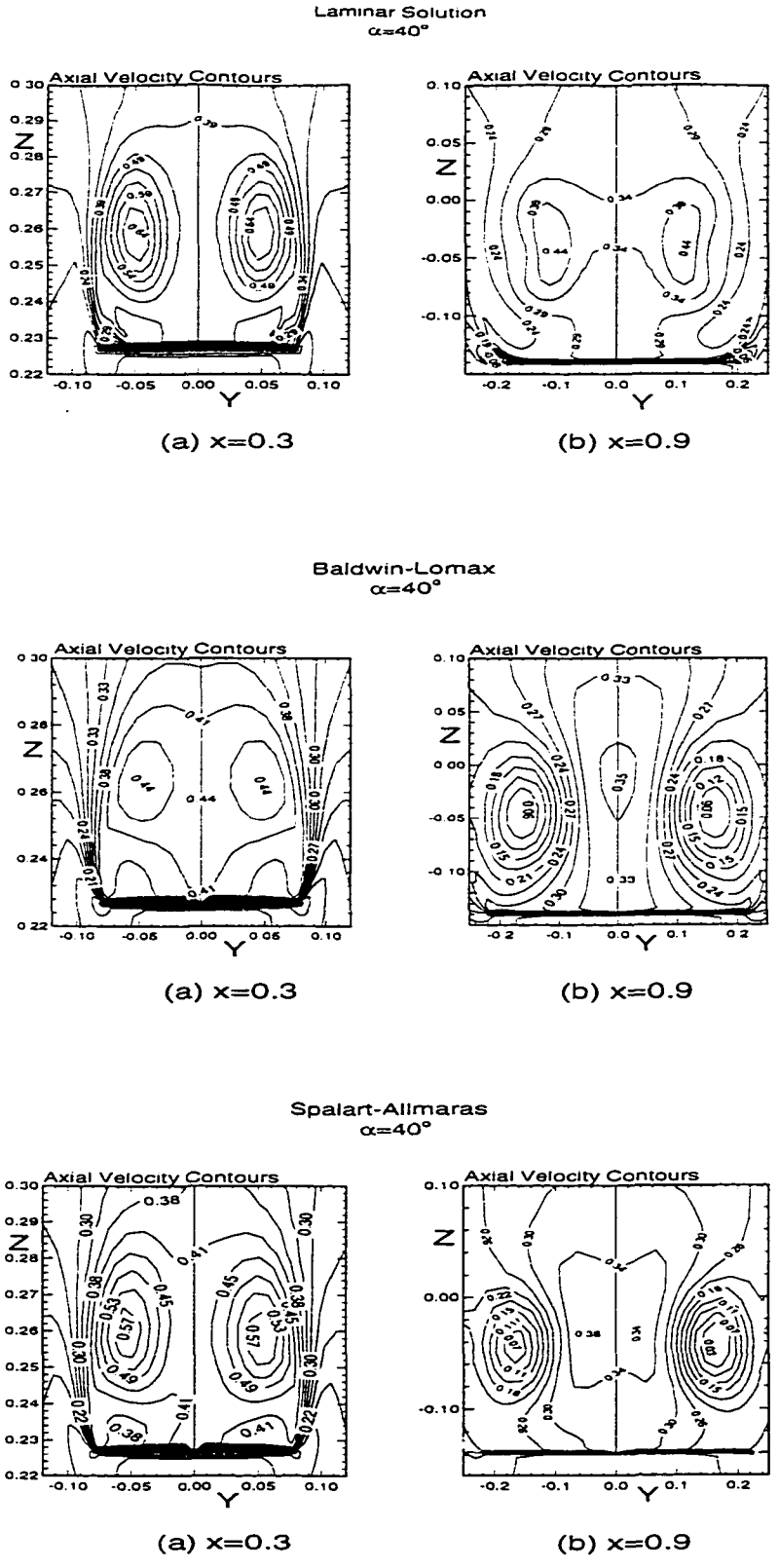

Figure 6.29: Axial velocity contours for $\alpha = 40°$

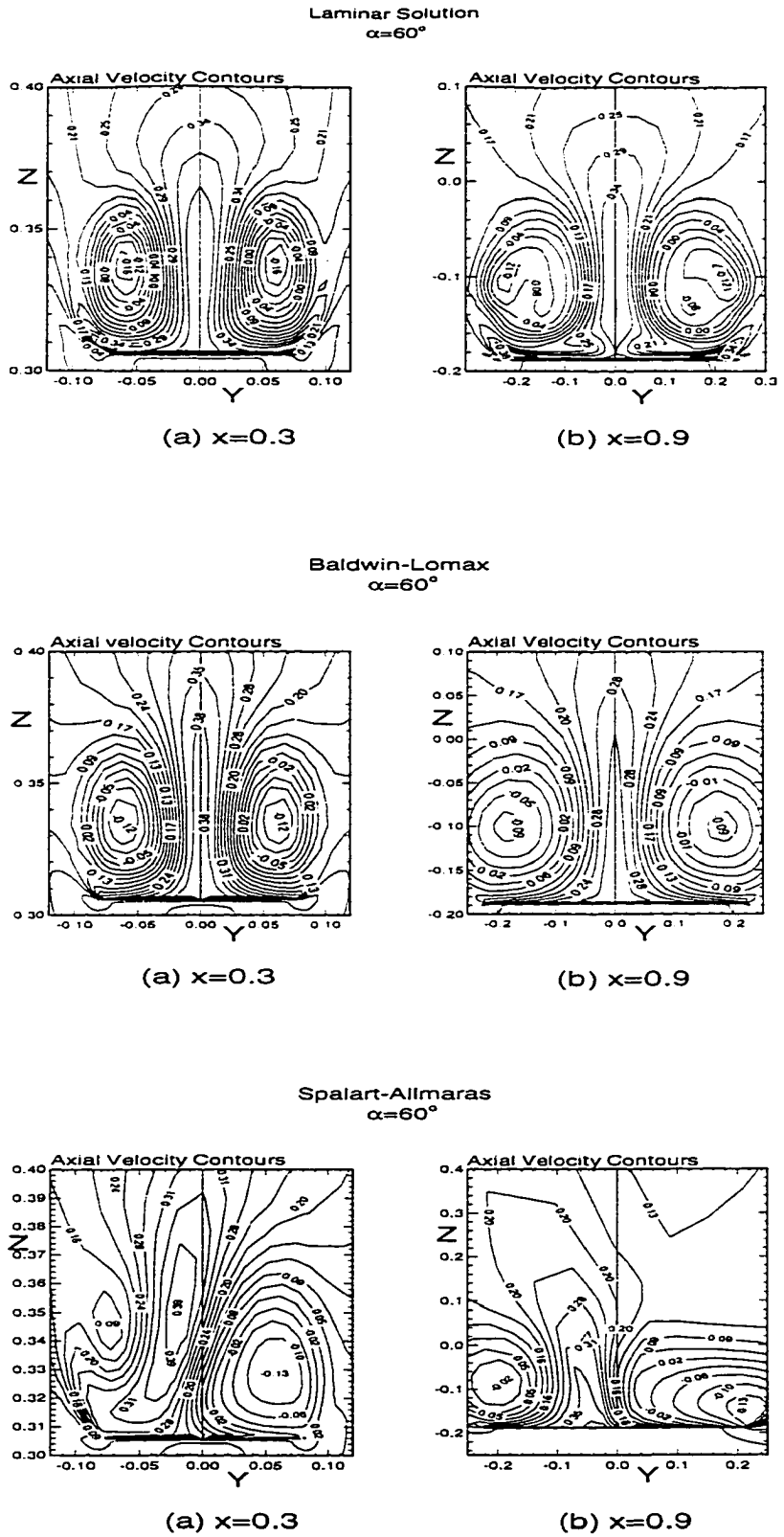

Figure 6.30: Axial velocity contours for $\alpha = 60°$

6.3 Pitch-Up Pitch-Down Case

The delta wing model used in the present computational study consists of a 63.5° swept back, sharp-edged wing with zero thickness and aspect ratio of two. The three-dimensional grid topology used in the calculations is an O-H grid of 84 x 65 x 43 in the axial, wrap-around, and outward directions, respectively, similar to that of Figure 5.1. The pitch axis is located at two thirds of the root chord station, as measured from the wing vertex.

The wing is forced to undergo a pitch-up pitch-down motion through a sinusoidal function shown in Figure 6.31, which is related to the reduced frequency. The freestream Mach number and Reynolds number are 0.3 and 0.45 x 10^6, respectively. The unsteady, RANS Equations are integrated time accurately with $\Delta t = 0.002$. The reduced frequency ($\Omega C/a_\infty$) is equal to 0.058. The Baldwin-Lomax turbulence model was used to account for the turbulent quantities. The total numbers of time steps, which are needed to complete one cycle (0° to 90° to 0°) are 205,800 time steps. Each iteration took 2.2 seconds of running time based on a CRAY-90 at NASA Ames Research Center.

Figure 6.32 shows the variations of C_L with α of the present computational results and the corresponding values of the experimental data of Jarrah (1988). Both results are in good agreement except around α near 20° to 50° in the upstroke and from 40° to 25° in the downstroke. The computed results under-estimate the experimental data in the upstroke motion and over-estimate the experimental data in the downstroke motion. This difference is attributed to the massive flow separation at very high angles of attack after the onset of the vortex breakdown. Another source might be the coarse grid used to

capture the massive flow separation and the vortex breakdown regions. Also, the uncertainty in measuring the normal force coefficient in the experimental data is around 7.5%.

Figure 6.33 shows the variations of C_D with α. A good agreement between the computed C_D values of the present study and those of the experimental data of Jarrah (1988) is observed except around α near 40° to 65° in the upstroke and from 45° to 30° in the downstroke. The computed results under-estimate the experimental data in the upstroke motion and overestimate the experimental data in the downstroke motion. Again this is attributed to the coarse grid resolution used in the vortex breakdown region. The difference between the upstroke and downstroke motion is because of the hysteresis effects of the unsteady flow. The vortex breakdown starts at the trailing edge around 30°, which is below the corresponding value from the previous cases.

Figures 6.34 and 6.35 show comparisons between particle traces at the leading edge vortices over the wing surface and spanwise pressure coefficient distributions for pitch-up at $\alpha = 25°$ and the corresponding graph for the pitch-down motion at the same angle of attack. Although the flow is relatively smooth over a large portion of the wing surface for the pitch-up motion the flow is highly turbulent in the pitch-down motion. Also in the pitch-down motion there are nearly no suction peaks. This difference can be attributed to the hysteresis effects of the unsteady motion. In the pitch-down period, while the wing is moving, the flow has a short period of time to adjust with the wing motion. In other words, the flow response is lagging behind the wing motion.

Figures 6.36 and 6.37 show cross-flow instantaneous streamlines at $\alpha = 25°$ and for three chord stations of $x = 0.3$, 0.6, and 0.9 for both pitch-up and pitch-down motion.

For pitch-up, the vortex breakdown is close to x = 0.9 station and the spiral motion is about to start near this location. Although the flow is symmetric in the pitch-up motion, the asymmetry of the flow can be seen from the pitch-down motion. Figures 6.38 and 6.39 show axial velocity contours at $\alpha = 25°$ and for three chord stations of x = 0.3, 0.6, and 0.9 for both pitch-up and pitch-down motion. While the flow does not yet breakdown at any axial station in the pitch-up motion, the vortex breakdown covers most of the wing surface in the pitch-down motion. Large portions of the flow in the pitch-down motion are reversing direction as can be seen from the negative values of the axial velocity at x = 0.3, 0.6 and 0.9. Figures 6.40 and 6.41 show Mach number contours at $\alpha = 25°$ and for three chord stations of x=0.3, 0.6, and 0.9 for both pitch-up and pitch-down motion. There is flow deceleration in the downstream direction and the vortex core does not yet develop in the pitch-down motion.

Figures 6.42 and 6-43 show comparison between streamlines over the wing surface and spanwise pressure coefficient distributions for pitch-up at $\alpha = 36°$ and the corresponding graph for the pitch-down motion at the same angle of attack. The vortex breakdown location for the pitch-up motion moved to the axial station of 0.6. The two-pressure suction peaks at x = 0.6 and 0.9 are weakened for the pitch-up motion. There is no pressure suction peak for the pitch-down motion. The particle traces show that vortex breakdown exists over a large portion of the wing surface for the pitch-down motion which correlates with the decrease in lift coefficient during the pitch-down motion. Again this difference is attributed to the hysteresis effects of the unsteady motion.

Figures 6.44 and 6.45 show cross-flow instantaneous streamlines at $\alpha = 36°$ and for three chord stations of x = 0.3, 0.6, and 0.9 for both pitch-up and pitch-down motion.

For pitch-up, the vortex breakdown is at x = 0.6 station and the spiral motion is getting stronger at this location. Again, although the flow is symmetric in the pitch-up motion, the asymmetry of the flow can be seen from the pitch-down motion. Figures 6.46 and 6.47 show axial velocity contours at $\alpha = 36°$ and for three chord stations of x = 0.3, 0.6, and 0.9 for both pitch-up and pitch-down motion. The flow starts to reverse direction at x = 0.6 for the pitch-up motion but the flow remains symmetric. Most of the flow in the vortex breakdown regions in the pitch-down motion is reversing direction. Figures 6.48 and 6.49 show Mach number contours at $\alpha = 36°$ and for three chord stations of x = 0.3, 0.6, and 0.9 for both pitch-up and pitch-down motion. The flow starts to decelerate inside the vortex core region in the pitch-up motion while some portions of the flow over the wing surface are nearly stagnant in the pitch-down motion.

Figures 6.50 and 6-51 show comparison between streamlines over the wing surface and spanwise pressure coefficient distributions for pitch-up at $\alpha = 48°$ and the corresponding graph for the pitch-down motion at the same angle of attack. The vortex breakdown reaches x = 0.3 for the pitch-up motion. A large portion of the flow in the pitch-down motion is stagnant. Figures 6.52 and 6.53 show cross-flow instantaneous streamlines at $\alpha = 48°$ and for three chord stations of x = 0.3, 0.6, and 0.9 for both pitch-up and pitch-down motion. The flow is still symmetric in the pitch-up motion and highly asymmetric in the pitch-down motion. Figures 6.54 and 6.55 show axial velocity contours at $\alpha = 48°$ and for three chord stations of x = 0.3, 0.6, and 0.9 for both pitch-up and pitch-down motion. Both pitch-up and pitch-down motions have large negative velocity areas over the wing surface with symmetric flow for the pitch-up motion and asymmetric flow for the pitch-down motion. Figures 6.56 and 6.57 show Mach number

contours at $\alpha = 48°$ and for three chord stations of x = 0.3, 0.6, and 0.9 for both pitch-up and pitch-down motion.

Figures 6.58, 6-59, 6.66, and 6.67 show comparison between particle traces over the wing surface and spanwise pressure coefficient distributions for pitch-up at $\alpha = 60°$ and 72° and the corresponding graph for the pitch-down motion at the same angle of attack. Figures 6.60, 6.61, 6.68, and 6.69 show cross-flow instantaneous streamlines at $\alpha = 60°$ and 72° and for three chord stations of x = 0.3, 0.6, and 0.9 for both pitch-up and pitch-down motion. Figures 6.62, 6.63, 6.70, and 6.71 show axial velocity contours at $\alpha = 60°$ and 72° and for three chord stations of x = 0.3, 0.6, and 0.9 for both pitch-up and pitch-down motion. Both pitch-up and pitch-down motions have large negative velocity areas over the wing surface with symmetric flow for the pitch-up motion and asymmetric flow for the pitch-down motion. Figures 6.64, 6.65, 6.72, and 6.73 show Mach number contours at $\alpha = 48°$ and for three chord stations of x = 0.3, 0.6, and 0.9 for both pitch-up and pitch-down motion. The flow remains symmetric for the pitch-up motion even at higher angles of attack and large vortex-breakdown regions of the flow.

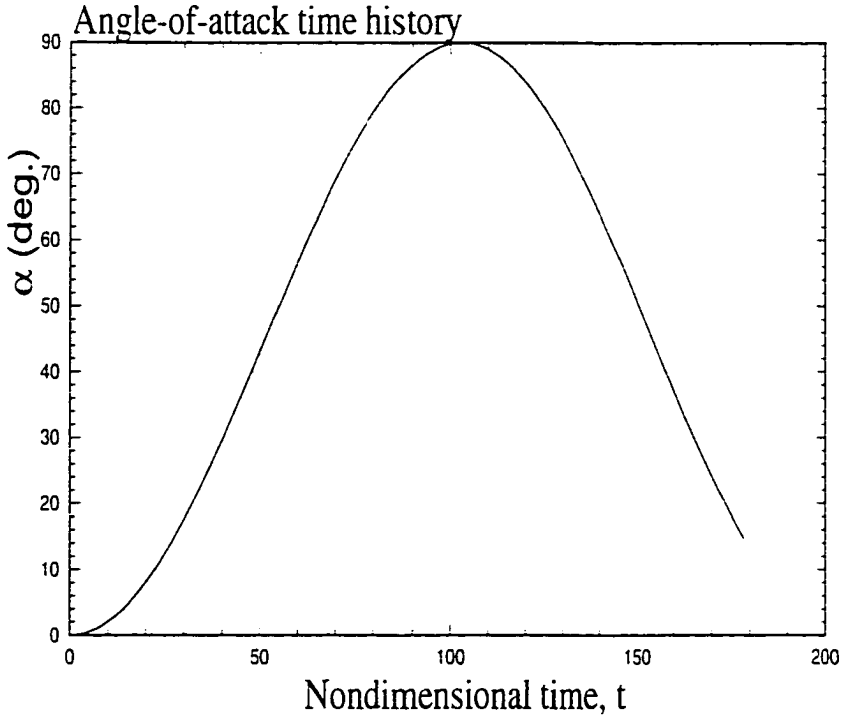

Figure 6.31: Forced Sinusoidal function time history

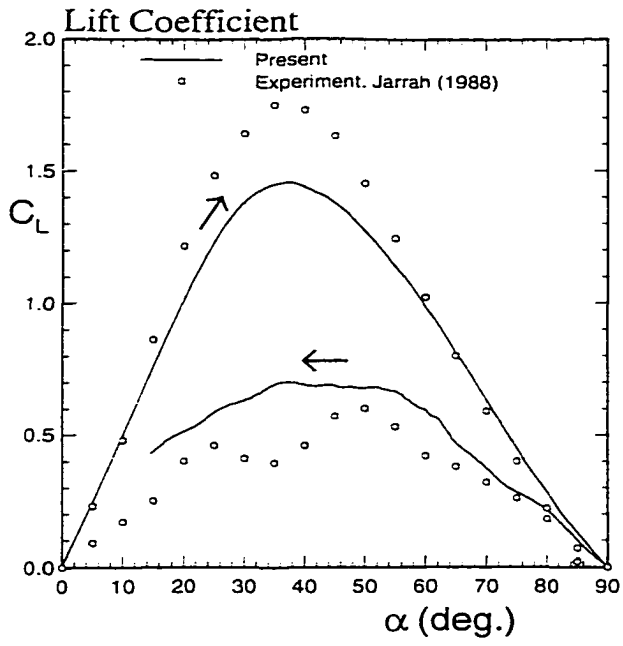

Figure 6.32: Lift coefficient vs. α using Reynolds Averaged NS equations.

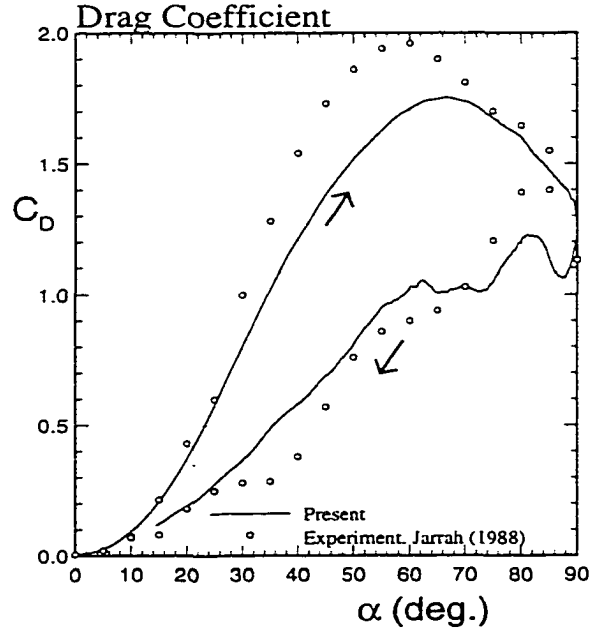

Figure 6.33: Drag coefficient vs. α using Reynolds Averaged NS equations.

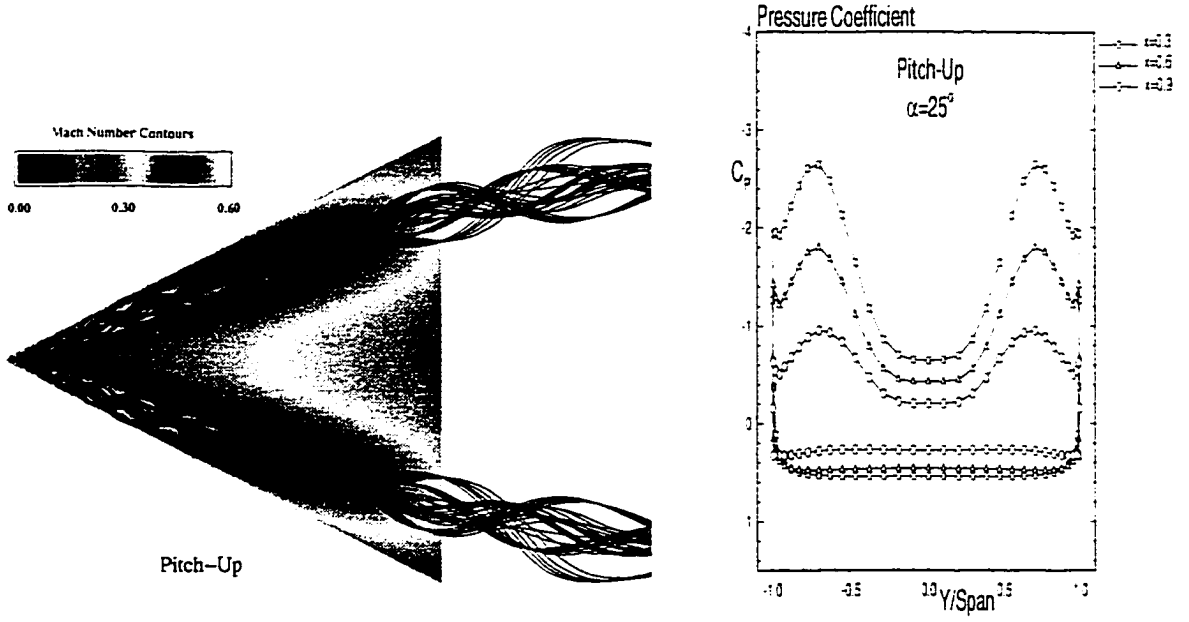

Figure 6.34: Particle traces over the delta wing and spanwise pressure coefficient distributions for pitch-up at $\alpha = 25°$

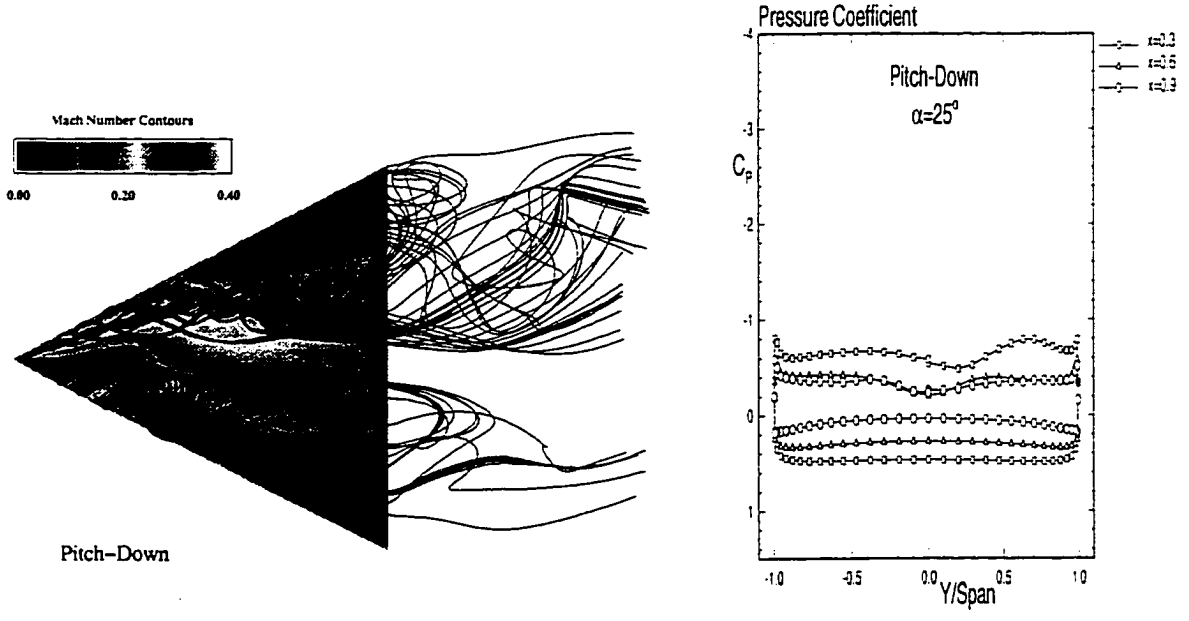

Figure 6.35: Particle traces over the delta wing and spanwise pressure coefficient distributions for pitch-down at $\alpha = 25°$

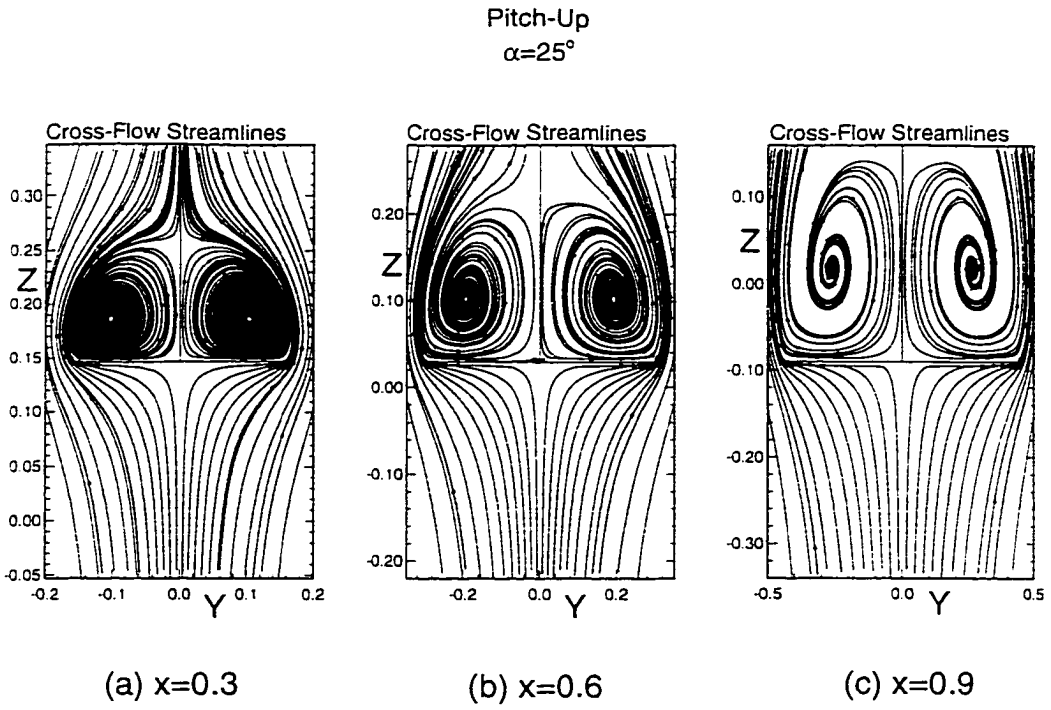

Figure 6.36: Cross-flow instantaneous streamlines for pitch-up at $\alpha = 25°$ and (a) x=0.3, (b) x=0.6, and (c) x=0.9

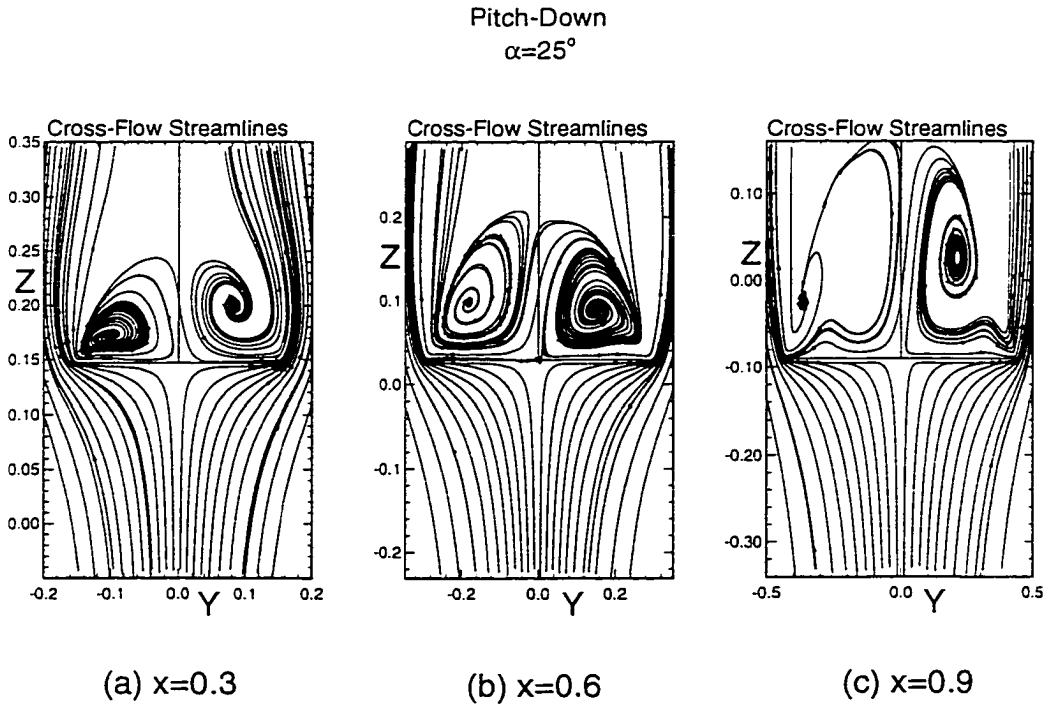

Figure 6.37: Cross-flow instantaneous streamlines for pitch-down at $\alpha = 25°$ and (a) x=0.3, (b) x=0.6, and (c) x=0.9

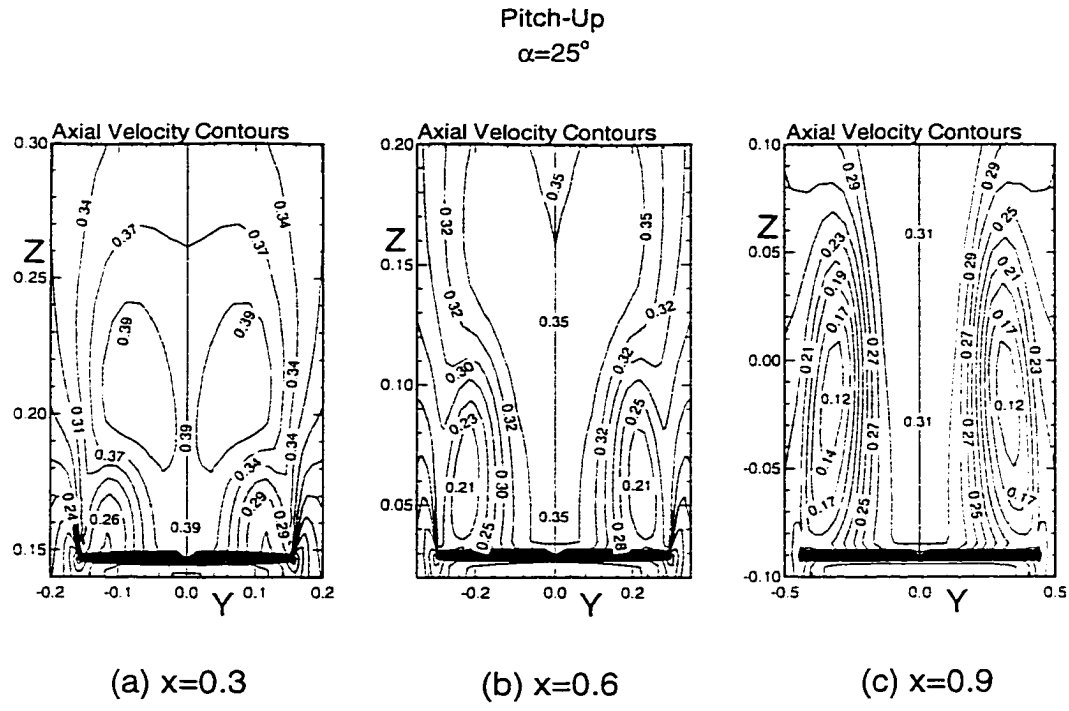

Figure 6.38: Axial velocity contours for pitch-up at $\alpha = 25°$ and (a) x=0.3, (b) x=0.6, and (c) x=0.9

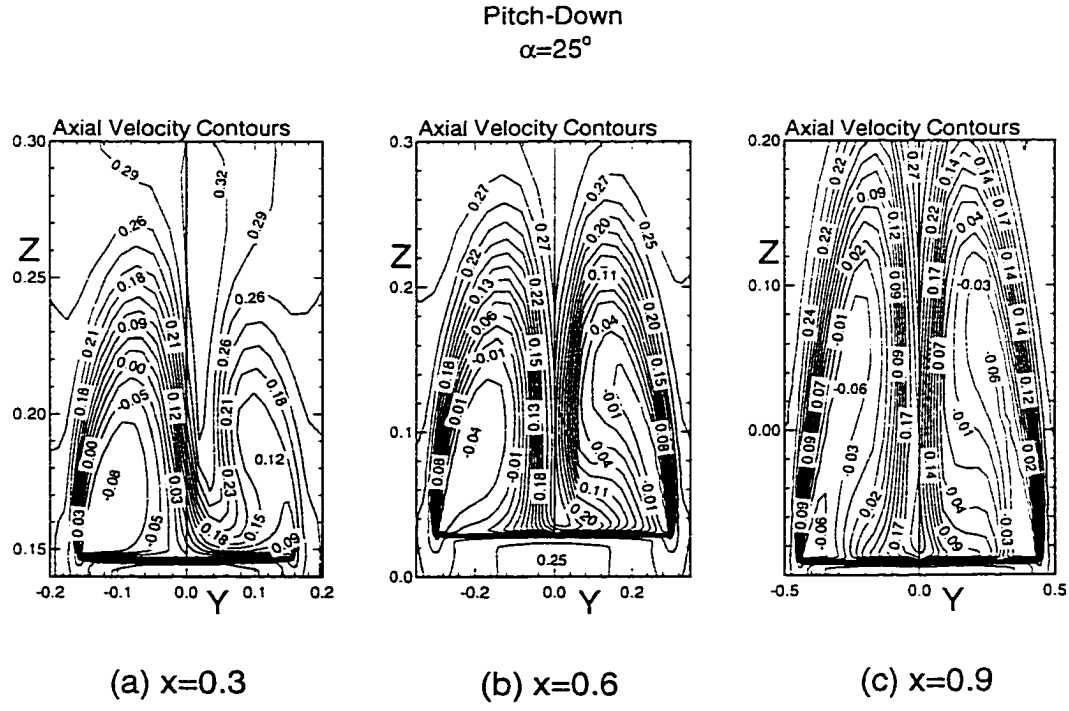

Figure 6.39: Axial velocity contours for pitch-down at $\alpha = 25°$ and (a) x=0.3, (b) x=0.6, and (c) x=0.9

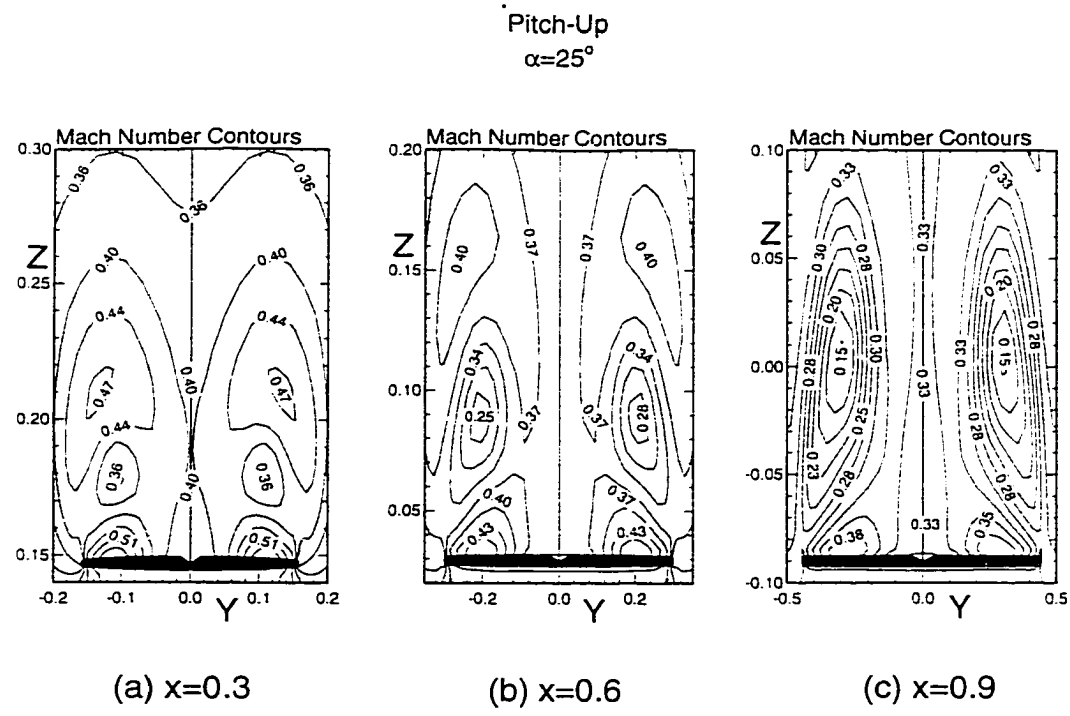

Figure 6.40: Mach Number contours for pitch-up at $\alpha = 25°$ and (a) x=0.3. (b) x=0.6. and (c) x=0.9

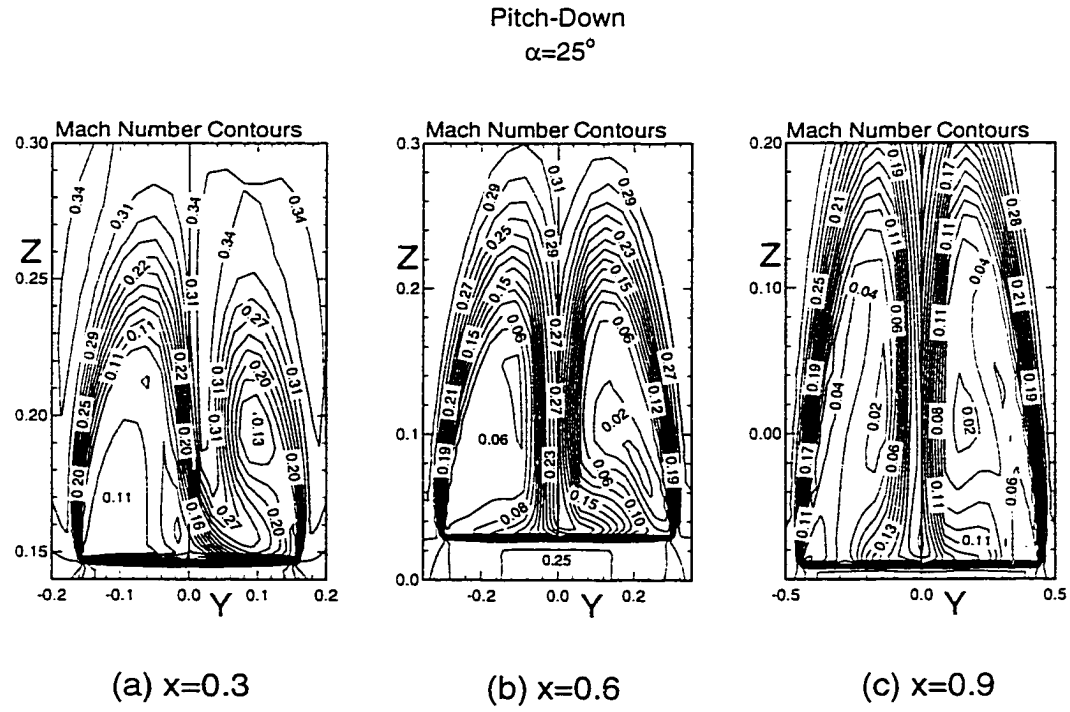

Figure 6.41: Mach Number contours for pitch-down at $\alpha = 25°$ and (a) x=0.3. (b) x=0.6, and (c) x=0.9

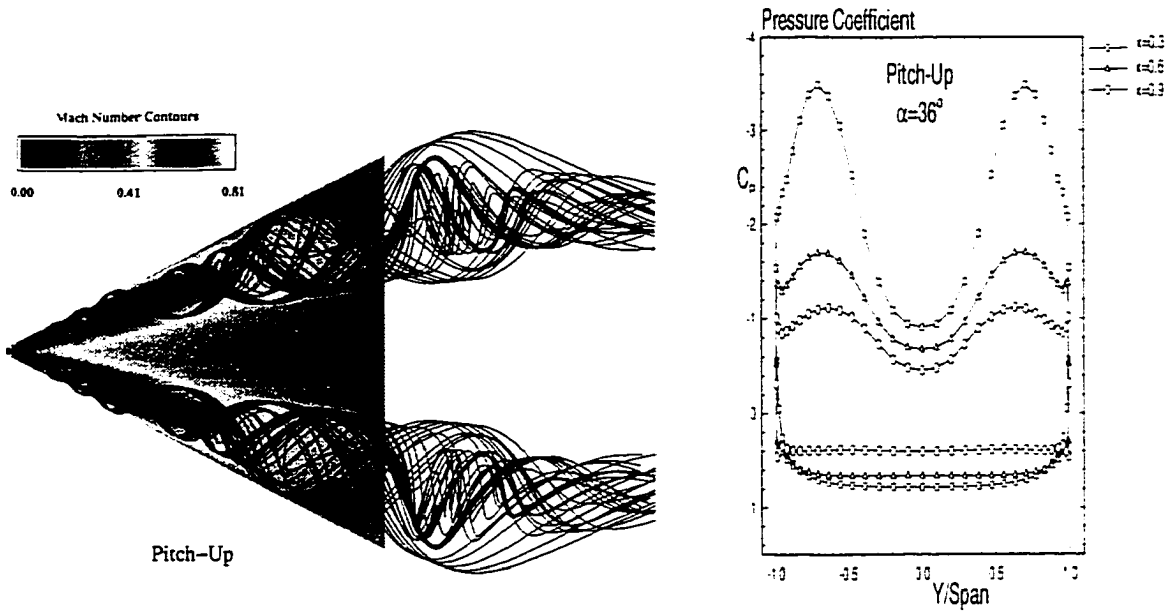

Figure 6.42: Particle traces over the delta wing and spanwise pressure coefficient distributions for pitch-up at $\alpha = 36°$

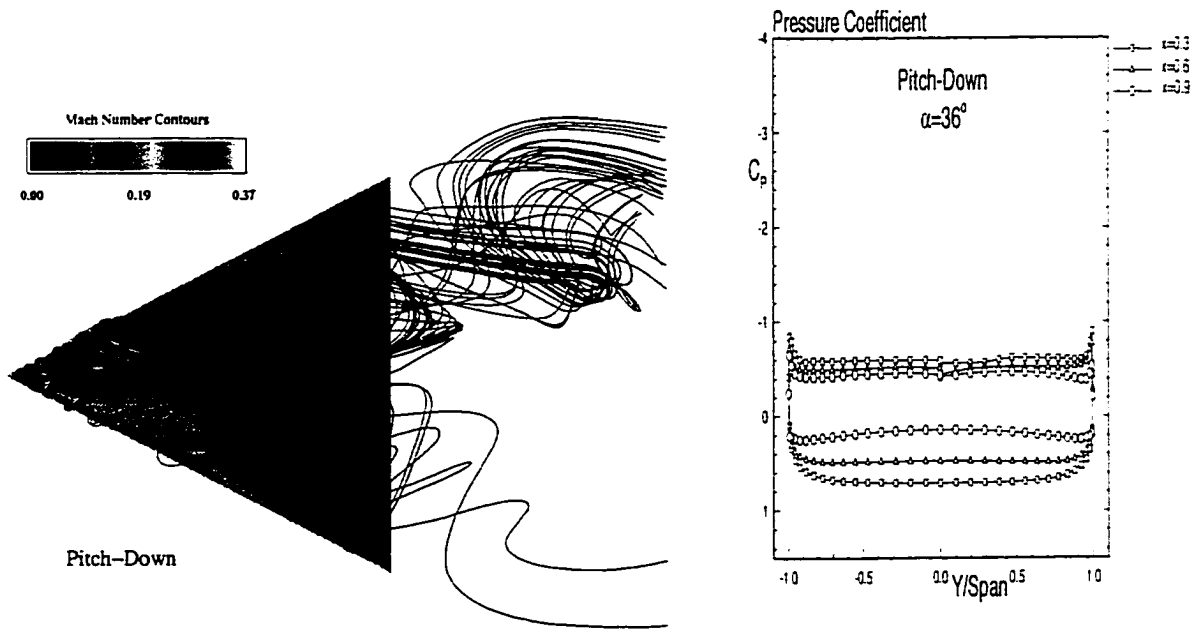

Figure 6.43: Particle traces over the delta wing and spanwise pressure coefficient distributions for pitch-down at $\alpha = 36°$

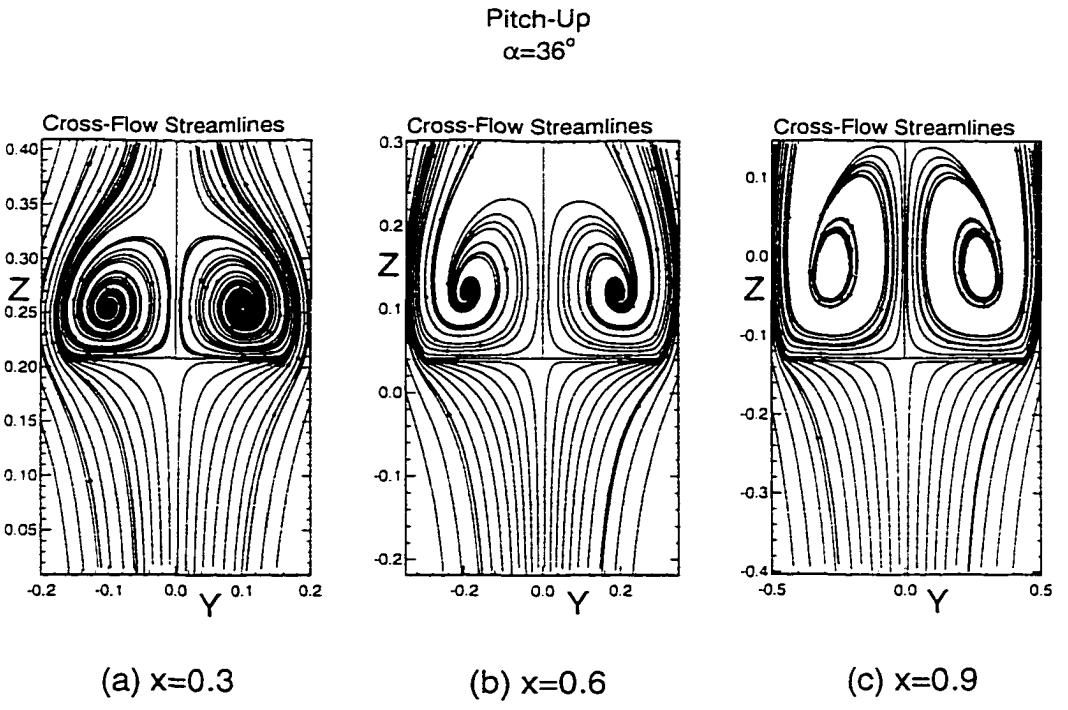

Figure 6.44: Cross-flow instantaneous streamlines for pitch-up at $\alpha = 36°$ and (a) x=0.3, (b) x=0.6, and (c) x=0.9

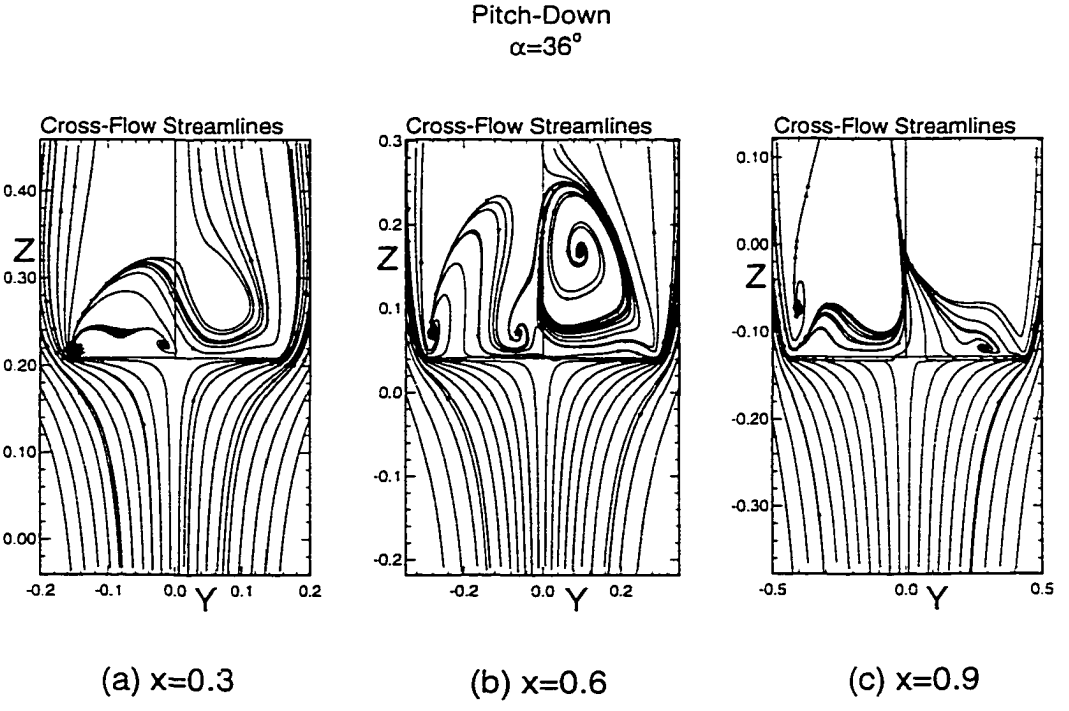

Figure 6.45: Cross-flow instantaneous streamlines for pitch-down at $\alpha = 36°$ and (a) x=0.3, (b) x=0.6, and (c) x=0.9

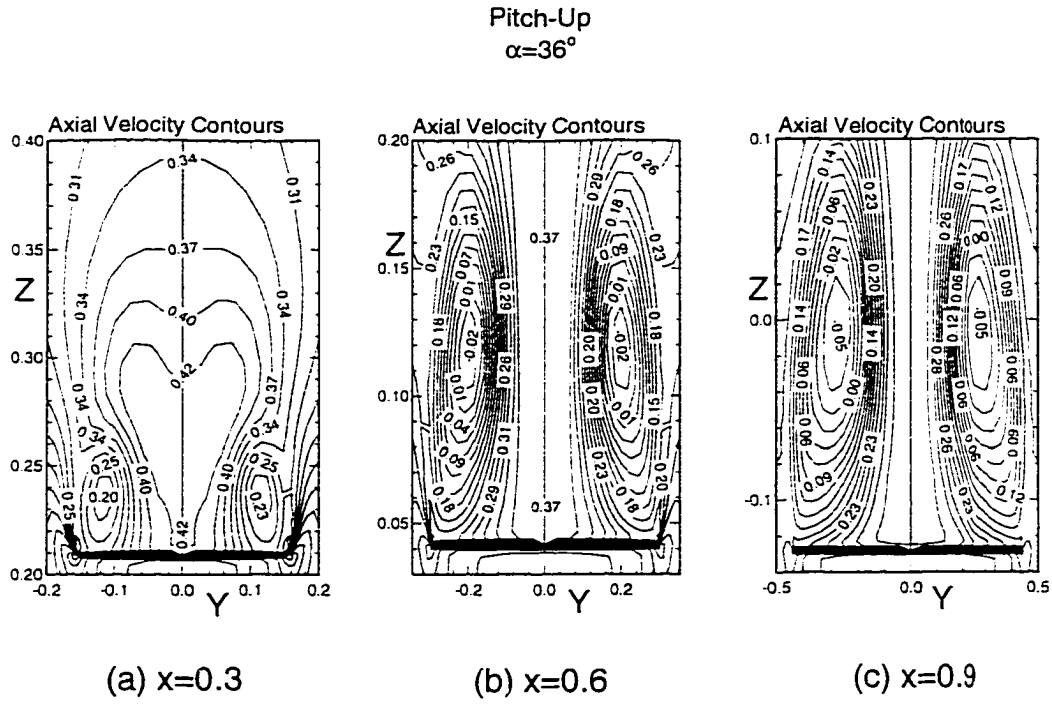

Figure 6.46: Axial velocity contours for pitch-up at $\alpha = 36°$ and (a) x=0.3, (b) x=0.6, and (c) x=0.9

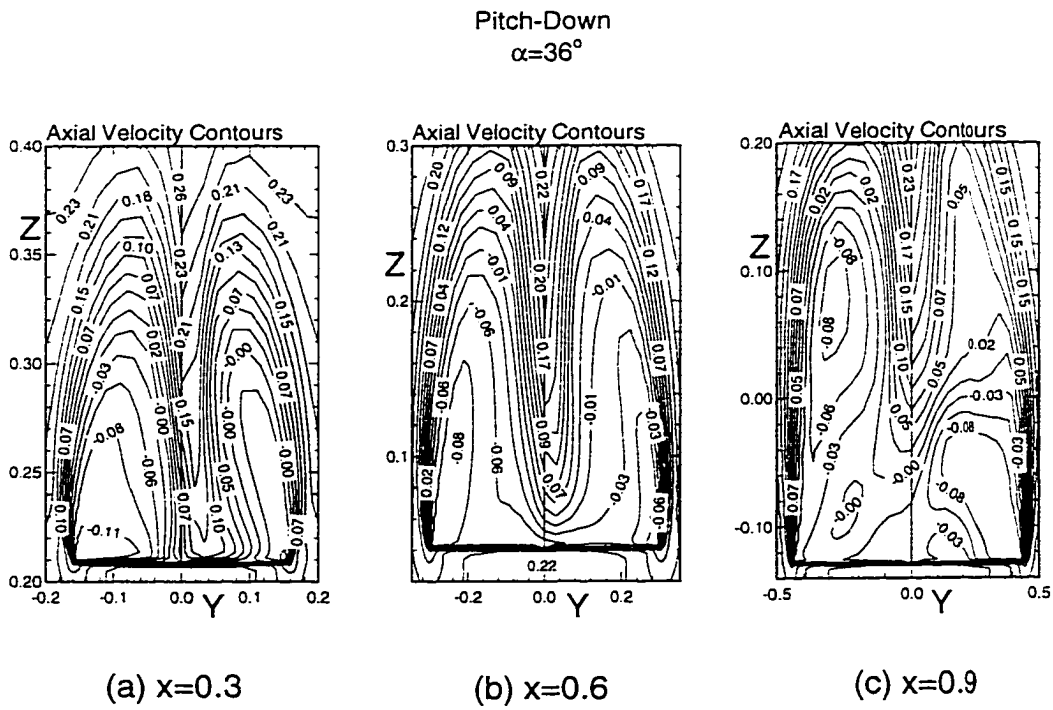

Figure 6.47: Axial velocity contours for pitch-down at $\alpha = 36°$ and (a) x=0.3, (b) x=0.6, and (c) x=0.9

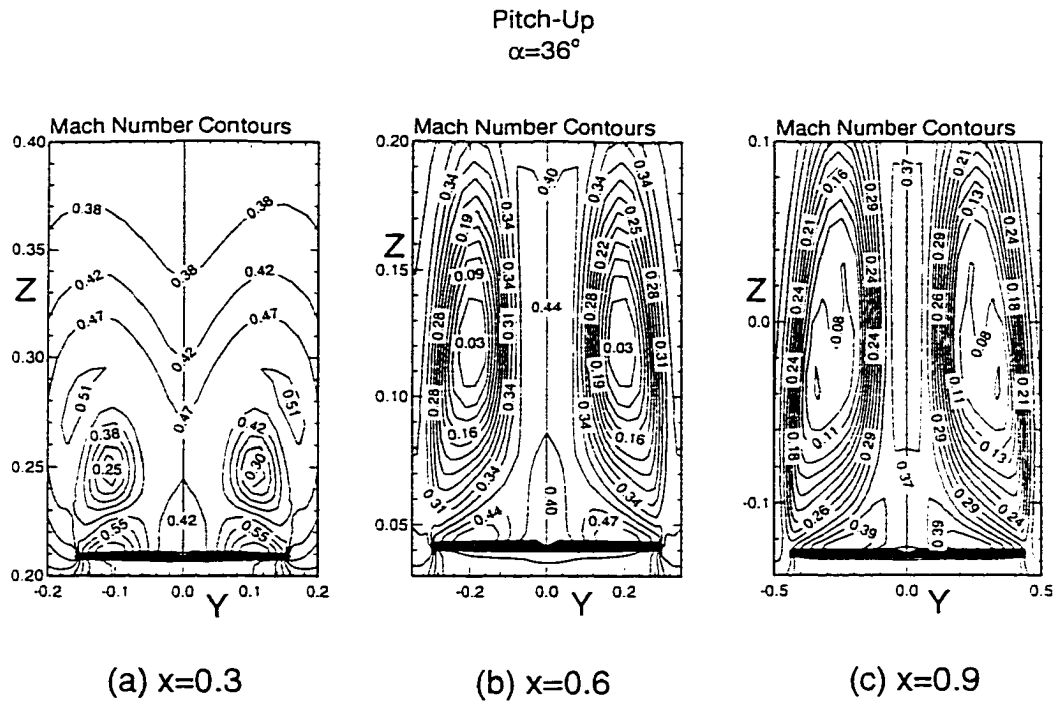

Figure 6.48: Mach Number contours for pitch-up at $\alpha = 36°$ and (a) x=0.3, (b) x=0.6, and (c) x=0.9

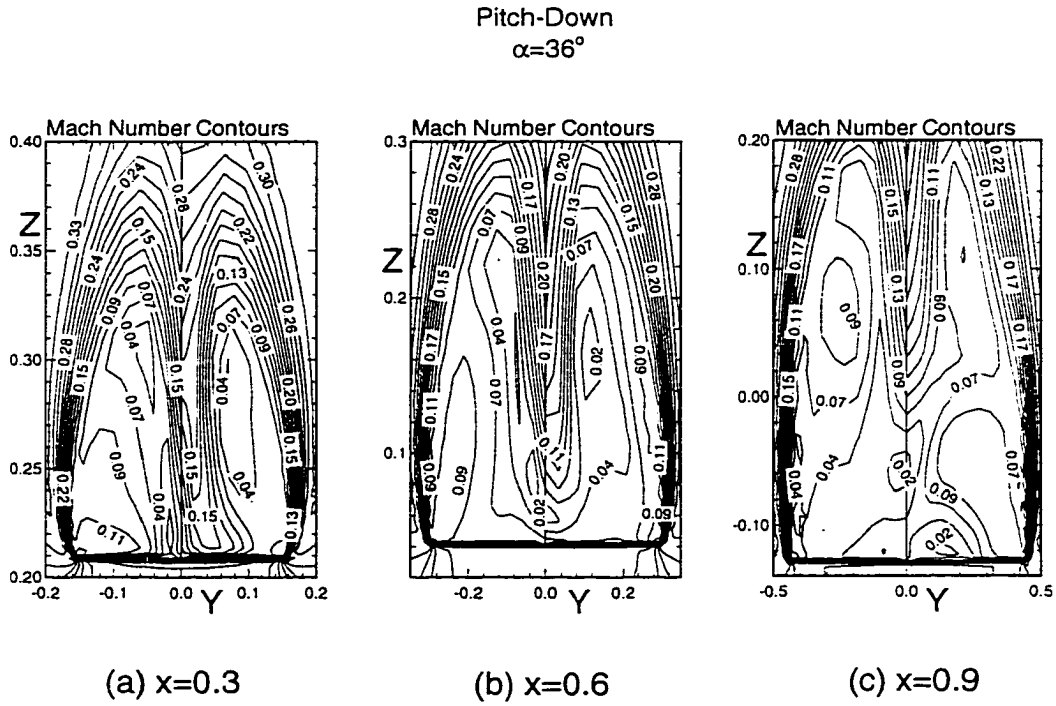

Figure 6.49: Mach Number contours for pitch-down at $\alpha = 36°$ and (a) x=0.3, (b) x=0.6, and (c) x=0.9

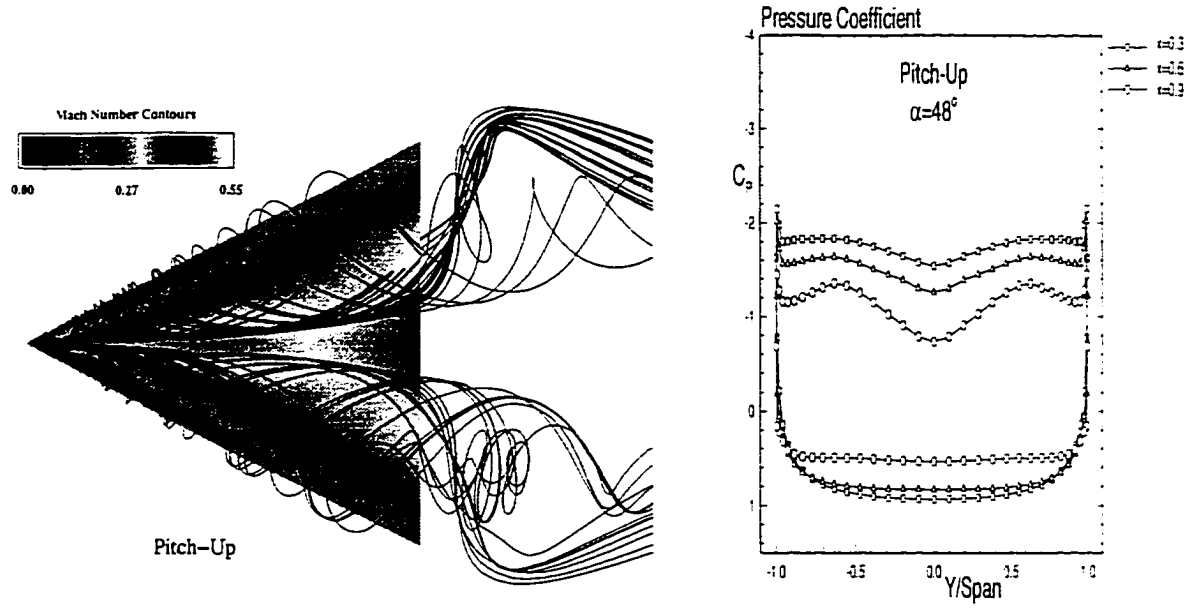

Figure 6.50: Particle traces over the delta wing and spanwise pressure coefficient distributions for pitch-up at $\alpha = 48^o$

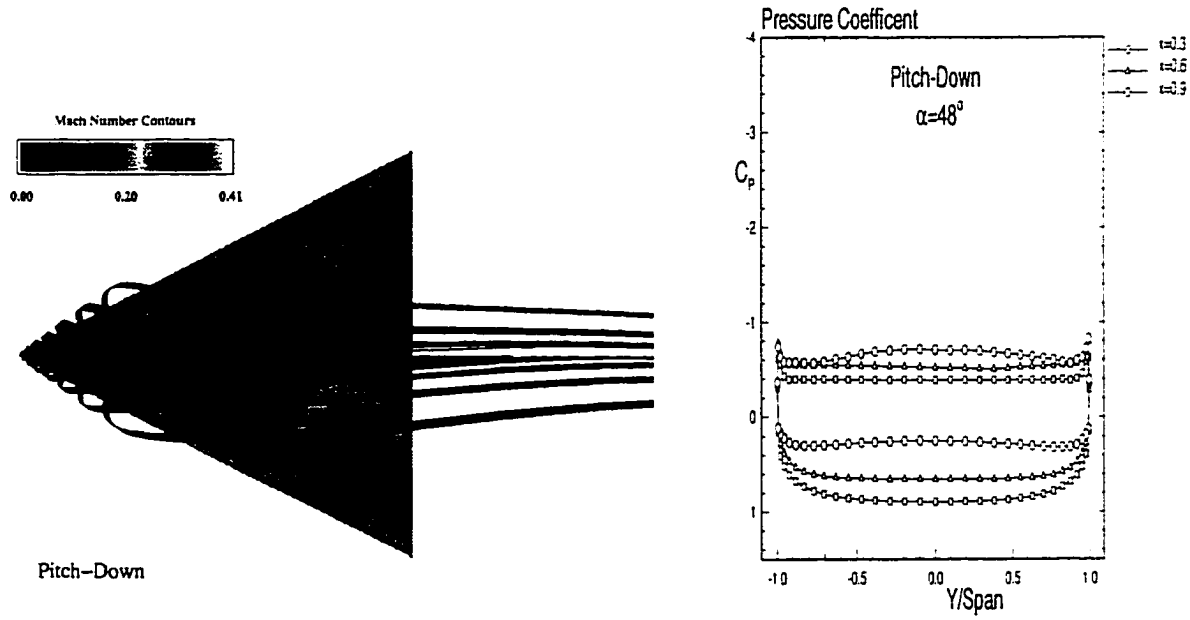

Figure 6.51: Particle traces over the delta wing and spanwise pressure coefficient distributions for pitch-down at $\alpha = 48^o$

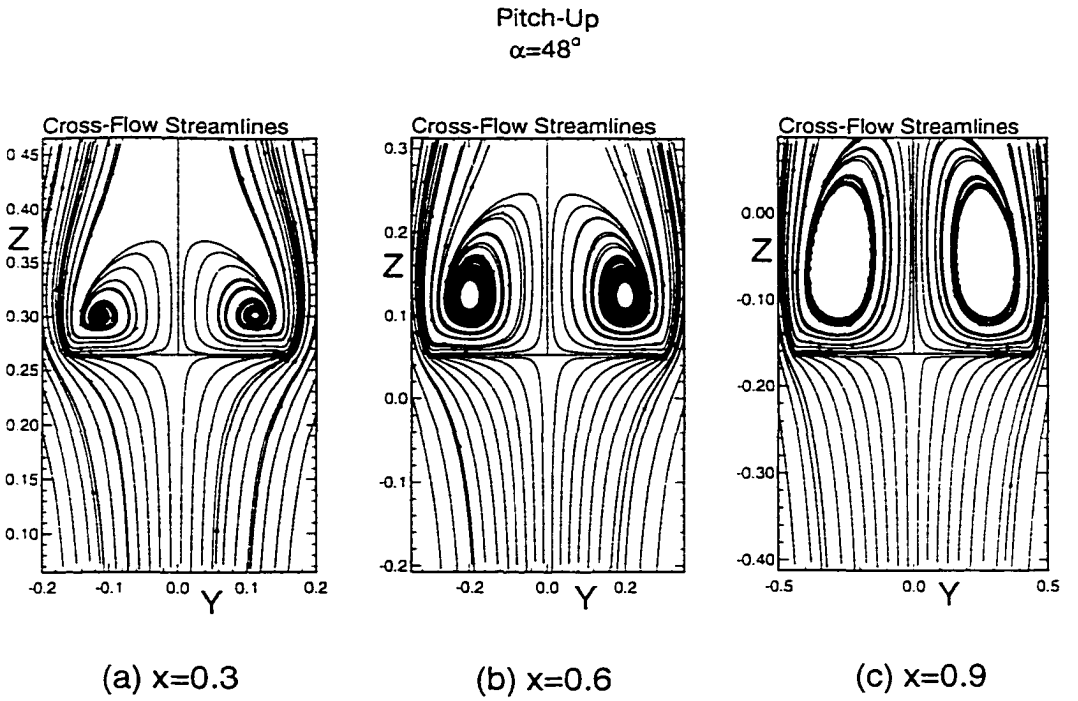

Figure 6.52: Cross-flow instantaneous streamlines for pitch-up at $\alpha = 48^{\circ}$ and (a) x=0.3, (b) x=0.6, and (c) x=0.9

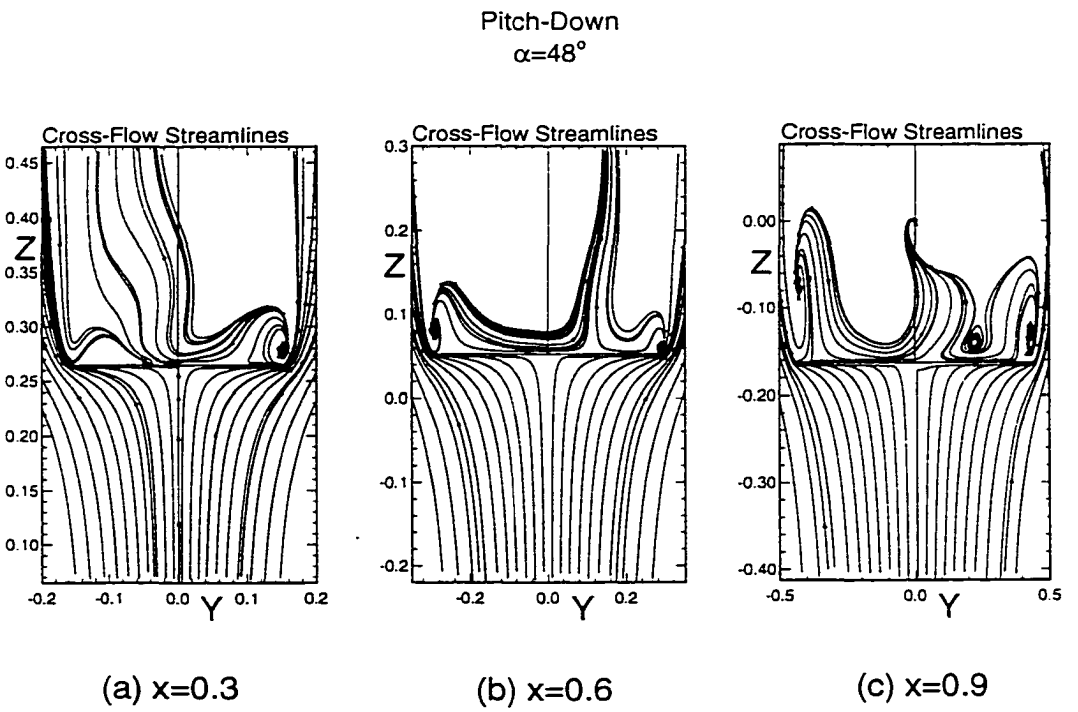

Figure 6.53: Cross-flow instantaneous streamlines for pitch-down at $\alpha = 48^{\circ}$ and (a) x=0.3, (b) x=0.6, and (c) x=0.9

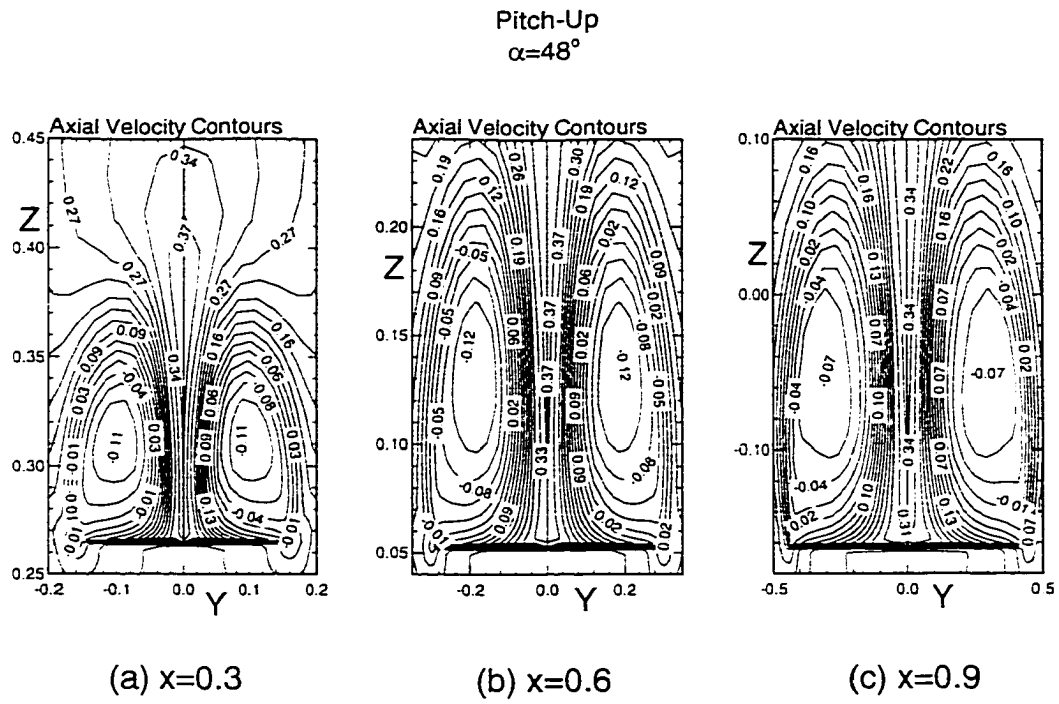

Figure 6.54: Axial velocity contours for pitch-up at $\alpha = 48^{o}$ and (a) x=0.3. (b) x=0.6, and (c) x=0.9

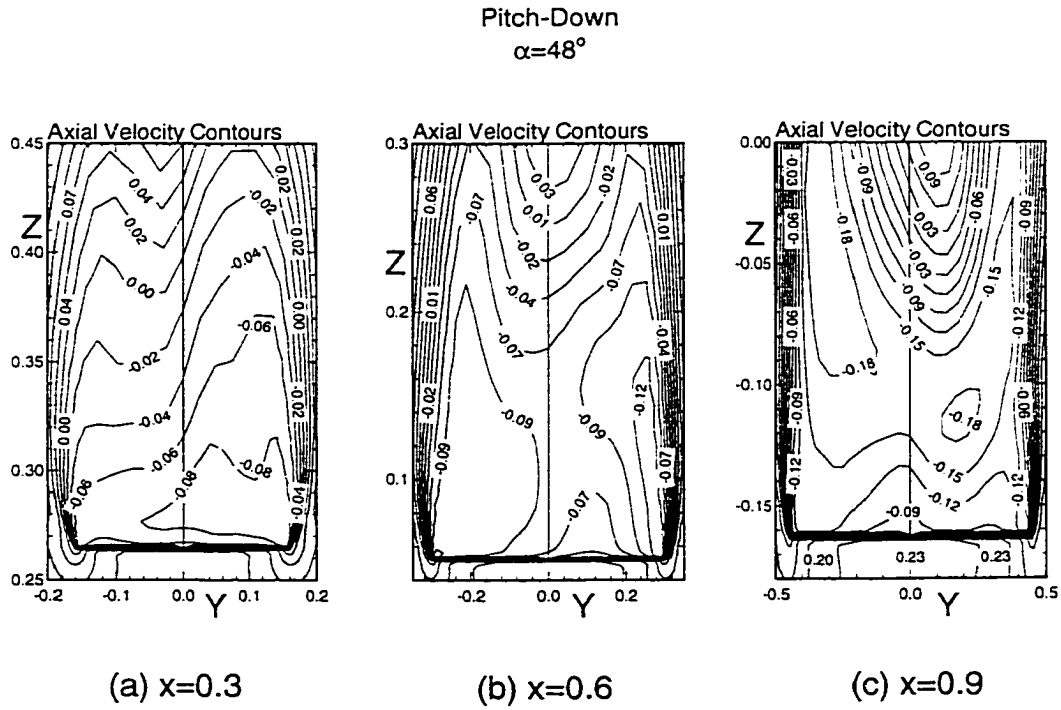

Figure 6.55: Axial velocity contours for pitch-down at $\alpha = 48^{o}$ and (a) x=0.3, (b) x=0.6, and (c) x=0.9

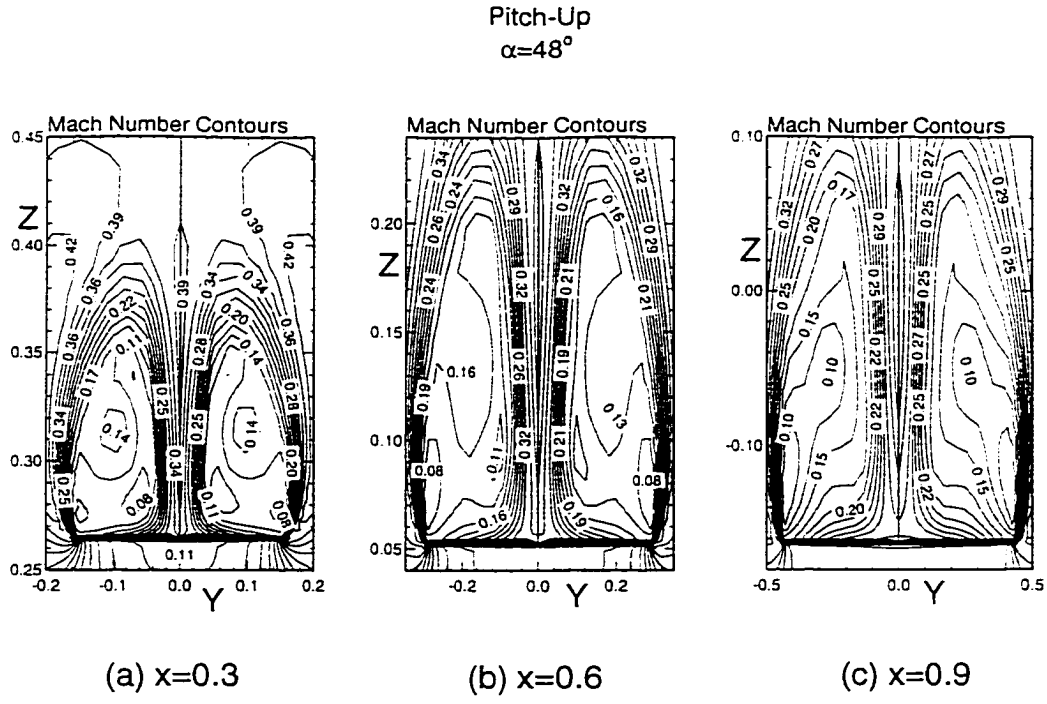

Figure 6.56: Mach Number contours for pitch-up at $\alpha = 48°$ and (a) x=0.3, (b) x=0.6, and (c) x=0.9

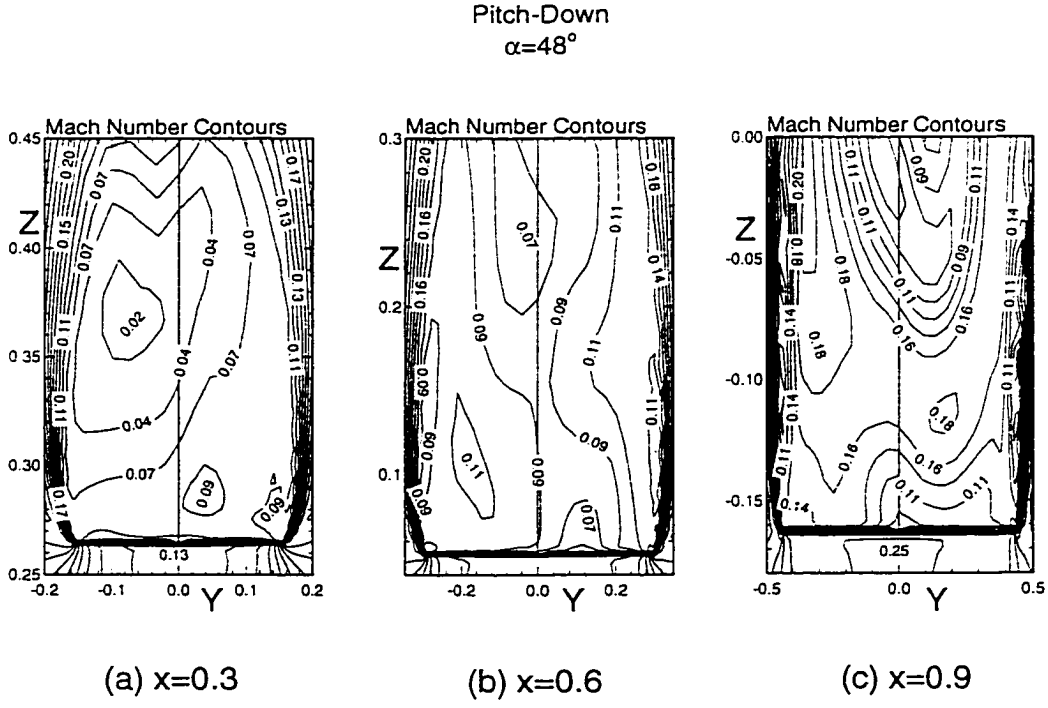

Figure 6.57: Mach Number contours for pitch-down at $\alpha = 48°$ and (a) x=0.3, (b) x=0.6, and (c) x=0.9.

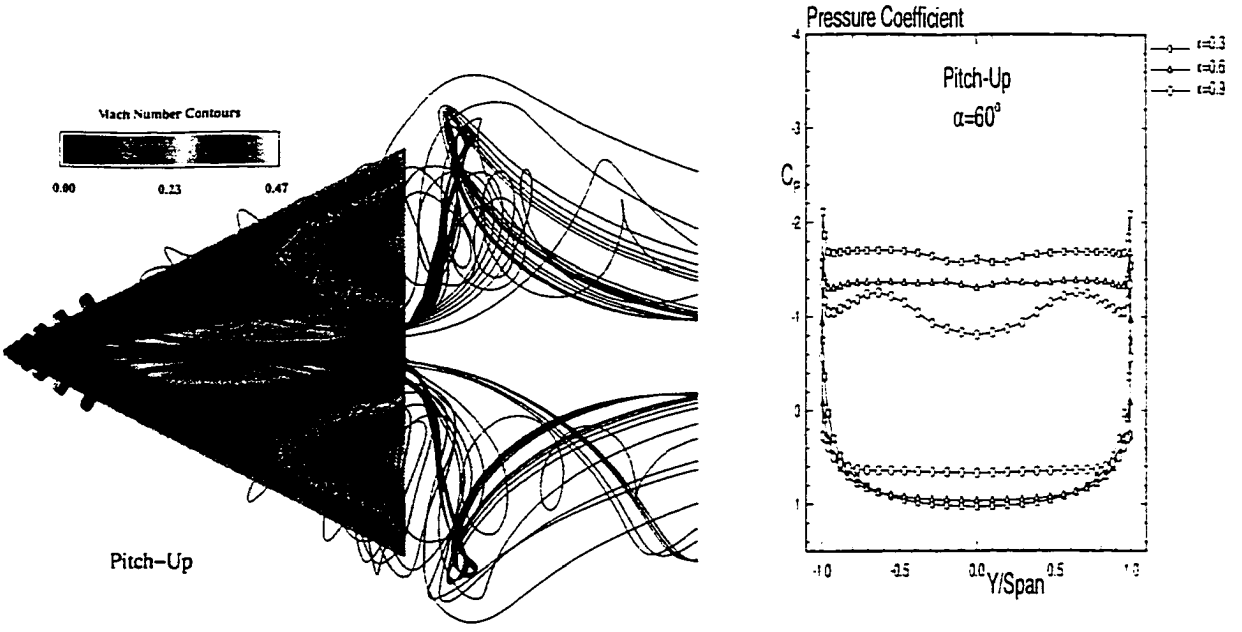

Figure 6.58: Particle traces over the delta wing and spanwise pressure coefficient distributions for pitch-up at $\alpha = 60^o$

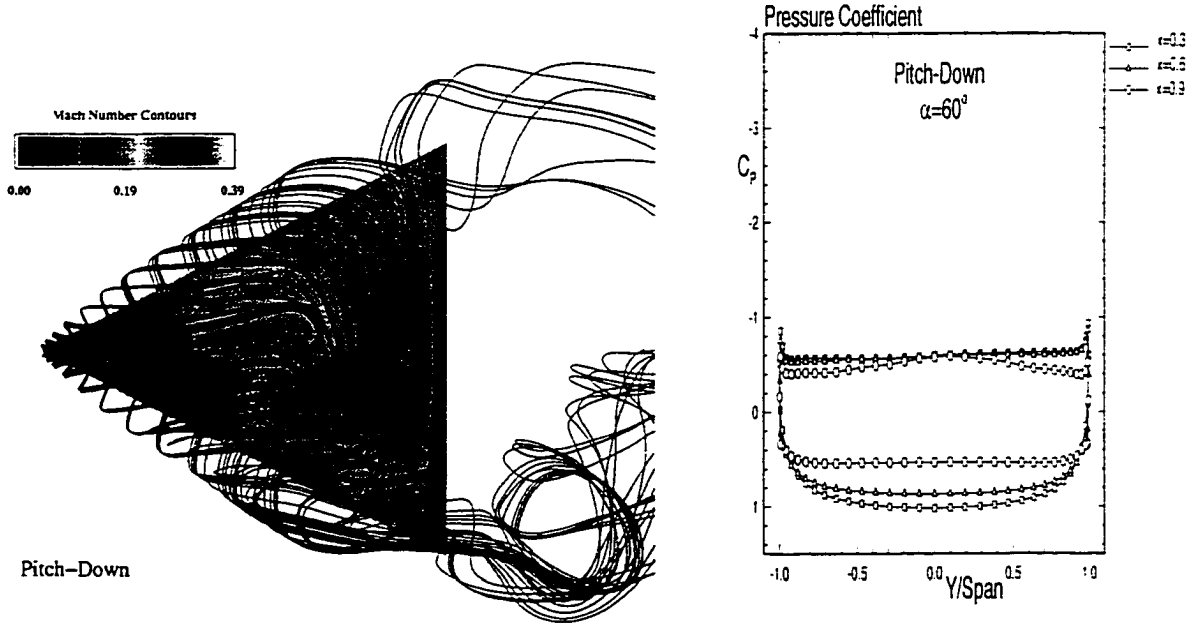

Figure 6.59: Particle traces over the delta wing and spanwise pressure coefficient distributions for pitch-down at $\alpha = 60^o$

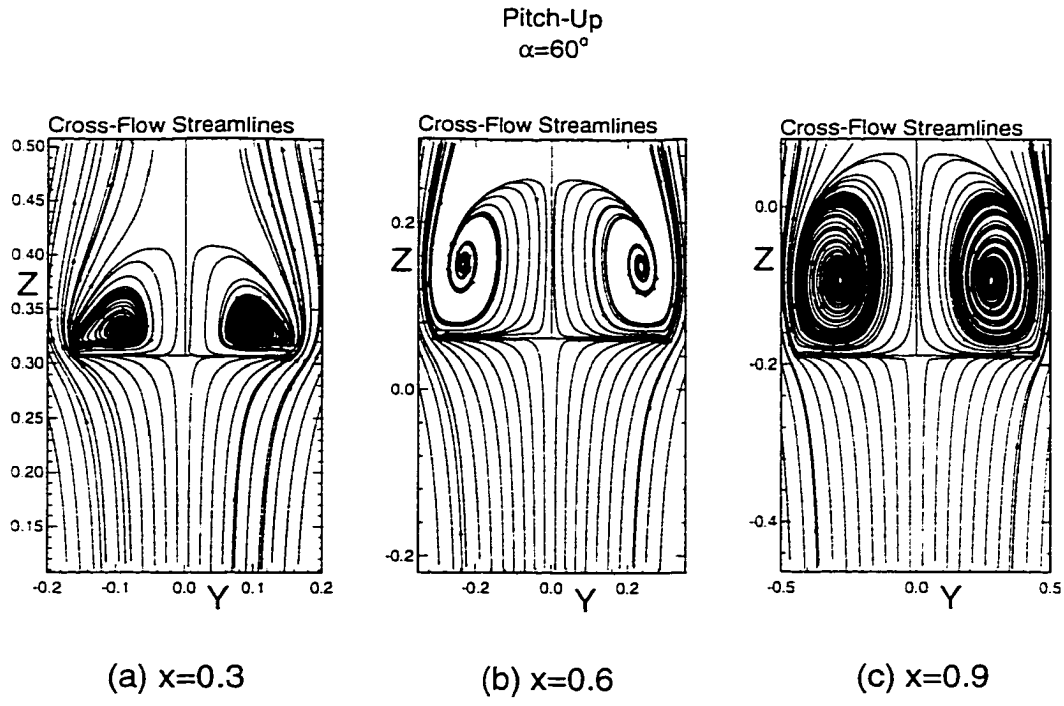

Figure 6.60: Cross-flow instantaneous streamlines for pitch-up at $\alpha = 60^o$ and (a) x=0.3, (b) x=0.6, and (c) x=0.9

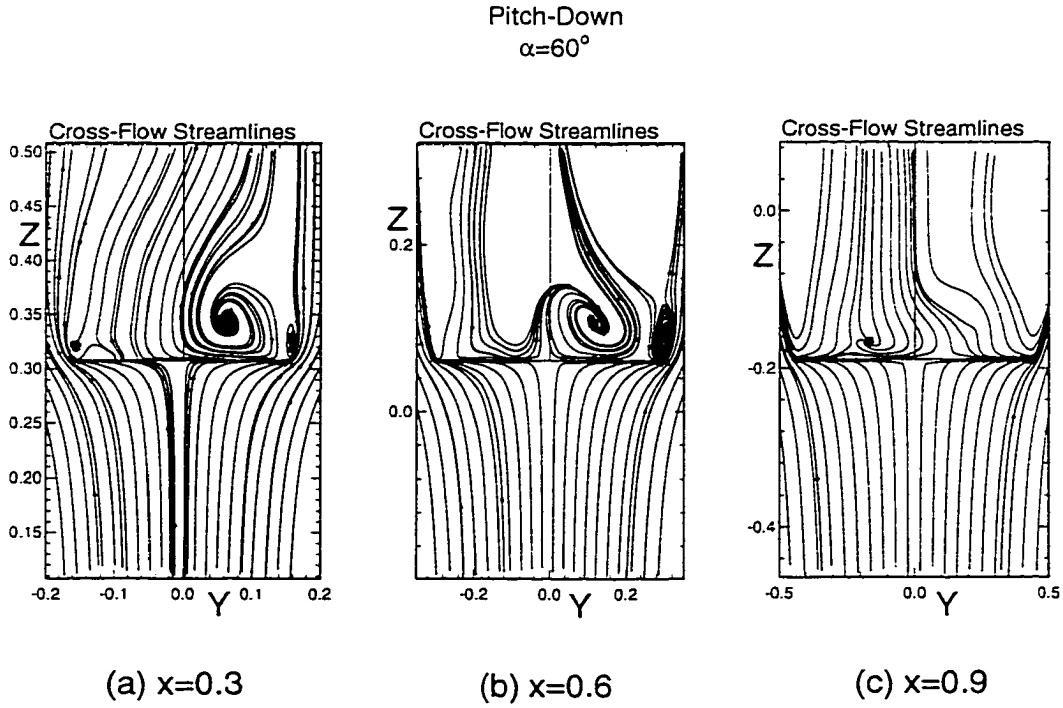

Figure 6.61: Cross-flow instantaneous streamlines for pitch-down at $\alpha = 60^o$ and (a) x=0.3, (b) x=0.6, and (c) x=0.9

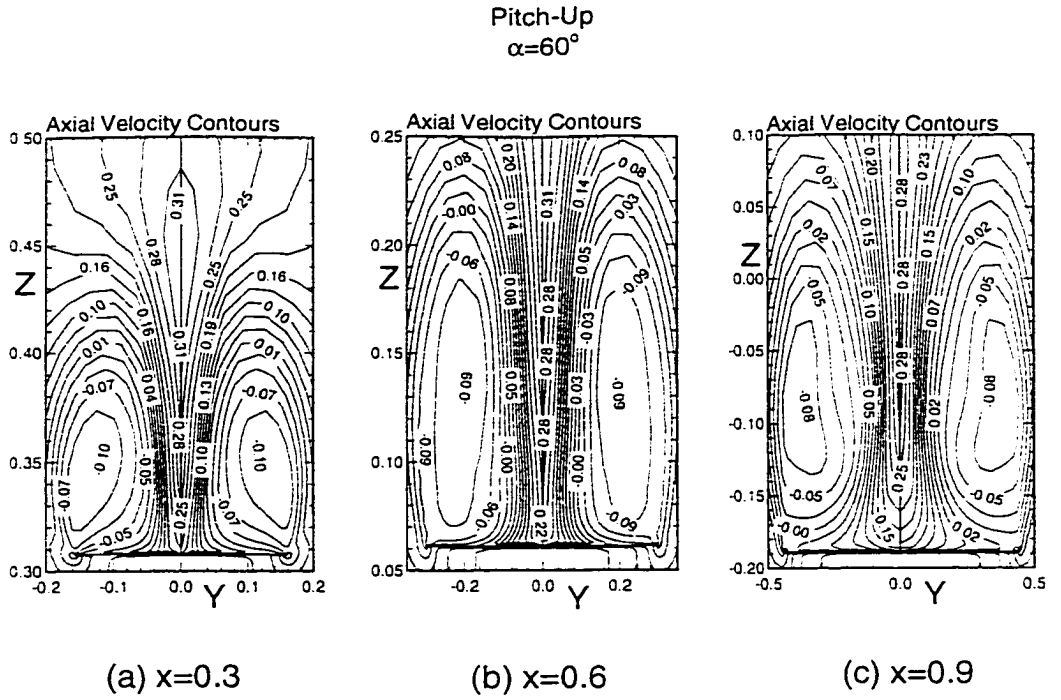

Figure 6.62: Axial velocity contours for pitch-up at $\alpha = 60°$ and (a) x=0.3. (b) x=0.6, and (c) x=0.9

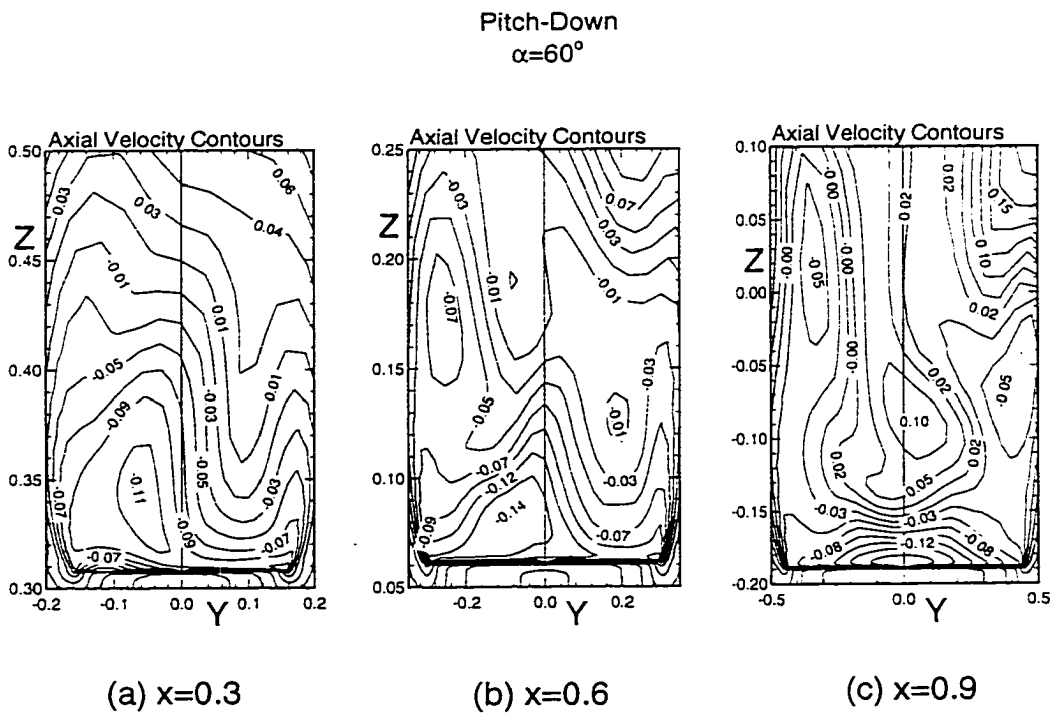

Figure 6.63: Axial velocity contours for pitch-down at $\alpha = 60°$ and (a) x=0.3. (b) x=0.6, and (c) x=0.9

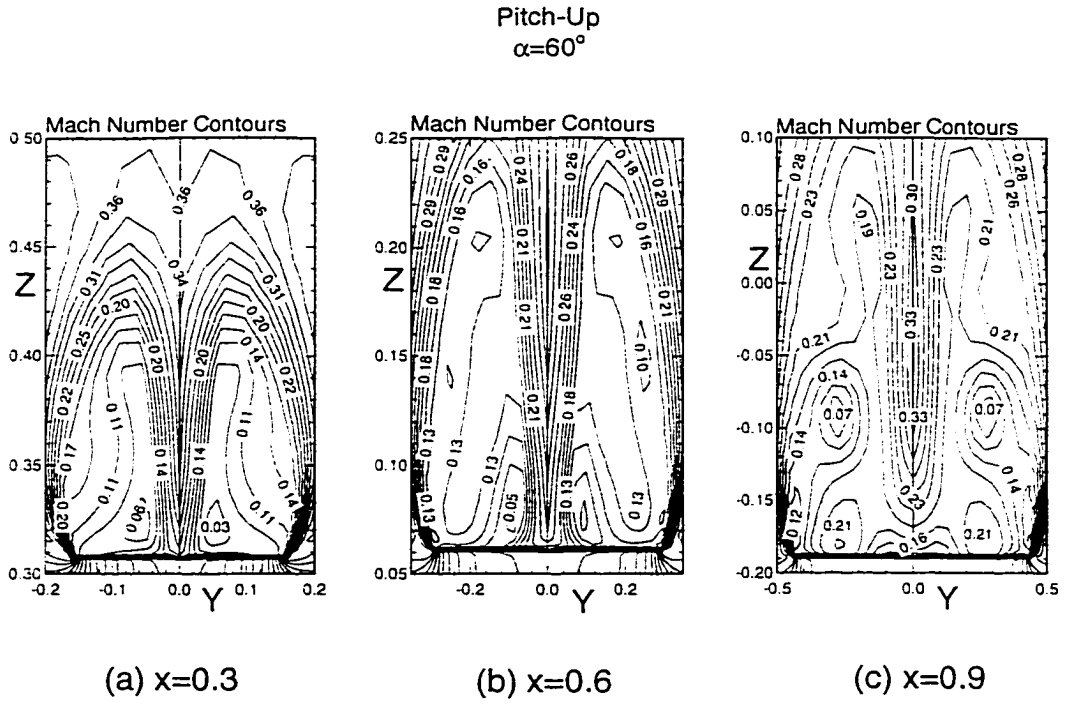

Figure 6.64: Mach Number contours for pitch-up at $\alpha = 60°$ and (a) x=0.3, (b) x=0.6, and (c) x=0.9

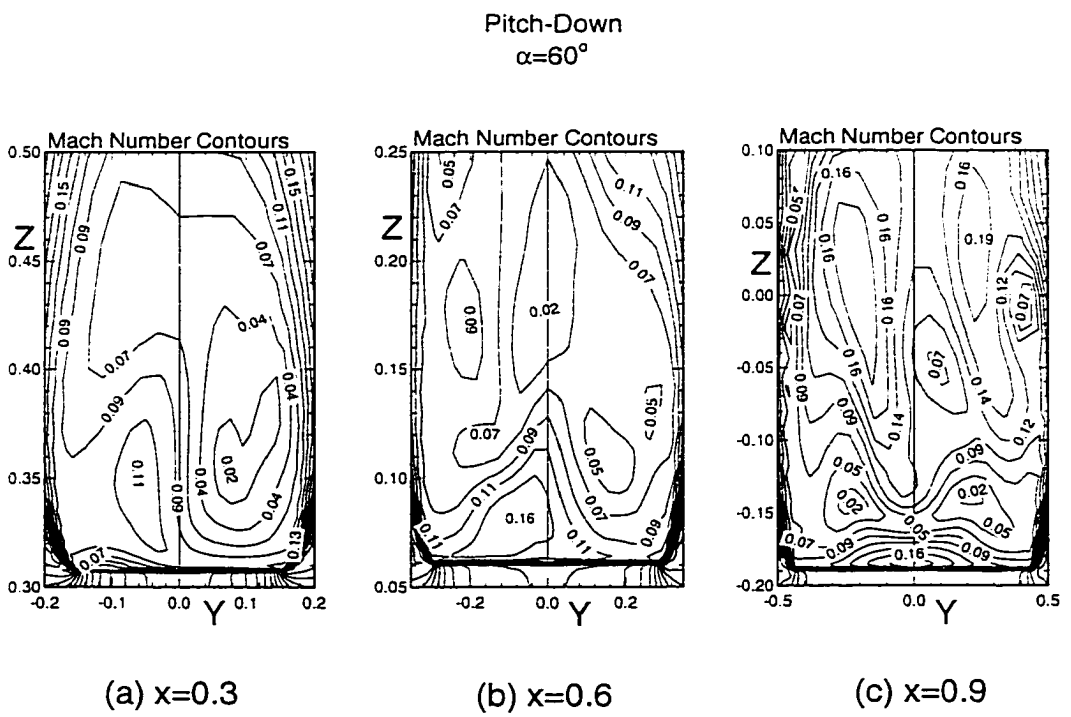

Figure 6.65: Mach Number contours for pitch-down at $\alpha = 60°$ and (a) x=0.3, (b) x=0.6, and (c) x=0.9

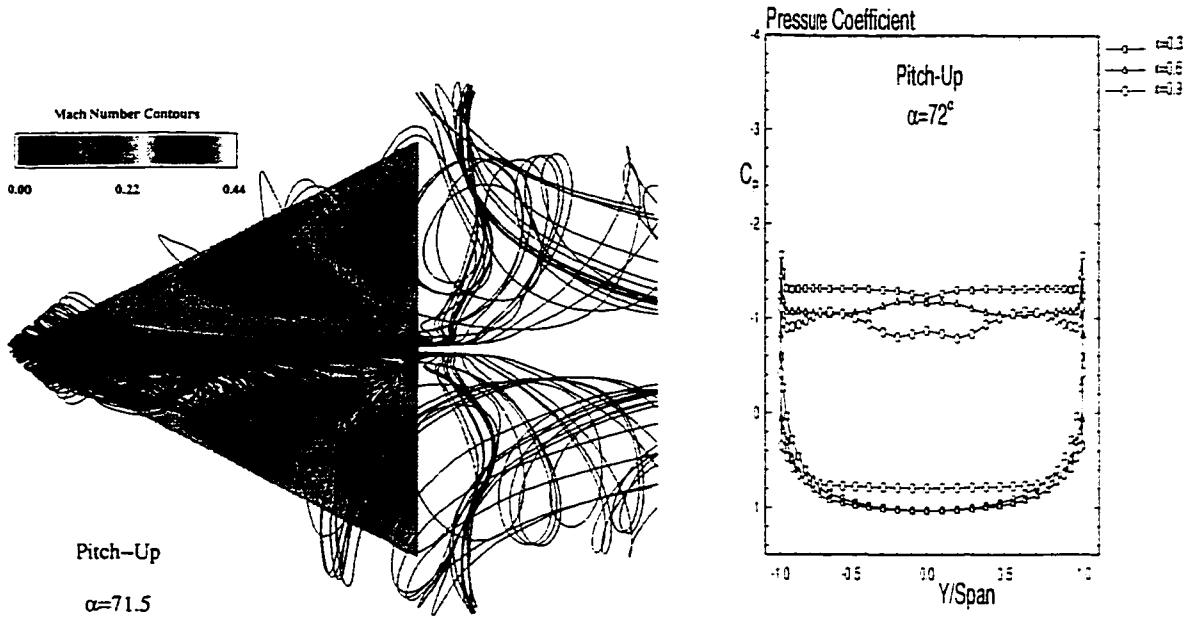

Figure 6.66: Particle traces over the delta wing and spanwise pressure coefficient distributions for pitch-up at $\alpha = 72^o$

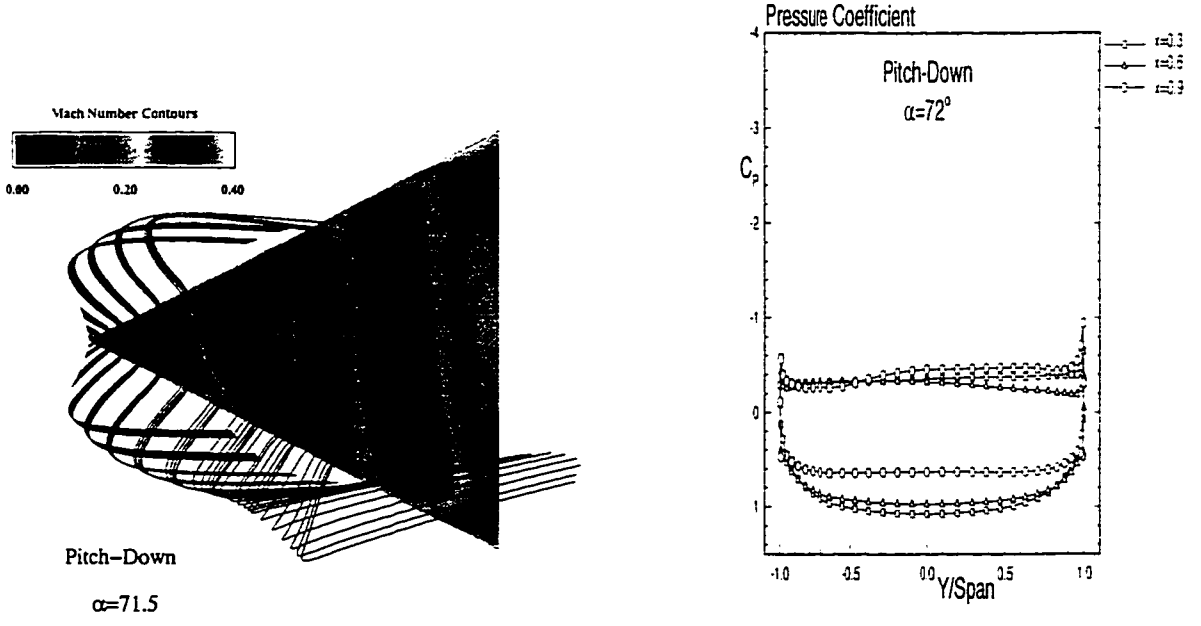

Figure 6.67: Particle traces over the delta wing and spanwise pressure coefficient distributions for pitch-down at $\alpha = 72^o$

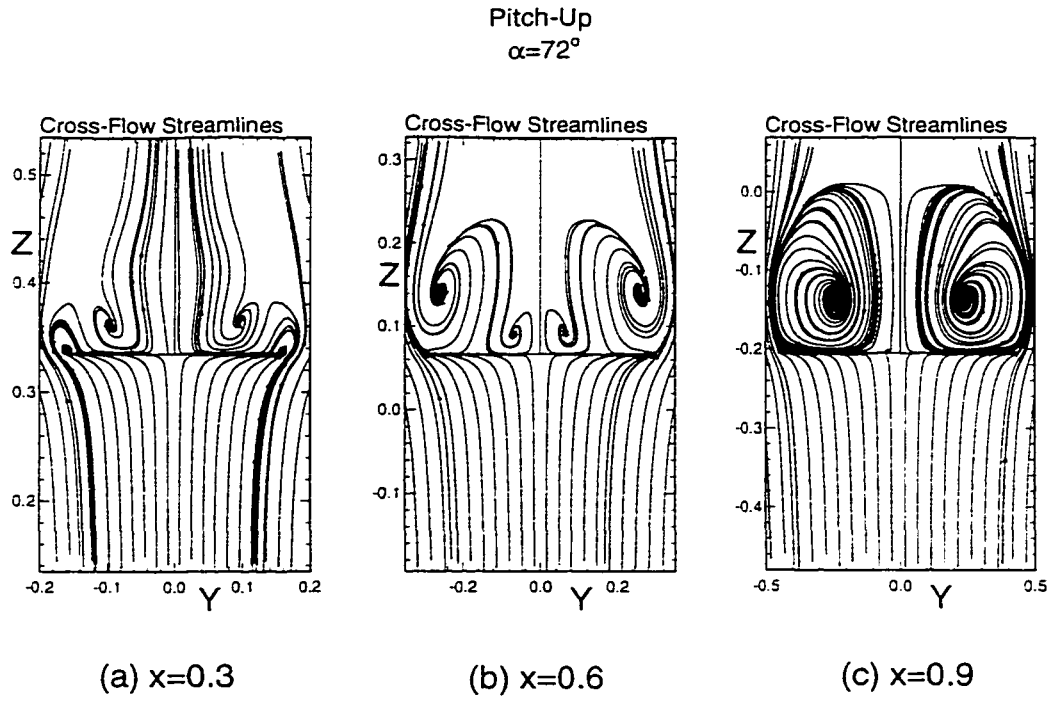

Figure 6.68: Cross-flow instantaneous streamlines for pitch-up at $\alpha = 72^o$ and (a) x=0.3, (b) x=0.6, and (c) x=0.9

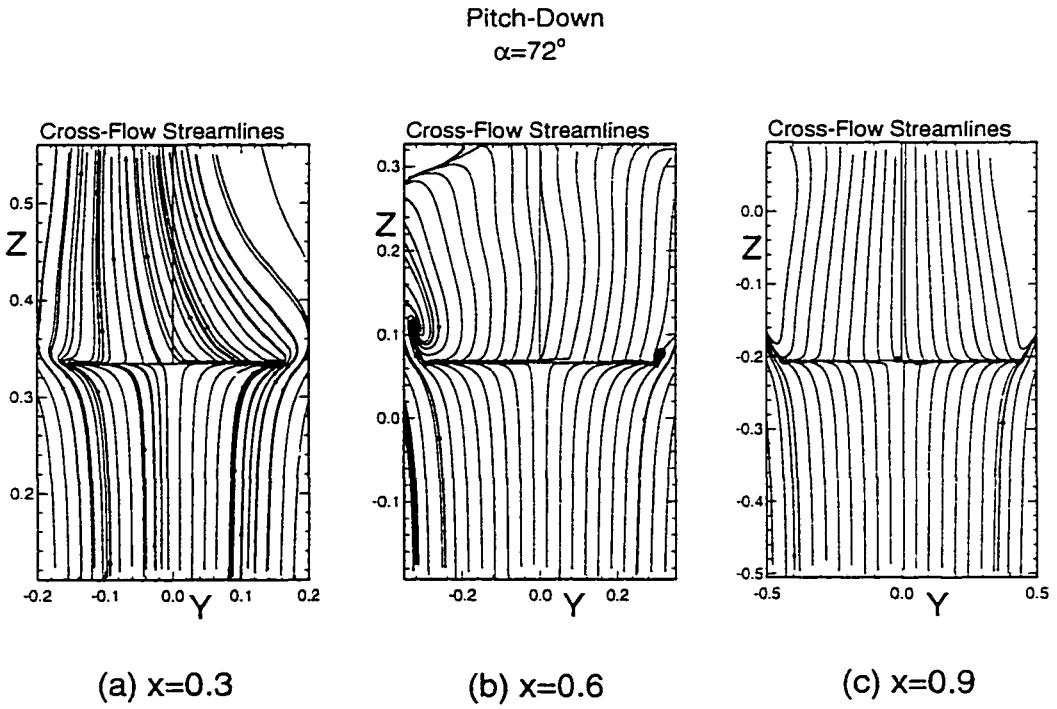

Figure 6.69: Cross-flow instantaneous streamlines for pitch-down at $\alpha = 72^o$ and (a) x=0.3, (b) x=0.6, and (c) x=0.9

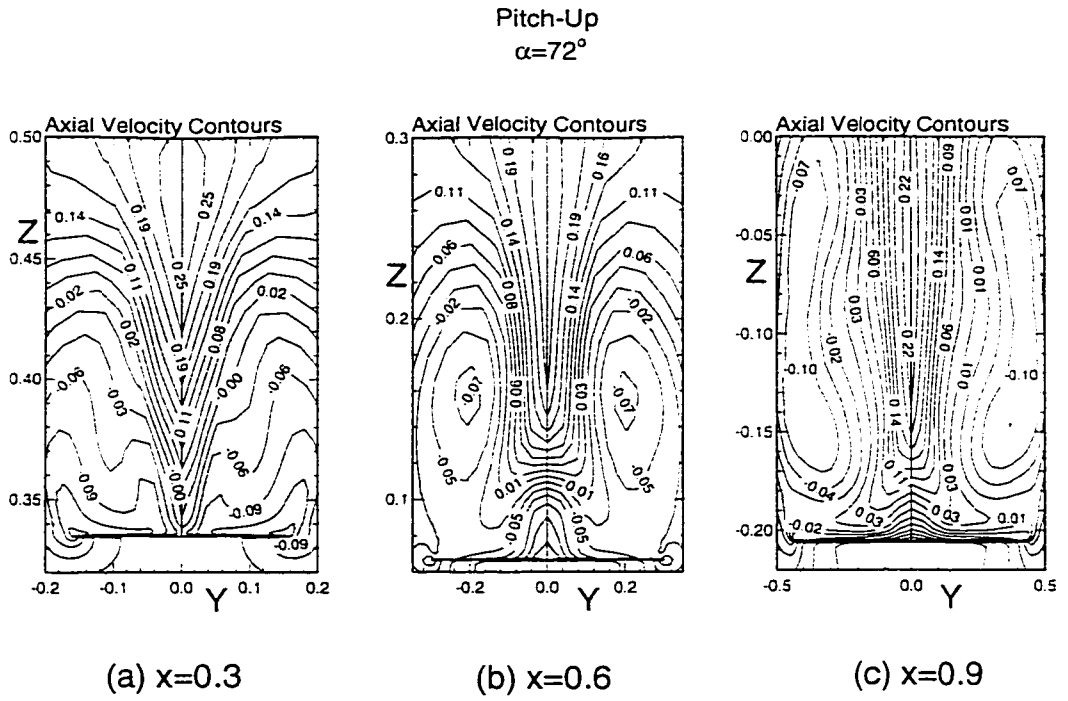

Figure 6.70: Axial velocity contours for pitch-up at $\alpha = 72^o$ and (a) x=0.3, (b) x=0.6, and (c) x=0.9

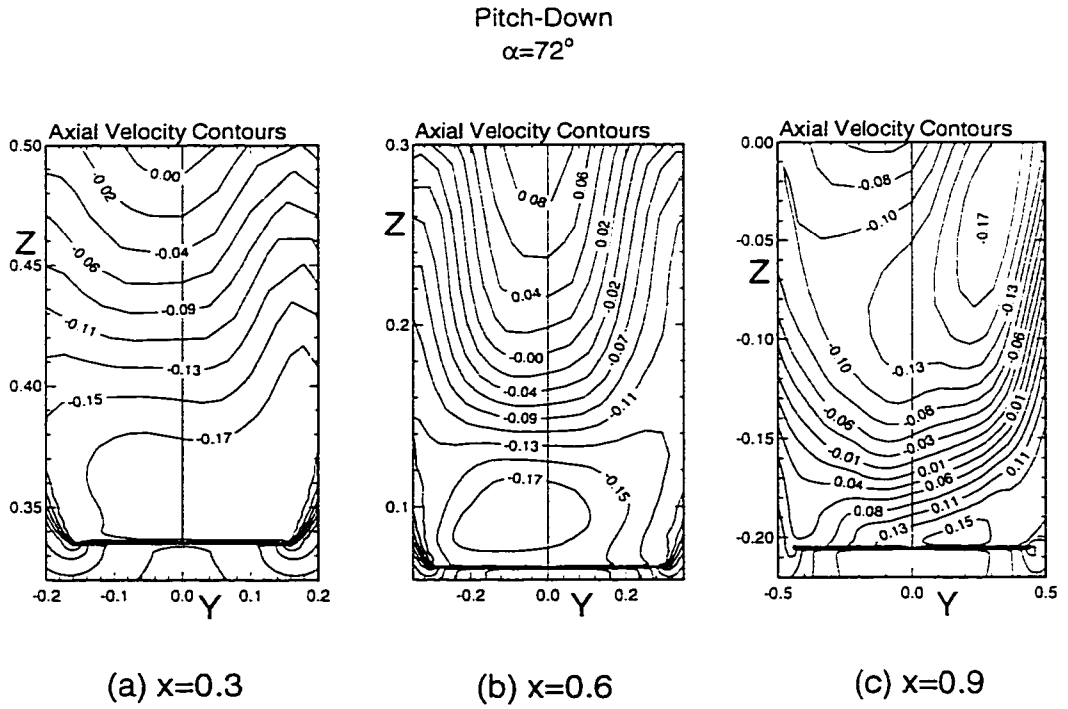

Figure 6.71: Axial velocity contours for pitch-down at $\alpha = 72^o$ and (a) x=0.3, (b) x=0.6, and (c) x=0.9

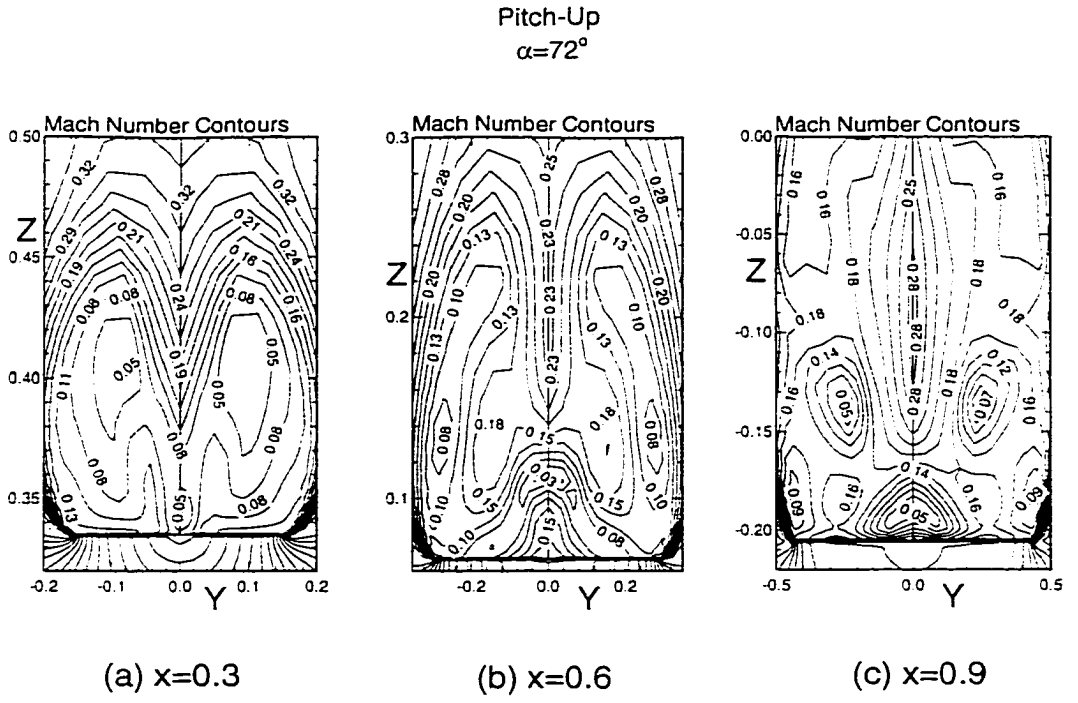

Figure 6.72: Mach Number contours for pitch-up at $\alpha = 72°$ and (a) x=0.3, (b) x=0.6, and (c) x=0.9

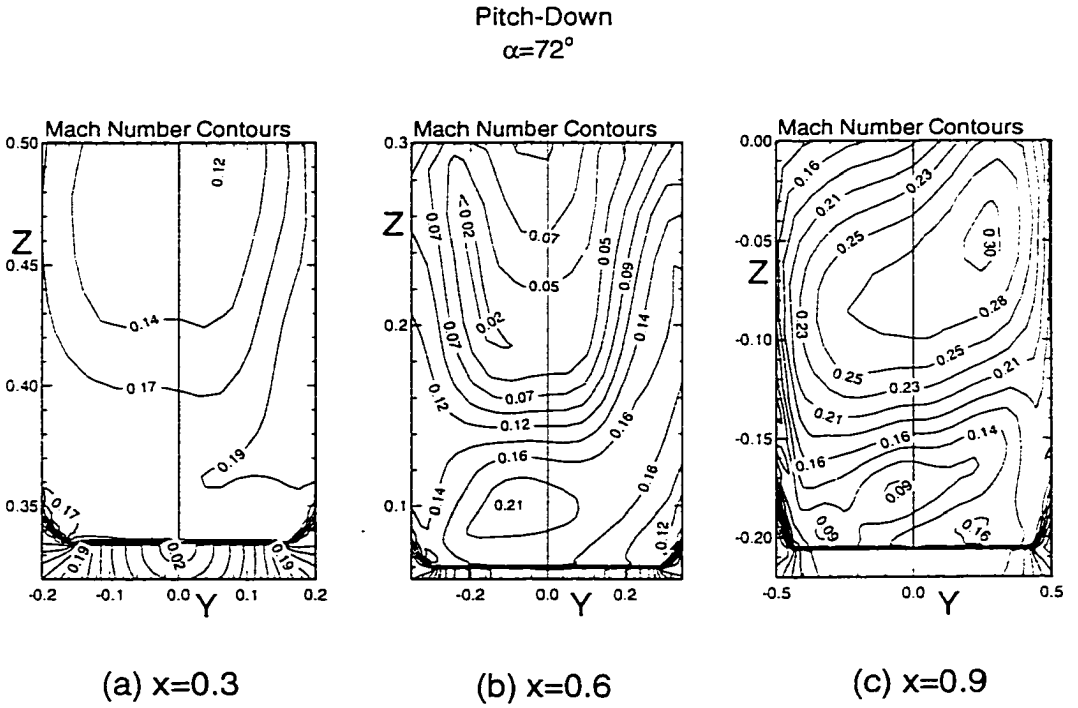

Figure 6.73: Mach Number contours for pitch-down at $\alpha = 72°$ and (a) x=0.3, (b) x=0.6, and (c) x=0.9

6.4 Summary

Both Baldwin-Lomax and Spalart-Allmaras turbulence models were used and the results were compared with each other and with those of the experimental data as well. A pitching sinusoidal motion of the wing was also investigated. The Baldwin-Lomax model introduced some improvements of the computational results of C_L and C_D. The standard Spalart-Allmaras model failed in modeling and simulating the flow at very large angles of attack ($> 60°$) with the current grid resolution. In the sinusoidal pitching case, there was a substantial difference in the lift and drag coefficients between the upstroke and downstroke motion because of the hysteresis effects of the unsteady motion. The asymmetry of the flow was obvious from the pitch-down motion at low angles of attack. Also, as the aspect ratio increased the vortex breakdown at the trailing edge started at a lower angle of attack, in comparison with that of a low aspect ratio wing.

CHAPTER 7

FLOW CONTROL

7.1 Initial Conditions

The delta wing model used in the current case consists of a 60° swept back, sharp-edged with zero thickness and an aspect ratio of 2.3. The three-dimensional grid topology used in the calculations along with a cross section at the trailing edge is shown in Fig. 7.1. The grid dimensions are 81 x 65 x 41 in the axial, wrap-around, and normal directions, respectively. The pitch axis is located at two third the root chord station. The freestream Mach number and Reynolds number are 0.3 and 0.45×10^6, respectively. The initial conditions used for the blowing case correspond to the solution of a stationary wing impulsively inserted into the freestream conditions. The wing is held at an angle of attack of 30° for 17,000 time steps which equals a total dimensionless time of 17 when $\Delta t = 0.001$.

Figure 7.2 shows spanwise pressure coefficient distributions for three axial locations; x = 0.3, 0.6, and 0.9. The vortex breakdown covers all the three axial station, as it is obvious from the pressure coefficient distributions. The pressure coefficient is flattening at x = 0.3. Figure 7.3 shows the axial velocity contours at x = 0.3, 0.6 and 0.9. The flow is decelerated inside the vortex core region showing negative axial velocity values. While the axial velocity inside the vortex core at x = 0.3 is equal – 0.14, its value at x = 0.6 and 0.9 is – 0.12 and – 0.08; respectively.

Figure 7.4 shows the cross-flow instantaneous streamlines at x =0.3, 0.6, and 0.9. Although vortex breakdown covers the three locations, the vortex core size is different at

the three locations. Also secondary vortices can be seen from Fig. 7.4 at x = 0.9. Figure 7.5 shows Mach number contours at x = 0.3, 0.6, and 0.9. The flow is slightly asymmetric as can be seen from the different Mach number values on both sides of the plane of symmetry. Figure 7.6 shows the particle traces and Mach number contours over the delta wing. It is obvious from this figure that the vortex breakdown covers most of the wing surface. The spiral motion of the particles becomes stronger as the particles move downstream.

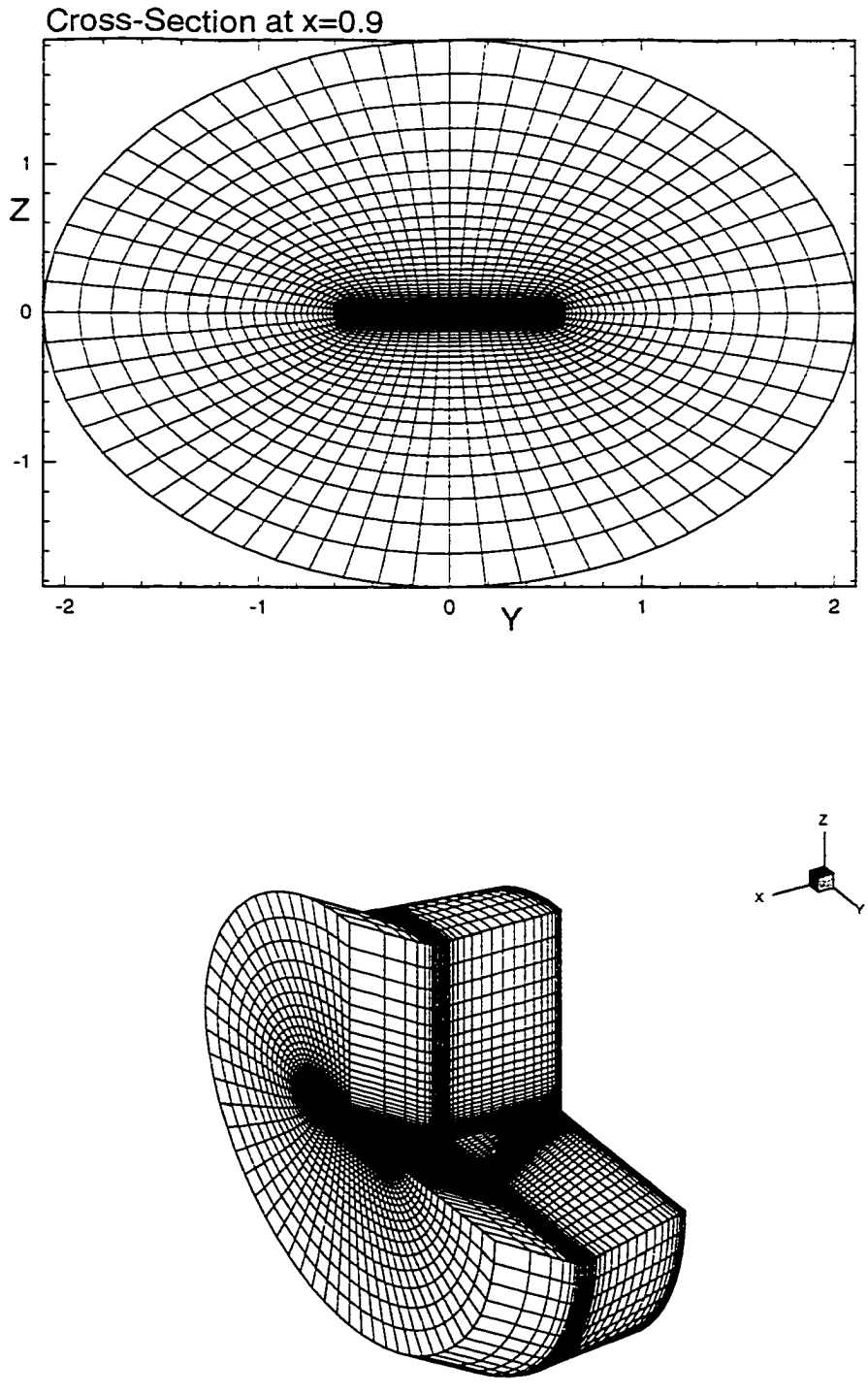

Figure 7.1: Portion of the three dimensional grid and cross section at x = 0.9

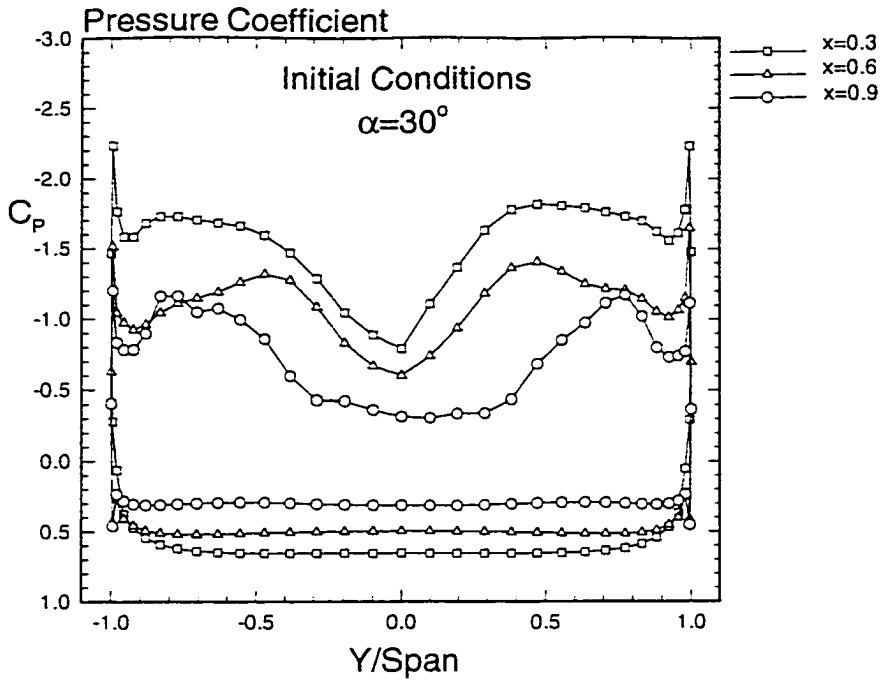

Figure 7.2: Spanwise pressure coefficient distribution for $\alpha = 30°$

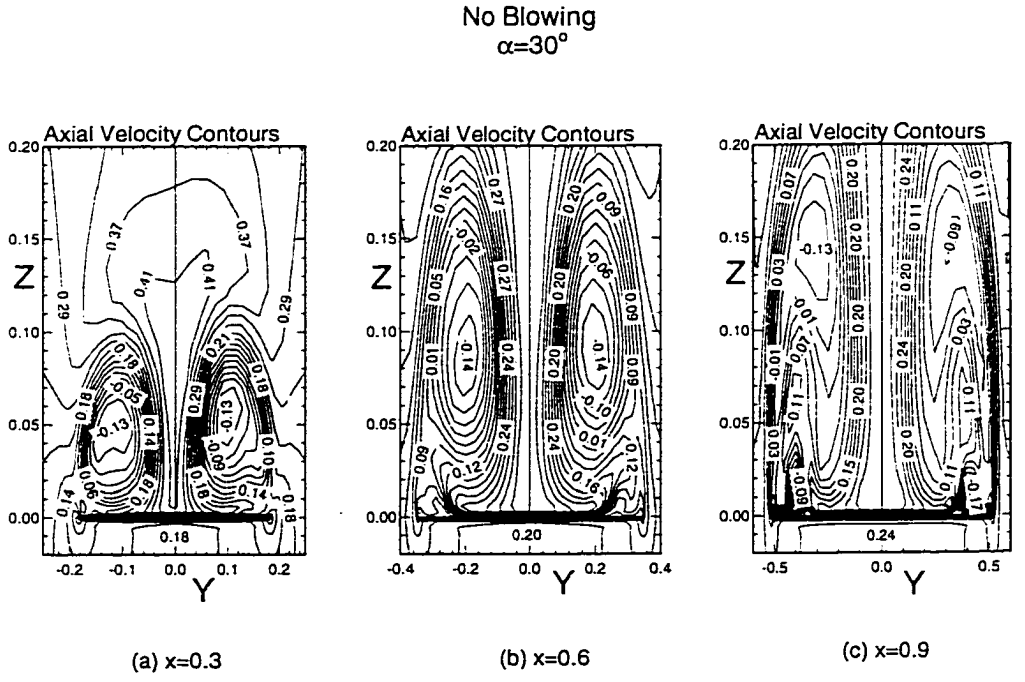

Figure 7.3: Axial velocity contours for $\alpha = 30°$

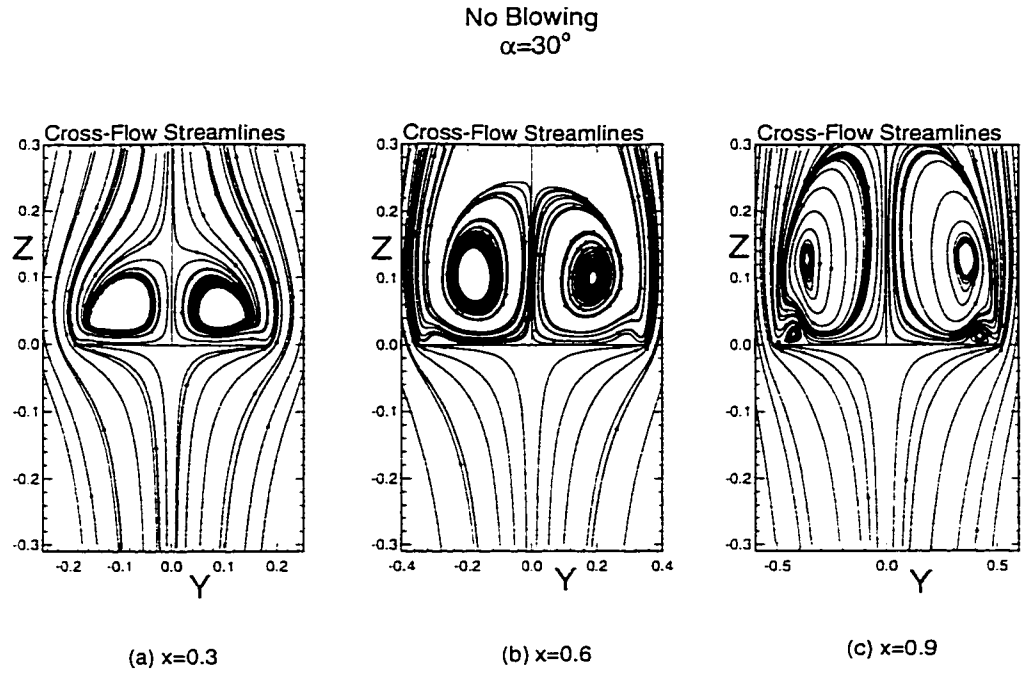

Figure 7.4: Cross-flow instantaneous streamlines at $\alpha = 30^{o}$ and (a) x=0.3, (b) x=0.6, and (c) x=0.9

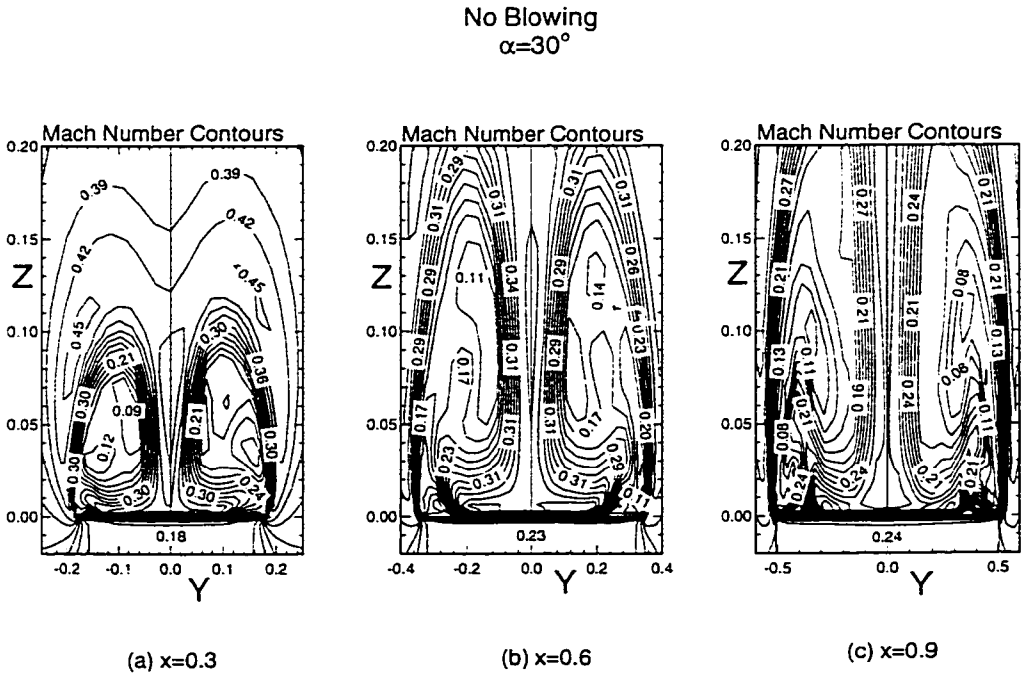

Figure 7.5: Mach number contours for $\alpha = 30^{o}$

Figure 7.6: Particle traces and Mach number contours over the delta wing at $\alpha = 30°$

7.2 Blowing Solution

The blowing type used in the current study is a new blowing technique where the blowing ports are located at the trailing edge of the wing. The fluid is injected downstream with an angle to the axial direction equal to 20° downward. See Fig. 7.7. After applying the blowing, the lift coefficient has increased slightly from 1.2 to 1.37 but in the same time the drag coefficient has increased from 0.70 to 0.8. The lift-to-drag ratio is remained constant at 1.71. Figure 7.8 shows the lift and drag coefficients history before and after applying the current blowing technique.

Figure 7.9 shows spanwise pressure coefficient distributions for three axial locations; x = 0.3, 0.6, and 0.9. The pressure coefficient is flattening at x = 0.3 and its value on suction side is relatively smaller than the corresponding value of no blowing solution. Figure 7.10 shows the axial velocity contours at x = 0.3, 0.6 and 0.9. All the three locations indicate negative axial velocity inside the vortex core. The absolute value of the axial velocity inside the vortex core is higher than the no-blowing solution at all locations. After applying blowing the asymmetry of the flow starts as can be seen from Figures 7.9 and 7.10.

Figure 7.11 shows the cross-flow instantaneous streamlines at x = 0.3, 0.6, and 0.9. The vortex breakdown is strengthened at all locations. Also the original vortex has been broken into smaller vortices near the wing surface. Figure 7.12 shows Mach number contours at x =0.3, 0.6, and 0.9. The flow is asymmetric as can be seen from the different Mach number values on both sides of the plane of symmetry. Figure 7.13 shows the particle traces and Mach number contours over the delta wing. The iso-

surface contours show that the vortex core has been broken near trailing edge. The spiral motion of the particles is strengthened as the particles move downstream.

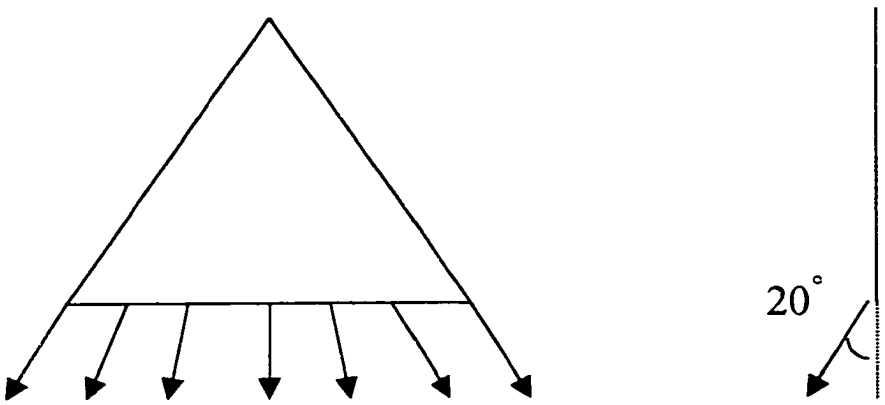

Figure 7.7: Schematic of the current blowing technique

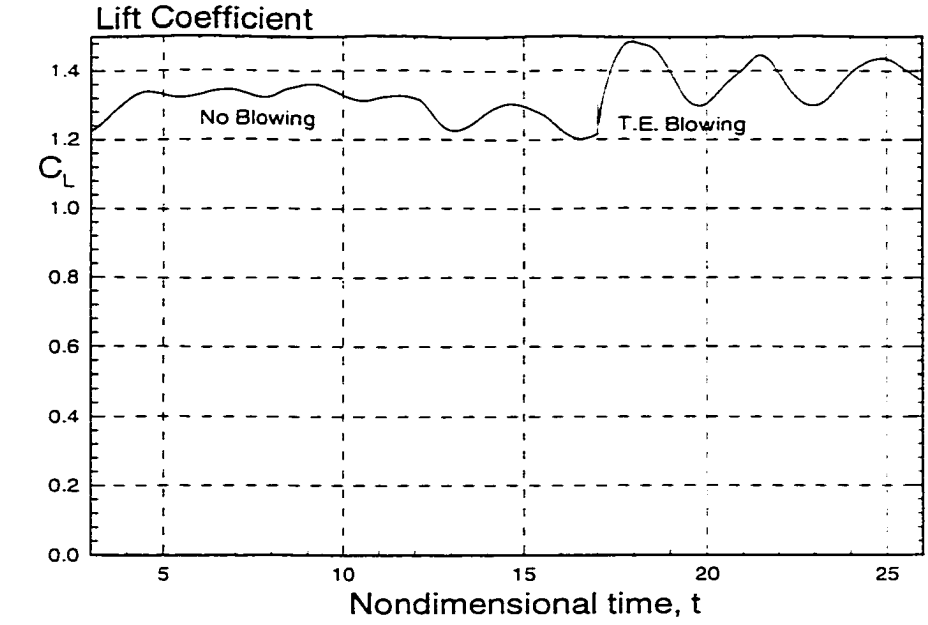

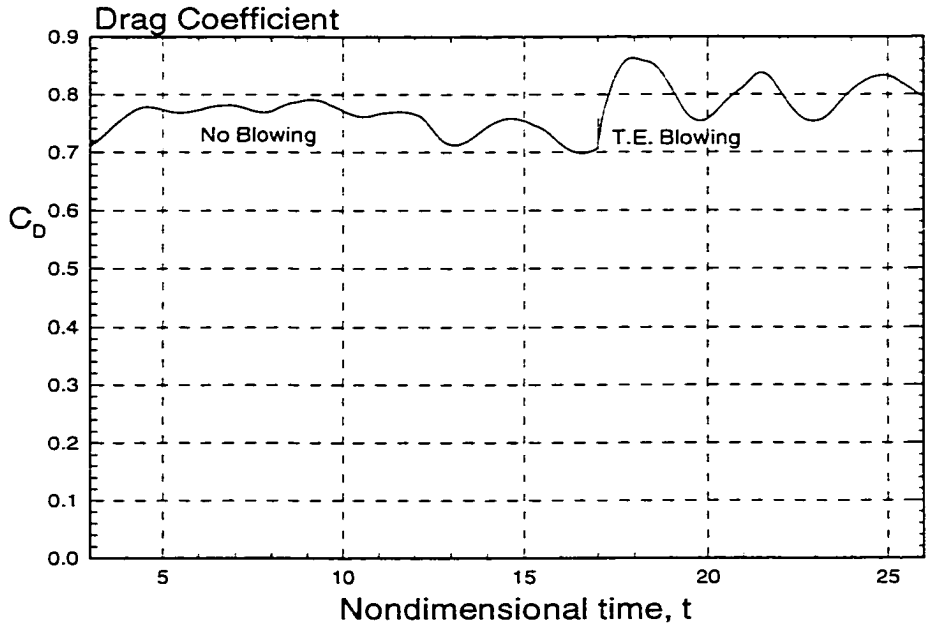

Figure 7.8: Lift and drag coefficient at $\alpha = 30^o$

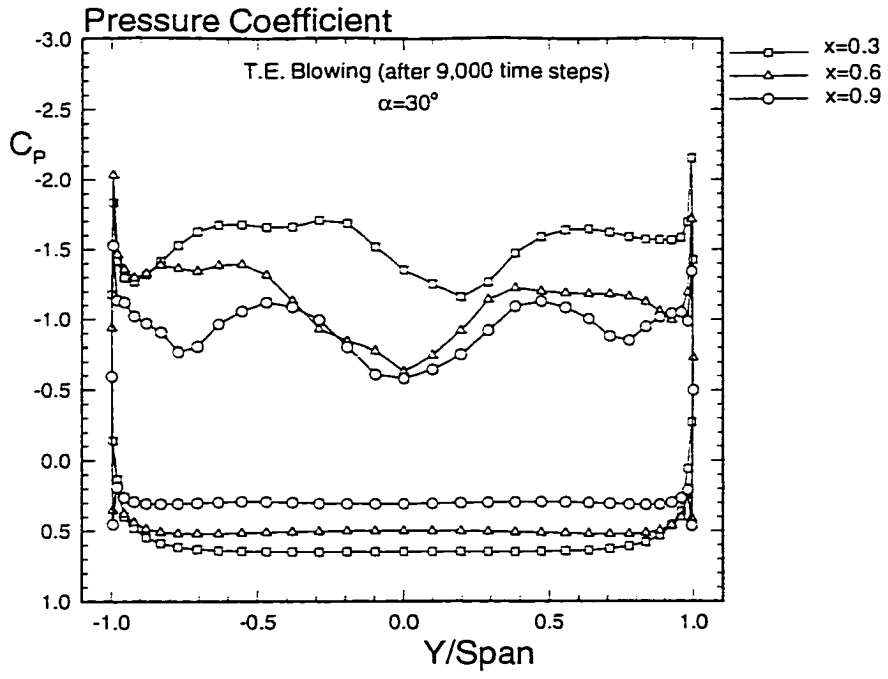

Figure 7.9: Spanwise pressure coefficient distribution for $\alpha = 30^o$

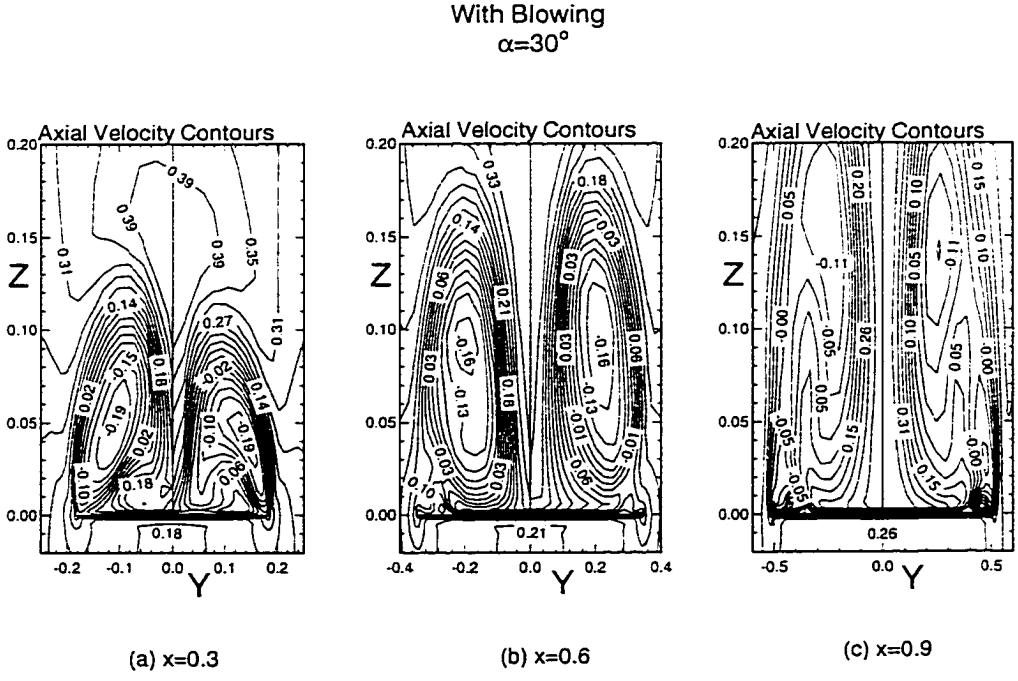

Figure 7.10: Axial velocity contours for $\alpha = 30^o$

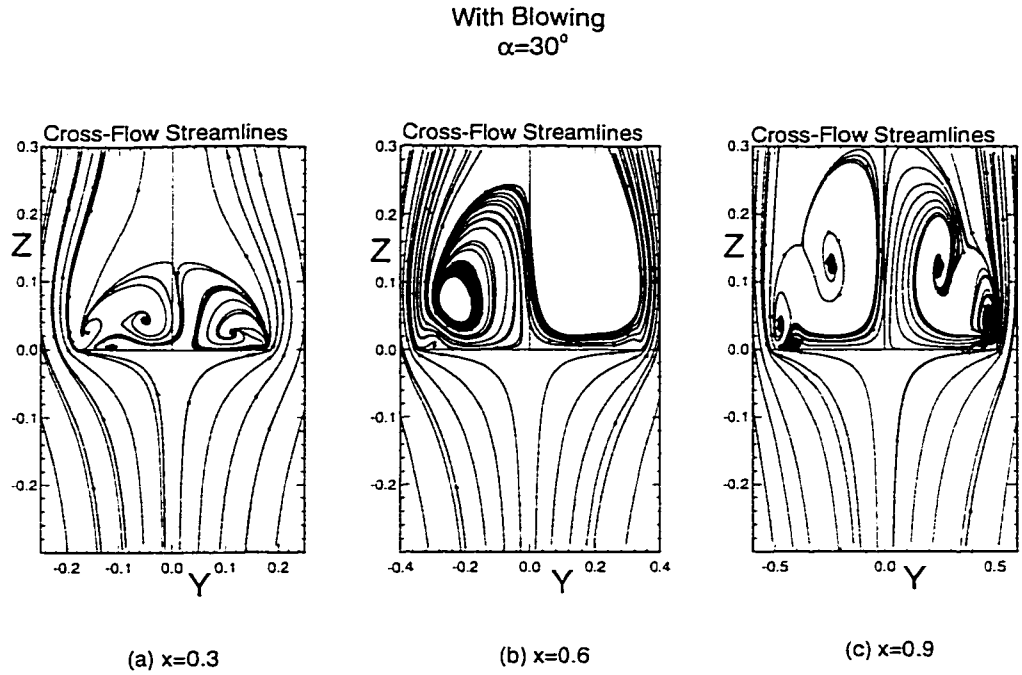

Figure 7.11: Cross-flow instantaneous streamlines at $\alpha = 30°$ and (a) x=0.3, (b) x=0.6, and (c) x=0.9

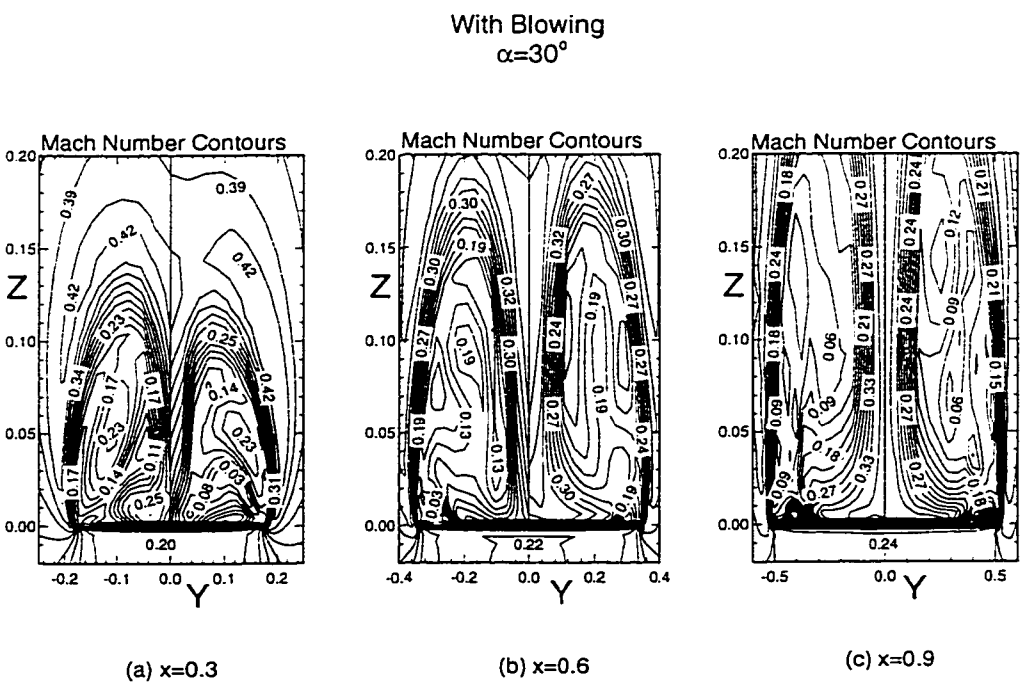

Figure 7.12: Mach number contours for $\alpha = 30°$

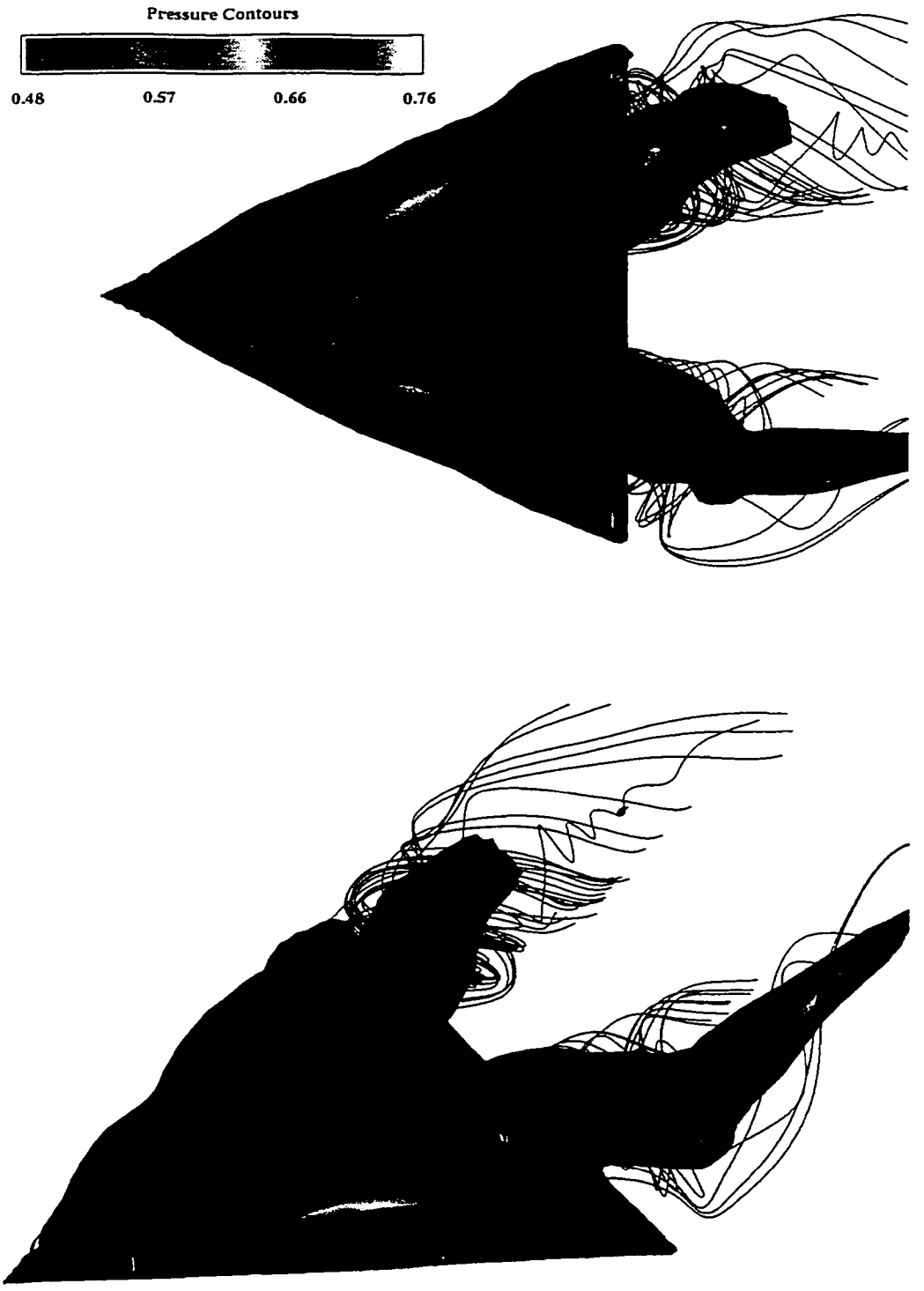

Figure 7.13: Particle traces and Mach number contours over the delta wing at $\alpha = 30°$

7.3 Summary

The concept of blowing to enhance aerodynamic performance at very large incidence was investigated. Blowing at the trailing edge with an angle equal to 20° downward was used. Both lift and drag coefficients were increased. The vortex breakdown has been strengthened and the vortex core has broken into small discrete vortices near the wing surface. Still there is a need to investigate other types of blowing. There are many parameters that can affect the blowing process (blowing rate, blowing ports location, continuous or pulsating, steady or unsteady blowing) and which should be investigated thoroughly.

CHAPTER 8

CONCLUSIONS AND RECOMMENDATIONS

8.1 Conclusions

Computational results provide complete information and details about the flowfield response, which was not available from existing experimental data. This investigation of the unsteady flow over a wide range of angles of attack provide crucial understanding of the variations of the leading edge vortex cores, their breakdown behavior and wing aerodynamic characteristics at very high angles of attack. The current study also shows that the computational solutions and results in the very high angle of attack range are obtainable. Such calculations were thought to be unattainable as recently as the 1980's.

8.1.1 Laminar Flow Solutions

8.1.1.1 Validation with Experimental Data

In general, the current predicted results were in very good agreement with the corresponding experimental data. The lift coefficient values were within the uncertainty error range of the experimental data. For the drag coefficient, the laminar results showed good agreement with the corresponding experimental data except at very high angles of attack ($\alpha > 60°$) where the difference between the predicted values and the experimental values reached about 24% maximum (not including the experimental uncertainty error). The differences were believed to be due to the grid resolution particularly at the trailing edge where the vortex breakdown crosses this location at

$\alpha = 39°$. As the angle of attack increased above this critical angle the vortex breakdown advanced upstream with an upward displacement and lateral expansion.

At low angles of attack, a tight vortex core developed at the leading edge of the wing. As the angle of attack increased, the vortex core expand until it broke down at the trailing edge around $\alpha = 39°$, due to the adverse axial pressure gradient. Then, the breakdown point moved upstream and expanding the size of the vortex core, due to the axial momentum loss. After the angle of attack reached $\alpha = 40°$, the breakdown moved upstream of the trailing edge and as the angle of attack increased the breakdown moved further upstream. In the same time, the vortex core pair flows expanded and coalesced. Flow asymmetry started also after breakdown moved upstream over the wing and increased with increasing the angle of attack. At $\alpha = 70°$ the breakdown moved significantly upstream overwhelming a larger area of the wing making this region a non-lifting area. The remaining area of the wing continued to generate a lift force. At $\alpha = 90°$, the whole wing was no longer generating any lift.

8.1.1.2 Fine Grid Solution

The grid resolution had a major effect in obtaining accurate results but unfortunately there was a trade-off between using fine grid and obtaining a highly accurate solution on one hand and obtaining a faster solution on the other hand. The fine grid solution gave better resolution of the flow details. Although the coarse grid was refined by adding few points in the wrap-around and normal directions (16 and 7 grid points), the resulting fine grid was able to capture the secondary vortices. Lift and drag coefficients were slightly different from those of the coarse grid solution.

8.1.1.3 Reduced Frequency Effect

As the reduced frequency increased, the lift and drag coefficient peaks increased. The vortex core expanded more rapidly as the reduced frequency was decreased, and early vortex breakdown occurred. Flow asymmetry was also pronounced as the reduced frequency decreased. These flow responses were attributed to the fact that as the reduced frequency decreased, the flow would have longer time to adjust to the forced wing motion. Aerodynamically, highly swept-back winged aircraft could fly safely (delayed vortex breakdown and consequently delayed stall) during maneuvers using very high reduced frequency values at high angles of attack.

8.1.2 Turbulent Flow Solutions

8.1.2.1 Results Using Baldwin-Lomax Model

Using Baldwin-Lomax turbulence model enhanced the computed C_L values. On the other hand, the computed C_D values were slightly enhanced. The good agreement with the experimental data has been improved up to $\alpha = 65°$. The turbulent model smoothed the pressure coefficient near the leading edge and only one suction peak was present in the flow, which corresponds to the primary vortex. The effects of secondary vortices disappeared from the pressure coefficient curves due to the thick turbulent boundary layer flow on the wing surface.

8.1.2.2 Results Using Spalart-Allmaras Model

Spalart-Allmaras produced good results compared to experimental data until $\alpha = 35°$, then the differences increased as α increased. The turbulent quantities were

applied in only one direction (normal) and a coarse grid was used in the investigation. The coarse grid was used because of the restrictions on computational costs. In general, Baldwin-Lomax model introduced some improvements of the computational results of the lift and drag coefficients in comparison with those of the Spalart-Allmaras model.

8.1.2.3 Pitch-Up Pitch-Down Sinusoidal Case

There was a substantial difference in the lift and drag coefficients between the upstroke and downstroke motion because of the hysteresis effects of the unsteady motion. As the aspect ratio increased the vortex breakdown at the trailing edge started at a lower angle of attack, in comparison with that of a low aspect ratio wing. Although the flow stayed symmetric in the pitch-up motion even at high angles of attack values, the asymmetry of the flow was obvious from the pitch-down motion at low angles of attack. Vortex breakdown occurred over a large portion of the wing surface for the pitch-down motion, which justified the decrease in lift coefficient during this part of the motion. The vortex core reformation was delayed during the pitch-down motion because of the hysteresis effects of the unsteady motion.

8.1.3 Flow Control

The vortex breakdown was strengthened and the vortex core was broken into small discrete vortices near the wing surface. Although the current blowing technique has enhanced the lift coefficient, it increases the drag coefficient.

8.2 Recommendations

The current study concentrated on sharp-edged delta wings and it is recommended in future work to include thickness and camber. Also, it is of great value if the current study could be tested using different reduced frequencies at various Mach and Reynolds numbers to see the effect of the last two parameters on the results and compare these results with the experimental data. The aspect ratio (sweep angle) effects should also be investigated. All the cases considered in the present study have zero sideslip angles. In future work, investigation of the unsteadiness behavior of delta wing at large amplitude pitching and with sideslip angle is recommended. The pitch/roll and pitch/yaw interaction should also be considered in future work.

Due to the strong vortex movement and breakdown over the wing surface, there is a need for the development of a dynamic, adaptive, fine grid resolution compatible with the vortex breakdown motion and deformation. The use of a fine mesh with high order turbulence models is of great importance. The turbulence model should be tailored to be suitable for large separated flows. Also applying the turbulent quantities in all coordinate directions is highly recommended. Moreover, a higher-order turbulence model may improve the predictions at very large angles of attack.

There is a need still to investigate other types of blowing. Also the use of unsteady blowing techniques is recommended for forced dynamic motion (pitching, rolling, and yawing).

REFERENCES
(In Alphabetical Order)

Abdelhamid, Y. A. and Kandil, O. A. (1998) "Reduced Frequency Effect on Supermaneuver Aircraft Having Delta Wing Planform," AIAA 36th Aerospace Science Meeting, Reno, NV, January 12-15.

Agrawal, S., Barnett, R. M., and Robinson, B. A. (1991) "Investigation of Vortex Breakdown on a Delta Wing Using Euler and Navier-Stokes Equations," Vortex Flow Aerodynamics, AGARD-CP-494, Paper #24.

Anglin, E. L. and Satran, D. (1980) "Effects of Spanwise Blowing on Two Fighter Airplane Configurations," Journal of Aircraft, Vol. 17, No. 12, pp. 883-889.

Ashenberg, J. 1987. "A Model for Vortex Breakdown on Slender Wings," AIAA Journal, Vol. 25, No. 12, pp. 1622-1624.

Atta, R. and Rockwell, D. (1987) "Hysteresis of Vortex Development and Breakdown on an Oscillating Delta Wing," AIAA Journal, Vol. 25, No. 11.

Baldwin, B. S. and Lomax, H. (1978) "Thin Layer Approximation and Algebraic Model for Separated Turbulent Flows," AIAA 16th Aerospace Science Meeting, AIAA Paper-78-257, Huntsville, Alabama, January 16-18.

Bannink, W. J. and Houtman, E. M. (1992) "Experimental and Computational Study of the Vortical Flow over a Delta Wing at High Angles of Attack," IUTAM Symposium Tokyo/Japan, Fluid Dynamics of High Angle of Attack, pp. 399-411.

Baron, A., Boffadossi, M., and De Ponte, S. (1991) "Numerical Simulation of Vortex Flows Past Impulsively Started Wings," Vortex Flow Aerodynamics, AGARD-CP-494, Paper #33.

Benjamin, T. B. (1962) "Theory of the Vortex Breakdown Phenomenon," Journal of Fluid Mechanics, Vol. 14, Part 4, pp. 593-629.

Beran, P. S. (1987) "Numerical Simulations of Trailing Vortex Bursting," AIAA 19th Fluid Dynamics, Plasma Dynamics and Lasers Conference, AIAA Paper 87-1313, June 8-10.

Biedron, T. R. and Rumsey, C. L. (1997) "CFL3D User's Manual: Version 5.0," NASA Langley Research Center, Hampton, VA, September, 2nd Edition.

Bossel, H. H. (1969) "Vortex Breakdown Flowfield," Journal of Physics of Fluids, Vol. 12, No. 3, pp. 498-508.

Bradley, R. G. and Wray, W. O. (1974) "A Conceptual Study of Leading edge-Vortex Enhancement by Blowing," Journal of Aircraft, Vol. 11, No. 1, pp. 33-38.

Brandon, J. M. (1991) "Dynamic Stall Effects and Applications to the High Performance Aircraft," Special Course on Aircraft Dynamics at High Angles of Attack: Experiments and Modeling," AGARD-R-776, paper #2.

Cassidy, J. J. and Falvey, H. T. (1970) "Observation of Unsteady Flow arising after Vortex Breakdown," Journal of Fluid Mechanics, Vol. 41, Part 4, pp. 727-736.

Cornelius, K. C. (1995) "Analysis of Vortex Bursting Utilizing Three-Dimensional Laser Measurements," Journal of Aircraft, Vol. 32, No. 2, pp. 297-306.

Degani, D. and Schiff, L. (1983) "Computation of Supersonic Viscous Flows Around Pointed Bodies at Large Incidence," AIAA 83-0034.

Ekaterinaris, J. A. and Schiff, L. B. (1995) "Navier-Stokes Solutions for an Oscillating Double-Delta Wing," Journal of Aircraft, Vol. 32, No. 2, pp. 228-296.

Elsenaar, A. and Hoeijimakers, H. W. M. (1991) "An Experimental Study of the Flow Over a Sharp-Edged Delta Wing at Subsonic and Transonic Speeds," Vortex Flow Aerodynamics, AGARD-CP-494, Paper #15.

Ericsson, L. E. (1992) "Some Challenges in High-Alpha Vehicle Dynamics," IUTAM Symposium Tokyo/Japan, Fluid Dynamics of High Angle of Attack, pp. 313-338.

Faler, J. H. and Leibovich, S. (1977) "Disrupted States of Vortex Flow and Vortex Breakdown," Journal of Physics of Fluids, Vol. 20, No. 9, pp. 1385-1400.

Gad-el-Hak, M. and Ho, C. (1986) "Unsteady Vortical Flow Around Three-Dimensional Lifting Surfaces," AIAA Journal, Vol. 24, No. 5, pp. 715-721.

Gad-el-Hak, M. and Blackwelder, R. (1985) " The Discrete Vortices from a Delta Wing," AIAA Journal, Vol. 23, No. 6, pp. 961-962

Gad-el-Hak, M. and Blackwelder, R. (1987) "Control of the Discrete Vortices from a Delta Wing," AIAA Journal, Vol. 25, No. 8, pp. 1042-1049.

Gal-Or, B. (1996) "Civilizing Military Thrust Vectoring Flight Control [CTV] to Maximize Transport Jets Flight Safety," Second Seminar on RRDPAE'96.

Gordnier, R. E. and Visbal, M. R. (1994) "Unsteady Vortex Structure over a Delta Wing," Journal of Aircraft, Vol. 31, No. 1, pp. 243-248.

Gordon, R. and Rom, J. (1985) "Calculation of Nonlinear Subsonic Characteristics of Wings with Thickness and Camber at High Incidence," AIAA Journal, Vol. 23, No. 6, pp. 817-825.

Gregoriou, G. (1982) "Modern Missile Design for High Angle of attack," High-Angle of attack Aerodynamics, AGARD-LSP-121, Paper #5.

Gu, W., Robinson, O., and Rockwell, D. (1993) "Control of Vortices on a Delta Wing by Leading edge Injection," AIAA Journal, Vol. 31, No. 7, pp. 1177-1186.

Guyton, R. W., Osborn, R. F., and LeMay, S. P. (1991) "Forebody Vortex Control Aeromechanics," AGARD-CP-497, Maneuvering Aerodynamics, Paper #16.

Hall, M. G. (1966) " The Structure of Concentrated Vortex Cores," Progress in Aeronautical Sciences, Vol. 7, pp. 53-110.

Hall, M. G. (1972) "Vortex Breakdown," Annual Review of Fluid Mechanics, Vol. 4, pp. 195-218.

Harvey, J. K. (1962) "Some Observations of the Vortex Breakdown Phenomenon," Journal of Fluid Mechanics, Vol. 14, pp. 585-592.

Henkes, R. A. W. M. and Bakker, P. G. (1997) "Boundary-Layer Separation in Aircraft Aerodynamics," Proceedings of the Seminar held on 6 February 1997 in Delft, Delft University Press.

Ho, C. M. and Huerre, P. (1984) "Perturbed Free Shear Layers," Annual Review of Fluid Mechanics, Vol. 16, January, pp. 365-424.

Hoeijimakers, H. W. M. (1991) "Modeling and Numerical Simulation of Vortex Flow in Aerodynamics," Vortex Flow Aerodynamics, AGARD-CP-494, Paper #1.

Hoeijimakers, H. W. M. (1992) "Aspects of the Modeling and Numerical Simulation of Leading edge Vortex Flow," IUTAM Symposium Tokyo/Japan, Fluid Dynamics of High Angle of Attack, pp. 185-196.

Hoeijimakers, H. W. M. and Vaatstra, W. (1983) "A Higher Order Panel Method Applied to Vortex Sheet Roll-Up," AIAA Journal, Vol. 21, No. 4, pp. 516-523.

Hoffmann, K. A. and Chiang, S. T. (1993) "Computational Fluid Dynamics for Engineers," Vol. I&II, A publication of Engineering Education System, Wichita, Kansas.

Huang, X. Z., Sun, Y. Z., and Hanff, E. S. (1997a) "Circulation Criterion to Predict Leading edge Vortex Breakdown over Delta Wings," AIAA –97-2265.

Huang, X. Z., Sun, Y. Z., and Hanff, E. S. (1997b) "Further Investigation of Leading edge Vortex Breakdown over Delta Wings," AIAA –97-2263.

Hummel, D. (1973) "Study of the Flow Around Sharp-Edged Slender Delta Wings with Large Angle of Attack," NASA Technical Translation, September, NASA TT F-15,107.

Hummel, D. (1979) "On the Vortex Formation Over a Slender Wing at Large Angles of Incidence," High Angle of Attack Aerodynamics, AGARD CP-247, Paper #15.

Hunt, B., A. M. and F.I.M.A. (1982) "The Role of Computational Fluid Dynamics in High Angle of attack Aerodynamics," High-Angle of attack Aerodynamics, AGARD-LSP-121, Paper #6.

Jarrah, M. A. (1987) "Low Speed Wind Tunnel Test Program for Delta Wings Oscillating in Pich to al Angle of Attack," Technical Report, Workshop II on Unsteady Separated Flow, U.S. Air Force Academy, July.

Jarrah, M. A. (1988) "Unsteady Aerodynamics of Delta Wings Performing Maneuvers to High Angle of Attack," Ph. D Dissertation, Stanford University.

Jarrah, M. A. (1989) "Low-Speed Wind-Tunnel Investigation of Flow About Delta Wings, Oscillating in Pitch to Very High Angle of Attack," AIAA-89-0295 27th Aerospace Sciences Meeting, Reno, Nevada, January 9-12.

Jarrah, M. A. and Ashley, H. (1989) "Impact of Flow Unsteadiness on Maneuvers and Loads of Agile Aircraft," AIAA-89-1282-CP 30th AIAA/ASME/ASCE/AHS/ASC Structures, Structural Dynamics and Materials Conference, Mobile, Alabama, April 3-5.

Johari, H., Orlinger, D. J., and Fitzpatrick, K. C. (1995) "Delta Wing Vortex Control via Recessed Angled Spanwise Blowing," Journal of Aircraft, Vol. 32, No. 4, pp. 804-810.

Kandil, H. A. (1993) "Navier-Stokes Simulation of Quasi-Axisymmetric and Three-Dimensional Supersonic Vortex Breakdown," Ph.D. Dissertation, Old Dominion University.

Kandil, O. A. (1986) "Computational Technique for Compressible Vortex Flows: Integral Equation Approach," Progress Report For the period May 16, 1985 to March 15, 1986, Old Dominion University.

Kandil, O. A. and Abdelhamid, Y. A. (1997) "Computation and Validation of Delta Wing Pitching Up to 90° Amplitude," AIAA-97-3573-CP, AIAA Atmospheric Flight Mechanics Conference, New Orleans, LA-August 11-13.

Kandil, O. A. and Chuang, H. A. (1988) "Unsteady Vortex-Dominated Flows around Maneuvering Wings over a wide Range of Mach Numbers," AIAA Paper 88-0317.

Kandil, O. A. and Kandil, H. A. (1994) "Pitching Oscillation of a 65-Degree Delta Wing in Transonic Vortex Breakdown Flow," AIAA-94-1426-CP, AIAA/ASME/ASCE/AHS/ASC Structures, Structural Dynamics and materials Conference, Hilton Head, SC- April 18-20, pp. 955-966.

Kandil, O. A. and Menzies, M. A. (1996) "Coupled Rolling and Pitching Oscillation Effects on Transonic Shock-Induced Vortex-Breakdown Flow of a Delta Wing," AIAA-96-0828 34th Aerospace Sciences Meeting and Exhibit, Reno NV- January 13-18.

Kandil, O. A. and Menzies, M. A., and Kandil, H. (1994) "Unsteady Transonic Flow Around a Delta Wing Undergoing Pitching and Rolling Oscillations," AIAA-94-1887-CP.

Kandil, O. A. and Salman, A. A. (1991) "Recent Advances in Unsteady Computations and Applications of Vortex Dominated Flows," 4th International Symposium on Computational Fluid Dynamics.

Kandil, O. A. and Yates, E. C. (1986) "Computation of Transonic Vortex Flow Past Delta Wings-Integral Equation Approach," AIAA Journal, Vol. 24, No. 11, pp. 1729-1736.

Kandil, O. A., Kandil, H. A., and Liu, C. H. (1992) "Critical Effects of Downstream Boundary Conditions on Vortex-Breakdown," AIAA Paper No. 92-2601.

Kandil, O. A., Kandil, H. A., and Liu, C. H. (1993) "Shock-Vortex Interaction over a 65-Degree Delta Wing in Transonic Flow," AIAA Paper No. 93-2973.

Kandil, O. A., Kandil, H. A., and Liu, C. H. (1993) "Supersonic Vortex Breakdown Over a Delta Wing in Transonic Flow," AIAA Paper No. 93-3472.

Kandil, O. A., Mook, D. T., and Nayfeh, A. H. (1976) "Nonlinear Prediction of the Aerodynamic Loads on Lifting Surfaces," Journal of Aircraft, Vol. 13, No. 1, pp. 22-28.

Kandil, O. A., Wong, T. C., and Kandil, H. A. (1990) "Computation and Control of Asymmetric Vortex Flow Around Circular Cones Using Navier-Stokes Equations," 17th Congress International Council of the Aeronautical Sciences, ICAS-90-3.5.3, Stockholm, Sweeden, September 9-14.

Kandil, O. A., Yang, Z., and Sheta, E. F. (1999) "Flow Control and Modification for Alleviating Twin-Tail Buffet," AIAA 37th Aerospace Sciences Meeting & Exhibit, AIAA Paper 99-0138, January 11-14, Reno, NV.

Kowal, H. J. and Vakili, A. D. (1998) "An Investigation of Unsteady Vortex Flow for a Pitching-Rolling 70 Delta Wing," 36th Aerospace Sciences Meeting & Exhibit, January 12-15, Reno, NV AIAA-98-0416.

Krause, E., Menne, S., and Liu, C. H. (1986) "Initiation of Breakdown in Slender Compressible Vortices," 10th International Conference on Numerical Methods in Fluid Dynamics, June 23-27, Beijing, China.

Lamar, J. E. (1986) "Nonlinear Lift Control at High Speed and High Angle of Attack Using Vortex Flow Technology," Special Course on Fundamentals of Fighter Aircraft Design, AGARD-R-740, paper #4.

Legendre, R. (1966) "Vortex Sheets Rolling-Up Along Leading edges of Delta Wings," Progress in Aeronautical Sciences, Vol. 7, pp. 7-33.

Leibovich, S. (1978) "The Structure of Vortex Breakdown," Annual Review of Fluid Mechanics, Vol. 10, pp. 221-246.

LeMay, S. P., Batill, S. M., and Nelson, R. C. (1990) "Vortex Dynamics on a Pitching Delta Wing," Journal of Aircraft, Vol. 27, No. 2, pp. 131-138.

Liu, C. H. and Hsu, C. H. (1992) "Calculations of Separated Vortex Flows at Low Speed for Low-Aspect-Ratio Wings," IUTAM Symposium Tokyo/Japan, Fluid Dynamics of High Angle of Attack, pp. 353-362.

Longo, J. M. A. (1992) "Simulation of Complex Inviscid and Viscous Vortex Flow," IUTAM Symposium Tokyo/Japan, Fluid Dynamics of High Angle of Attack, pp. 363-370.

Lowson, M. V. and Riley, A. J. (1995) " Vortex Breakdown Control by Delta Wing Geometry," Journal of Aircraft, Vol. 32, No. 4, pp. 832-838.

Luat T. Nguyen, Raymond D. Whipple, and Jay M. Brandon, (1986) "Recent Experiences of Unsteady Aerodynamic Effects on Aircraft Flight Dynamics at High Angle of Attack," AGARD-CP-386, Paper #28.

Luckring, J. M. (1991) "Recent Progress in Computational Vortex-Flow Aerodynamics," Vortex Flow Aerodynamics, AGARD-CP-494, Paper #6.

Malcolm, G. N. (1991) "Forebody Vortex Control," Special Course on Aircraft Dynamics at High Angles of Attack: Experiments and Modeling," AGARD-R-776, paper #6.

Malcolm, G. N. and Ng, T. T. (1991) "Aerodynamic Control of Fighter Aircraft by Manipulation of Forebody Vortices," AGARD-CP-497, Maneuvering Aerodynamics, Paper #15.

Mangler, K. W. and Smith, J. H. B. (1959) "A Theory of the Flow past a Slender Wing with Leading edge Separation," Proc. Roy. Soc. London, Vol. 251, pp. 200-217.

McLachlan, B. G. (1989) "Study of a Circulation Control Airfoil with Leading/Trailing-Edge Blowing," Journal of Aircraft, Vol. 26, No. 9, pp. 817-821.

Menzies, M. A. (1996) "Unsteady, Transonic Flow Around Delta Wings Undergoing Coupled and Natural Modes Response- A Multidisciplinary Problem," Ph.D. Dissertation, Old Dominion University.

Menzies, M., Kandil, O., and Kandil, H. (1995) "Forced Rolling Oscillation of a 65° Delta Wing in Transonic Vortex-Breakdown Flow," AIAA-95-1771-CP.

Meyer, J. and Seginer, A. (1994) "Effects of Periodic Spanwise Blowing on Delta Wing Configuration Characteristics," AIAA Journal, Vol. 32, No. 4, pp. 708-715.

Miau, J. J., Kuo, K. T., Liu, W. H., Hsieh, S. J., and Chou, J. H. (1995) " Flow Development Above 50-Deg Sweep Delta Wings with Different Leading edge Profiles," Journal of Aircraft, Vol. 32, No. 4, pp. 787-794.

Miller, D. S. and Wood, R. M. (1985) "Leeside Flow over Delta Wings at Supersonic Speeds,""NASA TP-2430.

Moreira, J. and Johari, H. (1995) "Delta Wing Vortex Manipulation Using Pulsed and Steady Blowing During Ramp Pitching," AIAA Paper, AIAA-95-1817-CP.

Nakamura, Y., Nakajima, Y., and Jia, W. (1992) "Aerodynamic Characteristics of Thick Delta Wing," IUTAM Symposium Tokyo/Japan, Fluid Dynamics of High Angle of Attack, pp. 375-382.

Nayfeh, A. H., Elzebda, J. M., and Mook, D. T. (1989) "Analytical Study of the Subsonic Wing-Rock Phenomenon for Slender Delta Wings," Journal of Aircraft, Vol. 26, No. 9, pp. 805-809.

Nelson, R. C. (1991) "Unsteady Aerodynamics of Slender Wings," Special Course on Aircraft Dynamics at High Angles of Attack: Experiments and Modeling," AGARD-R-776, paper #1.

Nelson, R. C. and Visser, K. D. (1991) "Breaking Down the Delta Wing Vortex," Vortex Flow Aerodynamics, AGARD-CP-494, Paper #21.

Nelson, R. C., Arena Jr., A. S., and Thompson, S. A. (1991) "Aerodynamic and Flowfield Hysteresis of Slender Wing Aircraft Undergoing Large-Amplitude Motions," Maneuvering Aerodynamics, AGARD-CP-497, Paper #3.

Newsome, R. W. and Kandil, O. A. (1987) "Vortical Flow Aerodynamics-Physical Aspects and Numerical Simulation," AIAA 25th Aerospace Sciences Meeting, AIAA Paper 87-0205.

Orlik-Ruckemann, K. J. (1982) "Unsteady Aerodynamics and Dynamic Stability at High Angles of Attack," High-Angle of attack Aerodynamics, AGARD-LSP-121, paper #8.

Payne, F. M., Ng, T. T., and Nelson, R. C. (1988) "Visualization and Wake Surveys of Vortical Flow over a Delta Wing," AIAA Journal, Vol. 26, No. 2, pp. 137-143.

Polhamus, E. C. (1971) "Predictions of Vortex-Lift Characteristics by a Leading edge Suction Analogy," Journal of Aircraft, Vol. 8, No. 4, pp. 193-199.

Rediniotis, O. K., Klute, S. M., Hoang, N. T., and Telionis, D. P. (1992) "Pitching-Up Motions of Delta Wings," 30th Aerospace Sciences Meeting & Exhibit, January 6-9, Reno, NV AIAA-92-0278.

Rom, J. (1992) "High Angle of Attack Aerodynamics," 1st. Ed. Springer-Verlag, New York.

Roy, M. (1966) "On the Rolling-Up of the Conical Vortex Sheet above a Delta Wing," Progress in Aeronautical Sciences, Vol. 7, pp. 1-5.

Salman, A. A. (1992) "Unsteady Euler and Navier-Stokes Computations Around Oscillating Delta Wing Including Dynamics," Ph.D. Dissertation, Old Dominion University.

Samoylovich, O. (1996) "Aerodynamic Configurations of Contemporary and Perspective Fighters," Second Seminar on RRDPAE'96.

Sarpkaya, T. (1971) "On Stationary and Traveling Vortex Breakdowns," Journal of Fluid Mechanics, Vol. 45, Part 3, pp. 545-559.

Sawada, K. and Inoue, O. (1992) "Computation of Flows over a 3D Wing with a Vortex Generator," IUTAM Symposium Tokyo/Japan, Fluid Dynamics of High Angle of Attack, pp. 159-170.

Seginer, A. and Saomon, M. (1986) "Performing Augmentation of a 60-Degree Delta Aircraft Configuration by Spanwise Blowing," Journal of Aircraft, Vol. 23, No. 11, pp. 801-807.

Sheta, E. F., Kandil, O. A., and Yang, Z. (1998) "Effectiveness of Flow Control for Alleviation of Twin-Tail Buffet," World Aviation Conference, September 28-30, Anaheim, CA.

Smith, J. H. B. (1966) "Theoretical Work on the Formation of Vortex Sheets," Progress in Aeronautical Sciences, Vol. 7, pp. 35-51.

Solignac, J. L., Pagan, D., and Molton, P. (1989) "Experimental Study of Incompressible Flow on the Upper Surface of a Delta Wing," La Recherche Aerospatiale, English Edition, No. 1989-6, PP. 47-65.

Soltani, M. R. (1992) "An Experimental Study of the Relationship Between Forces and Moments and Vortex Breakdown on a Pitching Delta Wing," Ph.D. Dissertation, Dept. of Aeronautical and Astronautical Engineering, Univ. of Illinois, Urbana-Champaign, IL.

Soltani, M. R. and Bragg, M. B. (1988) "Experimental Measurements on an Oscillating 70-Degree Delta Wing in Subsonic Flow," AIAA 6th Applied Aerodynamics Conference, Williamsburg, VA, June 6-8, AIAA-88-2576-CP.

Soltani, M. R. and Bragg, M. B. (1990) "Measurements on an Oscillating 70-Deg Delta Wing in Subsonic Flow," Journal of Aircraft, Vol. 27, No. 3, pp. 211-217.

Soltani, M. R. and Bragg, M. B. (1993) "Early Vortex Burst on a Delta Wing in Pitch," AIAA Journal, Vol. 31, No. 12.

Stahl, W. H., Mahmood, M., and Asghar, A. (1992) "Experimental Investigations of the Vortex Flow on Delta Wings at High Incidence," AIAA Journal, Vol. 30, No. 4, pp. 1027-1032.

Thomas, J.L., Krist, S.T., and Anderson, W. K. (1990) "Navier-Stokes Computations of Vortical Flows Over Low-Aspect-Ratio Wings," AIAA Journal, Vol. 28, No. 2.

Thompson, S. A., Batill, S. M., and Nelson, R. C. (1991) "The Separated Flowfield on a Slender Delta Wing Undergoing Transient Pitching Motions," Journal of Aircraft, Vol. 28, No. 8, pp. 489-495.

Tobak, M. and Peake, D. J. (1982) "Topology of Three-Dimensional Separated Flows," Annual Review of Fluid Mechanics, Vol. 14, pp. 61-85.

Wendt, J. F. (1982) "Compressibility Effects on Flows Around Simple Components," High-Angle of attack Aerodynamics, AGARD-LSP-121, paper #7.

Wentz, W. H. and Kohlman, D. L. (1971) "Vortex Breakdown on Slender Sharp-Edged Wings," Journal of Aircraft, Vol. 8, No. 3, pp. 156-161.

Werle, H. (1958) "Aperçu sur les Possibilités Expérimentales du Tunnel Hydrodynamique a Visualization de l'O.N.E.R.A.," ONERA Tech. Note 48.

Werle, H. (1982) "Flow Visualization Techniques for the Study of High Incidence Aerodynamics," High-Angle of attack Aerodynamics, AGARD-LSP-121, paper #1.

Wong, T. C. (1991) "Prediction and Control of Asymmetric Vortical Flows Around Slender Bodies Using Navier-Stokes Equations," Ph.D. Dissertation, Old Dominion University.

Wood, N. J. and Roberts, L. (1988) "Control of Vortical Lift on Delta Wings by Tangential Leading Edge Blowing," Journal of Aircraft, Vol. 25, No. 3, pp. 236-243.

Wood, N. J., Roberts, L., and Celik, Z. (1990) "Control of Asymmetric Vortical Flows over Delta Wings at High Angle of Attack," Journal of Aircraft, Vol. 27, No. 5, pp. 429-435.

Yeh, D. T., Tavella, D. A., and Roberts, L. (1988) "Navier Stokes Computation of the Flow Field over Delta Wings with Spanwise Leading Edge Blowing," AIAA paper 88-2558-CP.

Yoshihara, H. (1986.) "Design of Wings and Wing/Body Configurations for Transonic and Supersonic Speeds," Special Course on Fundamentals of Fighter Aircraft Design, AGARD-R-740, paper #3.

Young, A. D. (1983) "Symposium on Aerodynamics of Vortical Type Flows in Three Dimensions," Fluid Dynamics Panel, Aerodynamics of Vortical Type Flows in Three Dimensions, AGARD-CP-342, pp. RTD.

VITA

Yahia Ahmed Abdelhamid was born in Maadi, Cairo, Egypt on September 28, 1967 to the family of Ahmed Abdelhamid and Mrs Fawzia Mohammad. He attended Cairo University where he graduated with his Bachelor of Science (with Honor Degree) in Aerospace Engineering in May of 1990. He received his Master of Science in Aerospace Engineering from Cairo University in October of 1993. Between June of 1990 and October of 1990 he worked as a stress analysis engineer in an aircraft factory in Cairo. Between October of 1990 and December of 1994, he worked as an Assisant Lecturer in Faculty of Engineering, Aerospace Engineering Department at Cairo University where he taught several engineering courses. Since January of 1995, Mr. Abdelhamid has pursued a doctoral degree program in Aerospace Engineering at Old Dominion University in Norfolk, Virginia in the area of Unsteady Aerodynamics of Supermaneuver Delta Wing.